

國立交通大學
土木工程學系碩士班
碩士論文

條形振動夯實造成砂土密度及土壓力變化
Variation of Soil Density and Earth Pressure
due to a Strip Compaction

研究生：簡煜倫
指導教授：方永壽 博士

中華民國九十六年九月

條形振動夯實造成砂土密度及土壓力變化

Variation of Soil Density and Earth Pressure due to a Strip Compaction

研究生：簡煜倫

Student : Yu-Lun Chien

指導教授：方永壽 博士

Advisor : Dr. Yung-Show Fang

國立交通大學土木工程學系碩士班

碩士論文

A Thesis

Submitted to the Department of Civil Engineering

College of Engineering

National Chiao Tung University

in Partial Fulfillment of the Requirements

for the Degree of

Master of Engineering

in Civil Engineering

September, 2007

Hsinchu, Taiwan, Republic of China

中華民國九十六年九月

條形振動夯實造成砂土密度及土壓力變化

研究生：簡煜倫

指導教授：方永壽 博士

國立交通大學土木工程學系碩士班

摘要

本論文以實驗方法探討條形振動夯實造成砂土密度和土壓力的變化。本研究以氣乾之渥太華砂為回填土，回填土高 1.5 公尺。回填土初始相對密度(D_r)為 34%。為了在實驗室模擬雙向平面應變的情況，本研究採用塑膠膜潤滑層來降低砂土和填砂槽側牆間的摩擦力。本研究進行一連串相關的實驗，來探察振動夯實對砂土所產生的影響。這些影響包括夯實後土壤表面的沉陷、相對密度的變化和夯實前後的垂直和側向殘餘土壓力。根據實驗結果，本研究獲得以下幾項結論：

1. 對於疏鬆砂土，土體內的垂直土壓力和水平土壓力可分別以 $\sigma_v = \gamma z$ 和 Jaky 公式來進行合理的估算。
2. 隨著夯實機夯實趟數的增加，條形夯實區之地表沉陷量隨之增大。地表沉陷量和夯實趟數之間的關係可以用雙曲線的模式來模擬。
3. 砂土的相對密度變化等高線範圍，會隨著夯實趟數增加而擴大。
4. 垂直土壓力變化量的等高線近似於同心圓的形狀，而殘餘垂直土壓力 $\Delta\sigma_v$ 會由圓心區域向外逐漸減少。土體內最大 $\Delta\sigma_v$ 值會隨著夯實趟數增加而增大。
5. 在夯實機夯實 1 和 2 趟後，殘餘水平土壓力 $\Delta\sigma_h$ 的等高線會形成兩個較高的應力區，水平土壓力變化量會由中心區域逐漸減少。然而在夯實機夯實 4 和 8 趟後，殘餘水平土壓力的等高線則近似於一個同心圓的形狀。夯實影響的區域 ($\Delta\sigma_h = 0.2 \text{ kN/m}^2$ 應力等高線) 深度會隨著夯實能量增加而增大。
6. 在夯實一趟後，土壤所受夯實影響的機制可以用基礎下方土壤之局部剪力破壞

的情況來解釋。然而，當夯實趟數增加到 8 趟後，被夯實土壤之機制可用方形鋼樁以振動打樁機貫入砂質地盤的情況來模擬。

關鍵字： 砂土、模型試驗、夯實、沉陷、相對密度、土壓力



Variation of Soil Density and Earth Pressure due to a Strip Compaction

Student : Yu-Lun Chien

Advisor : Dr. Yung-Show Fang

Institute of Civil Engineering

National Chiao Tung University

Abstract

This paper studies the variation of soil density and earth pressure due to the strip compaction with a vibratory compactor. In this study, dry Ottawa sand was used as backfill material, and the height of backfill was 1.5 m. The initial relative density of the backfill (D_r) was 34 %. To simulate a 2-way plane strain condition in the laboratory, the friction between the soil and sidewalls of the soil bin was reduced as much as possible. Experiments were conducted to investigate the effects of soil densification with a vibratory compactor. The surface settlement and change of relative density were measured after compaction. The vertical and horizontal stresses in the soil mass were measured before and after compaction. Based on the test results, the following conclusions can be drawn.

1. For loose sand, the vertical and horizontal earth pressure in the soil mass could be properly estimated with the equation $\sigma_v = \gamma z$ and Jaky's equation, respectively.
2. The surface settlement increased with the increasing number of passes of the compactor. The relationship between the surface settlement and the number of passes of the compactor could be modeled by the hyperbolic model.
3. After compaction, the range of contours of relative density ($D_r = 36\%$) would become larger with increasing number of passes.
4. The contours of $\Delta\sigma_v$ were analogous to concentric circles, and the $\Delta\sigma_v$ would

decrease gradually from the central region. The vertical stress increment $\Delta\sigma_v$ increased with increasing number of passages of the compactor.

5. The contours of $\Delta\sigma_h$ formed two circles of high stresses and $\Delta\sigma_h$ decreased gradually from the center region after the first and the second passes of compactor. The contours of $\Delta\sigma_h$ were analogous to concentric circles after 4 and 8 passes of the compactor. The depth of the compaction-induced zone increased with increasing compaction energy input.
6. Based on the test results, the mechanism of soils after the first pass of the compactor could be explained by local shear failure. However, the mechanism of soils after 8 passes of the compactor could be simulated by a steel square pile driven in sand with a vibratory hammer.



Keywords: sand, model test, compaction, settlement, relative density, earth pressure.

Acknowledgements

The author wishes to give his sincere appreciation to his advisor, Dr. Yung-Show Fang for his continuous encouragement, enthusiastic support and helpful discussions in the past two years. The author also felt a great gratitude to the members of his supervisory committee, Dr. Ching-Chuan Huang, Dr. Tsang-Jiang Chen for their valuable suggestions.

Appreciation is extended to all my friends and classmates, especially for Mr. Shih-Da Hsu, Mr. Hao-Chen Chang, Mr. Chuan-Te Wu, Mr. Yung-Cheng Cheng, Mr. Pai-Shuo Chen, Mr. Sheng-Feng Huang for their encouragement and assistance.

Finally, the author would dedicate this thesis to his parents, sisters and brother for their continuing encouragement and moral support.

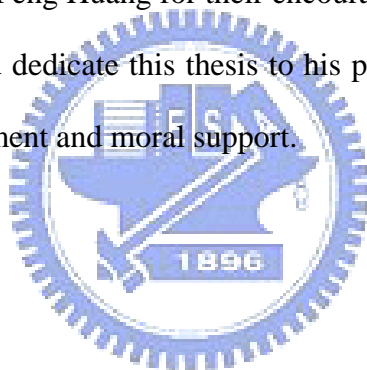


Table of Contents

	Page
Abstract (in Chinese)	i
Abstract	iii
Acknowledgements	v
Table of Contents	vi
List of Tables	ix
List of Figures	x
List of Symbols	xviii
Chapter 1 Introduction	1
1.1 Objectives of Study	1
1.2 Research Outline	2
1.3 Organization of Thesis	3
Chapter 2 Literature Review	4
2.1 Earth Pressure At-Rest	4
2.1.1 Coefficient of Earth Pressure At-Rest	4
2.1.2 Jaky's Formula	6
2.2 Effects of Soil Compaction on Earth Pressure	7
2.2.1 Study of Duncan and Seed	7
2.2.2 Study of Chen	9
2.3 Elastic Solutions for a Strip Surface Loading	10
2.4 Ultimate Bearing Capacity of Shallow Footing	11
2.5 Stresses in Soil during Penetration Test	12
2.6 Density Change due to Compaction	14

	Page
Chapter 3 Experimental Apparatus	15
3.1 Soil Bin	15
3.2 Soil Pressure Transducer	16
3.3 Data Acquisition System	17
3.4 Vibratory Compactor	17
Chapter 4 Backfill Characteristics	18
4.1 Backfill Properties	18
4.2 Reduction of Wall Friction	19
Chapter 5 Test Results for Loose Sand	21
5.1 Testing Procedure	21
5.2 Distribution of Soil Density	22
5.2.1 Air-Pluviation of Ottawa Sand	22
5.2.2 Uniformity of Soil Density	23
5.3 Distribution of Earth Pressures	23
Chapter 6 Surface Settlement and Density Change due to Compaction	25
6.1 Testing Procedure	25
6.2 Pilot Tests	26
6.3 Surface Settlement	28
6.4 Change of Relative Density	28
Chapter 7 Change of Vertical Stresses due to Compaction	31
7.1 Testing Procedure	31
7.2 Vertical Stress Distribution under Compaction Strip	32
7.3 Vertical Stress Change on Intermediate Principal Plane	32

	Page
Chapter 8 Change of Horizontal Stresses due to Compaction ...	34
8.1 Horizontal Stress Distribution under Compaction Strip	34
8.2 Horizontal Stress Change on Intermediate Principal Plane	35
8.3 Mechanism of Soils under Strip Compaction	36
8.3.1 Mechanism after First Pass of Compactor	36
8.3.2 Mechanism after 8 Passes of Compactor	37
Chapter 9 Conclusions	39
References	40
Tables	44
Figures	49
Appendix A: Calibration of Soil Pressure Transducers	149
Appendix B: Operation of Softwares Surfer 8 and Grapher 7	163
Appendix C: Test Results at Grid Points	173
Appendix C1: Relative Density of Sand at Grid Points	174
Appendix C2: $\Delta\sigma_v$ in Soil Mass at Grid Points	178
Appendix C3: $\Delta\sigma_h$ in Soil Mass at Grid Points	182

List of Tables

Number	Page
2.1 Terzaghi's Bearing Capacity Factors (after Kumbhojkar,1993)	44
3.1 Technical Information of the Eccentric Motor	45
4.1 Properties of Ottawa Sand (after Hou, 2006)	46
6.1 Relationship between the Surface Settlement and Number of Pass (a) S_{max} divided into Five Equal Parts and the Corresponding Number of Passes (b) 1, 2, 4, and 8 Compactor Passes and Corresponding Surface Settlement	47
6.2 Differences between Test Results from the Laboratory and Test Results from the Field	48



List of Figures

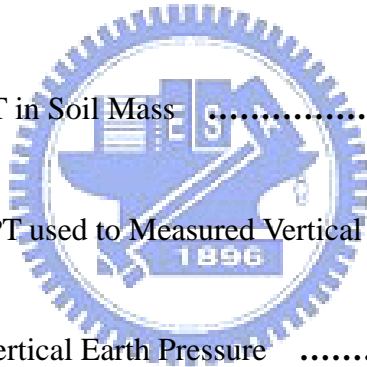
Number	Page
1.1 Compaction of Soil with Vibratory Compactor	49
2.1 Development of in-situ Stresses	50
2.2 Principal Stresses in a Soil Element	51
2.3 Jaky's Formulation of the Relationship between K_o on OC and ϕ Mobilized in OAB (after Mesri and Hayat, 1993)	52
2.4 Basic Components of Hysteretic K_o -Loading/Unloading Model (after Duncan and Seed, 1986)	53
2.5 Comparison between Final Pressure Distributions Based on Incremental Analysis and Hand Solution (after Duncan and Seed, 1983)	54
2.6 Distribution of Horizontal Earth Pressure after Compaction (after Chen, 2002)	55
2.7 Horizontal Earth Pressure Estimated with Various Methods after Compaction (after Chen, 2002)	56
2.8 Uniform Vertical Loading on an Infinite Strip	57
2.9 Stress beneath a Strip (after Jurgenson, 1934)	58
2.10 Bearing Capacity Failure in Soil under a Rough Rigid Continuous Foundation (after Terzaghi, 1943)	59
2.11 Definition of Failure Mode (after Vesic, 1973)	60
2.12 Mode of Foundation Failure in Sand (after Vesic, 1973)	61

Number	Page
2.13 Bearing Capacity Failure in Soil (after Vesic, 1973)	62
2.14 Ultimate Load-Carrying Capacity of Pile (after Meyerhof, 1976)	63
2.15 Variation of the Maximum Values of N_q^* with Soil Friction Angle ϕ' (after Meyerhof, 1976)	64
2.16 Influence Zone Assumed for Piles in Sand (after Yang, 2006)	65
2.17 Mean Range of Influence Zone for Pile in Clean Sand (after Yang, 2006)	66
2.18 Growth Curves for a Silty Clay – Relationship between Dry Unit Weight and Number of Passes of Three-Wheel Roller Compactor (after Johnson and Sallberg, 1960)	67
2.19 Vibratory Compaction of a Sand - Variation of Dry Unit Weight with Number of Roller Passes; Thickness of Lift = 2.45 m (after D'Appolonia, Whitman and D'Appolonia, 1969)	68
3.1 NCTU Non-Yielding Retaining-Wall Facility (after Chen, 2002)	69
3.2 Soil-Pressure Transducer (Kyowa BE-2KCM17) (after Chen, 2002) ..	70
3.3 Data Acquisition System	71
3.4 Side-View of Vibratory Soil Compactor	72
3.5 Vibratory Soil Compactor	73
3.6 Eccentric Motor with Eccentric Steel Plate (Mikasa KJ75) (after Wang, 2005)	74

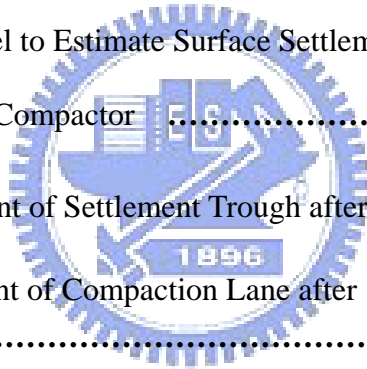
Number	Page
3.7 Vertical Dynamic Force Generated by Compactor as a Function of No. of Eccentric Plate (after Chen, 2002)	75
4.1 Grain Size Distribution of Ottawa Sand (after Hou, 2006)	76
4.2 Shear Box of Direct Shear Test Device(after Wu, 1992)	77
4.3 Relationship between Unit Weight γ and Internal Friction Angle ϕ (after Chang, 2000)	78
4.4 Lubrication Layer on the Walls	79
4.5 Schematic Diagram of Sliding Block Test (after Fang et al., 2004) ...	80
4.6 Sliding Block Test Apparatus (after Fang et al., 2004)	81
4.7 Variation of Interface Angle with Normal Stress(after Fang et al., 2004)	82
5.1 Relationship among Slot Opening, Drop Height, and Relative Density (after Ho, 1999)	83
5.2 Method to Control Drop Height = 1.0 m	84
5.3 Method to Control Slot Opening = 15 mm	85
5.4 Pluviation of Ottawa Sand into Soil Bin	86
5.5 Dimensions of Soil Density Cup (after Ho, 1999)	87
5.6 Soil Density Cup	88



Numbe	Page
5.7 Soil Density Cups Buried at Different Elevations	89
5.8 Arrangement of Soil Density Cups at Same Elevation	90
5.9 Density Control Test (a) Placement of Density Cup; (b) Measurement of Soil Mass in Cup	91
5.10 Distribution of Soil Density for Loose Sand	92
5.11 Locations of SPT to Measure Distribution of Vertical Earth Pressure ..	93
5.12 Placement of SPT in Soil Mass	94
5.13 Photograph of SPT used to Measured Vertical Stress	95
5.14 Distribution of Vertical Earth Pressure	96
5.15 Locations of SPT to Measure Distribution of Horizontal Earth Pressure	97
5.16 Photograph of SPT used to Measured Horizontal Stress	98
5.17 Distribution of Horizontal Earth Pressure	99
6.1 Testing Procedure of Strip Compaction	100
6.2 Compaction on Surface of Backfill	101

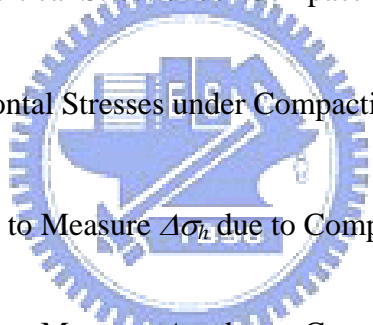


Number	Page
6.3	Definition of X-Y-Z Axes, XZ, YZ, and XY - Plane 102
6.4	Surface of Backfill: (a) before Compaction; (b) after Compaction 103
6.5	Measurement of Surface Settlement on (a) XZ – Plane; (b) YZ - Plane 104
6.6	Surface Settlement along Compaction Lane with Regions of Sidewall Effects 105
6.7	Surface Settlement along Compaction Lane after Compactor 106
6.8	Hyperbolic Model to Estimate Surface Settlement S as a Function of No. of Passes of Compactor 107
6.9	Surface Movement of Settlement Trough after First Pass of Compactor 108
6.10	Surface Settlement of Compaction Lane after 1, 2, 4 and 8 Passes of Compactor 109
6.11	Surface Settlement along Compaction Lane after First Pass of Compactor 110
6.12	Surface Settlement along Compaction Lane after 1, 2, 4 and 8 Passes of Compactor 111
6.13	Locations of Density Cups (Side - View) 112
6.14	Locations of Density Cups (Top - View) 113
6.15	Locations of Soil Density Cups at Same Elevation 114
6.16	Relative Density of Sand at Grid Points after 1 – Pass of Compactor .. 115



Number	Page
6.17	Contours of Relative Density after 1 – Pass of Compactor 116
6.18	Contours of Relative Density after 2 – Passes of Compactor 117
6.19	Contours of Relative Density after 4 – Passes of Compactor 118
6.20	Contours of Relative Density after 8 – Passes of Compactor 119
6.21	Comparison between Test Results from Laboratory and Test Results from Field (Johnson et al., 1960) 120
6.22	Comparison between Test Results from Laboratory and Test Results from Field (D’Appolonia et al., 1969) 121
7.1	Locations of SPT to Measure Variation of Vertical Stress under Compaction Strip 122
7.2	Distribution of Vertical Stress under Compaction Strip 123
7.3	Change of Vertical Stresses under Compaction Strip 124
7.4	Locations of SPT to Measure $\Delta \sigma_v$ due to Compaction (Side - View) 125
7.5	Locations of SPT to Measure $\Delta \sigma_v$ due to Compaction (Top - View) 126
7.6	Locations of SPT at Same Elevation 127
7.7	$\Delta \sigma_v$ at Grid Points after 1 – Pass of Compactor 128
7.8	Contours of $\Delta \sigma_v$ after 1 – Pass of Compactor 129

Number	Page
7.9	Contours of $\Delta\sigma_v$ after 2 – Passes of Compactor 130
7.10	Contours of $\Delta\sigma_v$ after 4 – Passes of Compactor 131
7.11	Contours of $\Delta\sigma_v$ after 8 – Passes of Compactor 132
8.1	Locations of SPT to Measure Variation of Horizontal Stress under Compaction Lane 133
8.2	Distribution of Vertical Stress under Compaction Lane 134
8.3	Change of Horizontal Stresses under Compaction Lane 135
8.4	Locations of SPT to Measure $\Delta\sigma_h$ due to Compaction (Side - View) ... 136
8.5	Locations of SPT to Measure $\Delta\sigma_h$ due to Compaction (Top - View) ... 137
8.6	Locations of SPT at Same Elevation 138
8.7	$\Delta\sigma_h$ at Grid Points after 1 – Pass of Compactor 139
8.8	Contours of $\Delta\sigma_h$ after 1 – Pass of Compactor 140
8.9	Contours of $\Delta\sigma_h$ after 2 – Passes of Compactor 141
8.10	Contours of $\Delta\sigma_h$ after 4 – Passes of Compactor 142
8.11	Contours of $\Delta\sigma_h$ after 8 – Passes of Compactor 143



Number	Page
8.12 Comparison between Change of Relative Density after 1 Pass of Compactor in This Study and Vesic’s Theory (1973)	144
8.13 Bearing Capacity Failure in Soil (after Vesic, 1973)	145
8.14 Comparison between Test Results and Local Shear Failure (Vesic, 1973)	146
8.15 Influence Zone Assumed for Piles in Sand (after Yang, 2006)	147
8.16 Comparison between Test Results and Influence zone for Piles in Sand (Yang, 2006)	148



List of Symbols

- B = Width of Vibratory Soil Compactor
- C_u = Coefficient of Uniformity
- D_f = Distance Form Ground Surface to the Bottom of Shallow Foundation
- D_r = Relative Density of Soil
- d_L = Distance from Left Sidewall
- d_M = Distance from Model Sidewall
- d_s = Element Strip of Width
- δ_w = Angle of Wall Friction
- E = Young's Modulus
- e_{max} = Maximum Void Ratio of Soil
- e_{min} = Minimum Void Ratio of Soil
- ε = Normal Strain
- ϕ = Effective Stress Friction Angle
- ϕ' = Effective Stress Friction Angle for Local Shear Failure
- G_s = Specific Gravity of Soil
- γ = Unit Weight of Soil
- γ_d = Dry Unit Weight of Soil
- $\gamma_{d,max}$ = Maximum Dry Unit Weight Measured in Tests
- K_a = Coefficient of Active Earth Pressure
- K_o = Coefficient of Earth Pressure At-Rest
- K_p = Coefficient of Passive Earth Pressure
- ν = Poisson's Ratio
- N = Number of Passes of Compactor
- q = Element Strip Load Per Unit Length



q_{ult} = Ultimate Bearing Capacity of Soil

S = Surface Settlement

σ_1 = Major Principal Stress

σ_3 = Minor Principal Stress

σ_{cyc} = Compaction Loading

σ_h = Effective Horizontal Stress

$\Delta\sigma_h$ = Change of Horizontal Stress

σ_n = Normal Stress

σ_v = Effective Vertical Stress

$\Delta\sigma_v$ = Change of Vertical Stress



Chapter 1

Introduction

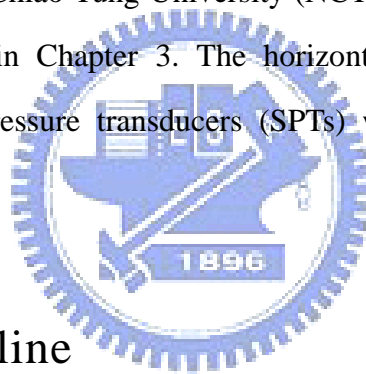
In the construction of highway embankments, earth dams, and many other engineering structures, engineers will compact loose soils to increase their unit weights. The objective of the compaction operation is to improve the engineering properties of soil such as increasing the fill bearing capacity or reducing settlement. In various methods of compaction, vibratory compactors are used mostly for the densification of granular soils as shown in Fig. 1.1.

Before compaction, the vertical earth pressure is calculated by the equation $\sigma_v = \gamma z$, and the horizontal earth pressure is estimated with Jaky's formula. Many researchers had conducted studies regarding soil compaction, however most of their investigating were focused on compaction-induced stresses. It should be mentioned that the effects of compaction on a soil mass are not limited to stress change only. This study discusses the compaction-induced effects on a loose sandy soil which includes: (1) the surface settlement; (2) the change of relative density; (3) the change of vertical stresses; and (3) the change of horizontal stresses in the soil mass. Based on the experimental evidence, the mechanism of soil behavior under compaction is preposed.

1.1 Objectives of Study

Compaction is a particular kind of soil stabilization methods and it is one of the oldest methods for improving existing soil or man-placed fills. To analyze the residual

lateral earth pressure induced by soil compaction, several methods of analysis have been proposed by Rowe (1954), Broms (1971), Ingold (1979), Duncan and Seed (1986), Peck and Mesri (1987) and other researchers. However, little information regarding the mechanism of the compacted soil has been reported. From a practical point of view, this study simulates the strip compaction with a vibratory compactor on the surface of a loose granular soil in the field. The tests results include the change of soil density and the change of stress in the soil mass due to compaction. Based on the test data, the mechanism of the compacted soil due to the strip compaction on the surface of a sandy soil mass is proposed. All experiments mentioned in this study were conducted in the National Chiao Tung University (NCTU) non-yielding retaining wall facility that is described in Chapter 3. The horizontal and vertical stresses were measured with the soil pressure transducers (SPTs) which were embedded in the backfill.



1.2 Research Outline

This research utilizes the NCTU model wall facility to investigate the effects of compaction. The review of at-rest earth pressure theories and compaction-induced stresses are summarized in Chapter 2. Details of the experimental apparatus for this study are discussed in Chapter 3. The characteristics of backfill and the method used to reduce the sidewall friction are introduced in Chapter 4. Chapter 5 discusses the test results for loose sand before compaction.

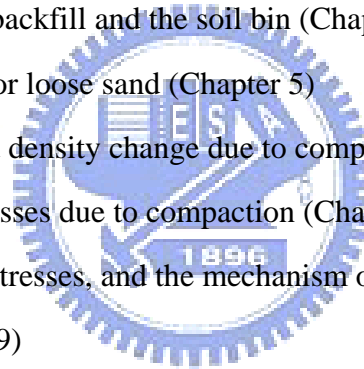
To investigate effects of compaction, the backfill was prepared by air-pluviated method and then compacted with a vibratory compactor. To decide the procedure of compaction, pilot tests were carried out and introduced in Chapter 6. Test results regarding surface settlement and change of relative density after 1, 2, 4 and 8 passes of

the vibratory compactor on the sand compaction line are reported in Chapter 6. Chapter 7 and Chapter 8 discuss the change of vertical stress and horizontal stress due to compaction, respectively. Based on the test results, the mechanism of the compacted soil as a result of the strip compaction is proposed.

1.3 Organization of Thesis

This paper is divided into the following parts:

1. Review of past investigations regarding soil compaction (Chapter 2)
2. Description of experimental apparatus (Chapter 3)
3. Characteristics of the backfill and the soil bin (Chapter 4)
4. Experimental results for loose sand (Chapter 5)
5. Surface settlement and density change due to compaction (Chapter 6)
6. Change of vertical stresses due to compaction (Chapter 7)
7. Change of horizontal stresses, and the mechanism of failure (Chapter 8)
8. Conclusions (Chapter 9)



Chapter 2

Literature Review

The Jaky's formula (1944) is commonly used to calculate the earth pressure at-rest. To improve the engineering properties, contractors are generally required to compact the loose soils to increase their unit weights and reducing settlements. Previous studies associated with the compaction-induced effects such as the change of soil density, the change of stresses in the soil mass and mechanism of soils under compaction are discussed in this chapter.

2.1 Earth Pressure At-Rest

2.1.1 Coefficient of Earth Pressure At-Rest

As shown in Fig. 2.1(a), a soil element A located at depth z is compressed by the overburden pressure $\sigma_v = \gamma z$. During the formation of the deposit, the element A is consolidated under the pressure σ_v . The vertical stress induces a lateral deformation against surrounding soils due to the Poisson's ratio effect. Over the geological period, the horizontal strain is kept to be zero and the surrounding soil would develop a lateral stress to counteract the lateral deformation. A stable stress state will develop that the principal stresses acts σ_1 and σ_3 on the vertical and horizontal planes, as shown in Fig. 2.1(b).

The soil in a state of static equilibrium condition is commonly termed as the K_o condition. Donath (1981) defined the ratio of the horizontal stress σ_h to

vertical stress σ_v is defined as the coefficient of earth pressure at-rest, K_o , or

$$K_o = \frac{\sigma_h}{\sigma_v} \quad (2.1)$$

since $\sigma_v = \gamma z$, then $\sigma_h = K_o \gamma z$, where γ is the unit weight of soil.

For an isotropic soil element shown in Fig. 2.2, if the soil behaved as an ideal elastic material, based on the mechanics of materials, the lateral strain ε_y can be expressed as:

$$\varepsilon_y = \frac{\sigma_y}{E} - \frac{\nu}{E}(\sigma_x + \sigma_z) \quad (2.2)$$

or

$$\varepsilon_h = \frac{\sigma_h}{E} - \frac{\nu}{E}(\sigma_h + \sigma_v) \quad (2.3)$$

where E is the elastic modulus and ν is the Poisson's ratio of the soil.

Base on the definition of the at-rest condition, the lateral strain would be zero under the application of stress state and the $\sigma_h = K_o \sigma_v$. Then the Eq. 2.3 can be written as:

$$\varepsilon_h = \frac{1}{E}(K_o \sigma_v - \nu K_o \sigma_v - \nu \sigma_v) = 0 \quad (2.4)$$

$$K_o = \frac{\nu}{1-\nu} \quad (2.5)$$

It should be mentioned that Eq. 2.5 is applicable for the isotropic and elastic materials only. However, the behavior of soil element is more complex and far from these assumptions. It is evident that the relationship between K_o and elastic parameter, ν of Eq. 2.5 is obsolescent for predicting in-situ horizontal stress.

2.1.2 Jaky's Formula

Several scholars attempted to set up a theoretical relationship between the strength properties of a soil and K_o . The empirical relationship to estimate K_o of coarse-grained soil is discussed in the following section.

Mesri and Hayat (1993) reported that Jaky (1944) established a relationship between K_o and maximum effective angle of internal friction ϕ by analyzing a talus of granular soil freestanding at the angle of repose. Jaky (1944) supposed that the angle of repose is analogous to the angle of internal friction ϕ . This is reasonable for sediment, normally consolidated material. Jaky (1944) reasoned that the sand cone OAD in Fig. 2.3 is in a state of equilibrium and its surface and inner points are motionless. The horizontal pressure acting on the vertical plane OC is the earth pressure at-rest. Slide planes exist in the inclined sand mass. However, as OC is a line of symmetry, shear stresses can not develop on it. Hence OC is a principal stress trajectory. Based on the equations of equilibrium, Jaky expressed the coefficient of earth pressure at-rest K_o with the angle of internal friction, ϕ :

$$K_o = (1 - \sin \phi) \frac{1 + \frac{2}{3} \sin \phi}{1 + \sin \phi} \quad (2.6)$$

In 1948, Jaky presented a modified simple expression given by Eq. 2.7.

$$K_o = 1 - \sin \phi \quad (2.7)$$

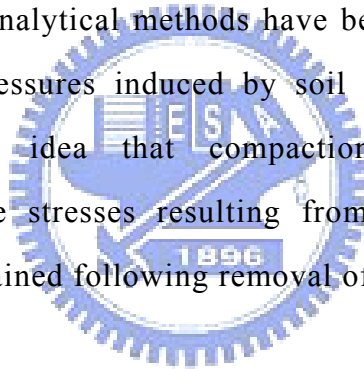
Mayne and Kulhawy (1982) reported that, the approximate theoretical relationship for K_o for normally consolidated soils supposed by Jaky appears

valid for cohesionless soils. Using Jaky's equation to estimate the in-situ lateral earth pressure is reliable for most engineering purposes.

2.2 Effects of Soil Compaction on Earth Pressure

Compaction a soil can produce a stiff, settlement-free and less permeable mass. It is usually accomplished by mechanical means that cause the density of soil to increase. At the same time the air voids are reduced. It has been realized that the compaction of the backfill material has an important effect on the earth pressure.

Several theories and analytical methods have been proposed to analyze the residual lateral earth pressures induced by soil compaction. Most of these theories introduce the idea that compaction represents a form of overconsolidation, where stresses resulting from a temporary or transient loading condition are retained following removal of this load.

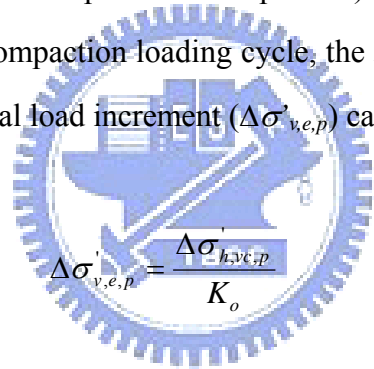


2.2.1 Study of Duncan and Seed

Duncan and Seed (1986) presented an analytical procedure for evaluation of peak and residual compaction-induced stresses either in the free field or adjacent to vertical, non-deflecting soil-structure interfaces. This procedure employs a hysteretic K_o -loading model shown in Fig. 2.4. The model is adapted to incremental analytical methods for the evaluation of peak and residual earth pressures resulting from the placement and compaction of soil. When the surcharge is applied on the soil surface, it will increase the vertical stress and the horizontal stress. In Fig. 2.4, as the virgin loading is applied on the soil, both σ_v and σ_h increase along the K_o -line ($K_o = 1 - \sin\phi$). Nevertheless, when the surcharge is removed, σ_v and σ_h would decrease along the

virgin unloading path. As virgin reloading was applied again, the increment of earth pressure is less than that induced by the first virgin loading.

The hysteretic model may be applied to the analysis of compaction as represented by a transient, moving surficial load of finite lateral extent by directly modeling loading due to increased overburden as an increase in vertical effective stress ($\Delta\sigma'_v$). To model compaction loading in terms of the peak virgin, compaction-induced horizontal stress increase ($\Delta\sigma'_{h,vc,p}$) is defined as the horizontal effective stress which would be induced by the most critical positioning of the compactor. The $\Delta\sigma'_{h,vc,p}$ could be evaluated by the simple elastic analysis if the soil had been previous uncompacted (if the soil had no “lock-in” residual stresses due to previous compaction). While the hysteretic model is applied to the analysis of compaction loading cycle, the $\Delta\sigma'_{h,vc,p}$ should be transformed to an equivalent peak vertical load increment ($\Delta\sigma'_{v,e,p}$) calculated as



$$\Delta\sigma'_{v,e,p} = \frac{\Delta\sigma'_{h,vc,p}}{K_o} \quad (2.8)$$

It is important to note the peak compaction loading must be based on directly calculated lateral stress increase rather than directly calculated peak vertical stress increase multiplied by K_o , K_a or some other coefficient. Seed and Duncan (1983) concluded that either in the free field, or at or near vertical, nondeflecting soil/structure interfaces, $\Delta\sigma'_{h,vc,p}$ resulting from surficial compaction loading can be calculated directly by simple elastic analysis. The parameter of Poisson’s ratio, ν for surficial compaction loading may be chosen according to the empirically derived relationship

$$\nu = \nu_o + \frac{1}{2}(0.5 - \nu_o) \quad (2.9)$$

where $\nu_o = \frac{K_o}{1 + K_o}$

$$K_o = 1 - \sin\phi$$

Seed and Duncan (1983) also brought up a simple hand calculation procedure which results in good agreement with the incremental procedure described above. In Fig. 2.5, it is apparent the simple hand solution has a good agreement with the incremental procedure.

2.2.2 Study of Chen

Chen (2002) reported some experiments in non-yielding retaining wall at National Chiao Tung University to investigate influence of earth pressure due to vibratory compaction. Air-dry Ottawa sand was used as backfill material. Vertical and horizontal stresses in the soil mass were measured in loose sand and compacted sand. Based on his test results, Chen (2002) proposed the following conclusions: (1) after compaction, the lateral stress measured near the top of backfill is almost identical to the passive earth pressure estimated with Rankine theory. The compaction-influenced zone rises with rising compaction surface. Below the compaction-influenced zone, the horizontal stresses converge to the earth pressure at-rest, as indicated in Fig. 2.6; (2) when total (static + dynamic) loading due to the vibratory compacting equipment exceeds the bearing capacity of foundation soils, the mechanism of vibratory compaction on soil can be described with the bearing capacity failure of foundation soils; (3) the vibratory compaction on top of the backfill transmits elastic waves through soil elements continuously. For soils below the compaction-influenced zone, soil particles are vibrated. The passive state of stress among particles is disturbed. The horizontal stresses among soil particles readjust under the application of a uniform overburden pressure and constrained lateral deformation, and eventually converge to the at-rest state of stress.

Chen's test results were compared with the design recommendations proposed by NAVFAC DM-7.2 (1982), Duncan and Seed (1986), Peck and Mesri (1987), and Duncan et al. (1991) as shown in Fig. 2.7. Parameter values used in the stress calculation including the unit weight γ , relative D_r , internal friction angle ϕ , wall friction angle δ , and cyclic compaction stress σ_{cyc} are shown in Fig. 2.7. The horizontal pressure distribution suggested by the Navy Design Manual DM-7.2 was based on the analytical method proposed by Ingold (1979). The pressure distribution calculated with the method proposed by Duncan et al. (1991) was obtained from the design chart for vibratory plates with a cyclic compaction stress $q = 34.9 \text{ kN/m}^2$ (5 psi).

In Fig. 2.7, Chen's test data are in good agreement with the proposed design methods. The horizontal stresses in the uppermost compacted lift are equal to or slightly less than the passive Rankine pressure. However, at a lower depth, the Chen's test data are apparently lower than the calculated horizontal stresses. It is important that the application of Chen's test findings are limited to estimating the horizontal stresses acting on a non-yielding wall induced by a small size vibratory hand tamper.

2.3 Elastic Solutions for a Strip Surface Loading

A simple equation to calculate the lateral pressure increase due to a uniform vertical strip surcharge was mentioned by Jurgenson (1934). Fig. 2.8 shows the case where a uniform vertical load of q per unit area is acting on a flexible infinite strip on the surface of a semi-infinite elastic mass. To obtain the stresses at a point $P(x,z)$, consider an elementary strip of width ds loaded at a distance s from the centerline of the load. The load per unit length of this elementary strip is $q.ds$, and the strip loading can be approximated as a line load.

The expression for σ_x given can be presented in a simplified form

$$\sigma_x = \frac{q}{\pi} [\alpha - \sin \alpha \cos(\alpha + 2\delta)] \quad (2.13)$$

The expression for σ_z given can be presented in a simplified form

$$\sigma_z = \frac{q}{\pi} [\alpha + \sin \alpha \cos(\alpha + 2\delta)] \quad (2.14)$$

where α and δ are the angle indicated in Fig. 2.8.

The contours of σ_x/q and σ_z/q due to the surface strip loading are shown in Fig. 2.9. The units of X and Y axes are the distance from center of the soil bin dividing by the half width of foundation (B/2).

2.4 Ultimate Bearing Capacity of Shallow Footing

Terzaghi (1943) suggested that the failure surface in soil at an ultimate load for a continuous strip footing was similar to Fig. 2.10. The effect of soils above the bottom of the footing may be assumed to be replaced by an equivalent surcharge, $q = \gamma D_f$ (where γ is the unit weight of soil). The failure zone under the footing can be separated into three parts: (1) the triangular zone ACD immediately under the footing; (2) the radial shear zones ADF and CDE, with the curves DE and DF being arcs of a logarithmic spiral; and (3) two triangular Rankine passive zones AFH and CEG. Using equilibrium analysis, Terzaghi expressed the ultimate bearing capacity as:

$$q_u = c' N_c + q N_q + \frac{1}{2} \gamma B N_\gamma \quad (2.15)$$

where c' = cohesion of soil

γ = unit weight of soil

$q = \gamma D_f$

N_c, N_q, N_γ = bearing capacity factors that are nondimensional and are functions only of the soil friction angle ϕ'

Table. 2.1 shows the variation of $N_c, N_q,$ and N_γ with the soil friction ϕ' (after Kumbhojkar, 1993).

For footings that exhibit the local shear failure mode for strip footing in soils, Terzaghi (1943) suggested the following modified as:

$$q_u = \frac{2}{3} c' N_c + q N_q + \frac{1}{2} \gamma B N_\gamma \quad (2.16)$$

$N'_c, N'_q,$ and $N'_\gamma,$ the modified bearing capacity factors, can be calculated by using the bearing capacity factor equations (for $N_c, N_q,$ and $N_\gamma,$ respectively) by replacing ϕ by $\phi' = \tan^{-1}(\frac{2}{3} \tan \phi)$.

Vesic (1963) conducted several laboratory load-bearing tests on circular and rectangular plates supported by soil at various relative densities of compaction. On the basis of experimental results, Vesic (1973) defined the three types of the bearing capacity failure mode including general shear failure, local shear failure and punching shear failure. Fig. 2.11 indicates the typical load-settlement relationship for these failure modes. The failure modes are dependent on the relative density of soil and the depth of embedment D_f as shown in Fig. 2.12. In Fig. 2.13, Vesic (1973) suggested that as the loaded soil fails, the composite failure surface would develop along bcde and acd₁e₁. The stresses of sand in zone I belong to active state. Zone II is known as the zone of radial shear, and zone III is identical to the passive Rankine zone.

2.5 Stresses in Soil during Penetration Test

Meyerhof (1976) proposed the ultimate load-carrying capacity of pile as

shown in Fig. 2.14. The ultimate load-carry capacity Q_u of a pile is given by the equation:

$$Q_u = Q_p + Q_s \quad (2.17)$$

where Q_p = load-carrying capacity of the pile point

Q_s = frictional resistance (skin friction) derived from the soil-pile interface

The point bearing capacity (Q_p) of a pile in sand generally increases with the depth of pile in the bearing stratum. Meyerhof (1976) suggested the Q_p in sand by the equation as:

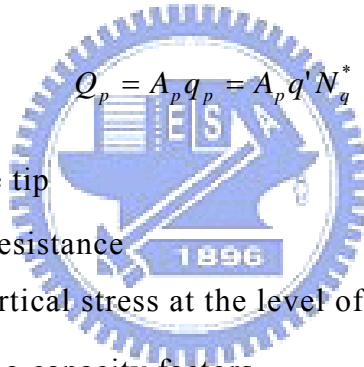
$$Q_p = A_p q_p = A_p q' N_q^* \quad (2.18)$$

where A_p = area of pile tip

q_p = unit point resistance

q' = effective vertical stress at the level of the pile tip

N_q^* = the bearing capacity factors



In Fig. 2.15, Meyerhof (1976) suggested the relationship between N_q^* and soil friction angle ϕ' .

Yang (2006) proposed an analytical method to estimate the influence zone surrounding the tip of a loaded pile in sand. In the framework of the cavity expansion theory and a confined local failure mechanism, explicit expressions are derived. The sizes of the upward and downward influence zone are properly linked with the angle of shearing resistance, the stiffness, the volumetric strain, and the mean effective stress of the sand at the pile tip. Based on a series of parametric analyses, the mean range of the influence zone is suggested. Fig. 2.16 shows that the confined local failure mechanism

provides a fairly good prediction for the end-bearing capacity of displacement piles in sand. For piles in clean sand, the influence zone above the pile tip is between $1.5D$ and $2.5D$ and the zone below the tip ranges from 3.5 to $5.5D$ as shown in Fig. 2.17, where D is pile diameter.

2.6 Density Change due to Compaction

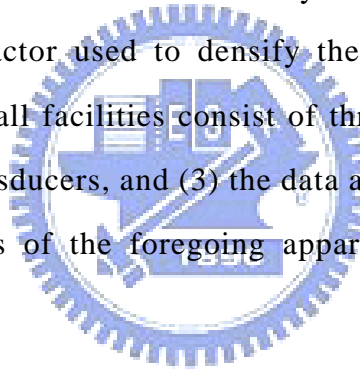
In the field, the factors affecting compaction include the thickness of lift, the intensity of pressure applied by the compacting equipment, and the area over which the pressure is applied. During compaction, the dry unit weight of soil is affected by the number of roller passes. Johnson and Sallberg (1960) used 84.5 kN (19kip) three-wheel roller to compact a silty clay in 229 mm (9 in) loose layers at different moisture contents. The test results shows the growth curve that indicated the dry unit weight of a soil at a given moisture content increases to a certain point with the number of roller passes in Fig. 2.18.

In Fig. 2.19, D'Appolonia et.al. (1969) reported the distribution of the unit weight of soil with depth for a poorly graded dune sand, for which compaction was achieved by a vibratory drum roller. Vibration was produced by mounting an eccentric weight on a single rotating shaft within the drum cylinder. The weight of the roller used for this compaction was 55.6 kN (12.5 kip), and the drum diameter was 1.19 m (47 in). The lifts were kept at 2.44m (8ft). The dry unit weight of compacted soil increased with the number of roller passes. However, the rate of increase in unit weight gradually decreases after about 15 passes. The dry unit weight and hence the relative density D_r reached maximum values at a depth of about 0.5 m (1.5 ft) and gradually decreased at lesser depths. This decrease occurs because of the lack of confining pressure toward the surface.

Chapter 3

Experimental Apparatus

To investigate the effects of vibratory compaction on the vertical and horizontal stresses in a cohesionless soil mass, the instrumented non-yielding model retaining wall facility at National Chiao Tung University (NCTU) was used. This chapter introduces the NCTU non-yielding retaining wall facilities and the vibratory compactor used to densify the loose backfill. The NCTU non-yielding retaining wall facilities consist of three components: (1) the soil bin, (2) soil pressure transducers, and (3) the data acquisition system (Chen and Fang, 2002). The details of the foregoing apparatuses are described in the following sections.



3.1 Soil Bin

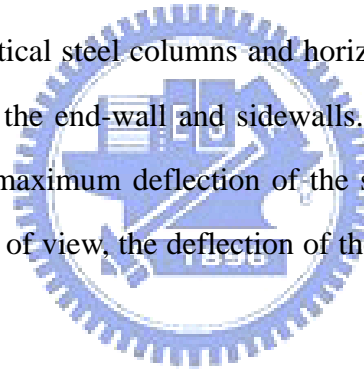
To simulate a plan strain condition for model test, the soil bin is designed to minimize the lateral deflection of sidewalls. In Fig. 3.1, the soil bin was fabricated of steel plates with inside dimensions of 1500 mm \times 1500 mm \times 1600 mm. The soil bin was divided into two parts to discuss in the following section: (1) model wall, and (2) sidewall and end wall.

The model wall shown in Fig. 3.1 is 1500 mm-wide and 1600 mm-high, and 45 mm-thick. To achieve at-rest condition, the wall material should be nearly rigid. It is hoped that the deformation of the wall could be neglected with the application of earth pressure. As indicated in Fig. 3.1, twenty-four 20 mm-thick steel columns were welded

to the four sidewalls to reduce any lateral deformation during loading. In addition, twelve C-shaped steel beams were also welded horizontally around the box to further increase the stiffness of the box.

Assuming a 1.5 m-thick cohesionless backfill with a unit weight $\gamma = 17.1 \text{ kN/m}^3$, and an internal friction angle $\phi = 41^\circ$ was pluviated into the box. A 45 mm-thick solid steel plate with a Young's modulus of 210 GPa was chosen as the wall material. The estimated deflection of the model wall would be only 1.22×10^{-3} mm. Therefore, it can be concluded that the lateral movement of the model wall is negligible and an at-rest condition can be achieved.

The end-wall and sidewalls of the soil bin were made of 35 mm-thick steel plates. Outside the steel walls, vertical steel columns and horizontal steel beams were welded to increase the stiffness of the end-wall and sidewalls. If the soil bin was filled with dense sand, the estimated maximum deflection of the sidewall would be 1.86×10^{-3} mm. From a practical point of view, the deflection of the four walls around the soil bin can be neglected.



3.2 Soil Pressure Transducer

To investigate the distribution of stress in the backfill, an series of soil pressure transducers (Kyowa BE-2KCM17, capacity = 98.1 kN/m^2) as shown in Fig. 3.2 was used. The transducers were buried in the soil mass to measure the variation of vertical and horizontal earth pressure during the filling and compaction process. The five radial extensions projected from the transducer are used to prevent possible rotation of the transducer due to filling and compaction. The effective diameter of the transducer is 22 mm and its thickness is 6 mm.

3.3 Data Acquisition System

A data acquisition system was used to collect and store the considerable amount of data generated during the tests. In the Fig. 3.3, the data acquisition system is composed of the following four parts: (1) dynamic strain amplifiers (Kyowa: DPM601A and DPM711B); (2) AD/DA card (NI BNC-2090); and (3) Personal Computer. The analog signals from the sensors were filtered and amplified by the dynamic strain amplifiers. Then, the analog experimental data were digitized by an A/D-D/A card. The digital signals were then transmitted to the personal computer for storage and analysis.

3.4 Vibratory Compactor

To simulate compaction of backfill in the field, the vibratory compactor shown in Fig. 3.4 and Fig.3.5 was made by attaching an eccentric motor (Mikasa Sangyo, KJ75-2P) to a 0.225 m \times 0.225 m steel plate. Fig. 3.6 shows that the eccentric force can be controlled by adjusting the number of eccentric steel plates attached to the rotating shaft of motor. For this study, a total of sixteen eccentric plates (8+8) were used. The detailed information regarding the eccentric motor is listed in Table 3.1. Fig. 3.7 shows the dynamic vertical force F_d measured with a load cell placed under the base plate of the vibratory compactor with 16 eccentric plate, the corresponding $F_d = 1.648$ kN. With the static mass of the compactor ($w = mg = 0.119$ kN), the cyclic vertical force (static + dynamic) was 1.767 kN. The measured frequency of vibration was 44 Hz. Assuming the distribution of contact pressure between the base plate (0.225 m \times 0.225 m) and soil is uniform, the cyclic normal stress σ_{cyc} applied on the surface of soil would be 34.9 kN/m² (5.06 psi). It should be mentioned that the distribution of contact pressure between the foundation and soil varies with the stiffness of the footing. If the footing is perfectly rigid, the static contact pressure on the footing increases from zero at the edge to a maximum at the center.

Chapter 4

Backfill Characteristics

The characteristics of the backfill and the method to reduce the wall friction are introduced in this chapter.

4.1 Backfill Properties

Air-dry Ottawa silica sand (ASTM C-778) was used as the backfill material in all experiments. Physical properties of the soil are summarized in Table 4.1. Grain-size distribution of the backfill is shown in Fig. 4.1. The major reasons to select Ottawa sand as the backfill material are listed below.

1. Its round shape, which avoids effect of angularity of soil grains.
2. Its uniform distribution of grain size (coefficient of uniformity $C_u = 1.78$), which avoids the effects due to soil gradation.
3. High rigidity of solid grains, which reduces possible disintegration of soil particles under loading.
4. Its high permeability, which allows fast drainage and therefore reduces water pressure behind the wall.

To establish the relationship between unit weight of backfill γ and its internal friction angle ϕ , direct shear tests have been conducted. The shear box used has a square (60 mm \times 60 mm) cross-section, and its arrangement is shown in Fig. 4.2. Before shearing, Ottawa sand was air-pluviated into the shear box and then compacted to the desired density. Details of the technique to control soil density are discussed in section 5.1.

Chang (2000) established the relationship between the internal friction angle ϕ and unit weight γ of Ottawa sand as shown in Fig. 4.3. It is obvious from the figure that soil strength increases with increasing soil density. For the air-pluviated backfill, the empirical relationship between soil unit weight γ and ϕ angle can be formulated as follows

$$\phi = 6.43 \gamma - 68.99 \quad (4.1)$$

where

ϕ = angle of internal friction of soil (degree)

γ = unit weight of soil (kN/m³)

Eq. (4.1) is applicable for $\gamma = 15.45 \sim 17.4$ kN/m³ only.

4.2 Reduction of Wall Friction

To constitute a plane strain condition for model wall tests, the shear stress between the backfill and wall should be minimized to nearly frictionless. To reduce the friction between wall and backfill, a lubrication layer fabricated with plastic sheets was furnished for all experiments. Two types of plastic sheeting, one thick and two thin plastic sheets, were adopted to reduce the interface friction. All plastic sheets were hung vertically on four walls before the backfill was deposited as shown in Fig. 4.4.

Multiple layers of thin plastic sheets (without any lubricant) were used by McElroy (1997) for shaking table tests of geosynthetic reinforced soil (GRS) slopes. Burgess (1999) used three thin plastic sheets to reduce side wall friction in full-scale GRS wall tests. The wall friction angle was approximately 15° as determined by the shear box tests. In this study, two thin (0.009 mm-thick) and one thick (0.152 mm-thick) plastic sheet were adopted for the earth pressure experiments. The friction angle δ_w developed between the plastic sheets and steel sidewall could be determined by the sliding block test. A schematic diagram and a photograph of the sliding block test proposed by Fang

et al. (2004) are illustrated in Fig. 4.5 and Fig. 4.6. The wall friction angle δ_w for the sliding block test was determined using the basic principles of physics. Fig. 4.7 shows the variation of friction angle δ_w as a function of the normal stress σ_n for the plastic sheet method (1 thick + 2 thin sheeting) used in this study. The measured friction angle with this method is about 7.5° . It is clear in Fig.4.7 that the interface friction angle δ_w is nearly independent of the applied normal stress σ_n . This constancy is an important advantage in establishing the input soil properties for analytical models that might be used to analyze the experimental results. For all experiments in this paper, the lubrication layer wall applied on four walls as indicated in Fig. 4.4. The plastic sheets not only can help to reduce the friction angle between the wall and the backfill. The plastic sheets can also help to reduce the reflection of elastic waves transmitted to the soil-wall boundaries during compaction.

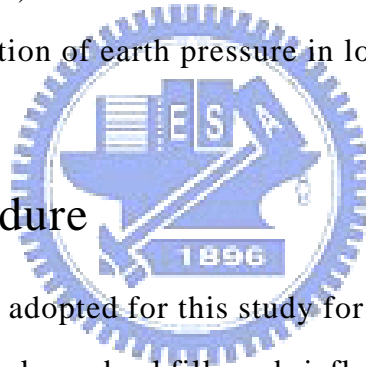


Chapter 5

Test Results for Loose Sand

This chapter introduces the distribution of soil density, horizontal and vertical stresses in the loose sand backfill before compaction. The sections discussed included: (1) the method to prepare the loose backfill; (2) the method to control soil density; (3) the measured distribution of soil density in loose sand; and (4) the distribution of earth pressure in loose sand.

5.1 Testing Procedure



The testing procedures adopted for this study for the measurement of relative density and stresses in the loose backfill are briefly described below.

For the measurement of the relative density:

- (1) Sand pluviated into the soil bin by controlling the drop height of soil and slot opening of the sand hopper.
- (2) Density cups placed at the different elevations and locations.
- (3) After the soil had been filled up to 1.5 m from the bottom of the soil bin, soil density cups were dug out from the soil mass carefully.
- (4) The weight of the cup and soil was measured and recorded.

For the measurement of the earth pressures:

- (1) Sand pluviated into the soil bin by controlling the drop height of soil and slot opening of the sand hopper.

- (2) Placed the SPTs at the desired locations.
- (3) When the backfill was filled up to 1.5 m, the earth pressures were recorded and stored.

5.2 Distribution of Soil Density

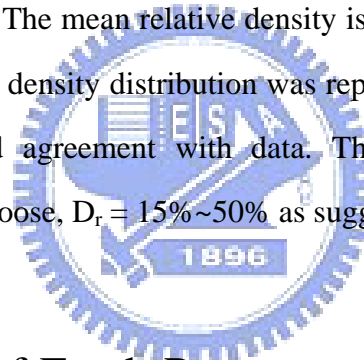
5.2.1 Air-Pluviation of Ottawa Sand

To achieve a uniform soil density in the backfill, Ottawa sand was deposited by air-pluviation method into the soil bin. The air-pluviation method had been widely used for a long period of time to reconstitute laboratory sand specimens. Rad and Tumay (1987) reported that pluviation is the method that provides reasonably homogeneous specimens with desired relative density. Lo Presti et al. (1992) reported that the pluviation method could be performed for greater specimens in less time.

Das (1994) suggested that relative densities of 15~50%, and 70~85% are defined as loose and dense condition, respectively. To achieve loose backfill ($D_r = 32\%$), Chen (2002) adopted the drop height of 1.0 m and hopper slot opening of 15 mm. According to the test results, Ho (1999) established the relationship among slot opening, drop height, and density as shown in Fig. 5.1. As a result, the drop height of 1.0 m and hopper slot-opening of 15 mm are selected to achieve the loose backfill for testing in this study. Fig. 5.2 shows the method to control the drop height = 1.0 m. In the picture, a 1.0 m-long rope was hung from the hopper to the surface of the soil to control the drop distance of soil. In Fig. 5.3, the soil hopper that lets the sand pass through a calibrated slot opening (15 mm) at the lower end was used for the spreading of sand. The raining of the Ottawa sand into soil bin is shown in Fig. 5.4.

5.2.2 Uniformity of Soil Density

To observe the distribution of soil density in the soil bin, the soil density cups were made. The soil density control cup made of acrylic is illustrated in Fig. 5.5 and Fig. 5.6. During the preparation of soil specimen, density cups were buried in the soil mass at different elevations and different locations in the backfill as shown in Fig. 5.7 and Fig. 5.8. After the soil had been filled up to 1.5 m from the bottom of the soil bin, soil density cups were dug out from the soil mass carefully. Fig. 5.9(a) shows the density cup was placed in the soil bin and Fig. 5.9(b) shows the weight of the cup and soil was measured with an electrical scale. The distribution of soil density with depth for loose sand is shown in Fig. 5.10. The mean relative density is $D_r = 34.1\%$ with the standard deviation of 2.4%. The soil density distribution was reported by Chen (2002). The test results are in fairly good agreement with data. The backfill achieved with the air-pluviation method was loose, $D_r = 15\% \sim 50\%$ as suggested by Das (1994).



5.3 Distribution of Earth Pressure

For comparison purposes, at the beginning of this study, experiments were conducted to investigate the stresses in an uncompacted backfill. Fig. 5.11 shows the location of soil pressure transducers to measure the distribution vertical earth pressure σ_v with depth. The method to confirm the location and depth of the SPT in the soil mass is shown in Fig. 5.12. Fig. 5.13 shows the photograph of SPT used to measure vertical stress in the soil mass. After the backfill had been filled up to 1.5 m thick, the vertical earth pressure σ_v measured in the soil mass was illustrated in Fig. 5.14. Obviously, the vertical pressure increased with increasing depth and the test data were in good agreement with the equation $\sigma_v = \gamma z$, where γ is the unit weight of the backfill. The locations of soil pressure transducers to measure the distribution of horizontal

earth pressure σ_h were shown in Fig. 5.15. Fig. 5.16 shows the photograph of SPT used to measure horizontal stress in the soil mass. The distribution of horizontal earth pressure σ_h with depth was illustrated in Fig. 5.17. In the figure, the earth pressure profile induced by the 1500 mm-thick loose backfill was approximately linear and was in good agreement with the Jaky's equation. Mayne and Kulhawy (1982), Mesri and Hayat (1993) reported the Jaky's equation is suitable for backfill in its loosest state. From a practical point of view, it may be concluded that for a loose backfill, the vertical and horizontal earth pressure in the soil mass can be properly estimated with the equation $\sigma_v = \gamma z$ and Jaky's equation, respectively.



Chapter 6

Surface Settlement and Density Change due to Compaction

This chapter introduces the pilot tests to determine the program of compaction tests. The surface settlement and change of soil density due to vibratory compaction are discussed in the following sections.

6.1 Testing Procedure

The testing procedures adopted for the measurement of the surface settlement and change of the relative density due to compaction are briefly described below.

- (1) Sand pluviated into the soil bin by controlling the drop height of soil and slot opening of the sand hopper.
- (2) Density cups placed at the different elevations and locations.
- (3) After the soil had been filled up to 1.5 m from the bottom of the soil bin, level the surface of the backfill.
- (4) After the first pass of the vibratory compactor, remove the compactor.
- (5) Measured the surface settlement on the XZ and YZ – plane..
- (6) Soil density cups were dug out from the soil mass carefully. Weight of the cup and soil was measured and recorded.
- (7) Repeated steps (1) through (6), change the number of passes of the

compactor to 2, 4, and 8 passes.

6.2 Pilot Tests

To investigate the effects of compaction on the surface of a sandy backfill with a vibratory compactor, a series of pilot tests were conducted at the beginning. The results of the pilot tests can help a researcher to set up the testing program.

The testing procedure of strip compaction was indicated in Fig. 6.1. The vibratory compactor was pulled over the compaction lane from the left sidewall to the right sidewall for the first pass as shown in Fig. 6.2. Then the vibratory compactor was turned around 180 degrees to compact the backfill at the second pass from the right to the left sidewall. As the end, the backfill below the compaction lane had been densified with eight passes of the vibratory compactor. Each pass was about 1.5 m-long and lasted a duration of 70 seconds.

Under a plane strain condition, there was zero lateral strain in the longitudinal direction, and the shear stress on the intermediate principal plane was by definition equal to zero. To simulate a plane strain condition in the NCTU non-yielding retaining wall facilities, the frictional resistance between the soil and the sidewalls should be minimized as much as possible. For all experiments in this paper, the lubrication layers were applied on both sidewalls as indicated in Fig. 6.3. As a result, in Fig. 6.3, the XZ – plane became the intermediate principal plane as shown in Fig. 6.3. For all tests in this study, the effects of compaction were observed on the XZ – plane. To reduce the friction on the model wall and the end wall, the lubrication layers were also hung on them. The plastic sheets not only can help to reduce the friction between the wall and the backfill. The plastic sheets can also help to reduce the reflection of elastic waves transmitted to the soil-wall boundaries during compaction.

In Fig. 6.4, the surface of the backfill has changed due to the strip compaction. After

compaction, a settlement trough was induced apparently on the surface of the backfill. The method to measure surface settlement on the XZ and YZ – planes was shown in Fig. 6.5(a) and (b), respectively. To determine the amount of compaction for testing, the surface settlement of the compaction lane was investigated in pilot tests.

Because of the sidewall friction, the surface settlement measured near the sidewall was less than the average settlement indicated in Fig. 6.6. Based on the test results, sidewall effects were limited to the regions about 300 mm from the sidewalls.

Fig. 6.7 shows the compaction-induced surface settlement increased with the increasing number of passes of the compactor. Based on the test results, a hyperbolic model relationship between surface settlement S and number of passes N was established as shown in Fig. 6.8. The surface settlement S was the average settlement of the seven points (point B to H) shown in Fig. 6.7. In Fig. 6.8, the data points obtained from tests 0701 and 0703 indicated that the test results were quite reproducible. Based on the test results, the hyperbolic model was established to estimate the surface settlement S as a function of No. of passes of the compactor.

The relationship can be expressed as:

$$S = \frac{N}{0.0178 + 0.0241N} \quad (6.1)$$

where S = surface settlement in mm

N = number of passes of the compactor

The asymptote of the hyperbolic model was $S_{\max} = 41.5$ mm. Table 6.1(a) shows that the S_{\max} was divided into five equal parts and their corresponding number of pass was obtained. In the field, at least 1 – pass of compactor would be carried out to compact the loose backfill. In Table 6.1(a), $0.6S_{\max}$ is related to 1.11 pass of the compactor. However, the non-integer pass of the compactor do not exist for engineering

applications. Therefore, 1 – pass of the compactor would be the minimal. From a practical point of view, while the numbers of passes of the compactor were doubled, the compaction-induced effects would be concerned by engineers. Table 6.1(b) shows the surface settlement corresponding to 1, 2, 4, and 8 passes. The effects of compaction associated with 1, 2, 4 and 8 passes of the compactor were discussed in this study.

6.3 Surface Settlement

Before compaction, the height of backfill was 1.5m and the surface of the backfill was horizontal. After the first pass of the compactor, Fig. 6.9 shows the average settlement of the compaction lane was approximately 18.75 mm. The surface settlement was about 8.3% of the width of the vibratory compactor ($S/B = 8.3\%$). Heaving of sand at the both edges of the compactor lane was observed in Fig. 6.9. Fig. 6.10 shows the surface settlement profiles after 1, 2, 4 and 8 passes of the compactor. It is obvious in the figure that the surface settlement increased with the increasing compaction effort.

Fig. 6.11 shows the surface settlement along the compaction lane after the first pass of the compactor. After compactor was pulled horizontally by the operator on the compaction lane, the surface settlement was not uniform. The settlements measured near the sidewall were less than the average surface settlement. Except the regions of sidewall effect, the surface settlement was in fairly agreement with the average settlement of 21.8 mm. Fig. 6.12 shows the surface settlement increased with the increasing number of passes of the compactor.

6.4 Change of Relative Density

By controlling the drop height of soil and slot opening of the sand hopper, a loose

sand specimen ($D_r=34\%$) was prepared testing. To investigate the change of relative density due to compaction, many soil density cups were embedded in the backfill to measure the local densities at different locations. To constitute the grid points for density measurements, the density cups were placed densely as shown in Fig. 6.13 and Fig. 6.14. The technique to control the location of density cup was described in section 5.2.2. Fig. 6.15 shows the locations of soil density cups placed at the same elevation. After the desired number of compactor passages, the soil density cups were dug out from the soil mass and measured carefully.

The relative density of sand at the grid points after the first passage of the compactor is indicated in Fig. 6.16. By using the Golden Software Surfer 8, the values of D_r at grid points were converted into a Grapher Grid file. The Grapher Grid file included the test data of relative density. Opening the file with the program Golden Software Grapher 7, the contours of relative density after the first passage of the compactor can be obtained as illustrated in Fig 6.17. The detail operation of the softwares Surfer 8 and Grapher 7 are illustrated in Appendix B. The value of D_r of sand at the grid points after 2, 4, and 8 passes of compactor are listed in Appendix C1.

Fig. 6.17 shows the contours of relative density in soil mass after the first passage of the compactor. Before compaction, the backfill has a uniform relative density of 34%. The soil density became quite dense ($D_r=64\%$) under the vibratory compactor, and the soil density decreased gradually with the distance from the compactor. From the relative density of 34% to 65%, the effects of vibratory compaction on soil density were quite obvious right below the compactor. As the number of passes increased to 2, 4, and 8 passes, more compaction energy was transmitted to the soil. In Fig. 6.18, Fig. 6.19, and Fig. 6.20, the region of dense sand ($D_r=60\%\sim 80\%$) expanded with the increasing number of the compactor passes. The maximum relative density below the compactor was 68%, 72%, and 75%, respectively. The relative density 64%, 68%, 72%

and 75% are correspond to the dry unit weight 16.3 kN/m^3 , 16.4 kN/m^3 , 16.5 kN/m^3 and 16.6 kN/m^3 , respectively.

Fig. 6.21 shows the relationship between dry unit weight and number of passes of the compactor in this study. Johnson and Sallberg (1960) used 84.5 kN (19kip) three-wheel roller to compact a silty clay in 229 mm (9 in) loose layers at different moisture contents. The tests results in this study were in fairly good agreement with the tests result in the field reported by Johnson et al. (1960).

Fig. 6.22 shows the comparison between the tests results obtained from this study and the test results obtained from the field reported by D'Appolonia (1969). The obvious difference is the depth of the maximum dry unit weight. D'Appolonia et al. (1969) proposed that the less value of γ near the surface was relative to the lack of confining pressure. However, based on the test results in this study, the lack condition didn't appear. The dry unit weight decreased gradually with the distance from the compactor. The vibratory compactor put the vertical energy into the sand and the vibratory compactor compress sand coercively. In Table 6.2, it shows the difference between the laboratory tests in NCTU and the field tests from D'Appolonia et al. (1969)

Chapter 7

Change of Vertical Stresses due to Compaction

This chapter reports the variation of vertical earth pressure $\Delta\sigma_v$ in a cohesionless soil mass due to compaction. The following sections include the distribution of vertical stress under the compaction lane and the vertical stress change $\Delta\sigma_v$ in the soil mass due to the compaction.

7.1 Testing Procedure

The testing procedures adopted for the measurement of change of the stresses after compaction are briefly described below.

- (1) Sand pluviated into the soil bin by controlling the drop height of soil and slot opening of the sand hopper.
- (2) SPTs placed in the soil bin at the different elevations and locations.
- (3) After the soil had been filled up to 1.5 m from the bottom of the soil bin, level the surface of the backfill.
- (4) After the first pass of the compactor, remove the vibratory compactor.
- (5) The test data were recorded and stored.
- (6) Repeated steps (1) through (5), change the number of passes of the compactor to 2, 4 and 8 passes.

7.2 Vertical Stress Distribution under Compaction Strip

To investigate the change of vertical earth pressure due to compaction, experiments were conducted to investigate stress distribution under the compaction lane as the first step. Fig. 7.1 shows SPTs were arranged under compaction lane to measure the variation of vertical stress. In Fig. 7.2, it can be seen that before compaction, the test data are in fairly good agreement with the values predicted using the traditional equation $\sigma_v = \gamma z$. With increasing number of passes of the compactor, the vertical stresses measured at the depth from to 0.8 m increased. Fig. 7.3 shows the compaction-influenced zone was about 0.8 m below the ground level. Below $z = 0.8$ m, the vertical stress change was negligible.

7.3 Vertical Stress Change on Intermediate Principal Plane

Based on the test results of section 7.2, in this study, the measurements of σ_v were made at the depth of 0 to 0.8m. Fig. 7.4 and Fig. 7.5, show the location of SPT placed on the intermediate principle plane, which was perpendicular to the compaction lane. The technique to control the location of the SPT was described in section 5.3. Fig. 7.6 shows the series of SPTs placed at the same elevation. By repeating an identical compaction tests with SPT placed at different elevations, the change of vertical stresses σ_v (kN/m^2) at different grid points after the first passage of the compactor were illustrated in Fig. 7.7. The $\Delta\sigma_v$ at grid points after 2, 4, and 8 passes of the compactor were reported in Appendix C2.

In Fig. 7.8, it is seen that the contours of $\Delta\sigma_v$ after the first passage of the compactor

were analogous to concentric circles. The center of the concentric circles corresponding to the max $\Delta\sigma_v$ was located at the depth of 300 mm below the compactor. The $\Delta\sigma_v$ would decrease gradually from the central region. Before compaction, vertical stress at the depth of 300 mm calculated by $\sigma_v = \gamma z$ was 4.68 kN/m². The incremental vertical stress $\Delta\sigma_v$ was 2.2 kN/m² and the incremental stress ratio was 53.0%. In Fig. 6.20, the relative density of soil changed from the initial value 34% to the maximum value of 72%. At $z = 300$ mm, the vertical stress increment due to the change of γ (from 15.6 kN/m³ to 16.6 kN/m³) was 0.30 kN/m². The Comparison between 2.2 kN/m² and 0.30 kN/m², indicated that the vertical stress increment $\Delta\sigma_v$ was not only affected by change of unit weight of soil. The change of the vertical stress was related to the compaction-induced stresses.

It may be concluded that the compaction-induced vertical stresses were quite significant below the compactor. As the number of passes increased to 2, 4, and 8, more compaction energy was input into the soil mass. In Fig. 7.9, Fig. 7.10, and Fig. 7.11, the contours showed that the depth of the compaction-induced zone increased with increasing energy input. The vertical stress increment $\Delta\sigma_v$ increased with increasing number of passages of the compactor.

Chapter 8

Change of Horizontal Stresses due to Compaction

This chapter reports the variation of horizontal earth pressure $\Delta\sigma_h$ in a cohesionless soil mass due to compaction. The following sections include the distribution of horizontal stress under the compaction lane and the horizontal stress change $\Delta\sigma_h$ in the soil mass due to compaction.

8.1 Horizontal Stress Distribution under Compaction Strip

To study the change of horizontal earth pressure $\Delta\sigma_h$ due to compaction, experiments were conducted to explore the range of the compaction-induced zone in the soil mass. Fig. 8.1 shows SPTs were embedded under the compaction lane at different depths. Fig. 8.2 shows before compaction the distribution of horizontal earth pressure was near Jaky's prediction. With increasing the number of passes of the vibratory compactor, the increase of horizontal stresses were induced by compaction. Fig. 8.3 shows that the compaction-influenced zone was at least 1200 mm below the soil surface

8.2 Horizontal Stress Change on Intermediate Principal Plane

Based on the test results of section 8.1, the measurement of σ_h of this study was carried out from the soil surface to the depth of 1.2m. Fig. 8.4 shows the SPTs embedded on the intermediate principal plane. Fig. 8.5 shows the measurement plane perpendicular to the compaction lane. The technique to control the location of the SPT was described in the section 5.3. Fig. 8.6 shows the SPT placed at the same elevation. By repeating the identical compaction tests with SPTs buried at different elevations, the changes of horizontal stresses $\Delta\sigma_h$ at grid points after the first passage of the compactor were illustrated in Fig. 8.7. The $\Delta\sigma_h$ measured at the grid points after 2, 4, and 8 passes of compactor are shown in Appendix C3.

In Fig. 8.8, the contours of $\Delta\sigma_h$ formed two circles of stresses at the depth of 300 mm below the edge of the compactor. The $\Delta\sigma_h$ gradually decreased with increasing depth and the distance from the compactor. At $z = 300\text{mm}$, the initial horizontal stress at the depth of 300 mm calculated by Jaky's equation was 2.27 kN/m^2 . The incremental horizontal stress $\Delta\sigma_h$ was up to 1.40 kN/m^2 and the stress incremental ratio was 62 %. It may be concluded that the compaction-induced horizontal stresses were quite obvious below the compactor. When the number of passes of the compactor increased to 2 passes, the two circles of high stresses remained below the edge of the compactor as shown in Fig. 8.9. After 2 – passes of the compactor, $\Delta\sigma_h$ increased to 1.6 kN/m^2 . However, as the number of passes of the compactor increased to 4 and 8 passes, the double high stress circles disappeared, and the contours of $\Delta\sigma_h$ were analogous to concentric circles in Fig. 8.10 and Fig. 8.11. It is clear that the depth of the compaction-induced zone increased with increasing compaction energy input.

8.3 Mechanism of Soils under Strip Compaction

Based on the test results in previous sections, the mechanism of soils under strip compaction is discussed in the following section.

8.3.1 Mechanism after the First Pass of Compactor

Based on the test results of the first pass of the compactor, the mechanism of soils under the compaction lane can be explained by local shear bearing capacity failure mode. The evidence was the amount of surface settlement and relative density of soils observed after compaction. In Fig. 6.9, the backfill under the compactor has been densified and settled. The soils on both edges of the compaction lane were heaved. The observed surface profile was analogous to the nature of local shear failure shown in Fig. 2.11. The relative density of soil varied from 34 % to 65 %. These test results were compared with the Vesic's findings shown in Fig. 8.12. and Fig. 8.13. After the first passage of the compactor, the relative density of part of the soils below the compactor increased from 34 % to 65 %. In Fig. 8.12, the soils under a surface footing can be described with the local shear failure.

The loose sand has an internal friction $\phi = 31^\circ$ and the unit weight $\gamma = 15.6 \text{ kN/m}^3$. For foundations soils that exhibit local shear mode, Terzaghi (1943) suggested that the bearing capacity factors could be calculated by replacing ϕ with $\phi' = \tan^{-1}\left(\frac{2}{3} \tan \phi\right)$. For this study, the ϕ' angle of foundation used to estimate the ultimate bearing capacity is 21.8° . Based on Terzaghi's theory (Eq. 2.16), the ultimate bearing capacity of the strip compaction line with $B = 225 \text{ mm}$ is $q_{ult} = 8.48 \text{ kN/m}^2$. It is apparent that the cyclic dynamic stress $\sigma_{cyc} = 34.9 \text{ kN/m}^2$ applied by the vibratory compactor exceeds the ultimate bearing capacity of the foundation soils.

In Fig. 8.13, Vesic (1973) suggested that as the loaded soil fails with local shear

mode, the composite failure surface would develop. The stresses of sand in zone I belong to active state. Zone II is known as zone of radial shear. Based on the contours of $\Delta\sigma_h$ in the soil mass after the first passage of the compactor shown in Fig. 8.8, Fig. 8.14 shows the comparison between contours of $\Delta\sigma_h$ in this study and soils under the bearing capacity failure mode (Vesic, 1973). The horizontal stresses of sand under the compactor decreased which was analogous to the active zone. The sands in the radial zones were pushed by the downward penetration of the footing and soils in zone II. In Fig. 8.14, two high stress zones were thus induced.

8.3.2 Mechanism after 8 Passes of Compactor

The soils after 8 passes of the compactor showed a different mechanism. As the number of passes of the compactor increased to 8 passes, the compaction-input energy would induce a greater surface settlement and penetration effects. After 8 passes of the compactor, the surface settlement of sand increased to 39.7 mm. The region of dense sand ($D_r = 60\% \sim 80\%$) expanded to the depth of 1200 mm. The change of vertical and horizontal stresses in the soil mass formed the stress contours analogous to concentric circles. The depth of influence zone for $\Delta\sigma_v$ and $\Delta\sigma_h$ was penetrated down about 800 mm to 1200 mm, respectively.

Before compaction, loose sand has the internal friction $\phi = 31^\circ$ and a unit weight $\gamma = 15.6 \text{ kN/m}^3$. Based on Meyerhof's theory (Eq. 2.18) for a pile, the ultimate unit tip resistance of the compaction lane with $B = 225 \text{ mm}$ is $q_p = 36.75 \text{ kN/m}^2$. It is apparent that the cyclic dynamic stress $\sigma_{cyc} = 34.9 \text{ kN/m}^2$ applied by the compactor to the surface of soil approximately equals to the ultimate tip resistance of the foundation soils.

Based on the study of Yang (2006), the influenced zone of the compactor was assumed for piles driven in sand shown in Fig. 8.15. Fig. 2.17 shows the depth of

influence-zone for pile in sand was related to the diameter of pile (D). It shows the influence range below the pile tip in clean sand would be 3.5D~5.5D. Calculating the influence zone of compaction by substituting the width of compactor B = 225 mm for D, the influence range would be 788 ~1238 mm. Fig. 8.16 shows the contours of $\Delta\sigma_h$ measured after 8 passes of the compactor and the influence zone for a single pile driven in sand (Yang, 2006). The influenced zone of compaction is analogous to the stresses below the tip of the pile in sand. The mechanism after 8 passes of the compactor could be simulated by a single pile driven in sand.



Chapter 9

Conclusions

In this study, the effects of strip compaction on sand are investigated. Based on the test results, the following conclusions can be drawn.

1. For loose sand, the vertical and horizontal earth pressure in the soil mass could be properly estimated with the equation $\sigma_v = \gamma z$ and Jaky's equation, respectively.
2. The surface settlement increased with the increasing number of passes of the compactor. The relationship between the surface settlement and the number of passes of the compactor could be modeled by the hyperbolic model.
3. After compaction, the range of contours of relative density ($D_r = 36\%$) would become larger with increasing number of passes.
4. The contours of $\Delta\sigma_v$ were analogous to concentric circles, and the $\Delta\sigma_v$ would decrease gradually from the central region. The vertical stress increment $\Delta\sigma_v$ increased with increasing number of passages of the compactor.
5. The contours of $\Delta\sigma_h$ formed two circles of high stresses and $\Delta\sigma_h$ decreased gradually from the center region after the first and the second passes of compactor. The contours of $\Delta\sigma_h$ were analogous to concentric circles after 4 and 8 passes of the compactor. The depth of the compaction-induced zone increased with increasing compaction energy input.
6. Based on the test results, the mechanism of soils after the first pass of the compactor could be explained by local shear failure. However, the mechanism of soils after 8 passes of the compactor could be simulated by a steel square pile driven in sand with a vibratory hammer.

References

1. Burgess, G. P. (1999). "Performance of Two Full-scale Model Geosynthetic Reinforced Segmental Retaining Walls," MS thesis, Royal Military College of Canada, Kingston, Ontario, 207.
2. Chang, S. Y. (2000). "Effects of Backfill Density on Active Earth Pressure." MS thesis, Dept. of Civil Engineering, National Chiao Tung University, Hsinchu, Taiwan.
3. Chen, T. J. (2002). "Earth Pressure due to Vibratory Compaction." Ph.D. Dissertation, Department of Civil Engineering, National Chiao Tung University, Hsinchu, Taiwan.
4. Chen, T. J., and Fang, Y. S, (2002). "A New Facility For Measurement of Earth Pressure At-Rest," *Geotechnical Engineering Journal*, SEAGS, 3(12), 153-159.
5. Chen, T. J., (2003). "Earth Pressure Due to Vibratory Compaction", Doctor of Philosophy Dissertation, National Chiao Tung University, Hsinchu, Taiwan.
6. D'Appolonia, D. J., Whitman, R. V., and D'Appolonia, E. (1969). "Sand Compaction with Vibratory Rollers." *Journal of the Soil Mechanics and Foundations Division*, ASCE, 95(SM1), 263-284.
7. Das, B. M., (1994), "Principal of Geotechnical Engineering. " 3rd Edition, PWS Publishing Company, Boston.
8. Donath, A. D. (1891). "Untersuchungen ueber den erddruck auf stuetzwaende." *Zeitschrift fuer Bauwesen*, Berlin.
9. Duncan, J. M., and Seed, R. B. (1986). "Compaction-induced Earth Pressures under K_o -conditions." *Journal of Geotechnical Engineering*, ASCE, 112(1), 1-22.
10. Fang, Y. S., Chen, T. J., Holtz, R. D., and Lee, W. F., (2004). "Reduction of Boundary Friction in Model Tests", *Geotechnical Testing Journal*, ASTM, 27(1), 1-10.
11. Filz, G. M., and Duncan J. M. "Earth Pressures due to Compaction: Comparison of Theory with Laboratory and Field Behavior." *Transportation research record*,

- 1526, 28-37.
12. Ho, Y. C., (1999). "Effects of Backfill Compaction on Passive Earth Pressure." MS thesis, Dept. of Civil Engineering, National Chiao Tung University, Hsinchu, Taiwan.
 13. Hou, P. H. (2006). "Design and Construction of NCTU K_A Model Retaining Wall." MS thesis, Dept. of Civil Engineering, National Chiao Tung University, Hsinchu, Taiwan.
 14. Huang, C. C., Cheng, C. Y., Hsia, S. H., and Hsu, S. P. (1994). "Reinforcement Stiffness on Load-deformation Characteristics of Reinforcement." *Proceedings of the Fifth International Conference on Geotextiles, Geomembranes, and Related Products*, Singapore, 1, 197-200.
 15. Jaky, J. (1944). "The Coefficient of Earth Pressure at rest." *Journal for Society of Hungarian Architects and Engineers*, Budapest, Hungary, Oct., 355-358.
 16. Jaky, J., (1948), "Pressure in Soils," *Proceedings, 2nd International Conference on Soil Mechanics and Foundation Engineering*, 1, 103-107.
 17. Johnson, A. W., and Sallberg, J. R. (1960). "Factors That Influence Field Compaction of Soil." Highway Research Board, *Bulletin* No. 272.
 18. Jurgenson, L. (1934) The Application of Theories of Elasticity and Plasticity to Foundation Problems. Contributions to Soil Mechanics 1925-1940. Boston Society of Civil Engineers.
 19. Kumbhojkar, A. S. (1993) "Numerical Evaluation of Terzaghi's N_γ ." *Journal of Geotechnical Engineering*, American Society of Civil Engineers, 119(3), 598-607.
 20. Ladd, C. C., Foott, R., Ishihara, K., Schlosser, F., and Poulos, H. G. (1977). "Stress-deformation and Strength Characteristics." *Proc., 9th Int. Conf. on Soil Mechanics and Foundation Engineering*, Tokyo, 2, 421-494.
 21. Lo Presti, D. C. F., Pedroni, S., and Crippa, V. (1992). "Maximum Dry Density of Cohesionless Soils by Pluviation and by ASTM D 4253-83: A comparative study." *Geotechnical Testing Journal*, ASTM, 15(2), 180-189.
 22. Mayne, P. W., and Kulhawy, F. H. (1982). " K_o -OCR Relationships in Soil."

- Journal of Geotechnical Engineering Division*, ASCE, 108(GT6), 851-872.
23. McElroy, J. A. (1997). "Seismic Stability of Geosynthetic Reinforced Slopes: A shaking table study." MS thesis, University of Washington, Seattle, 286.
 24. Mesri, G., and Hayat, T. M. (1993). "The Coefficient of Earth Pressure at rest." *Canadian Geotechnical Journal*, 30(4), 647-666.
 25. Meyerhof, G. G. (1976). "Bearing Capacity and Settlement of Pile Foundation." *Journal of the Geotechnical Engineering Division*, ASCE, 102(3), 197-228.
 26. Rad, N. S., and Tumay, M. T. (1987). "Factors affecting sand specimen preparation by raining." *ASTM Geotechnical Testing Journal*, 10(1), 31-37.
 27. Seed, R. B., and Duncan, J. M. (1983). "Soil-Structure Interaction Effects of Compaction-induced Stresses and Deflections." *Geotechnical Engineering Research Report No. UcB/GT/83-06*, Univ. of California Berkeley, CA.
 28. Sowers, G. F., Robb, A. D., Mullis, C. H., and Glenn, A. J. (1957). "The Residual Lateral Pressures Produced by Compacting Soils." *Proceedings, 4th International Conference on Soil Mechanics and Foundation Engineering*, London, 243-247.
 29. Terzaghi, K. (1943). *Theoretical Soil Mechanics*, Wiley, New York.
 30. Tzeng, S. K., (2002). "Horizontal Pressure on an Unyielding Wall due to Strip Loading on Backfill with Different Densities." MS thesis, Dept. of Civil Engineering, National Chiao Tung University, Hsinchu, Taiwan.
 31. US NAVY. (1982). "Foundations and Earth Structures." *NAVFAC Design Manual DM-7.2*. Naval Facilities Engineering Command, U.S. Government Printing Office, Washington, D. C., 60.
 32. Vesic, A. S. (1973). "Analysis of Ultimate Loads of Shallow Foundations." *Journal of the Soil Mechanics and Foundations Division*, 99(SM1), 45-73.
 33. Vesic, A. S., Banks, D. C., and Woodard, J. M. (1965). "An Experimental Study of Dynamic Bearing Capacity of Footings on Sand." *Proceedings, Sixth International Conference on Soil Mechanics and Foundation Engineering*, Montreal, Canada, II, 209-213.
 34. Wu, F. J., (1992). "Effects of Adjacent Rock Face Inclination on Earth Pressure

- at-rest.” MS thesis, Dept. of Civil Engineering, National Chiao Tung University, Hsinchu, Taiwan.
35. Wu, B. F., (1992). “Design and Construction of National Chiao Tung University Model Retaining Wall.” MS thesis, Dept. of Civil Engineering, National Chiao Tung University, Hsinchu, Taiwan.
36. Yang, J. (2006). “ Influence Zone for End Bearing of Piles in Sand.” *Journal of Geotechnical Geoenvironmental Engineering*, ASCE, 132(9), 1229-1237.



Table. 2.1. Terzaghi's Bearing Capacity Factors (after Kumbhojkar, 1993)

ϕ'	N_c	N_q	N_γ	ϕ'	N_c	N_q	N_γ
0	5.70	1.00	0.00	26	27.09	14.21	9.84
1	6.00	1.10	0.01	27	29.24	15.90	11.60
2	6.30	1.22	0.04	28	31.61	17.81	13.70
3	6.62	1.35	0.06	29	34.24	19.98	16.18
4	6.97	1.49	0.10	30	37.16	22.46	19.13
5	7.34	1.64	0.14	31	40.41	25.28	22.65
6	7.73	1.81	0.20	32	44.04	28.52	26.87
7	8.15	2.00	0.27	33	48.08	32.23	31.94
8	8.60	2.21	0.35	34	52.64	36.50	38.04
9	9.09	2.44	0.44	35	57.75	41.44	45.41
10	9.61	2.69	0.56	36	63.53	47.16	54.36
11	10.16	2.98	0.69	37	70.01	53.80	65.27
12	10.76	3.29	0.85	38	77.50	61.55	78.61
13	11.41	3.63	1.04	39	85.97	70.61	95.03
14	12.11	4.02	1.26	40	95.66	81.27	115.31
15	12.86	4.45	1.52	41	106.81	93.85	104.51
16	13.68	4.92	1.82	42	119.67	108.75	171.99
17	14.60	5.45	2.18	43	134.58	126.50	211.56
18	15.12	6.04	2.59	44	151.95	147.74	261.60
19	16.56	6.70	3.07	45	172.28	173.28	325.34
20	17.69	7.44	3.64	46	196.22	204.19	407.11
21	18.92	8.26	4.31	47	224.55	241.80	512.84
22	20.27	9.19	5.09	48	258.28	287.85	650.67
23	21.75	10.23	6.00	49	298.71	344.63	831.99
24	23.36	11.40	7.08	50	347.50	415.14	1072.80
25	25.13	12.72	8.34				

Table 3.1. Technical Information of the Eccentric Motor

Manufacture	Mikasa
Type	KJ75-2P
Power (Watt)	75
Voltage (Volt)	220
Frequency (Hz)	50/60
Vibration per Minute	3000/3600
Mass (kg)	6.2



Table 4.1. Properties of Ottawa Sand (after Hou, 2006)

Shape	Rounded
e_{\max}	0.76
e_{\min}	0.50
G_s	2.65
D_{60}, mm	0.32
D_{10}, mm	0.21
C_u	1.78



Table 6.1. Relationship between the Surface Settlement and Number of Pass

(a) S_{\max} divided into Five Equal Parts and the Corresponding Number of Passes

Surface Settlement (mm)		Number of Pass (N)
0.2 S_{\max}	8.30	0.18
0.4 S_{\max}	16.60	0.49
0.6 S_{\max}	24.90	1.11
0.8 S_{\max}	33.20	2.95
1.0 S_{\max}	41.50	∞

(b) 1, 2, 4, and 8 Compactor Passes and Corresponding Surface Settlement

Number of Pass (N)	Surface Settlement (mm)	
1	23.87	0.58 S_{\max}
2	30.30	0.73 S_{\max}
4	35.03	0.84 S_{\max}
8	37.99	0.92 S_{\max}
∞	41.50	1.0 S_{\max}

Table 6.2. Differences between Test Results from the Laboratory
and Test Results from the Field

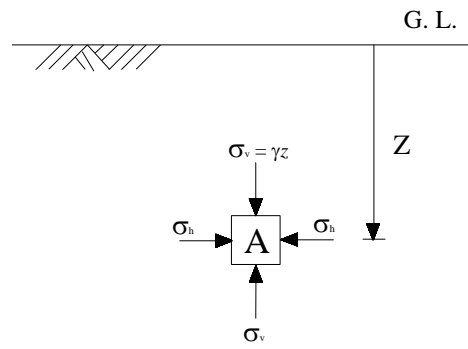
Item	NCTU	D'Appolonia
Soil type	Ottawa sand	Dune sand
Compactor	Hand tamper	Vibratory drum roller
Lift thickness	1.5 m	2.44 m
Construction	Lane compaction	Area compaction
Energy	Low (1.767 kN)	Big (55.6 kN)
Influenced depth	Shallow	Deep
$\gamma_{d,max}$	Small	Big
Place	Laboratory	Field



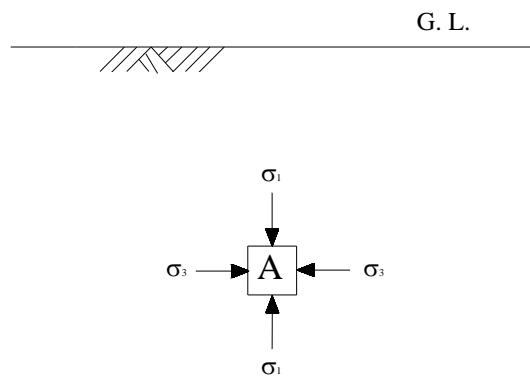


Fig. 1.1.Compaction of Soil with Vibratory Compactor





(a)



(b)

Fig. 2.1 Development of in-situ Stresses

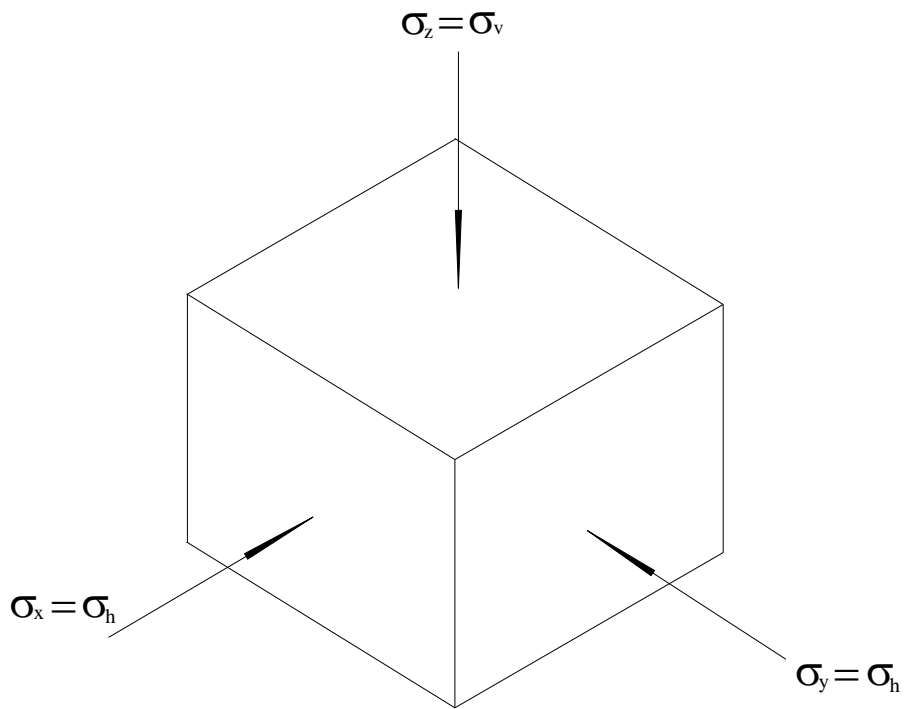


Fig. 2.2. Principal Stresses in a Soil Element



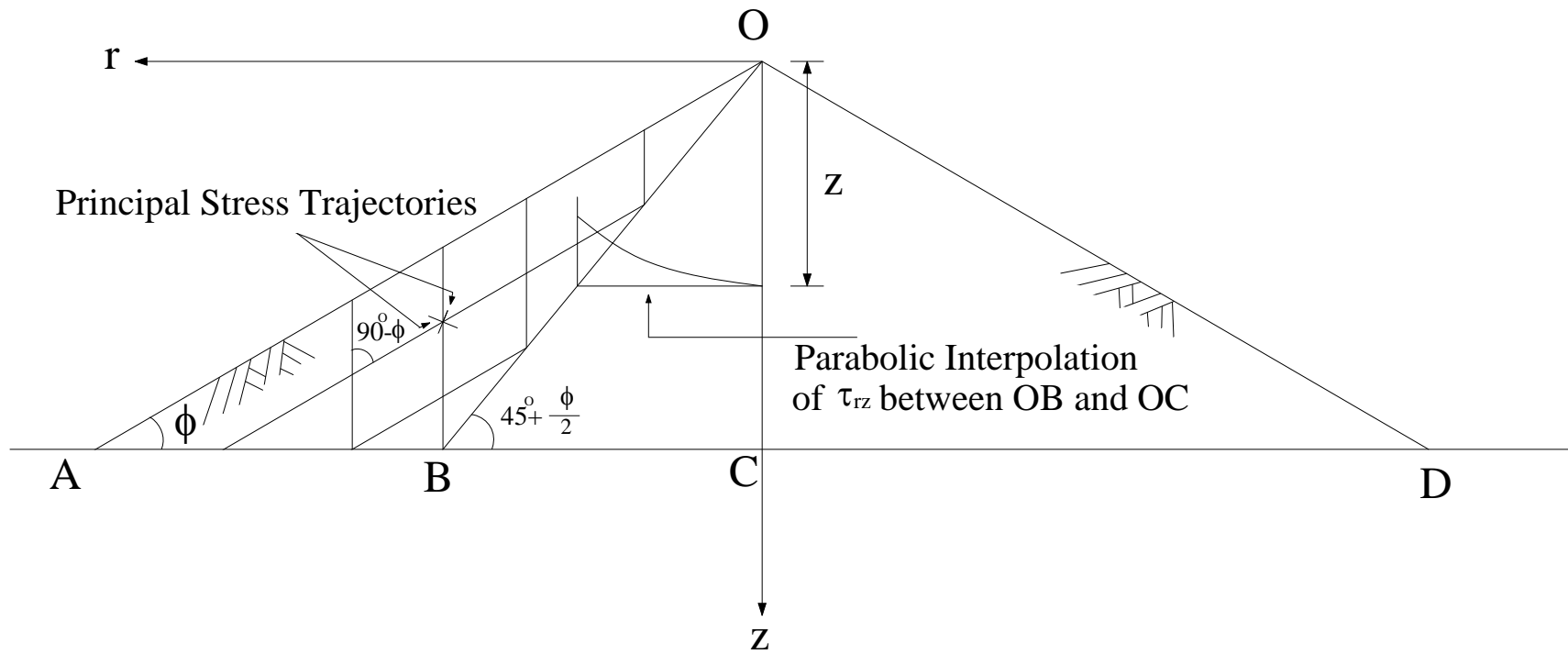


Fig. 2.3. Jaky's Formulation of the Relationship between K_o on OC and ϕ Mobilized in OAB
(after Mesri and Hayat, 1993)

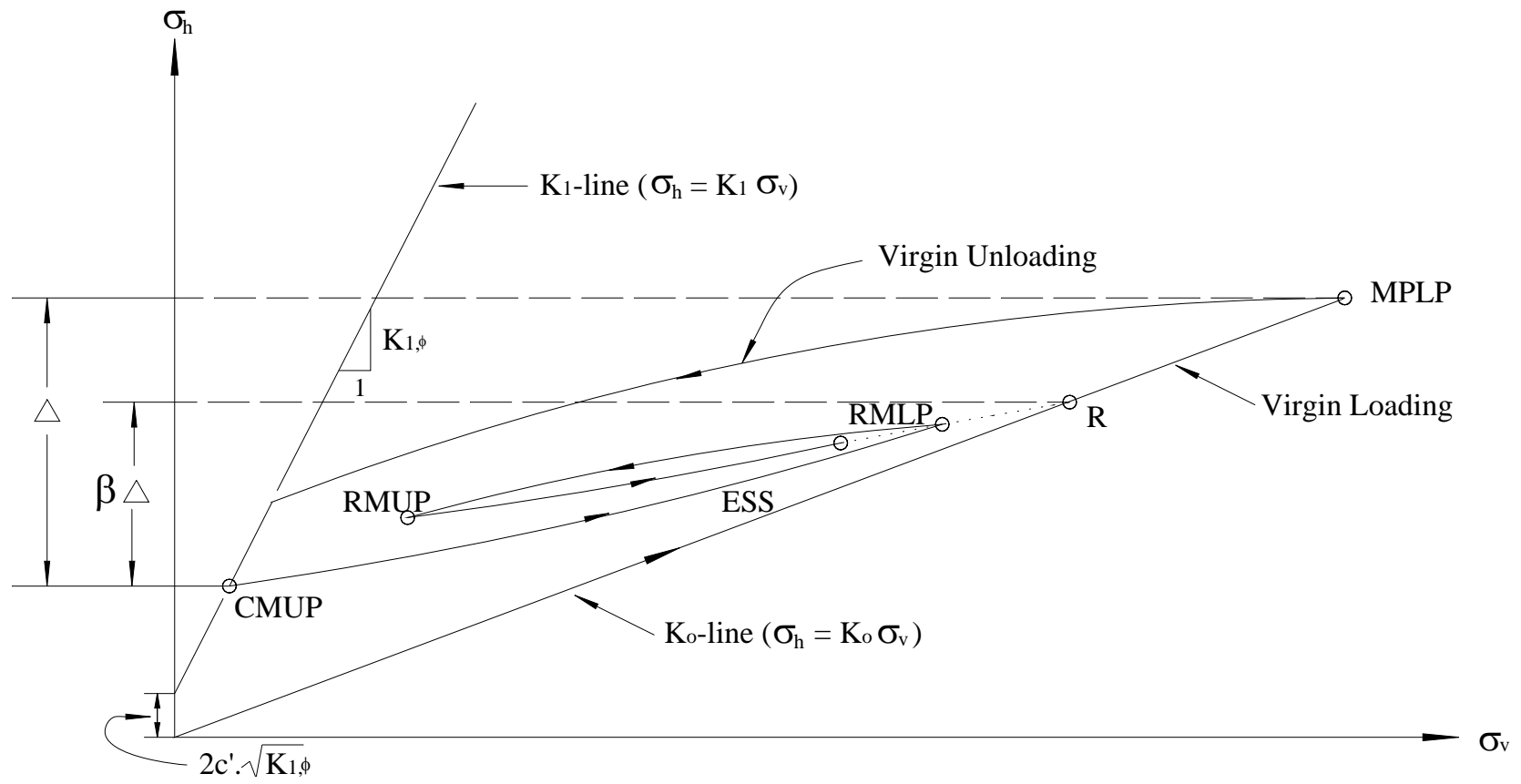


Fig. 2.4. Basic Components of Hysteretic K_0 -Loading/Unloading Model
(after Duncan and Seed, 1986)

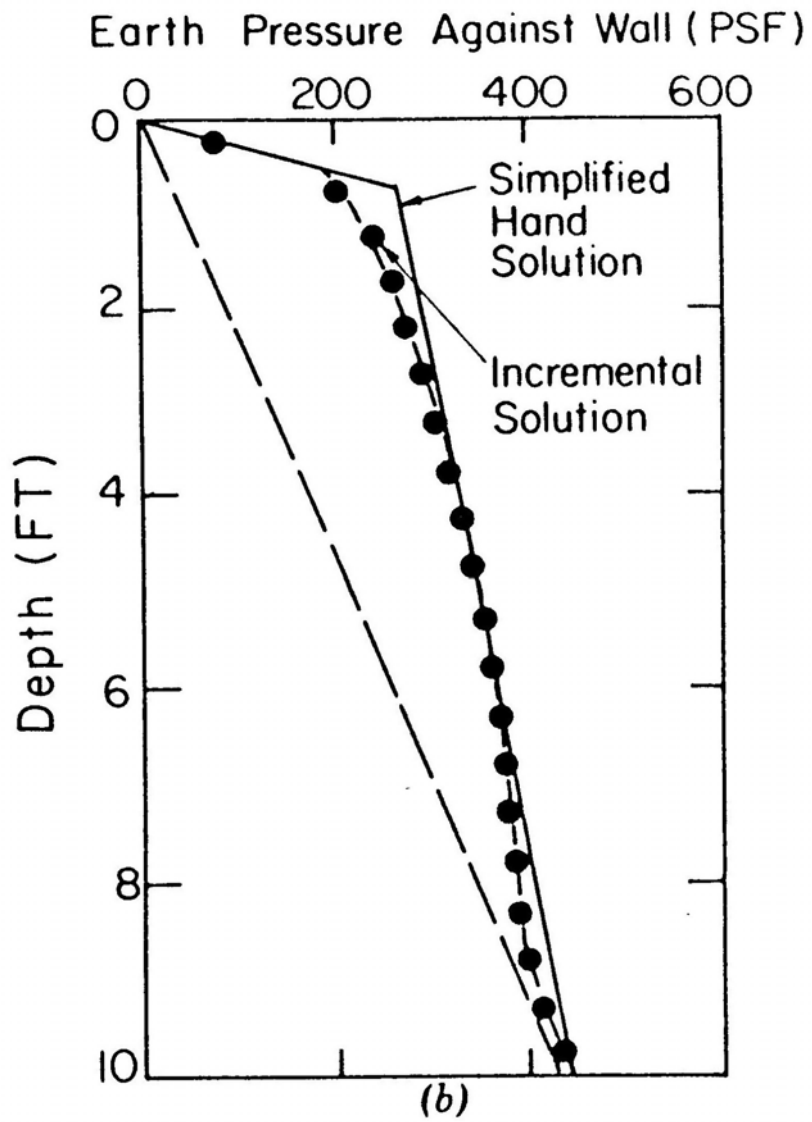


Fig. 2.5. Comparison between Final Pressure Distributions Based on Incremental Analysis and Hand Solution (after Duncan and Seed, 1983)

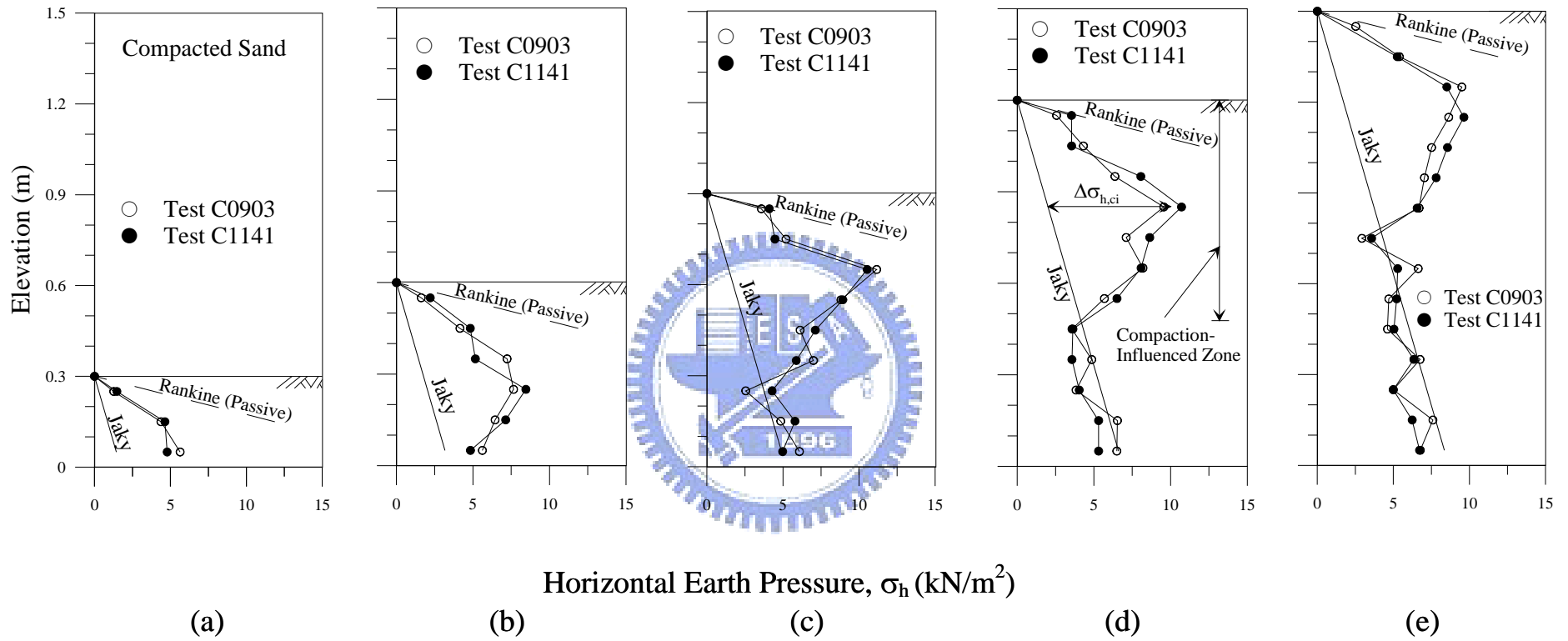


Fig. 2.6. Distribution of Horizontal Earth Pressure after Compaction
(after Chen, 2002)

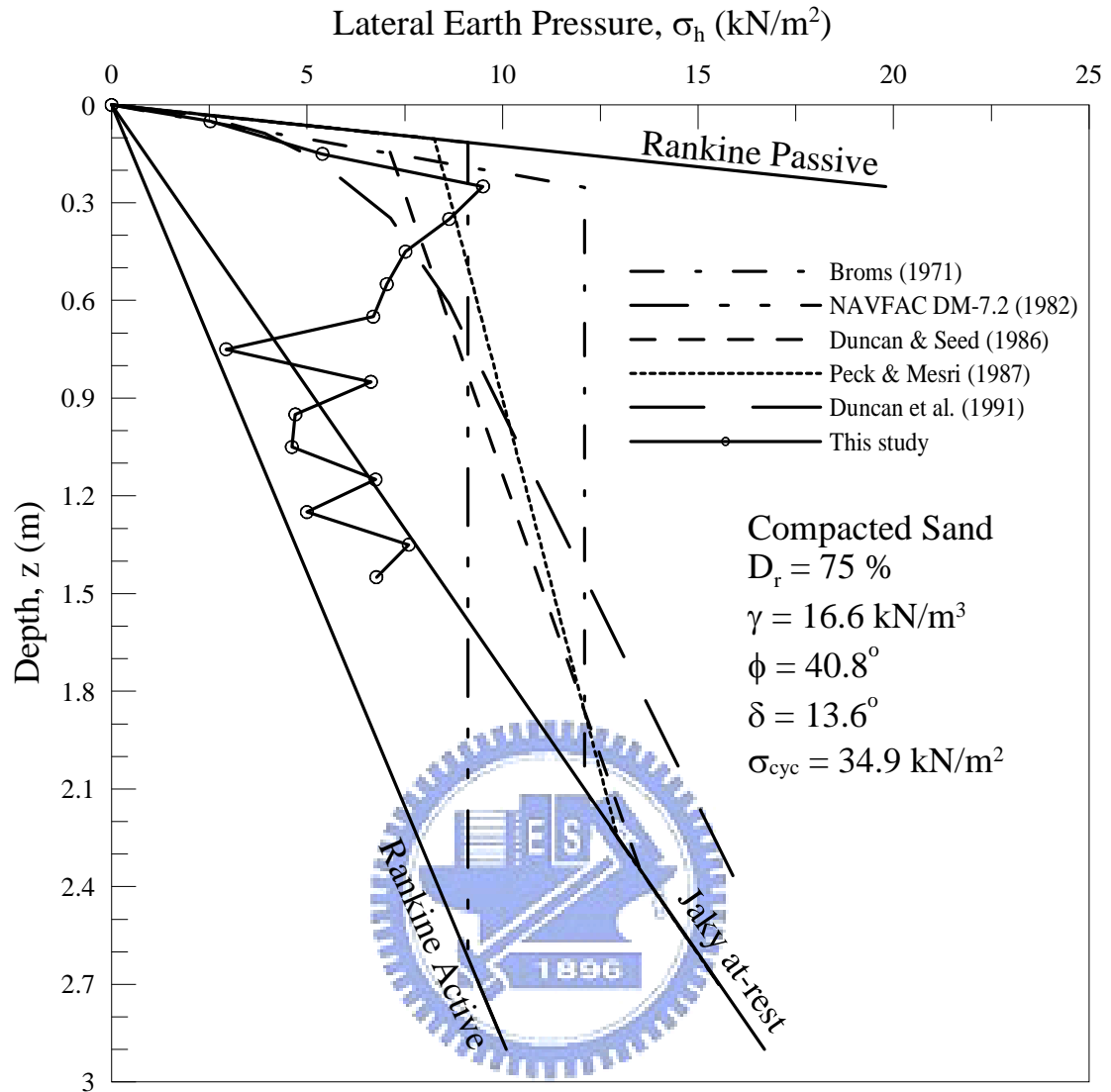


Fig. 2.7. Horizontal Earth Pressure Estimated with Various Methods after Compaction (after Chen,2002)

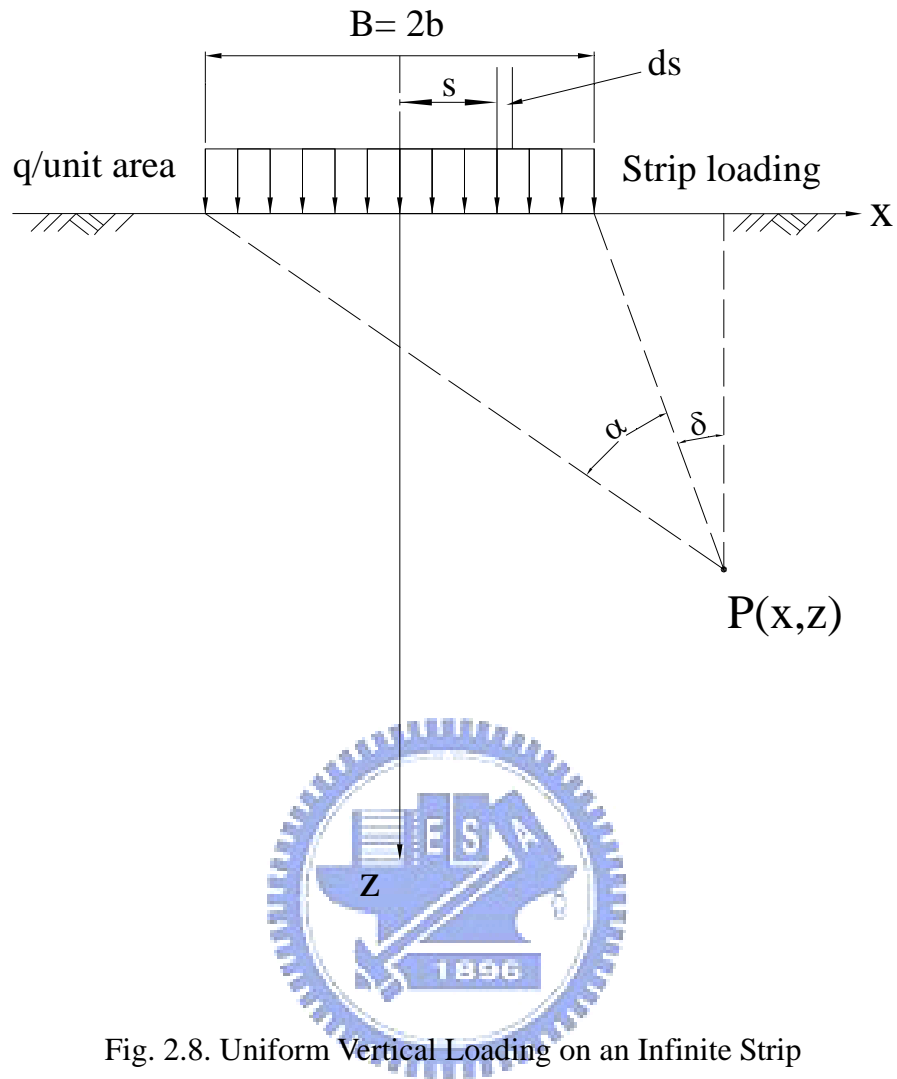


Fig. 2.8. Uniform Vertical Loading on an Infinite Strip

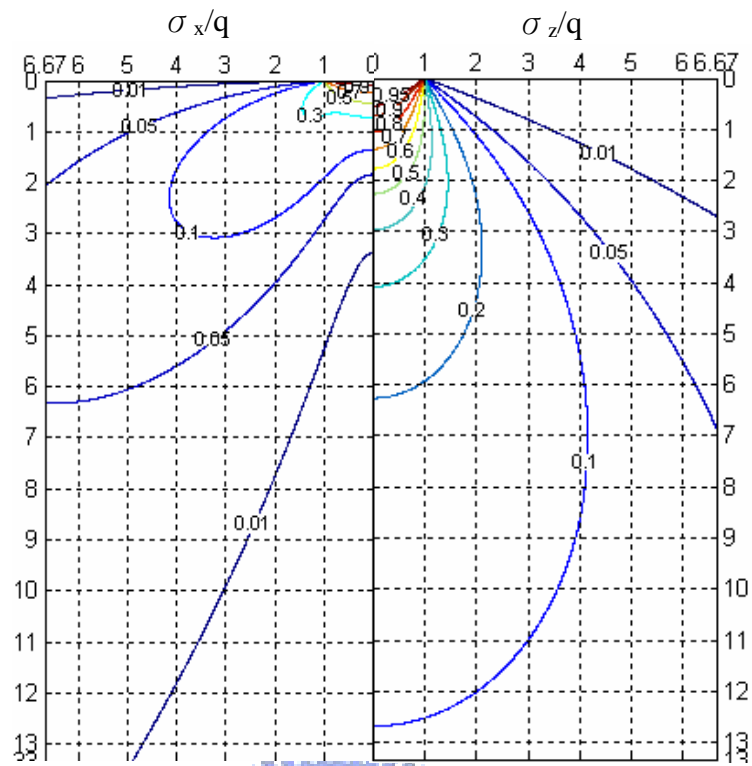


Fig. 2.9. Stress beneath a Strip (after Jurgenson, 1934)



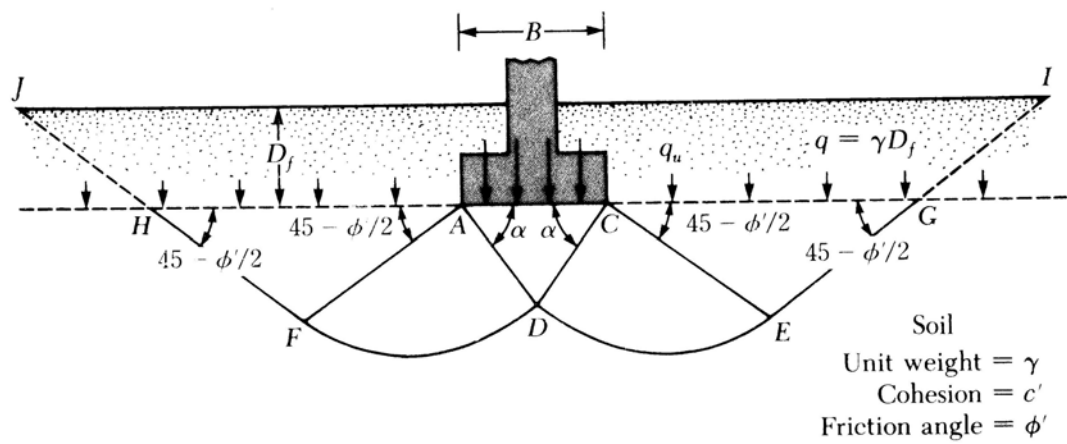


Fig. 2.10. Bearing Capacity Failure in Soil under a Rough Rigid Continuous Foundation (after Terzaghi, 1943)



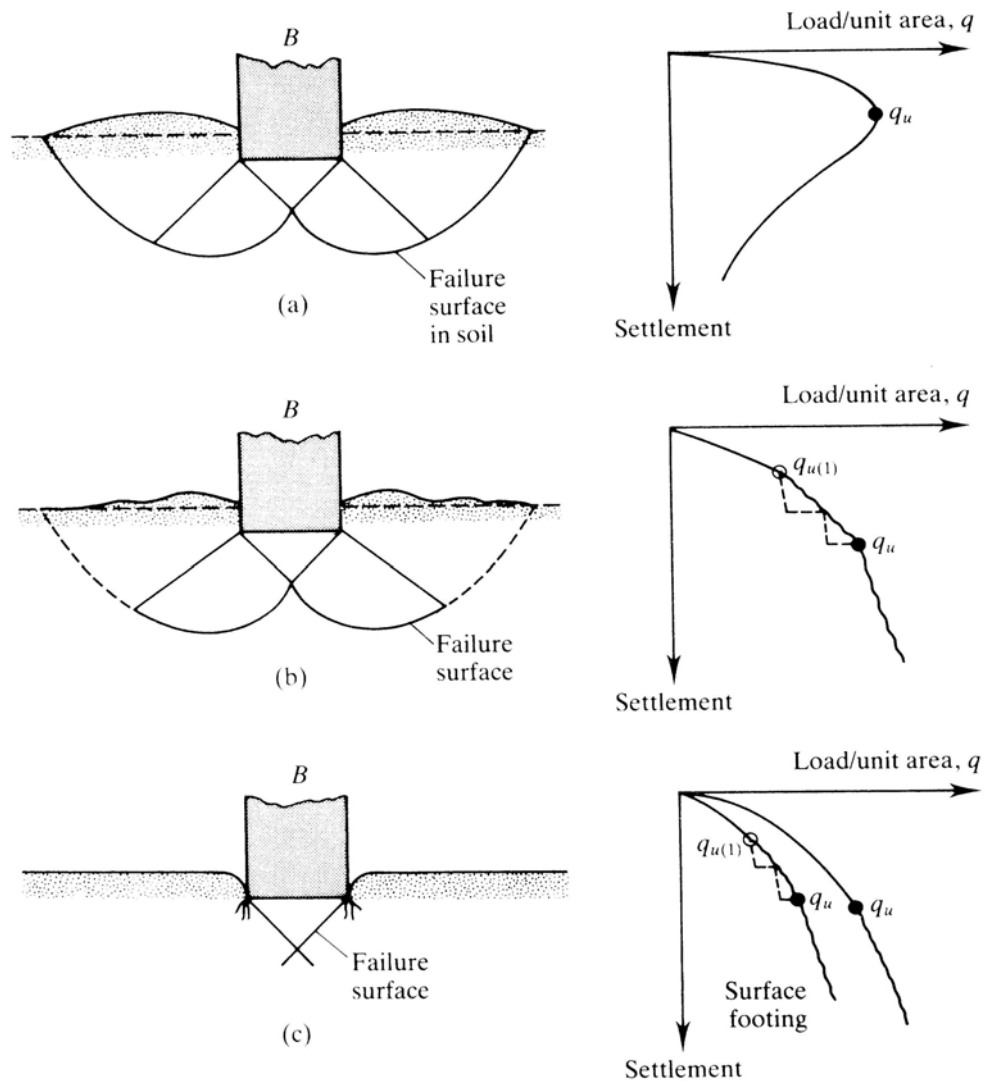


Fig. 2.11. Definition of Failure Mode (after Vesic, 1973)

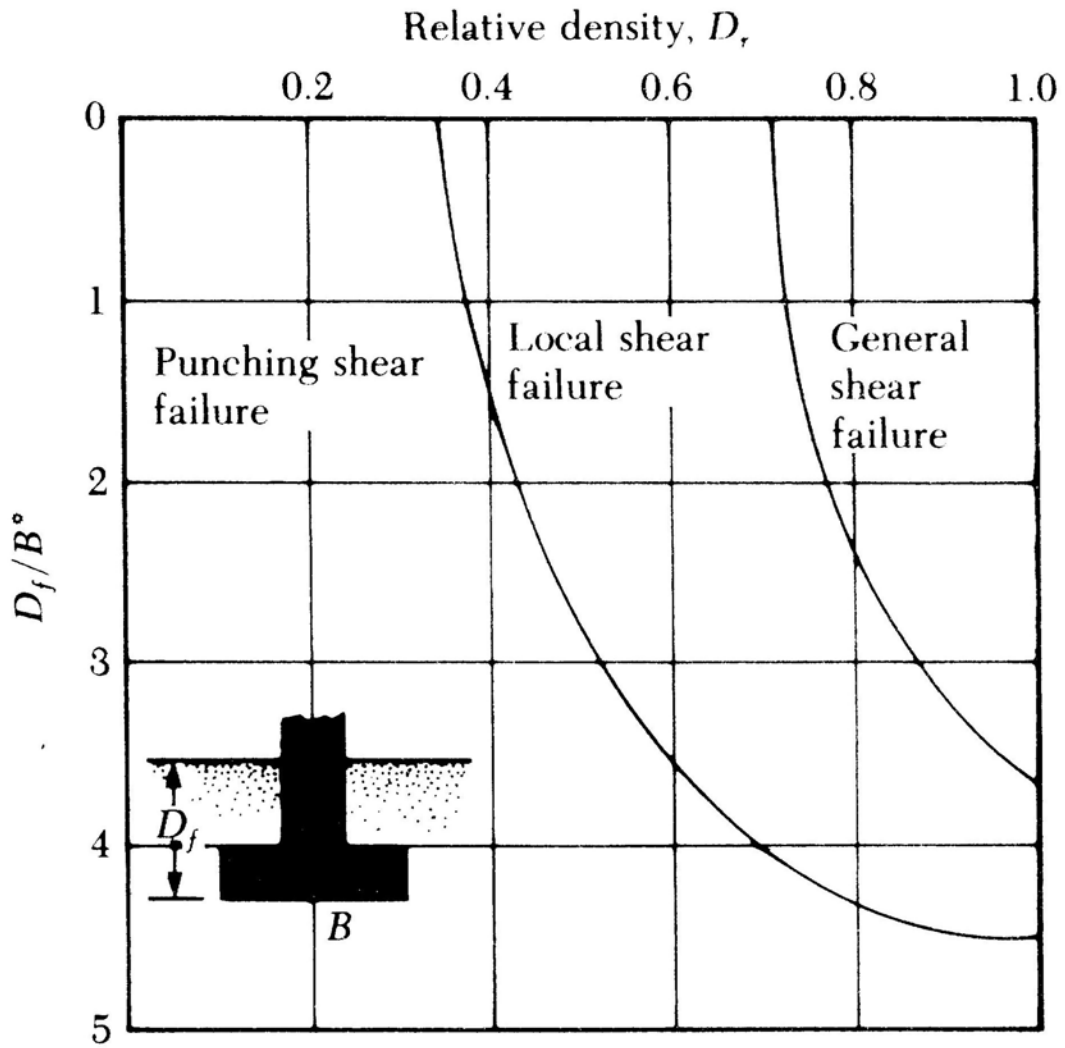


Fig. 2.12. Mode of Foundation Failure in Sand (after Vesic, 1973)

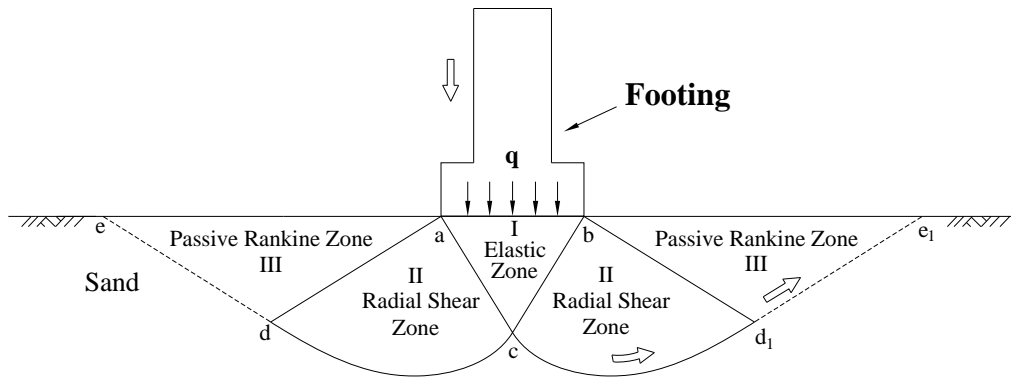
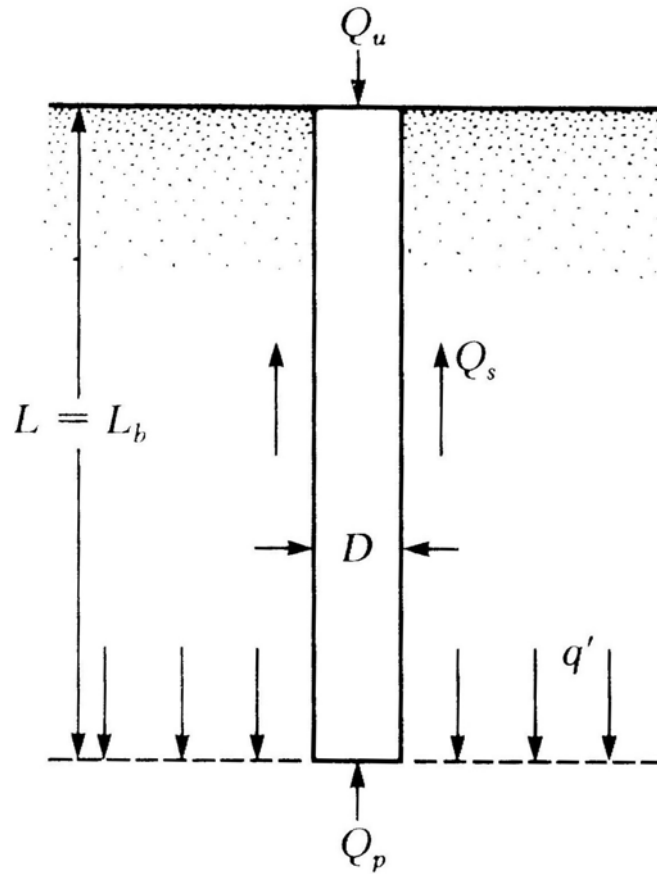


Fig. 2.13. Bearing Capacity Failure in Soil (after Vesic, 1973)





L = length of embedment
 L_b = length of embedment in bearing stratum



Fig. 2.14. Ultimate Load-Carrying Capacity of Pile (after Meyerhof, 1976)

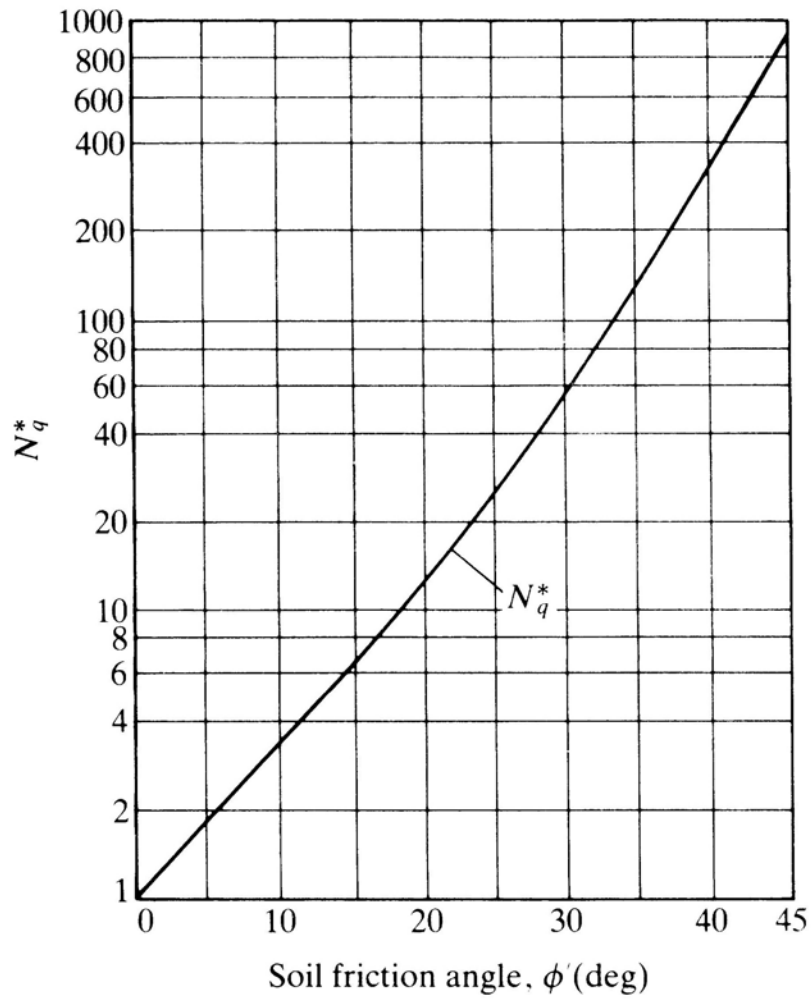


Fig. 2.15. Variation of the Maximum Values of N_q^* with Soil Friction Angle ϕ'
 (after Meyerhof, 1976)

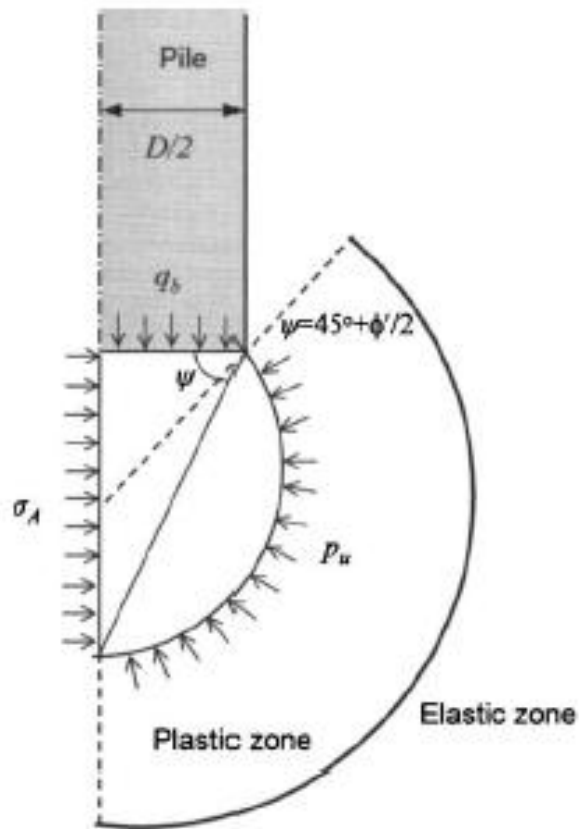


Fig.2.16. Influence Zone Assumed for Piles in Sand (after Yang, 2006)

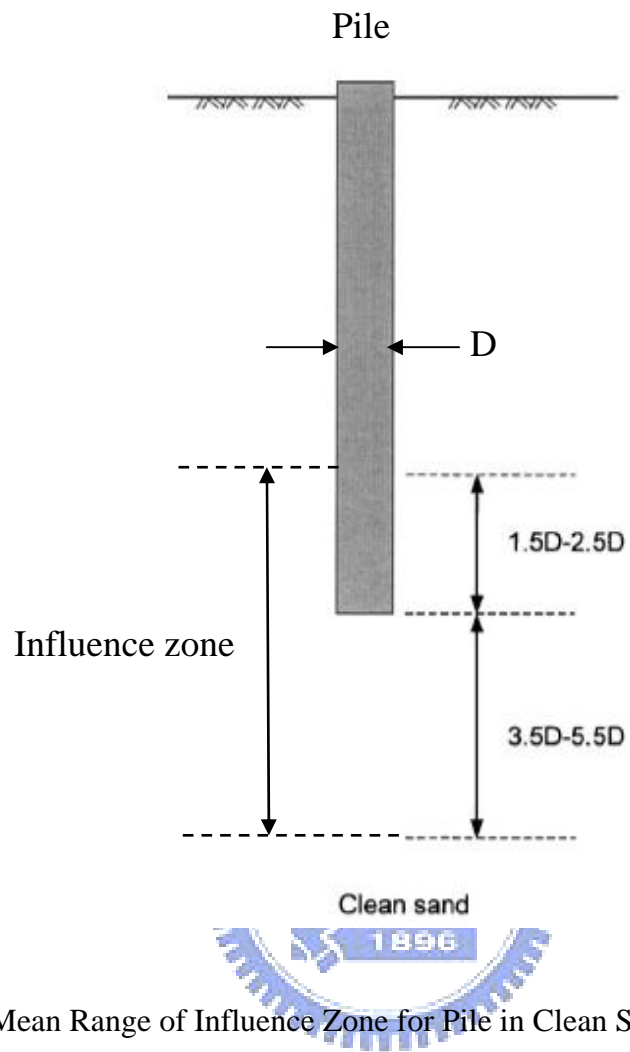


Fig. 2.17. Mean Range of Influence Zone for Pile in Clean Sand (after Yang, 2006)

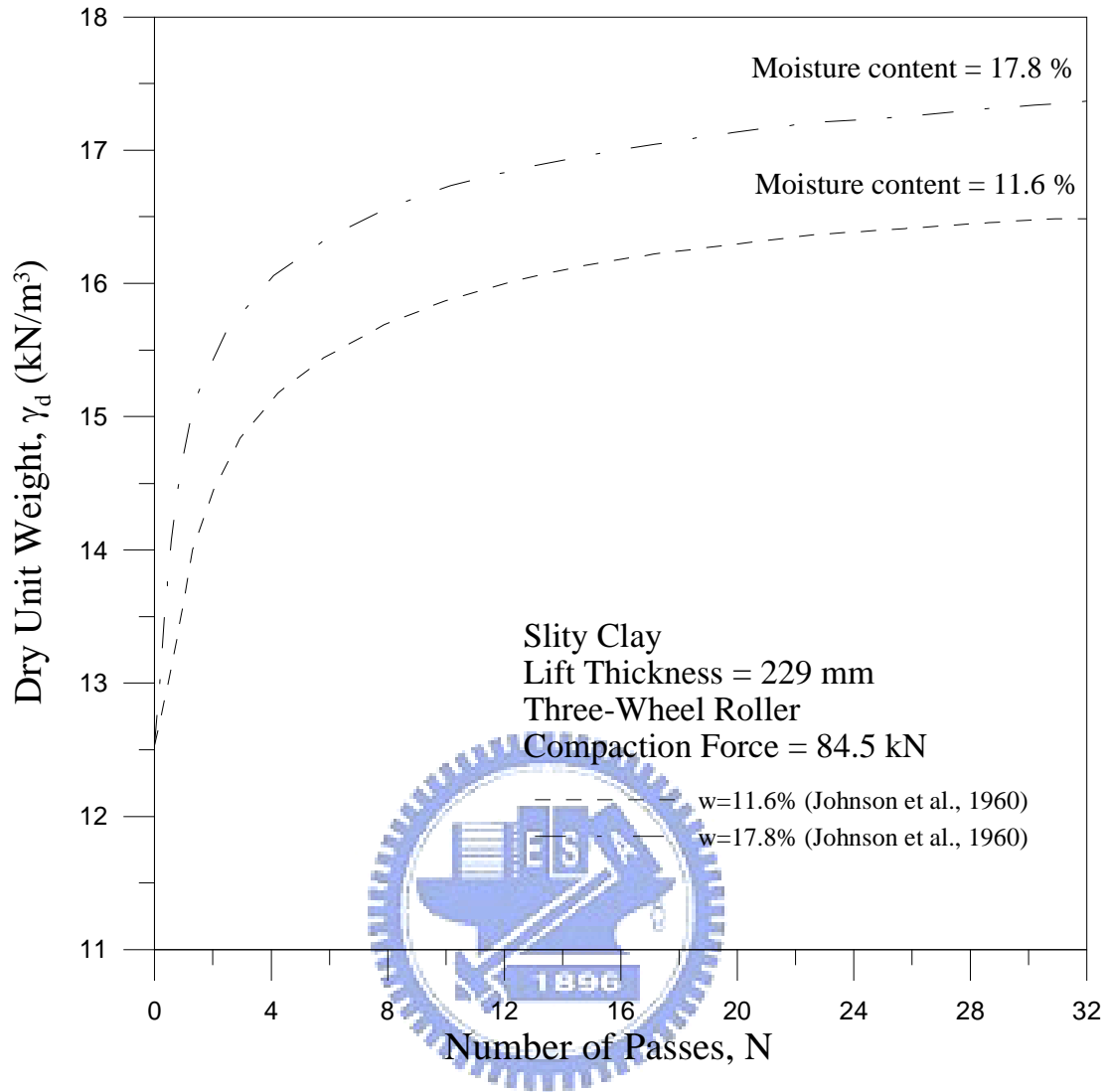


Fig. 2.18. Growth Curves for a Silty Clay – Relationship between Dry Unit Weight and Number of Passes of Three-Wheel Roller Compactor (after Johnson and Sallberg, 1960)

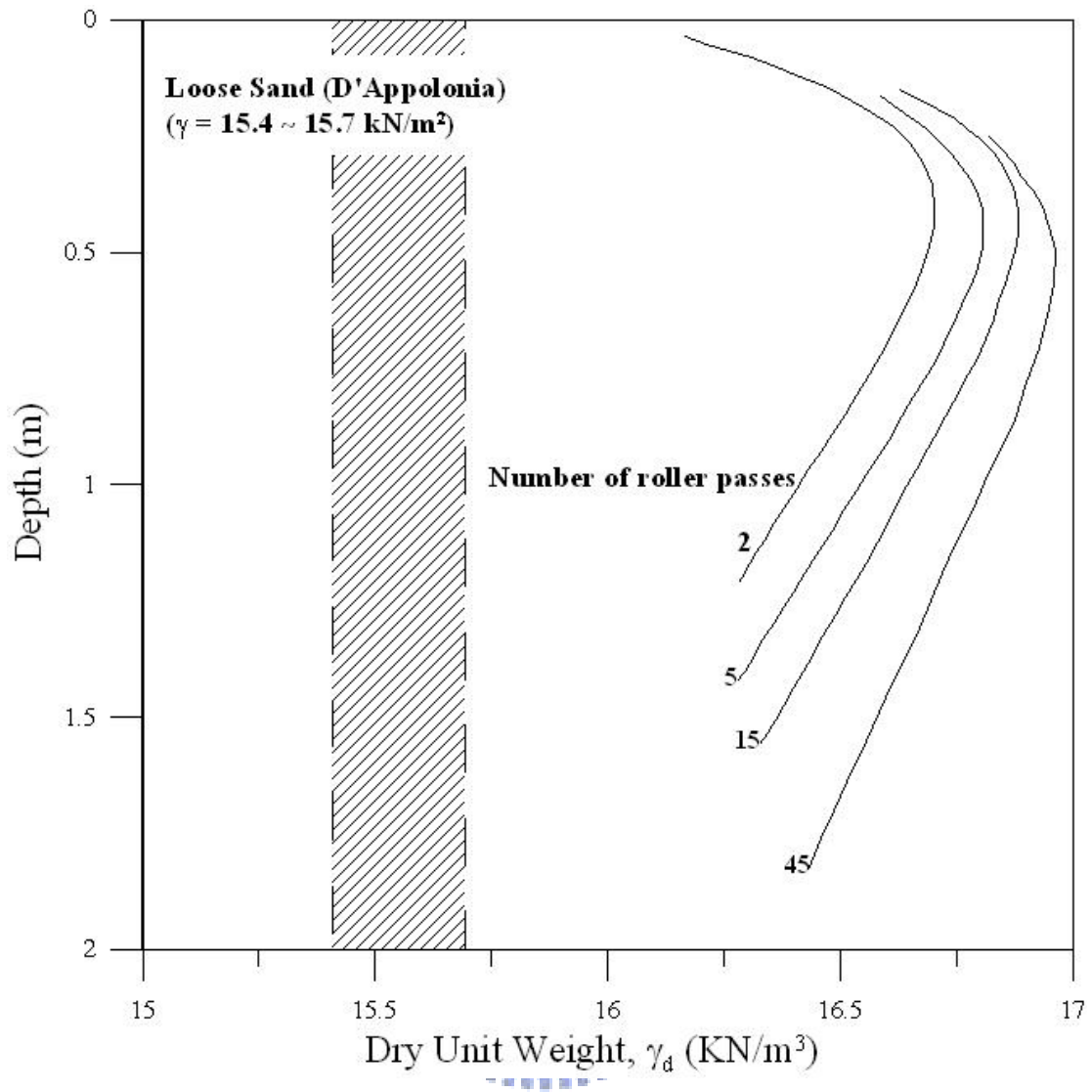
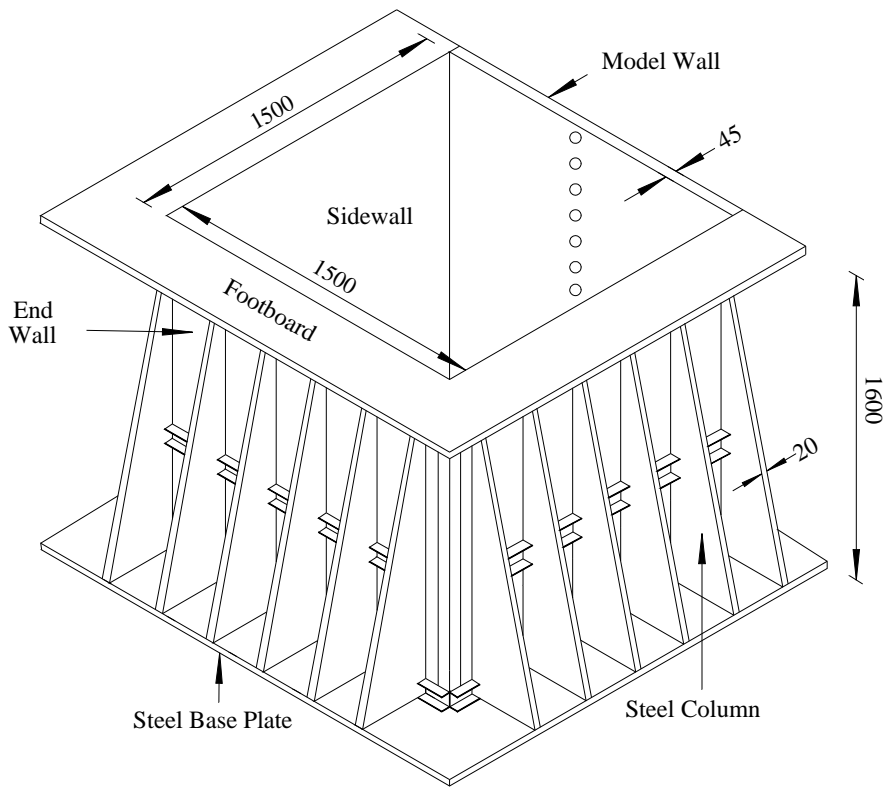


Fig. 2.19. Vibratory Compaction of a Sand - Variation of Dry Unit Weight with Number of Roller Passes; Thickness of Lift = 2.45 m (after D'Appolonia, Whitman and D'Appolonia, 1969)



Unit : mm



Fig. 3.1. NCTU Non-Yielding Retaining-Wall Facility (after Chen, 2002)



Fig. 3.2. Soil-Pressure Transducer (Kyowa BE-2KCM17) (after Chen, 2002)



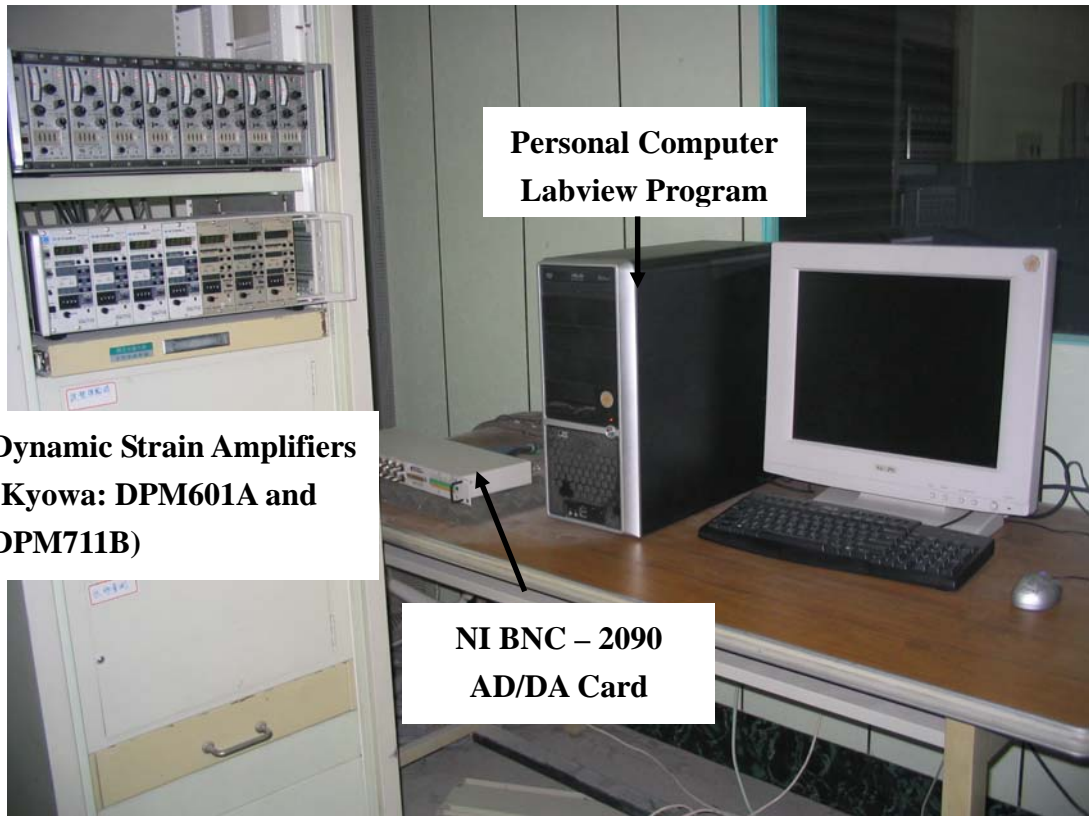


Fig. 3.3. Data Acquisition System



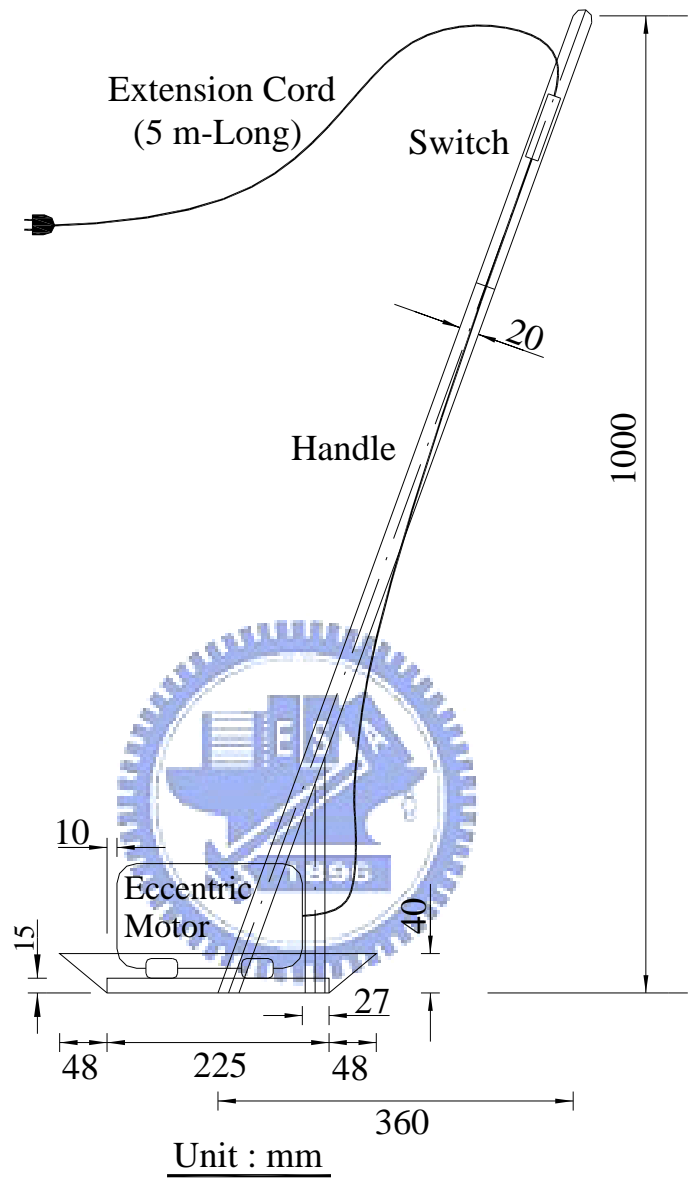


Fig. 3.3. Side-View of Vibratory Soil Compactor



Fig. 3.5. Vibratory Soil Compactor

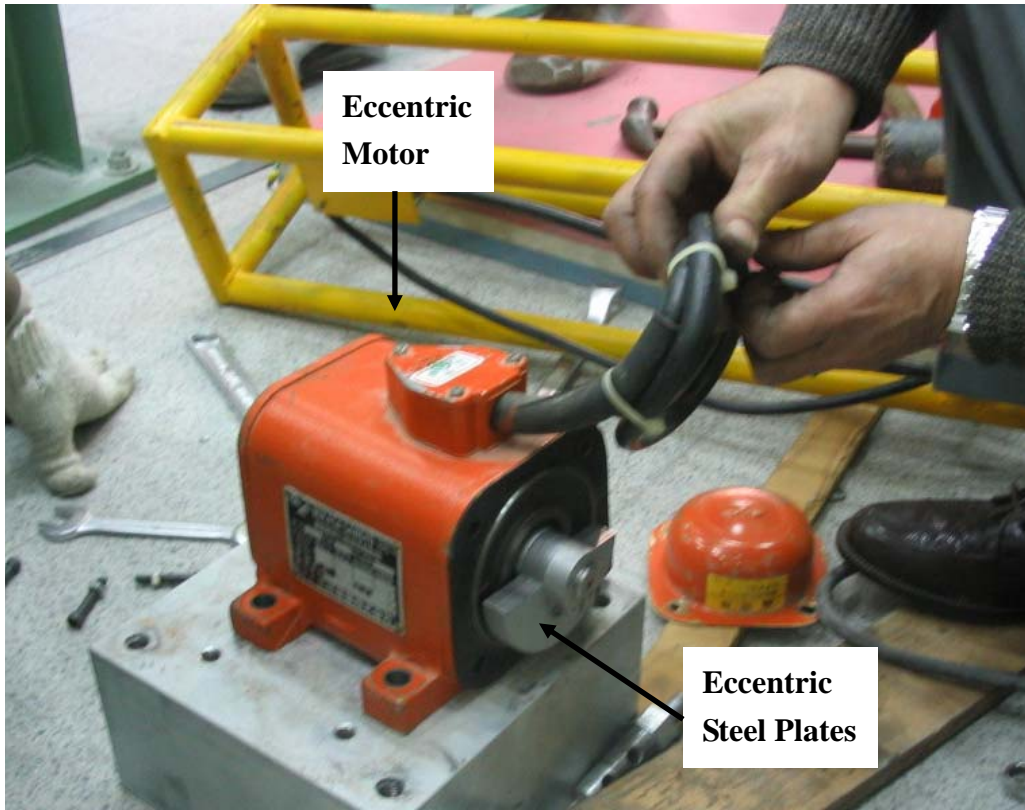


Fig. 3.6. Eccentric Motor with Eccentric Steel Plate (Mikasa KJ75)
(after Wang, 2005)

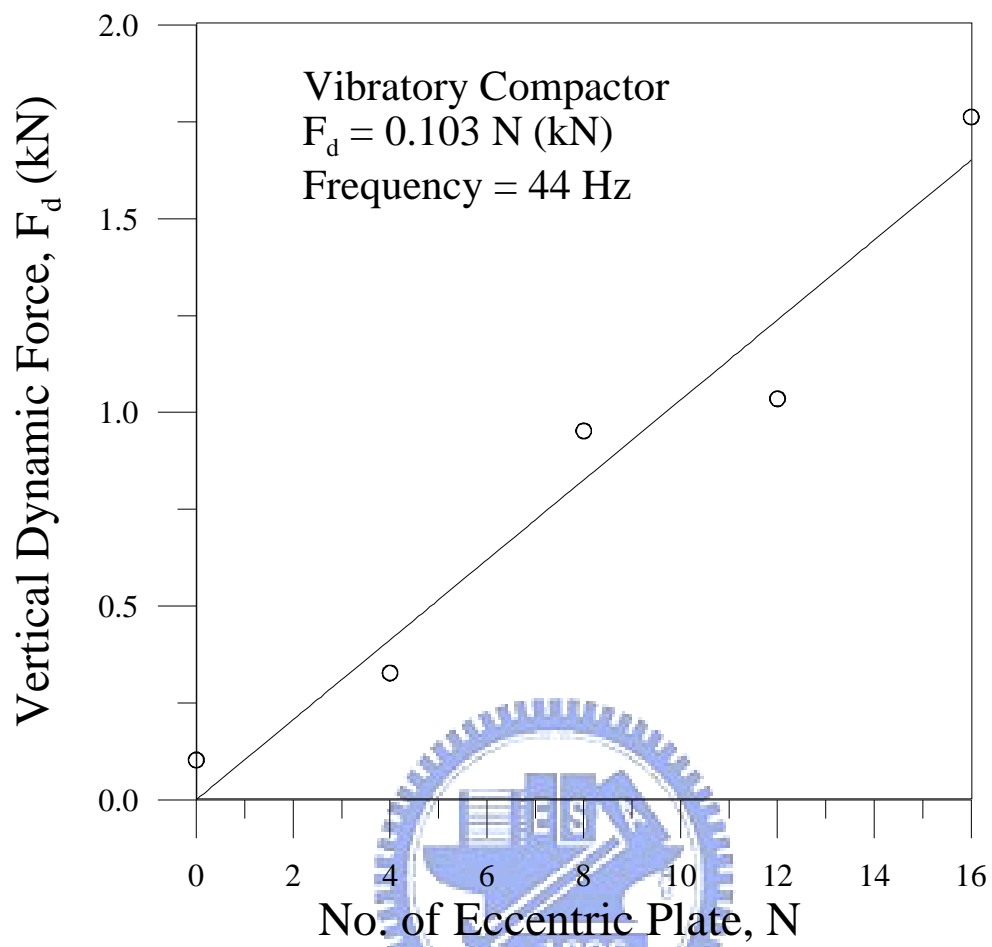


Fig. 3.7. Vertical Dynamic Force Generated by Compactor as a Function of No. of Eccentric Plate (after Chen, 2002)

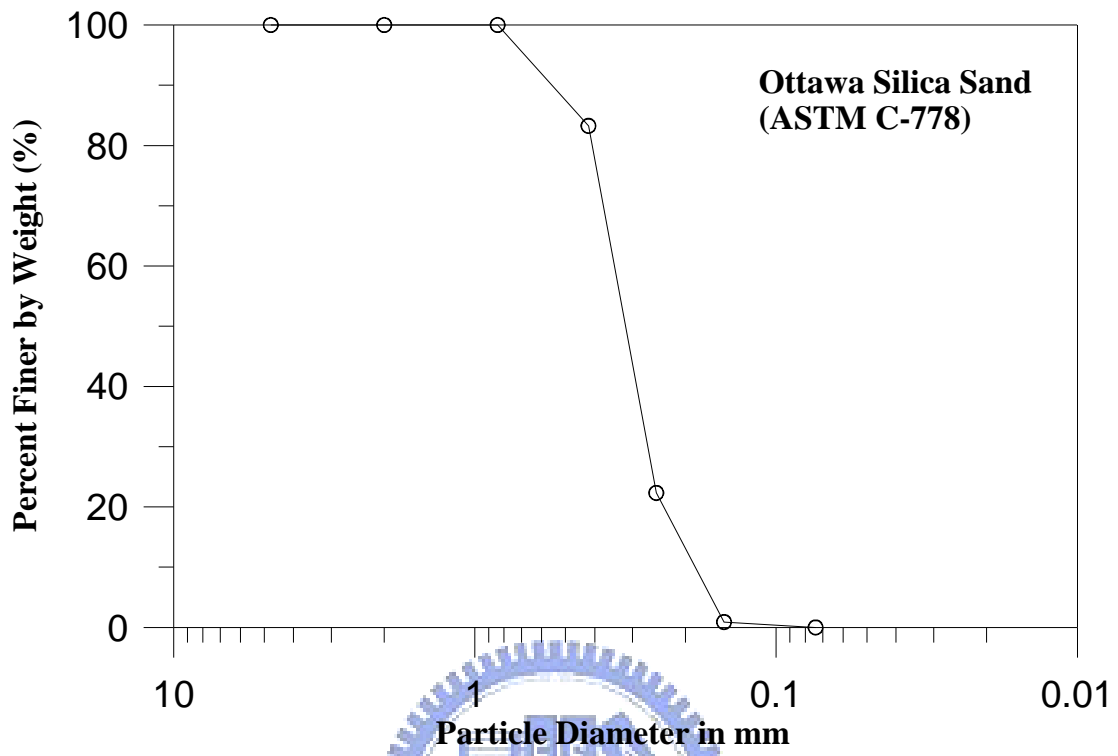
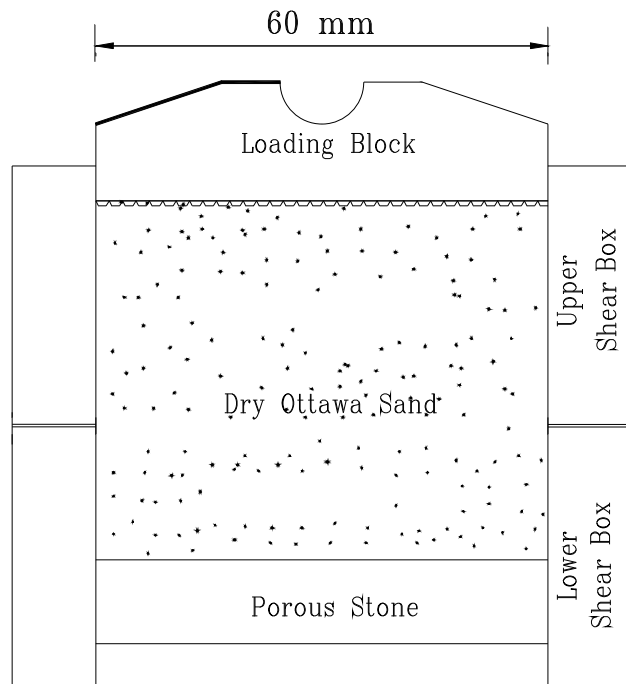


Fig. 4.1. Grain Size Distribution of Ottawa Sand (after Hou, 2006)





Unit : mm



Fig. 4.2. Shear Box of Direct Shear Test Device
(after Wu, 1992)

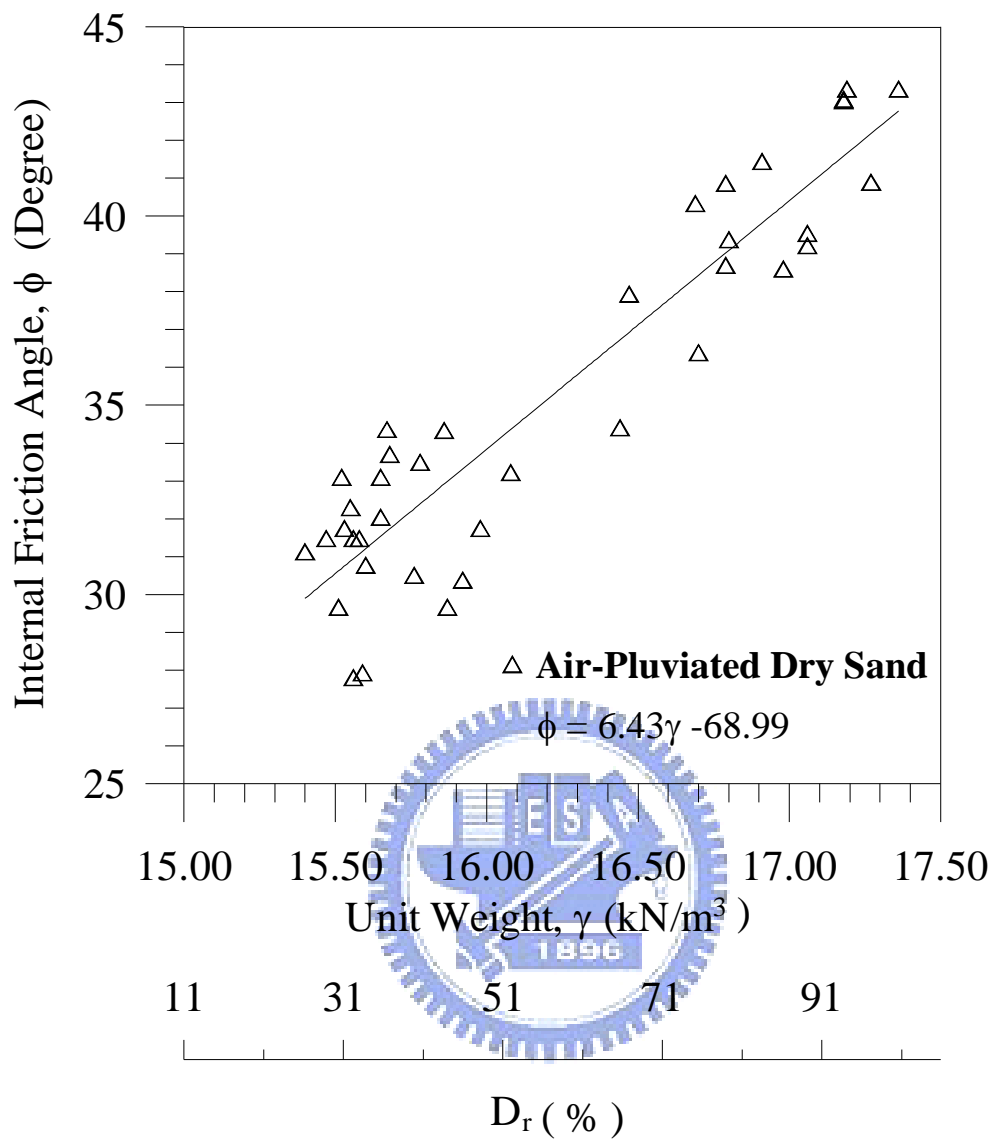


Fig. 4.3. Relationship between Unit Weight γ and Internal Friction Angle ϕ (after Chang, 2000)

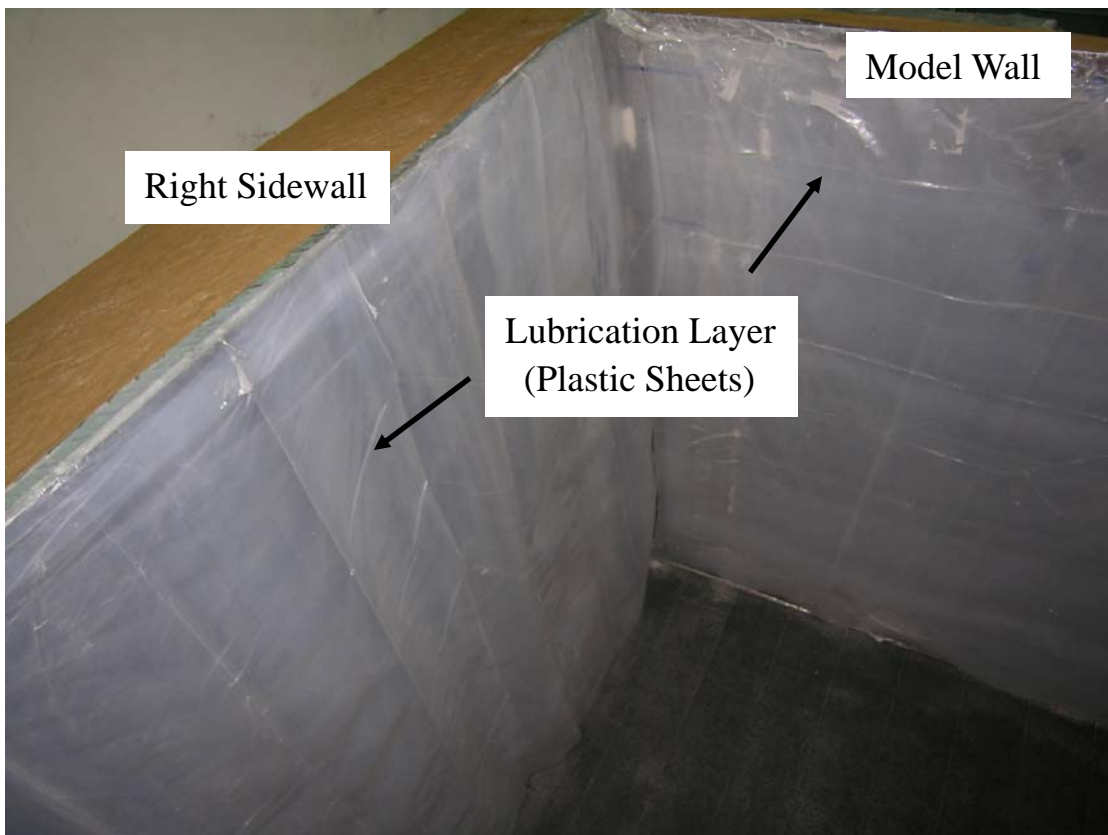


Fig. 4.4. Lubrication Layer on the Walls



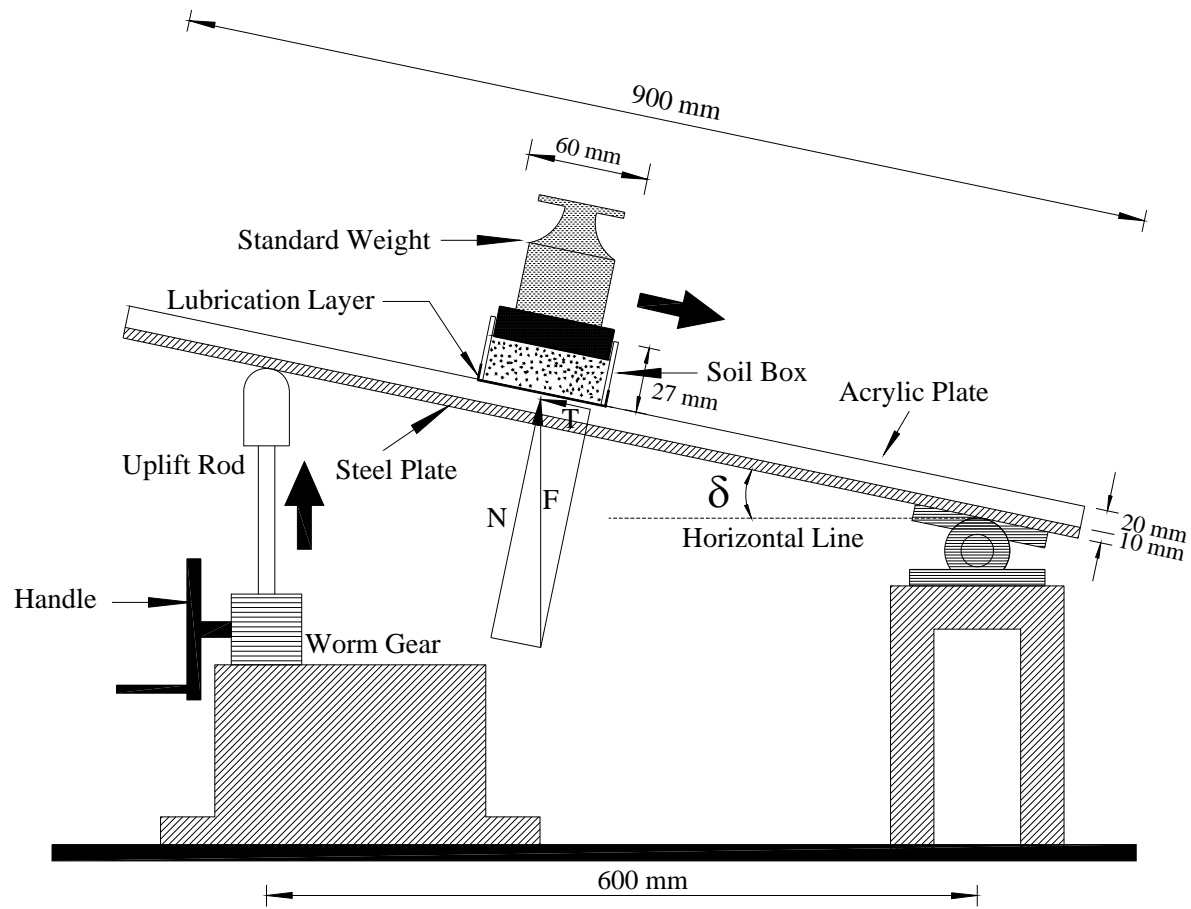


Fig. 4.5. Schematic Diagram of Sliding Block Test (after Fang et al., 2004)

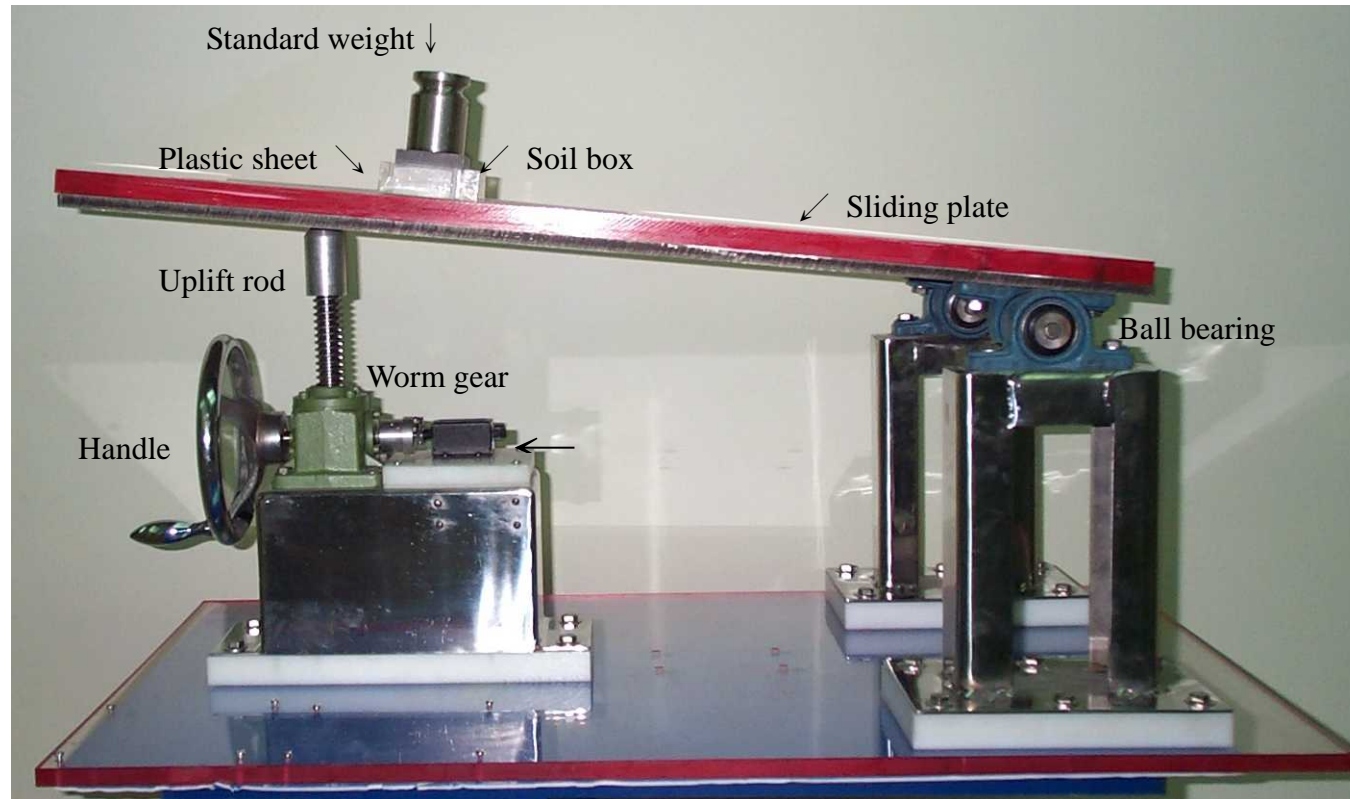


Fig. 4.6. Sliding Block Test Apparatus (after Fang et al., 2004)

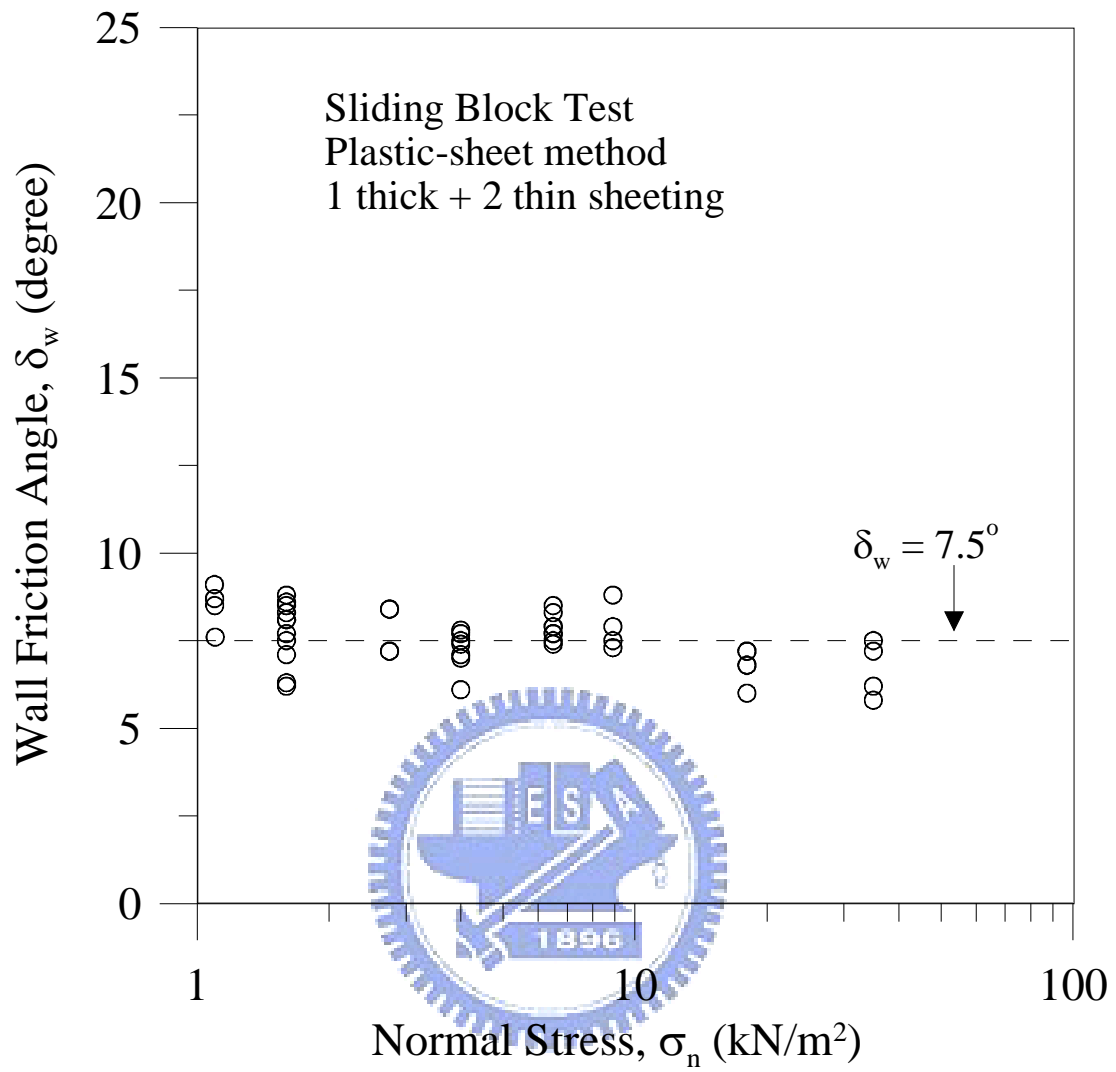


Fig. 4.7. Variation of Interface Angle with Normal Stress
(after Fang et al., 2004)

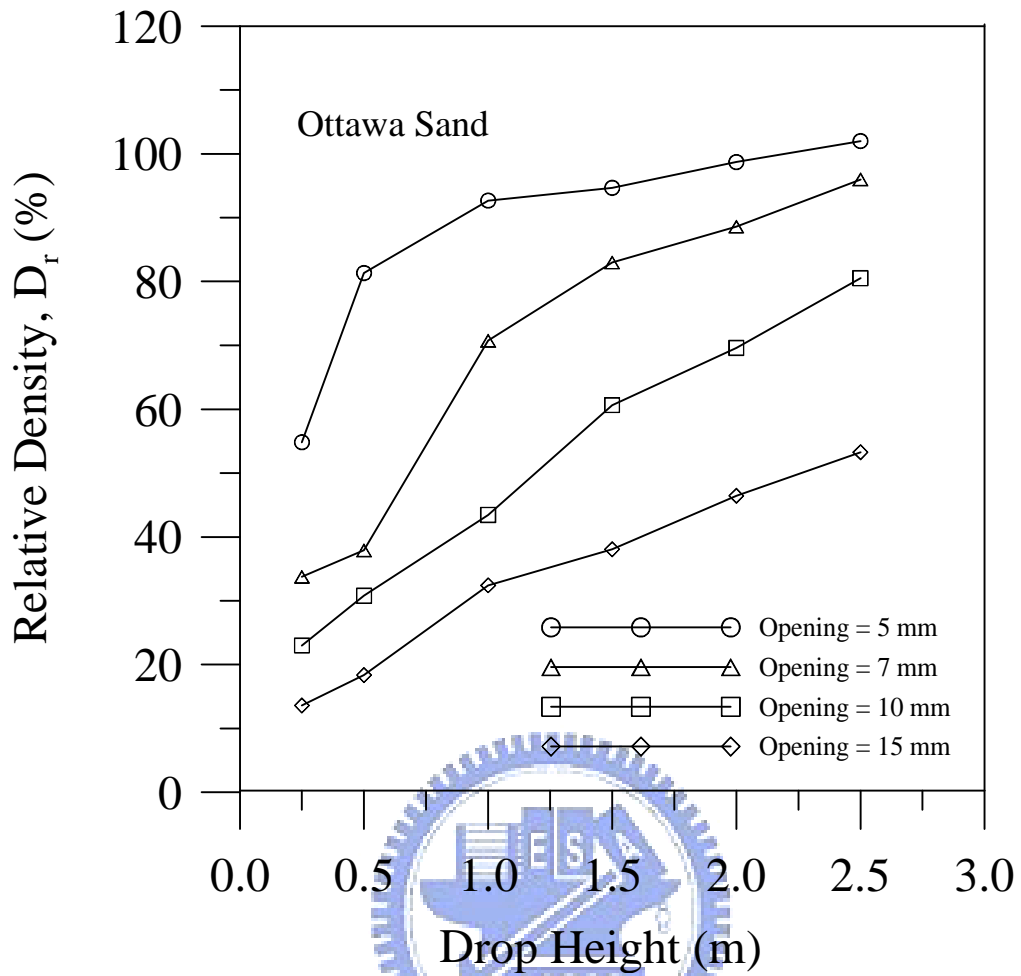


Fig. 5.1 Relationship among Slot Opening, Drop Height, and Relative Density (after Ho, 1999)

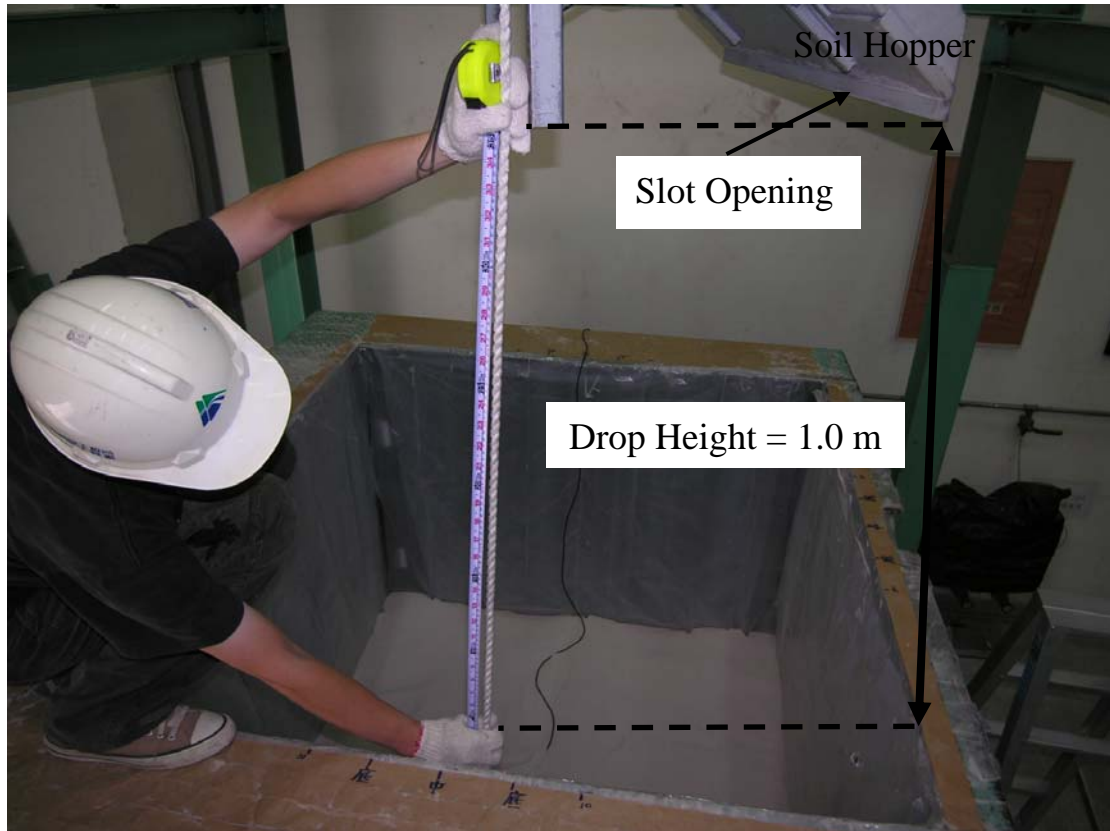


Fig. 5.2. Method to Control Drop Height = 1.0 m



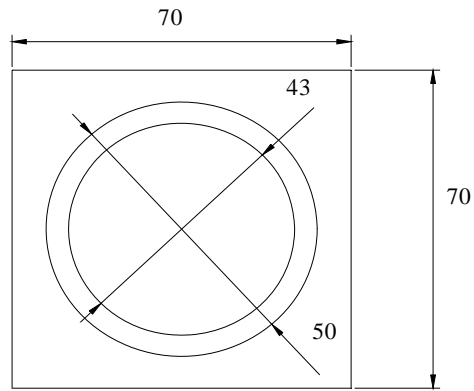
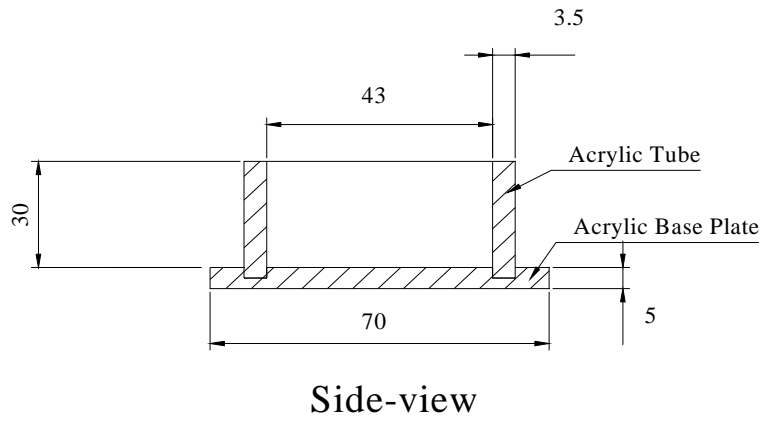


Fig. 5.3 Method to Control Slot Opening = 15 mm





Fig. 5.4 Pluviation of Ottawa Sand into Soil Bin



unit : mm

Fig. 5.5 Dimensions of Soil Density Cup (after Ho, 1999)

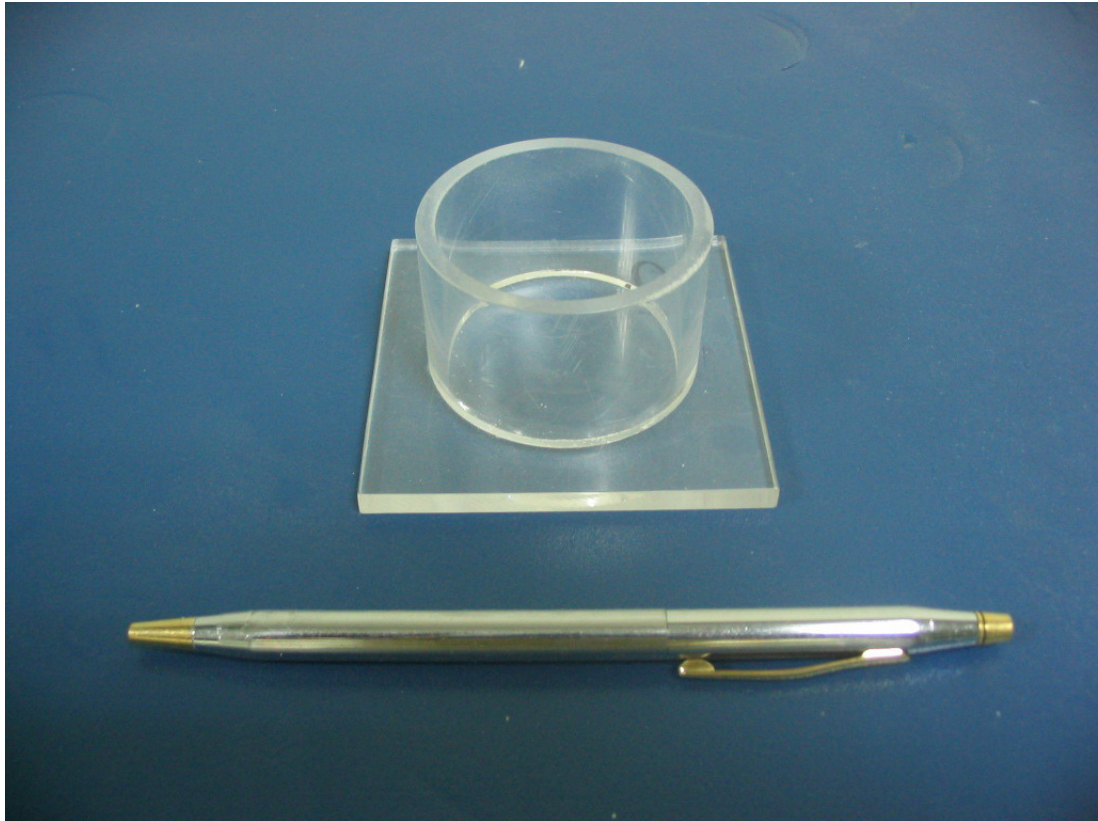


Fig. 5.6. Soil Density Cup



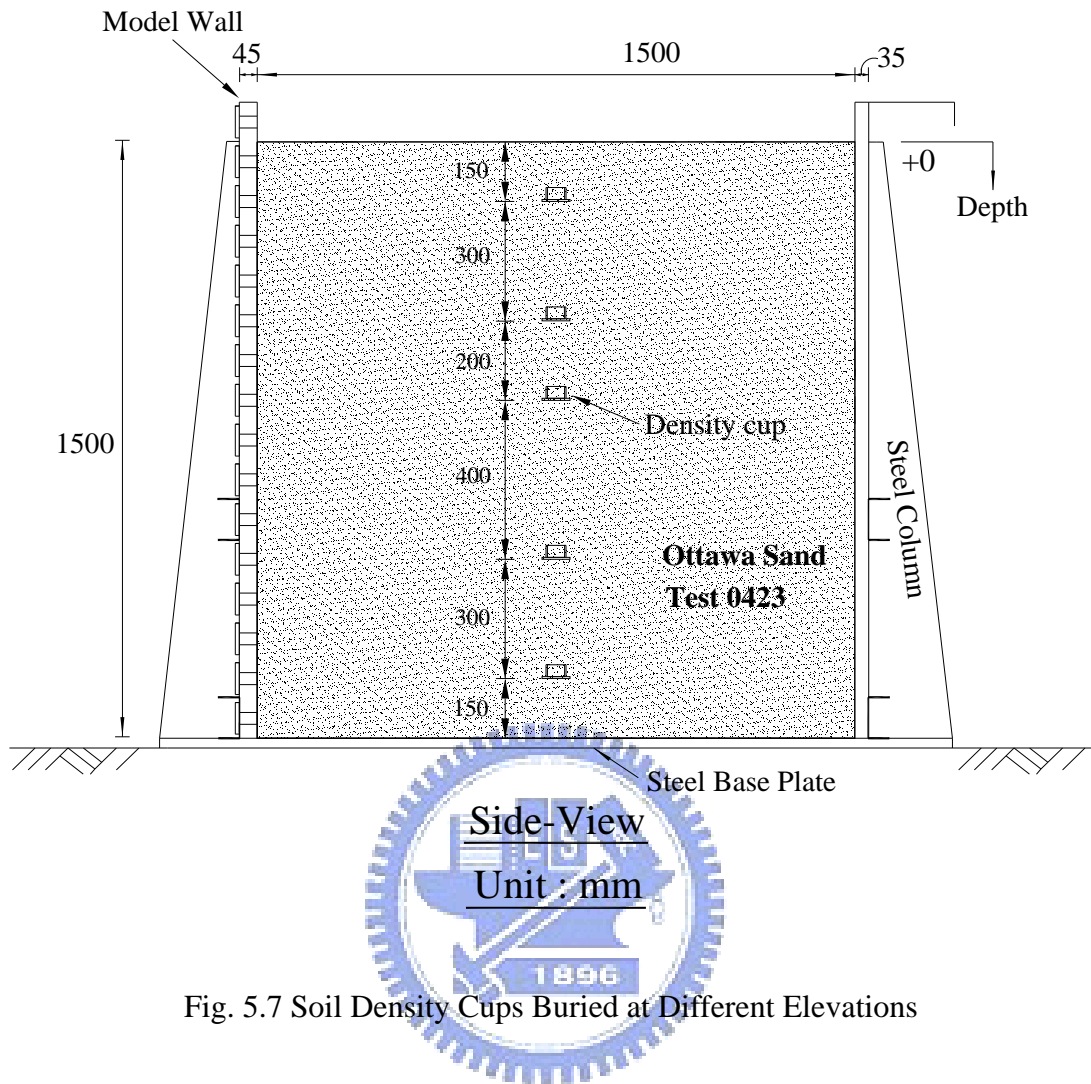


Fig. 5.7 Soil Density Cups Buried at Different Elevations

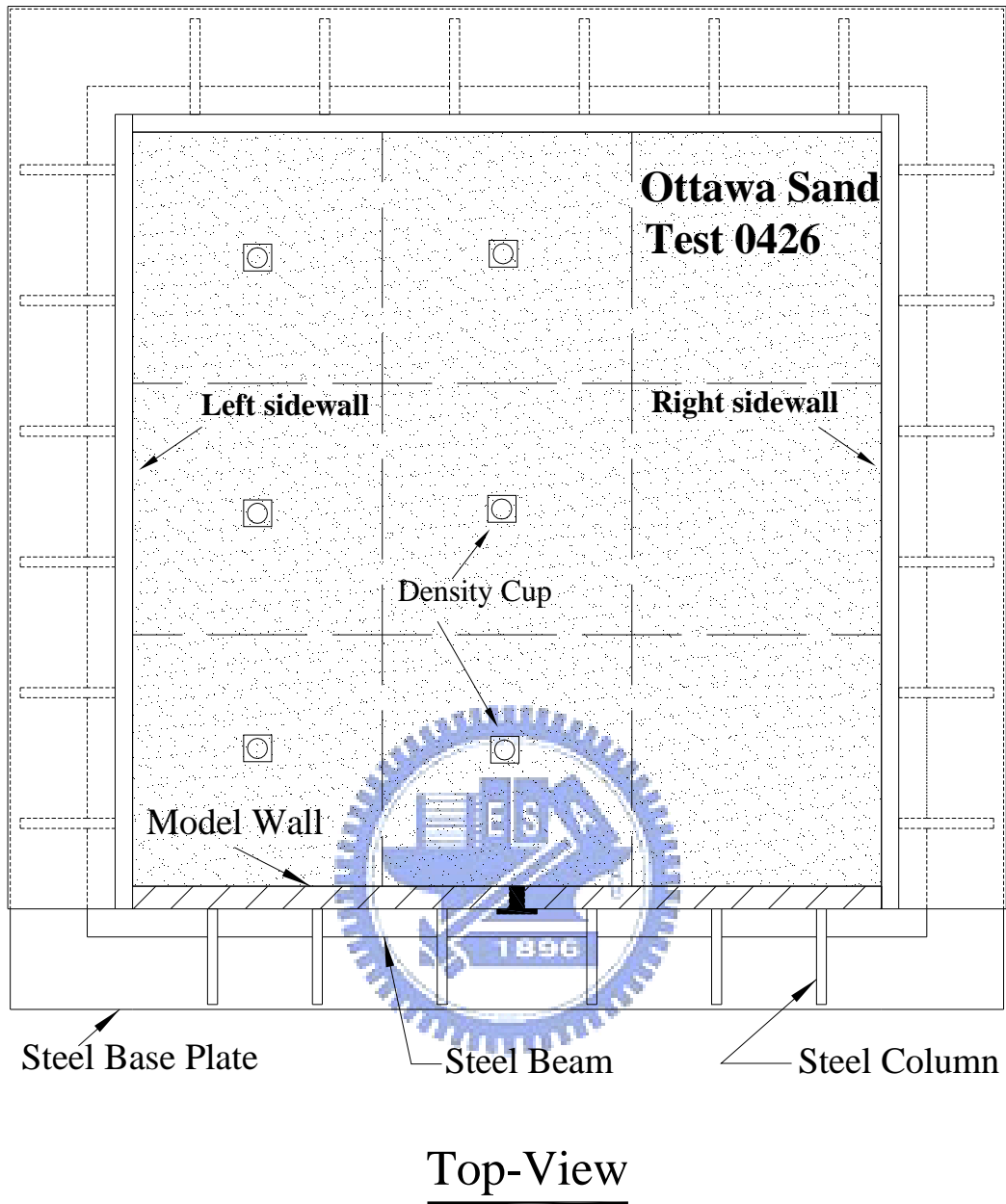
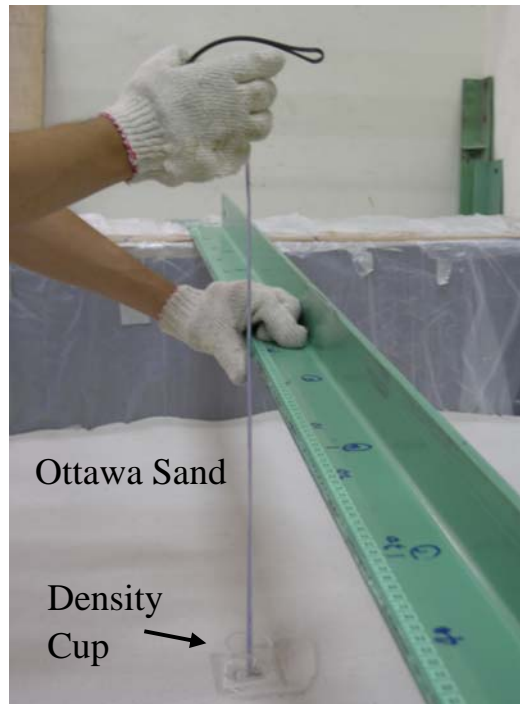


Fig. 5.8. Arrangement of Soil Density Cups at Same Elevation



(a)



(b)

Fig. 5.9. Density Control Test (a) Placement of Density Cup;
(b) Measurement of Soil Mass in Cup

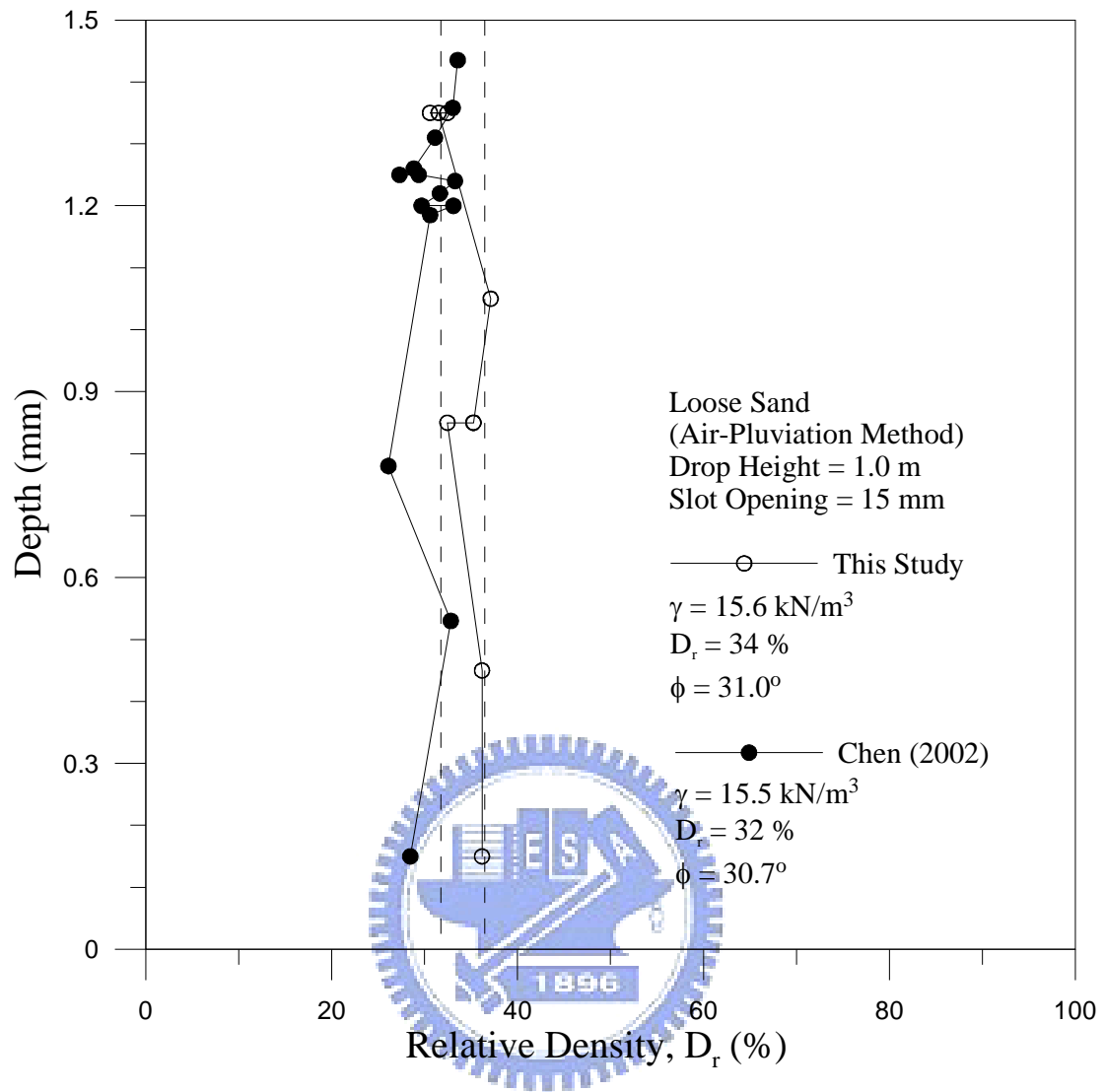


Fig. 5.10. Distribution of Soil Density for Loose Sand

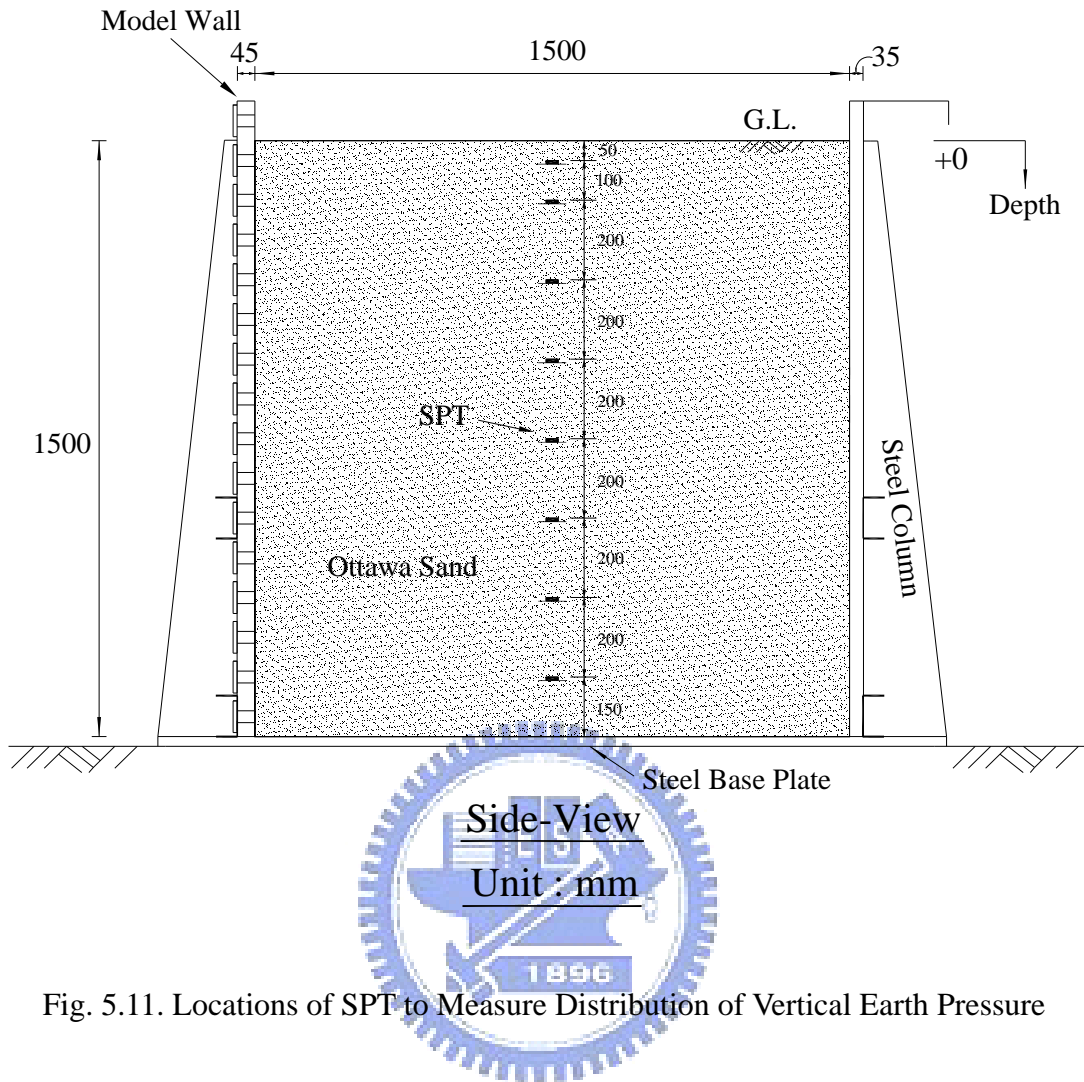


Fig. 5.11. Locations of SPT to Measure Distribution of Vertical Earth Pressure

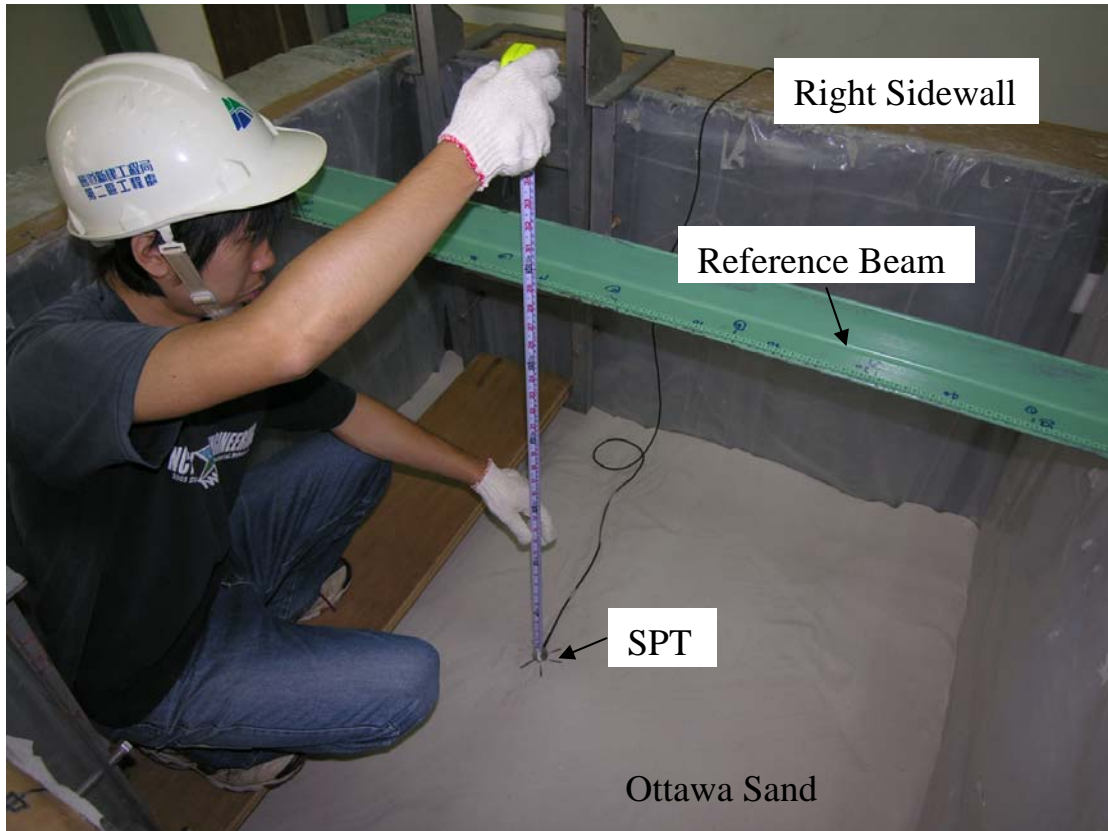


Fig. 5.12. Placement of SPT in Soil Mass



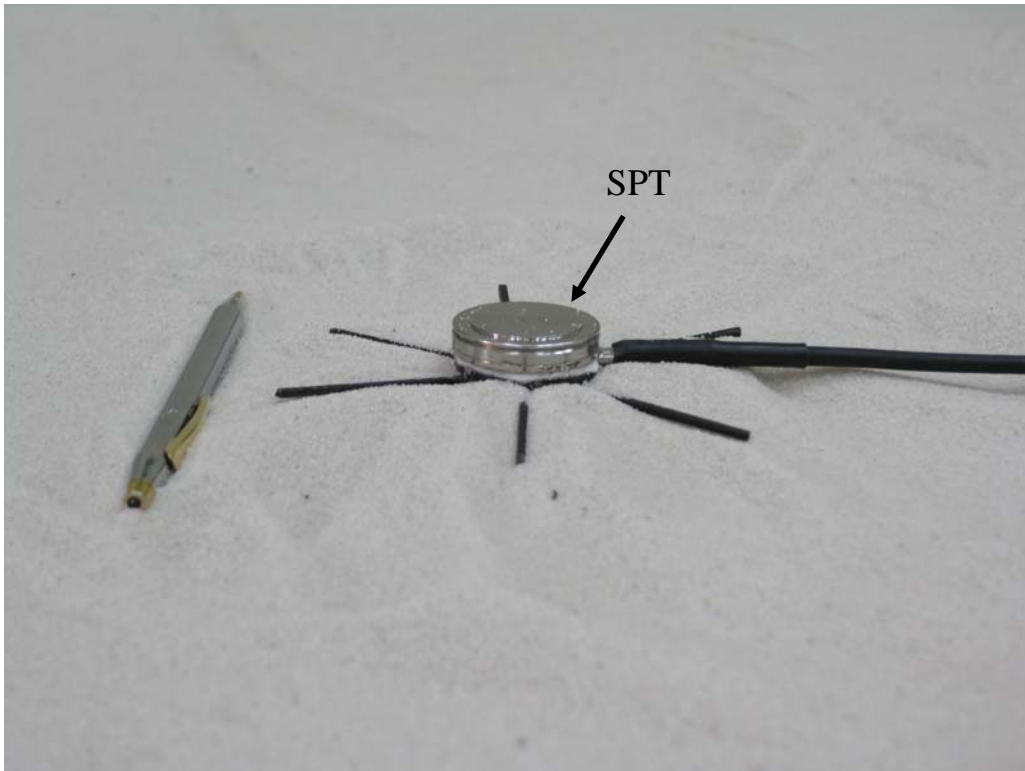


Fig. 5.13. Photograph of SPT used to Measured Vertical Stress



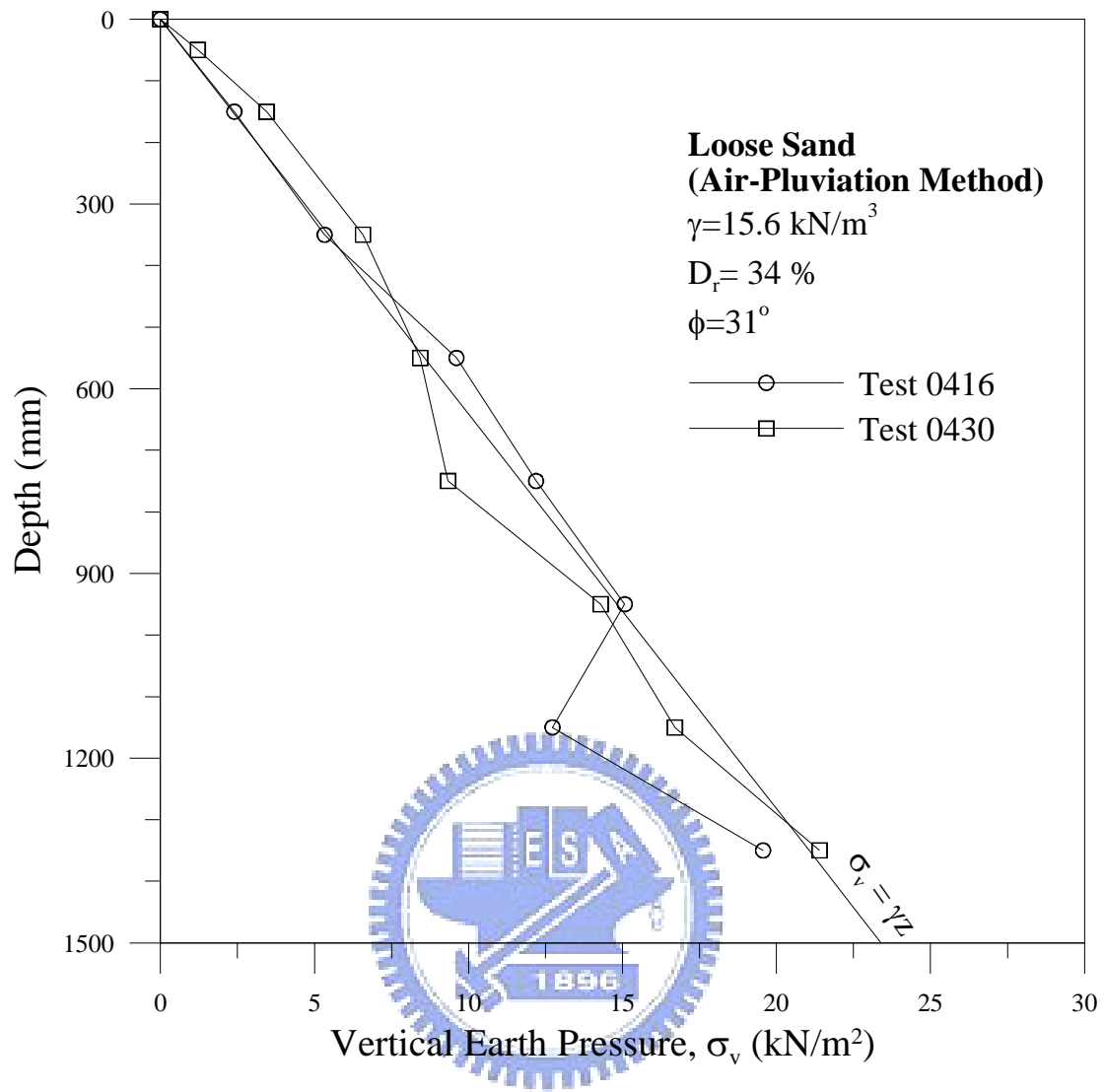


Fig. 5.14. Distribution of Vertical Earth Pressure

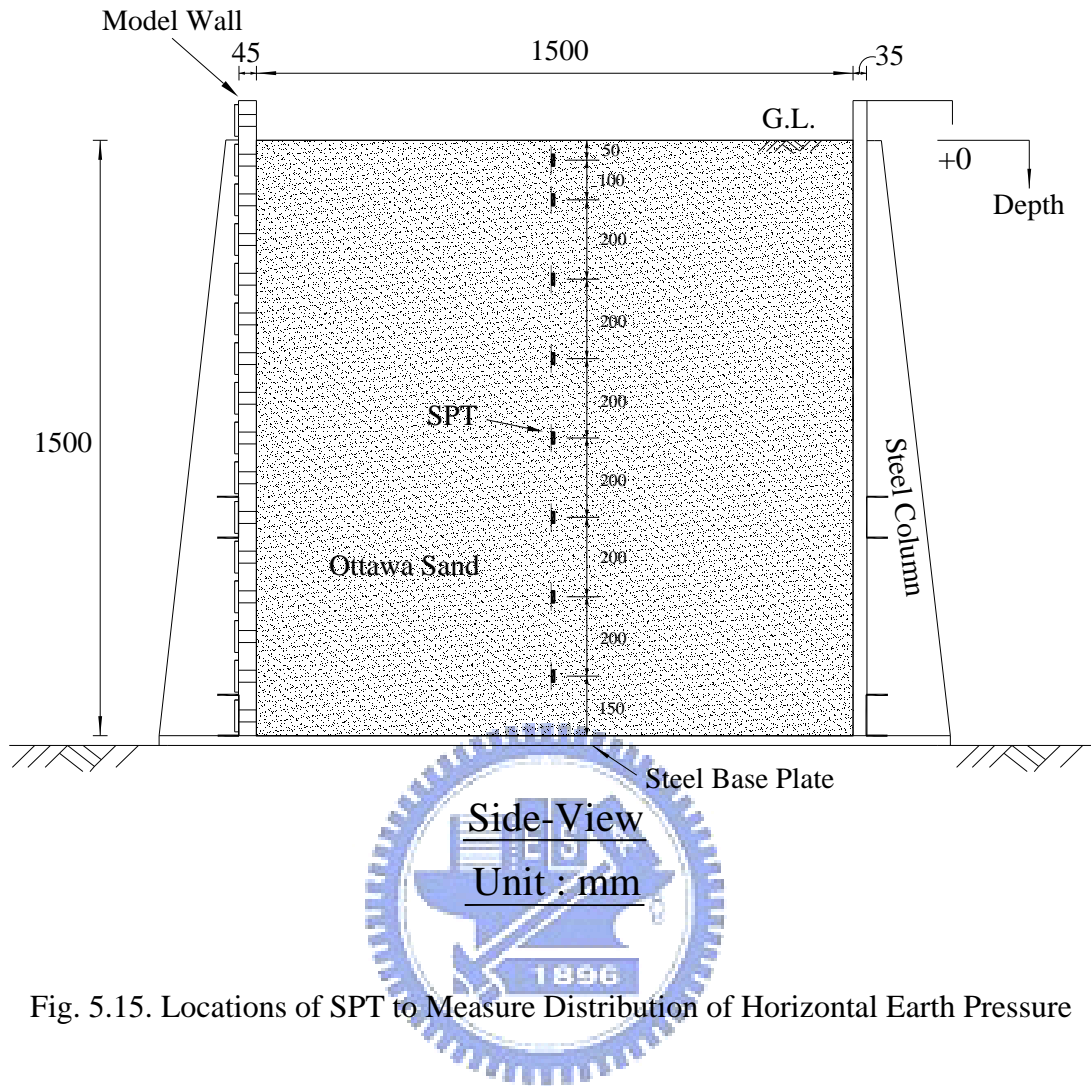


Fig. 5.15. Locations of SPT to Measure Distribution of Horizontal Earth Pressure

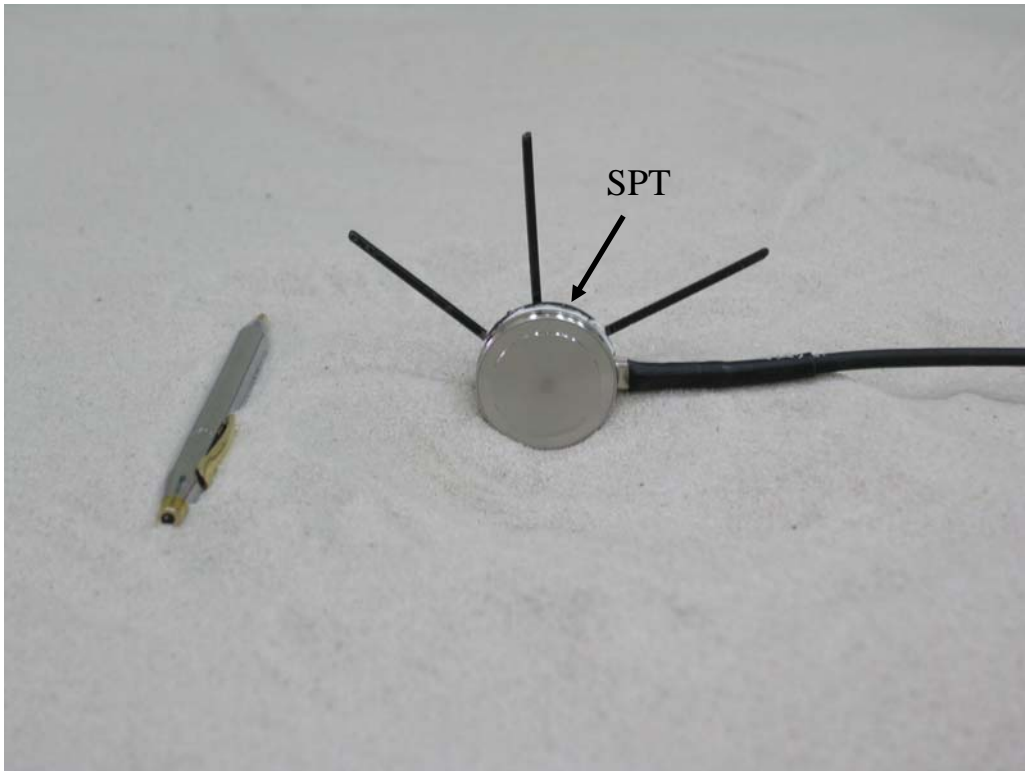
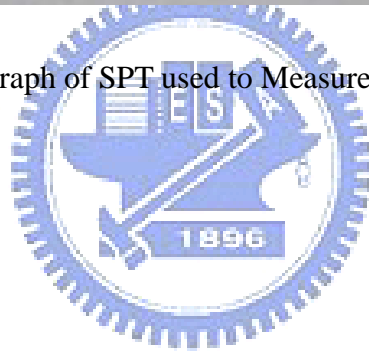


Fig. 5.16. Photograph of SPT used to Measure Horizontal Stress



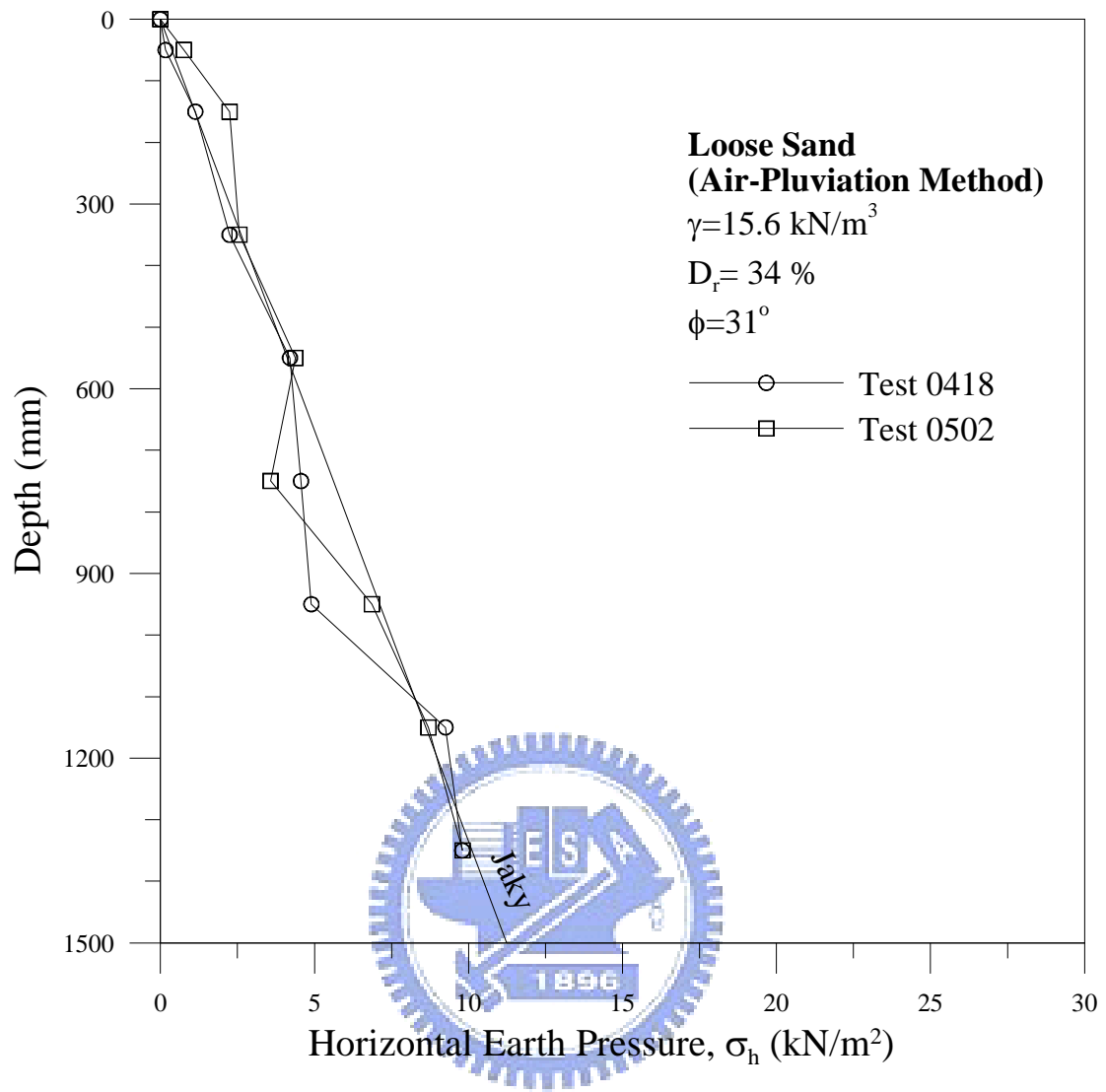


Fig. 5.17. Distribution of Horizontal Earth Pressure

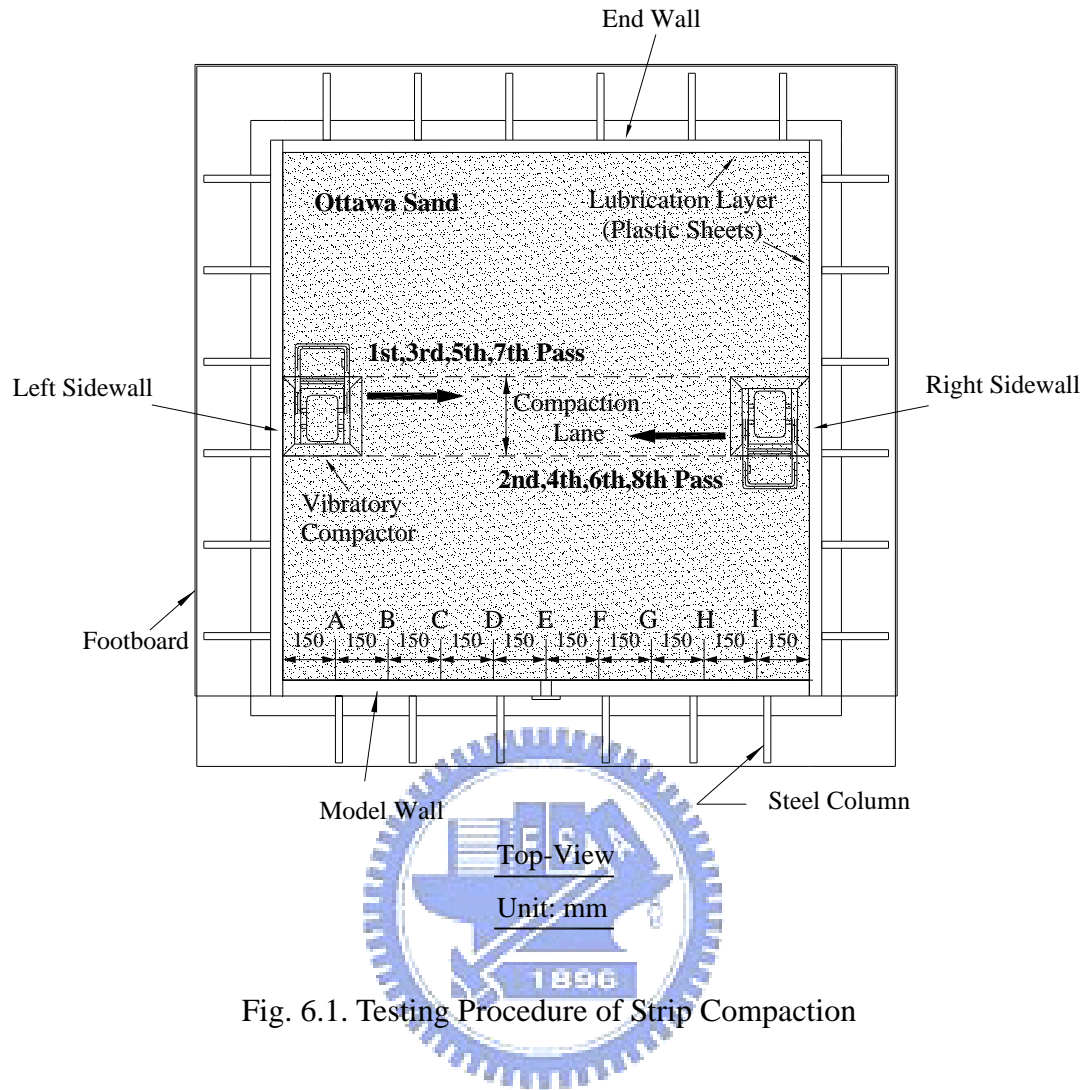


Fig. 6.1. Testing Procedure of Strip Compaction



Fig. 6.2. Compaction on Surface of Backfill

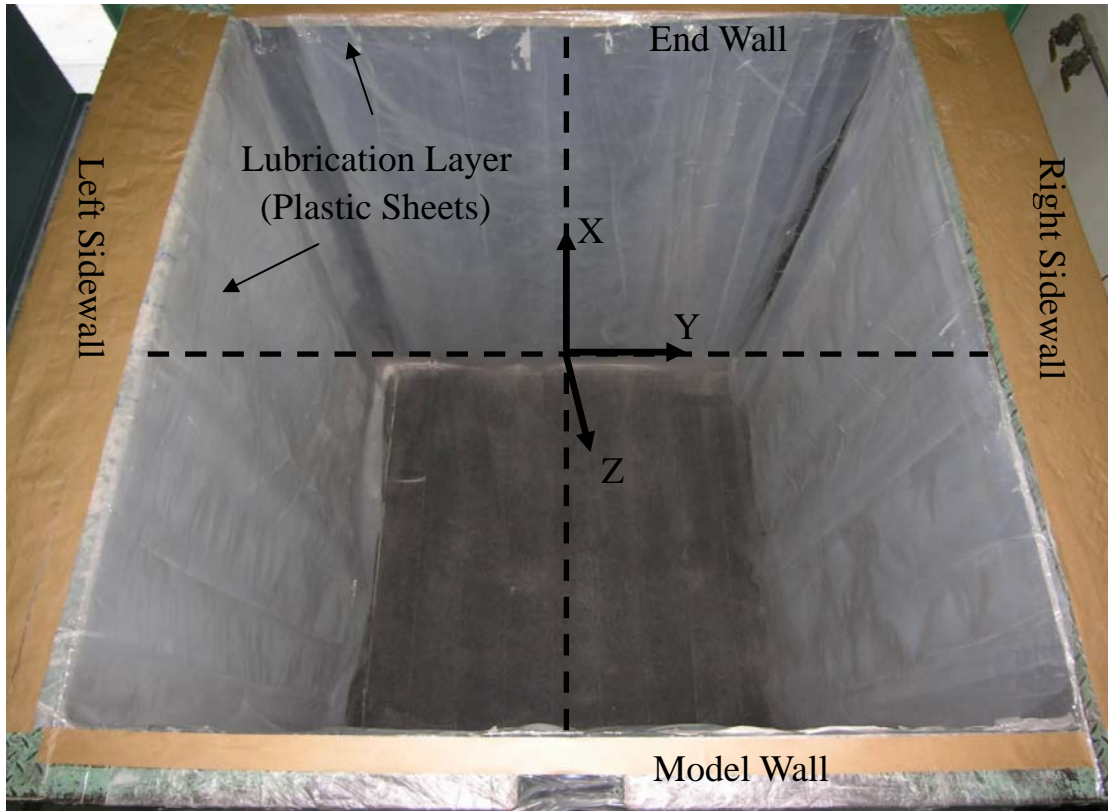
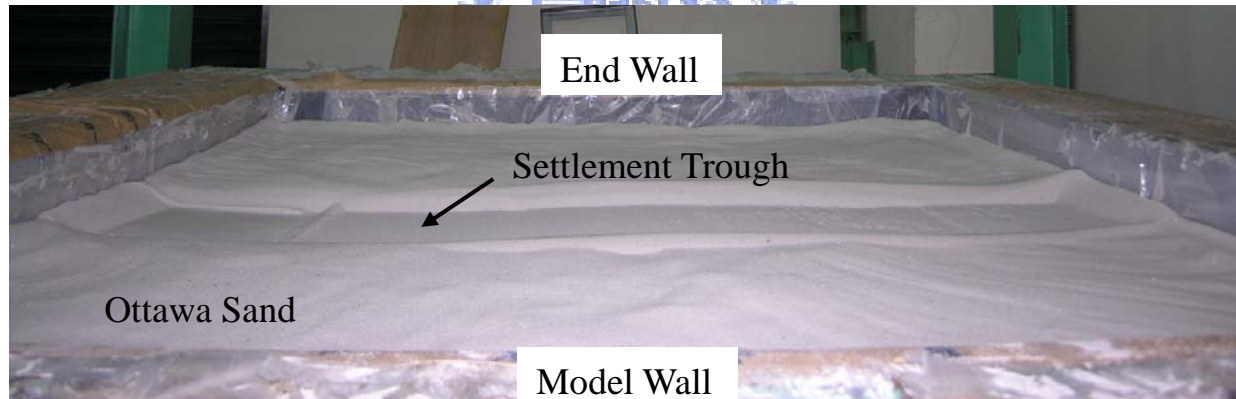


Fig. 6.3. Definition of X-Y-Z Axes, XZ, YZ, and XY - Plane



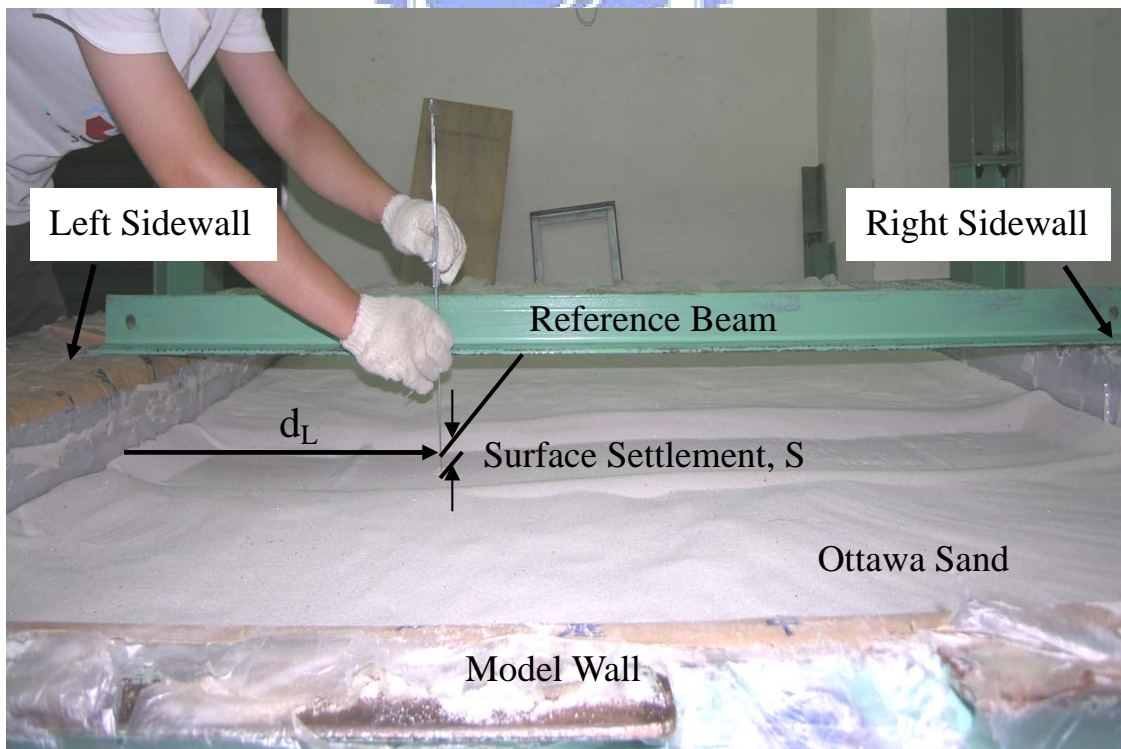
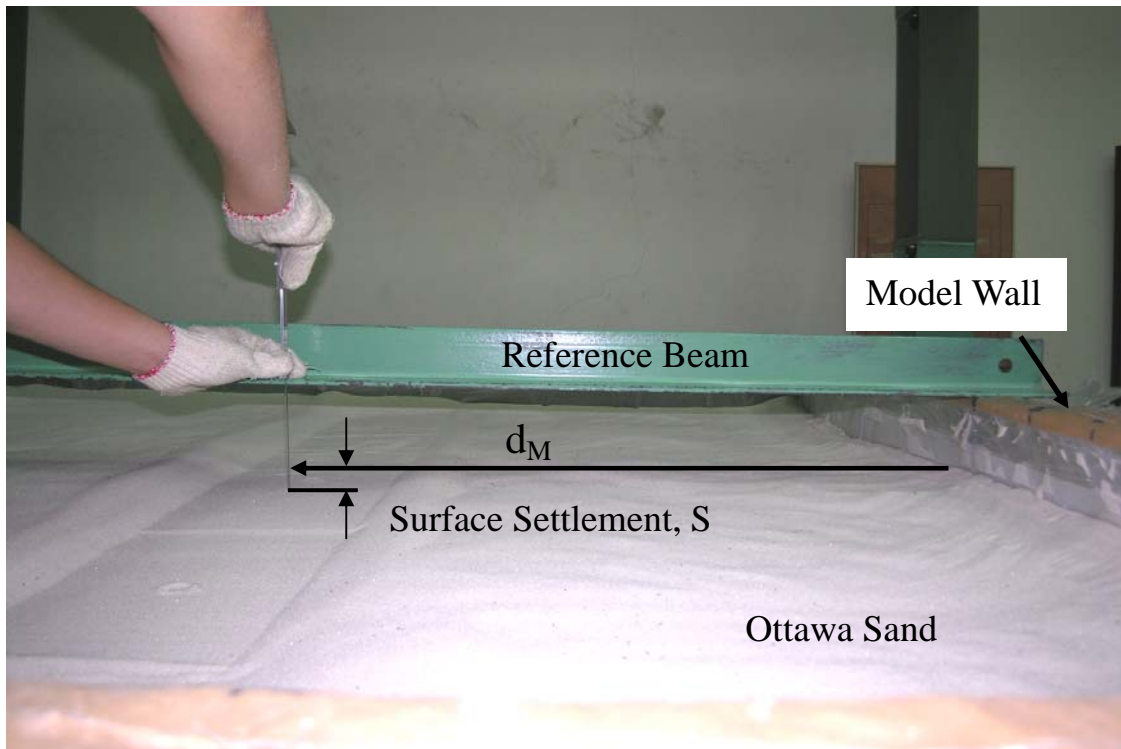


(a)



(b)

Fig. 6.4. Surface of Backfill: (a) before Compaction; (b) after Compaction



(b)

Fig. 6.5. Measurement of Surface Settlement on (a) XZ – Plane; (b) YZ - Plane

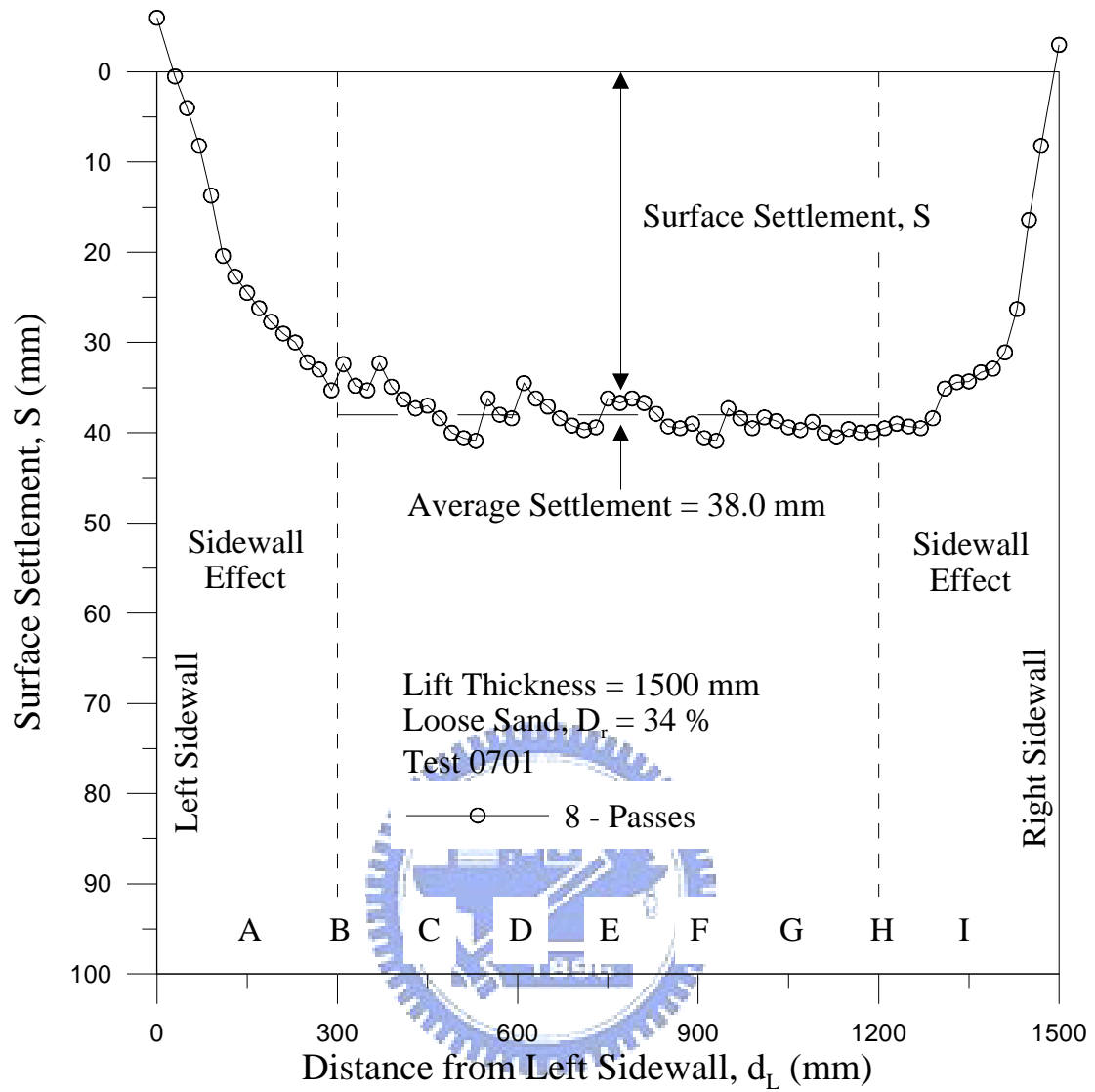


Fig. 6.6. Surface Settlement along Compaction Lane with Regions of Sidewall Effects

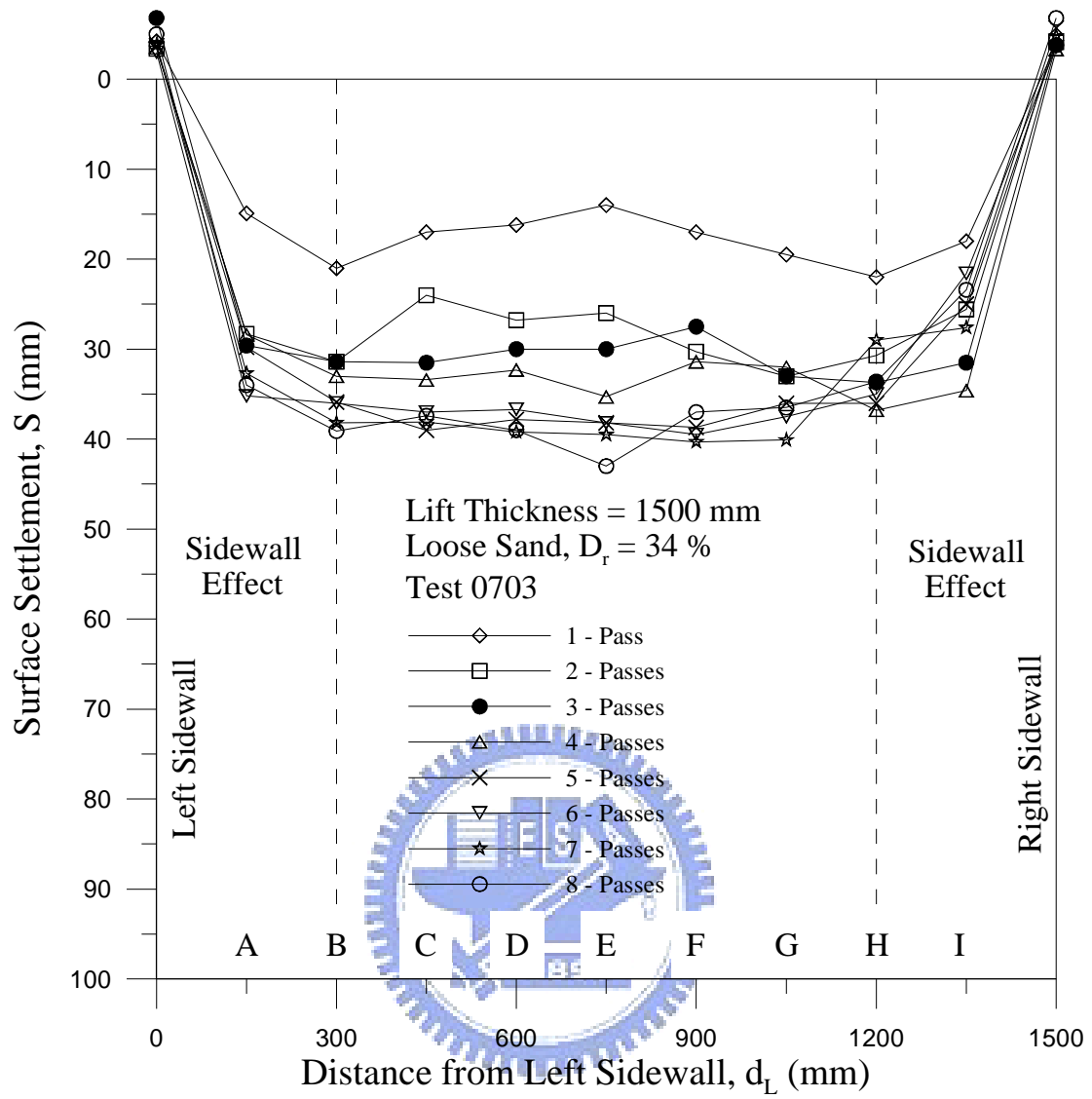


Fig. 6.7. Surface Settlement along Compaction Lane after Compactor

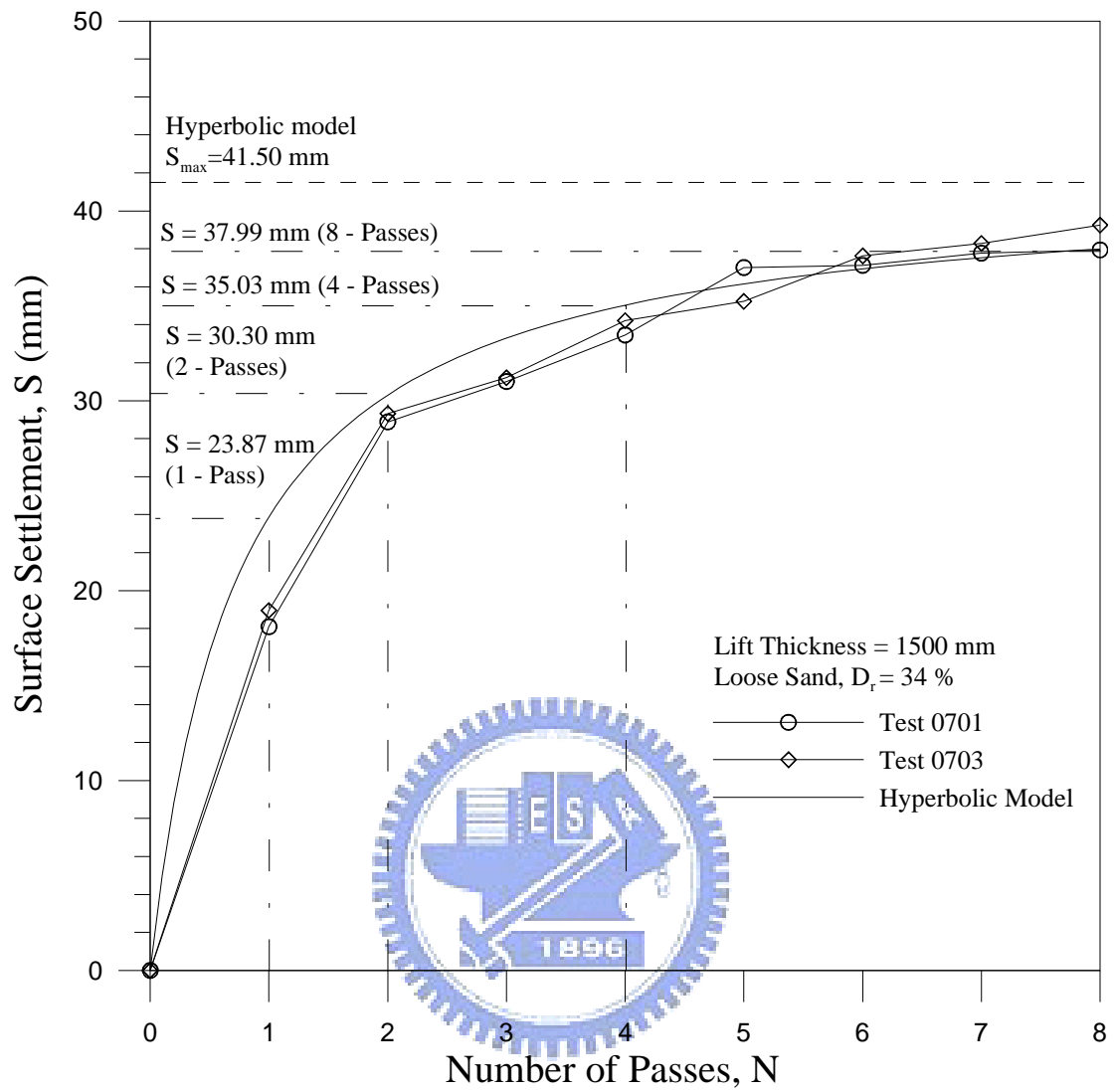


Fig. 6.8. Hyperbolic Model to Estimate Surface Settlement S as a Function of No. of Passes of Compactor

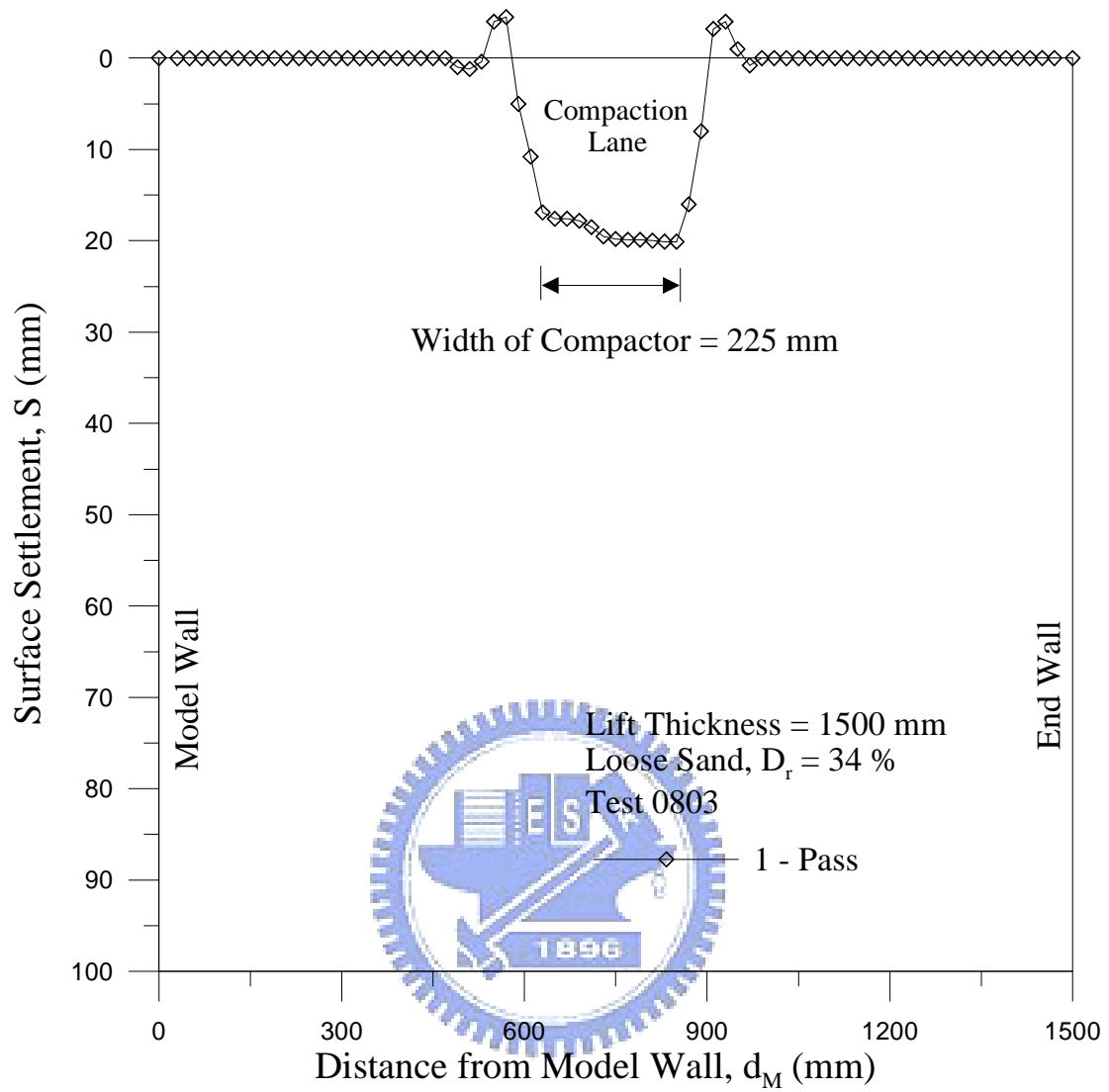


Fig. 6.9. Surface Movement of Settlement Trough after First Pass of Compactor

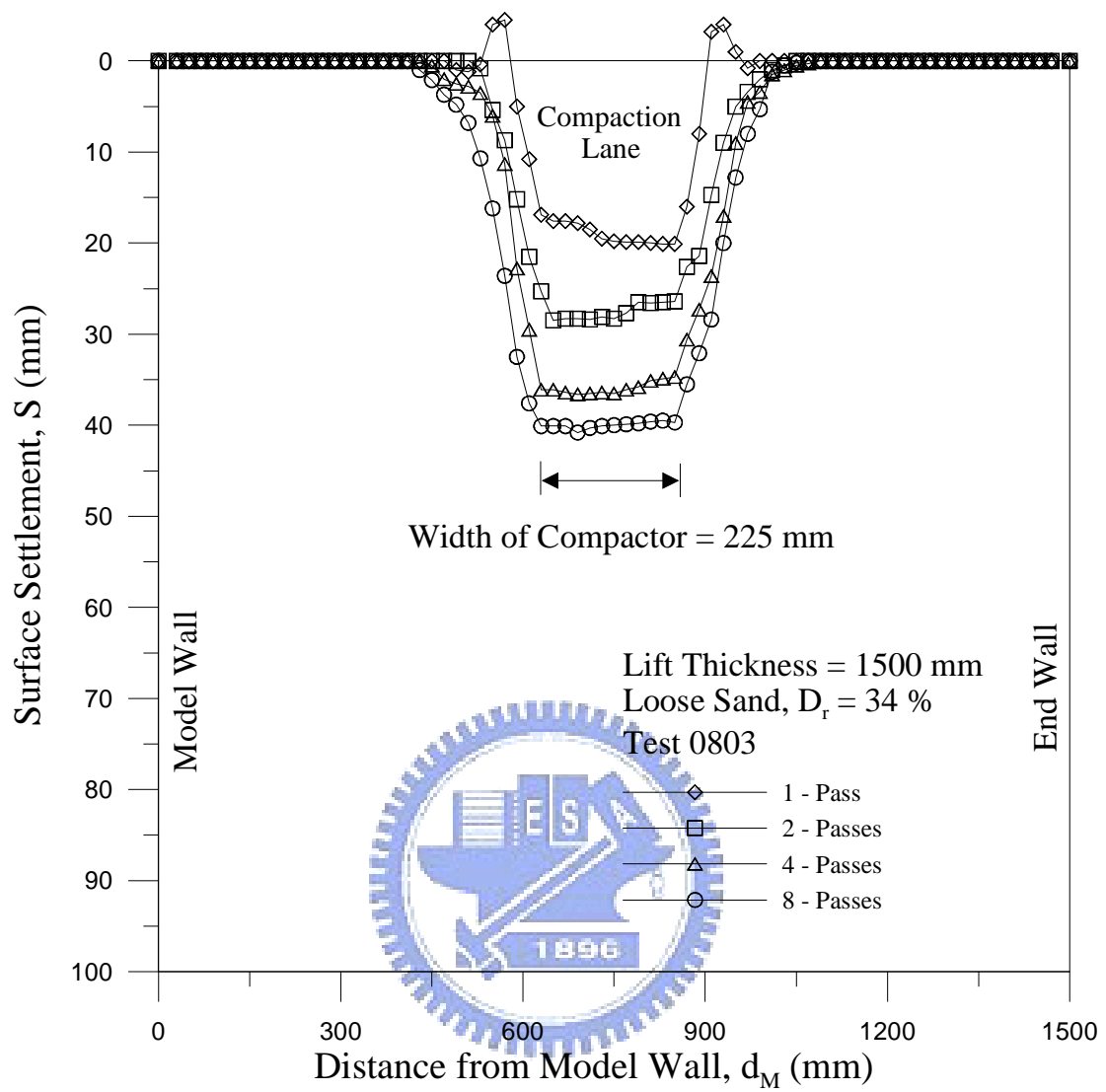


Fig. 6.10. Surface Settlement of Compaction Lane after 1, 2, 4 and 8 Passes of Compactor

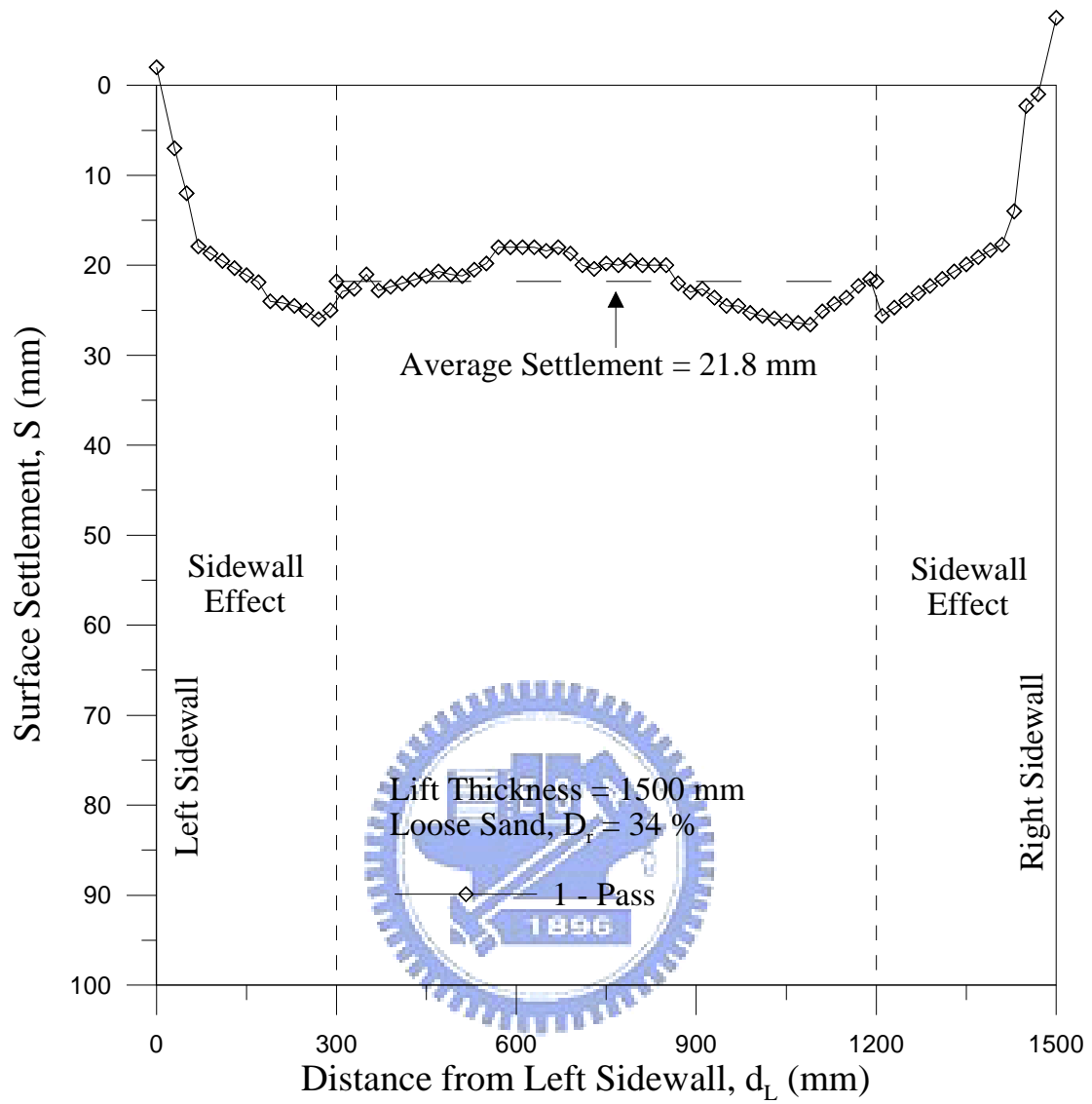


Fig. 6.11. Surface Settlement along Compaction Lane after First Pass of Compactor

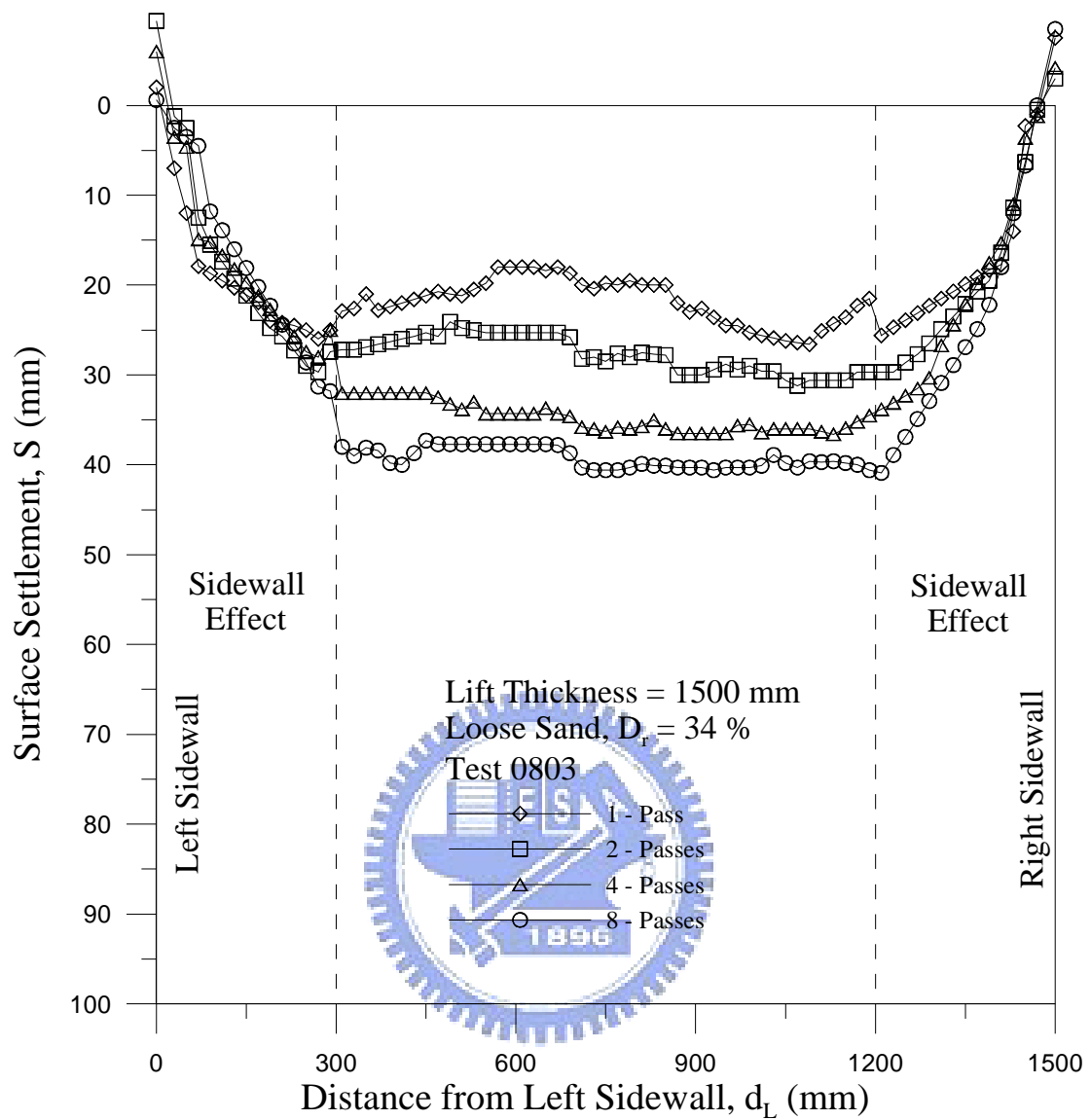
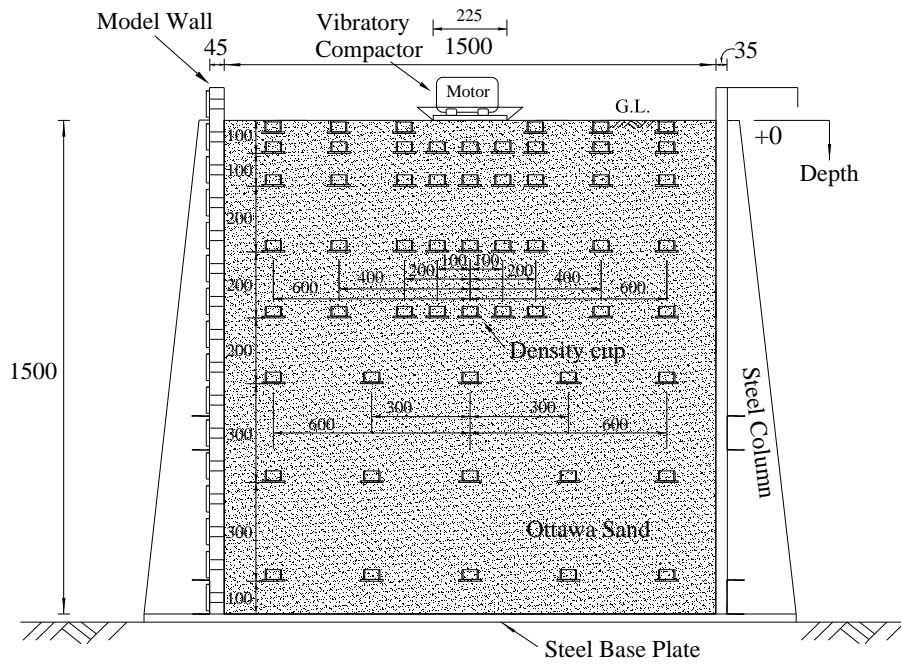


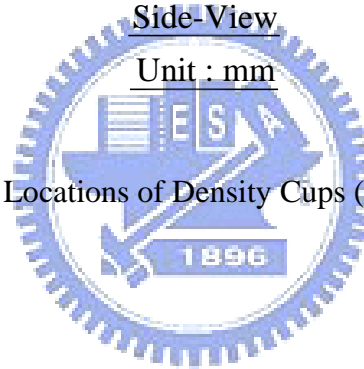
Fig. 6.12. Surface Settlement along Compaction Lane after 1, 2, 4 and 8 Passes of Compactor



Side-View

Unit : mm

Fig. 6.13. Locations of Density Cups (Side - View)



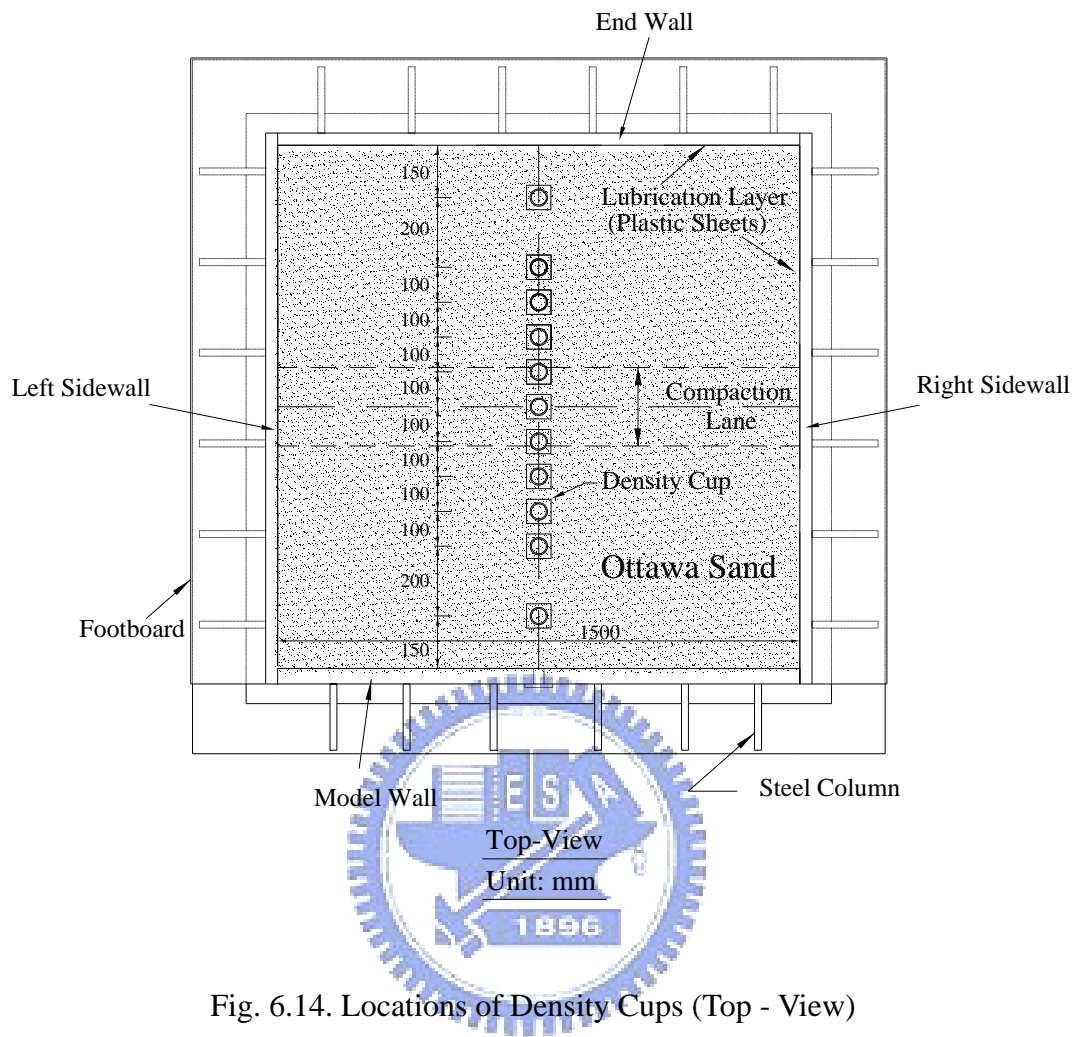


Fig. 6.14. Locations of Density Cups (Top - View)

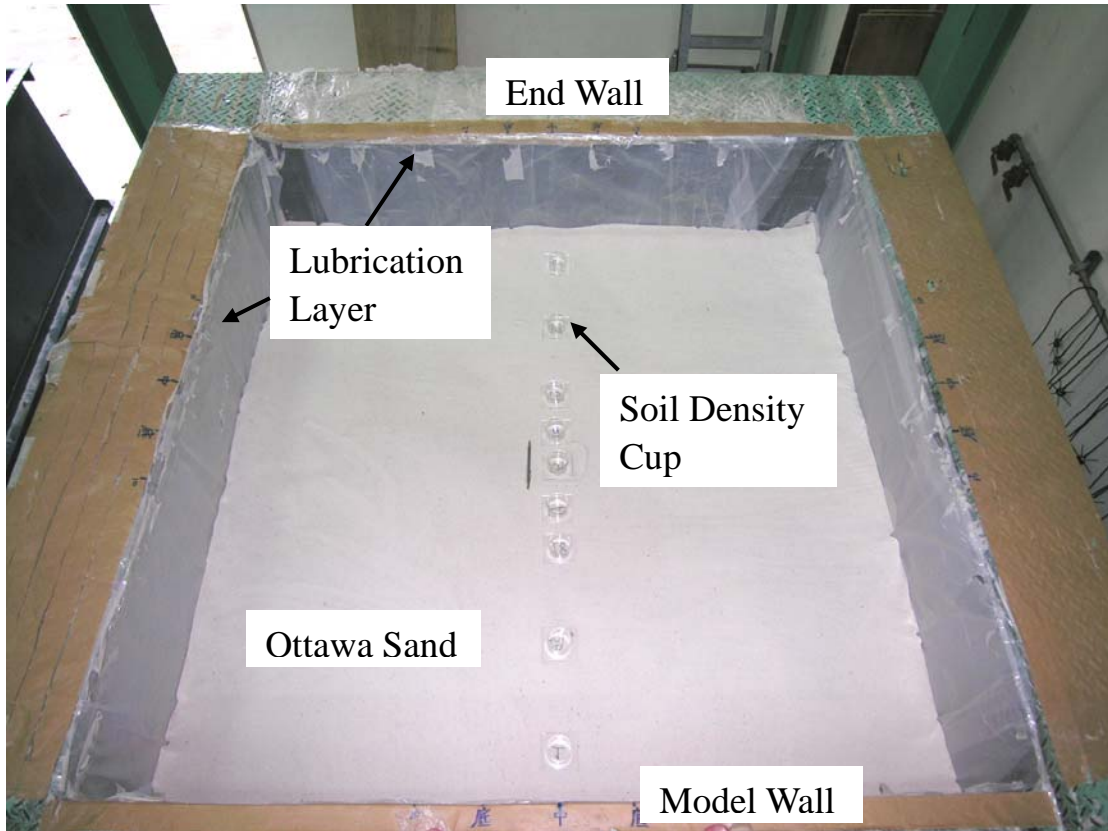


Fig. 6.15. Locations of Soil Density Cups at Same Elevation



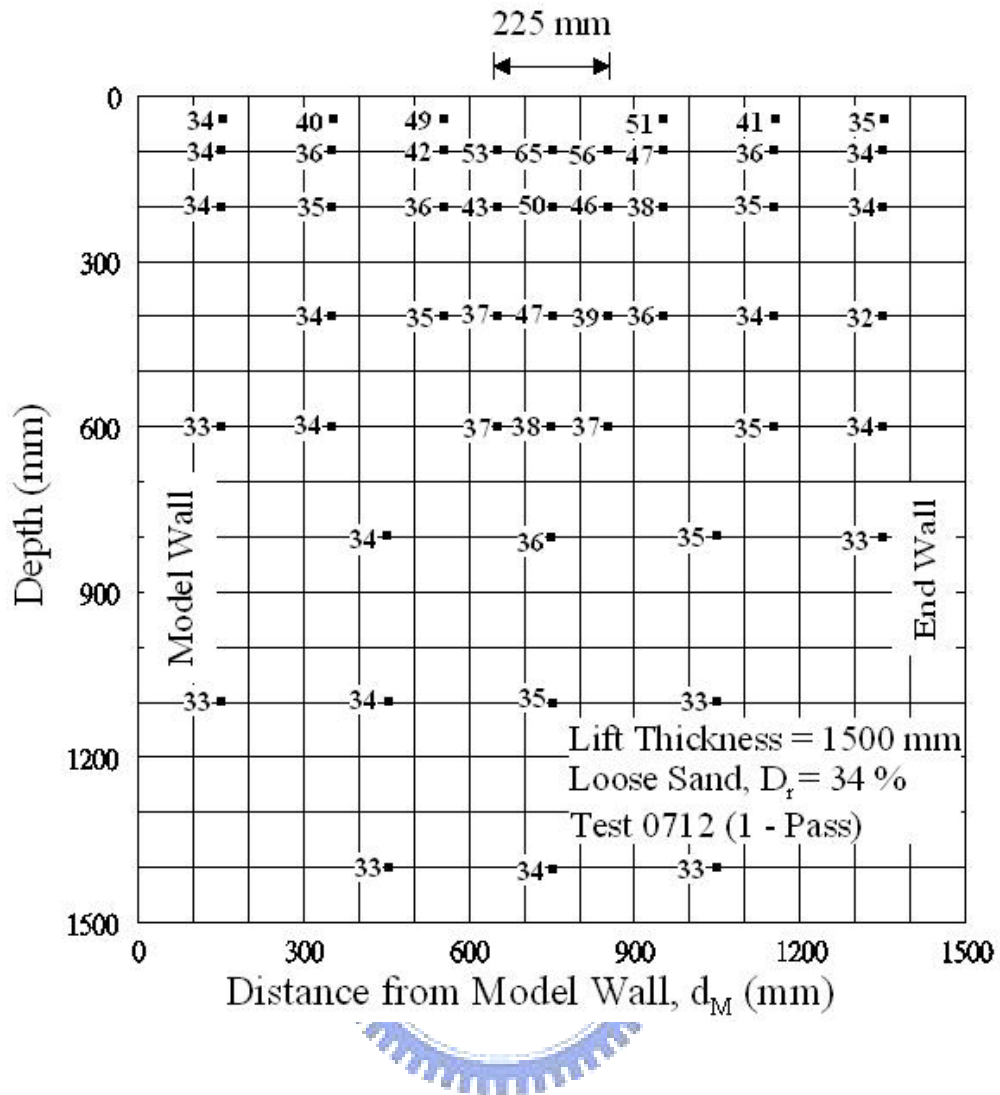


Fig. 6.16. Relative Density of Sand at Grid Points after 1 – Pass of Compactor

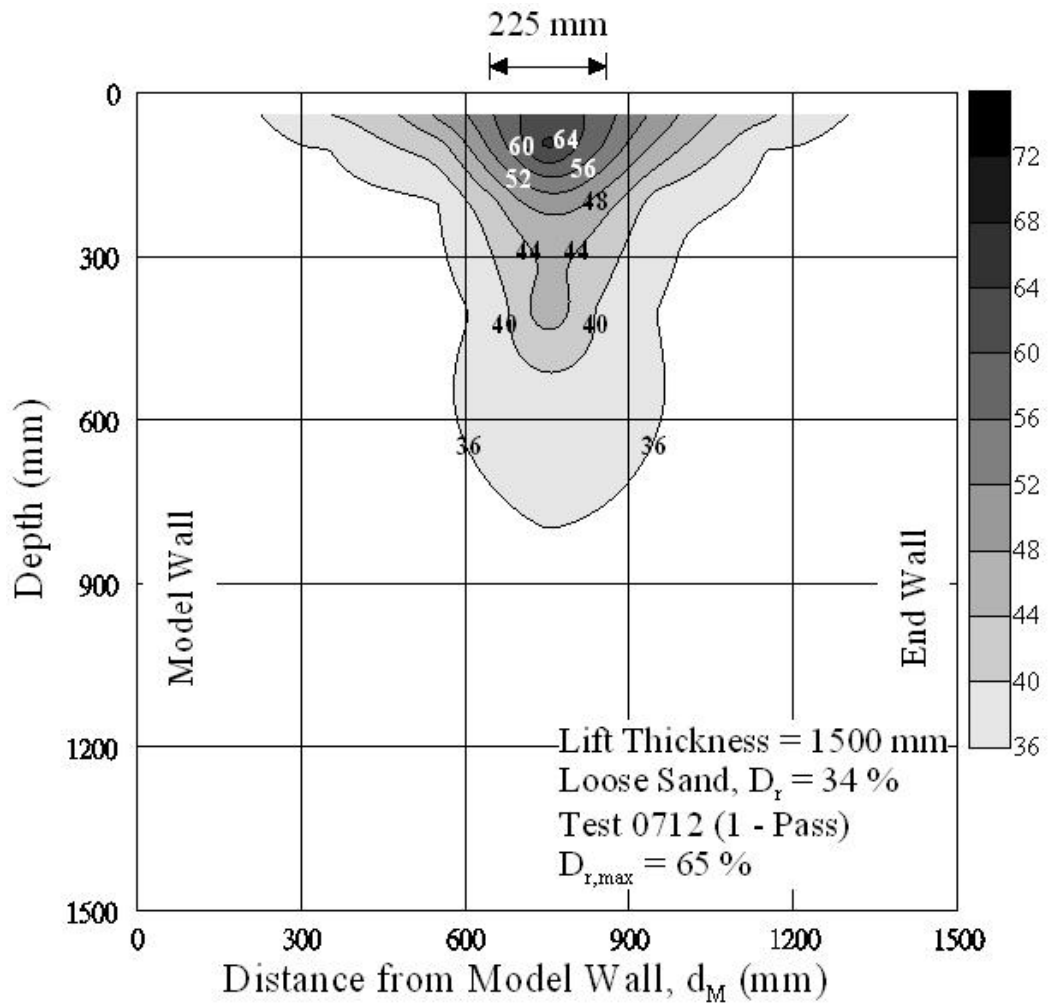


Fig. 6.17. Contours of Relative Density after 1 – Pass of Compactor

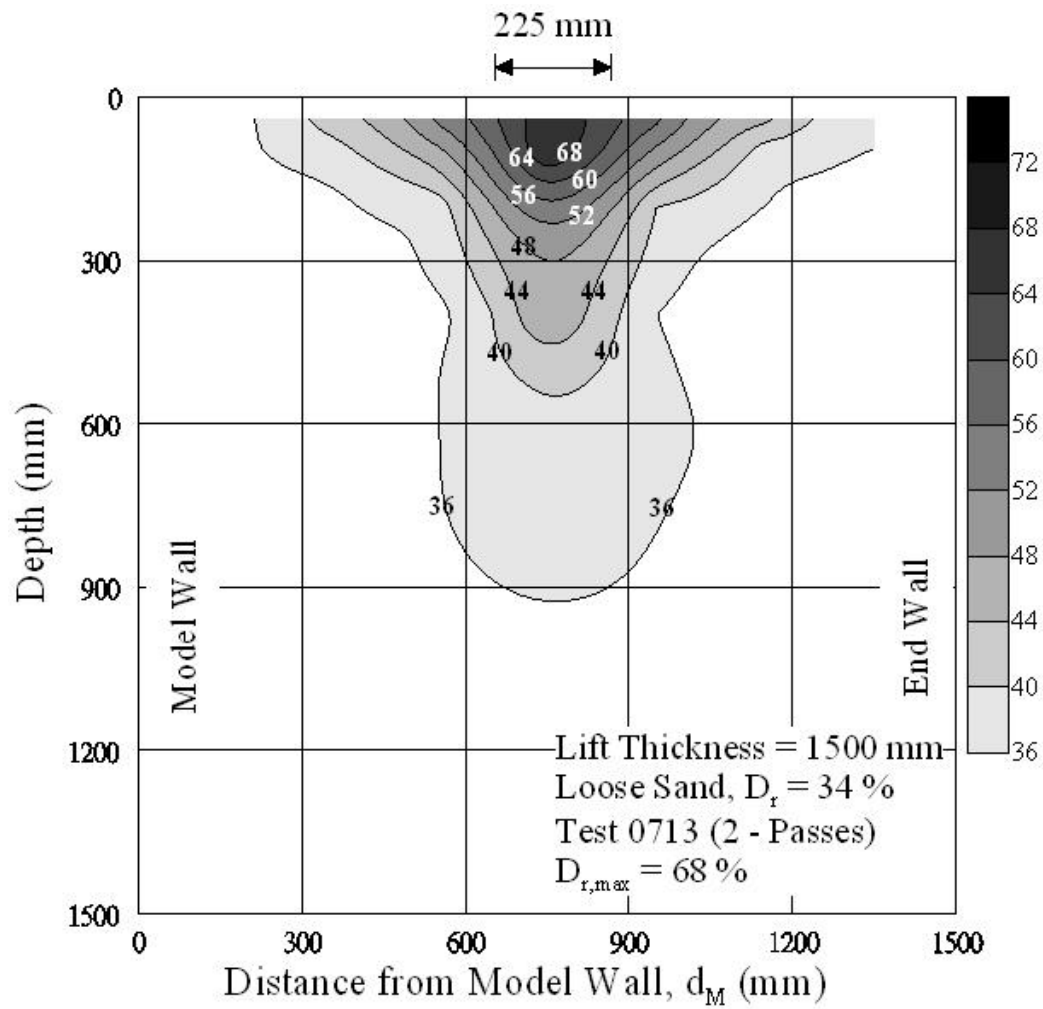


Fig. 6.18. Contours of Relative Density after 2 – Passes of Compactor

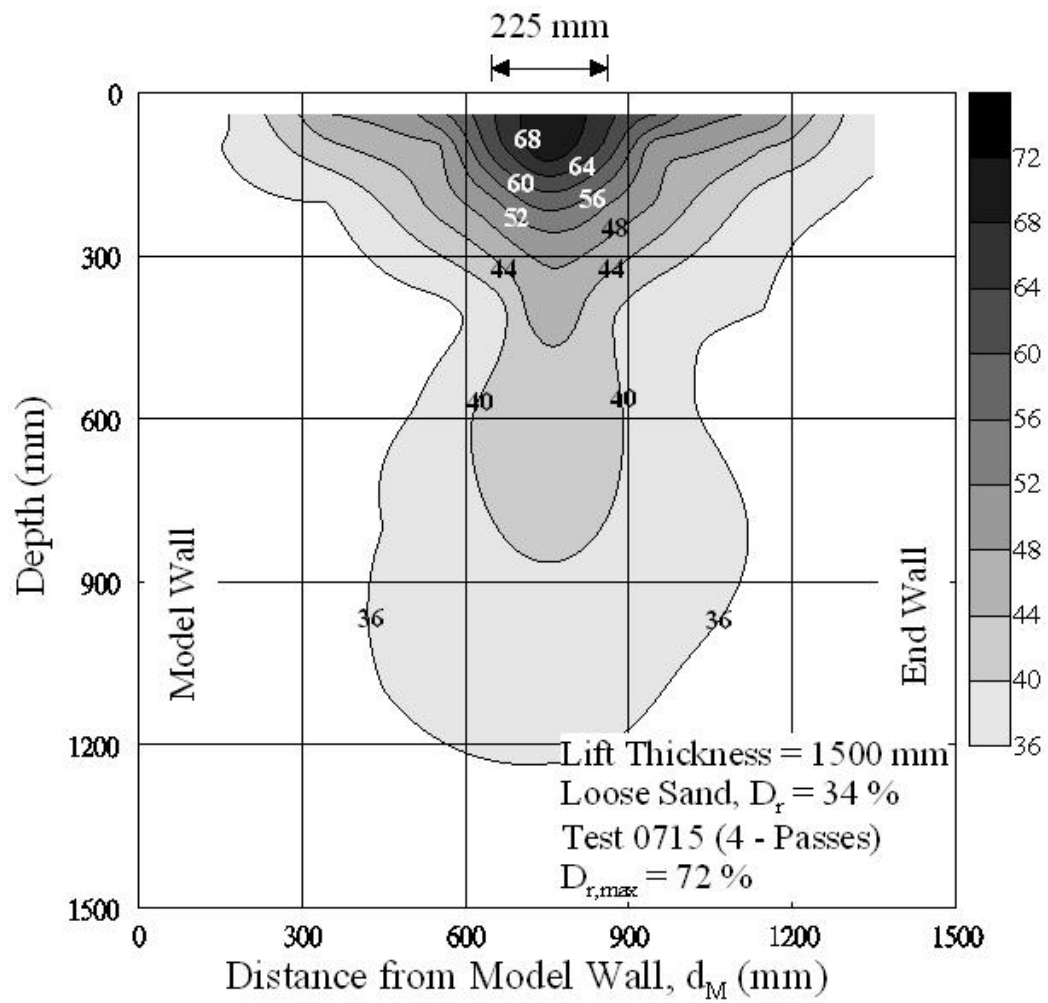


Fig. 6.19. Contours of Relative Density after 4 – Passes of Compactor

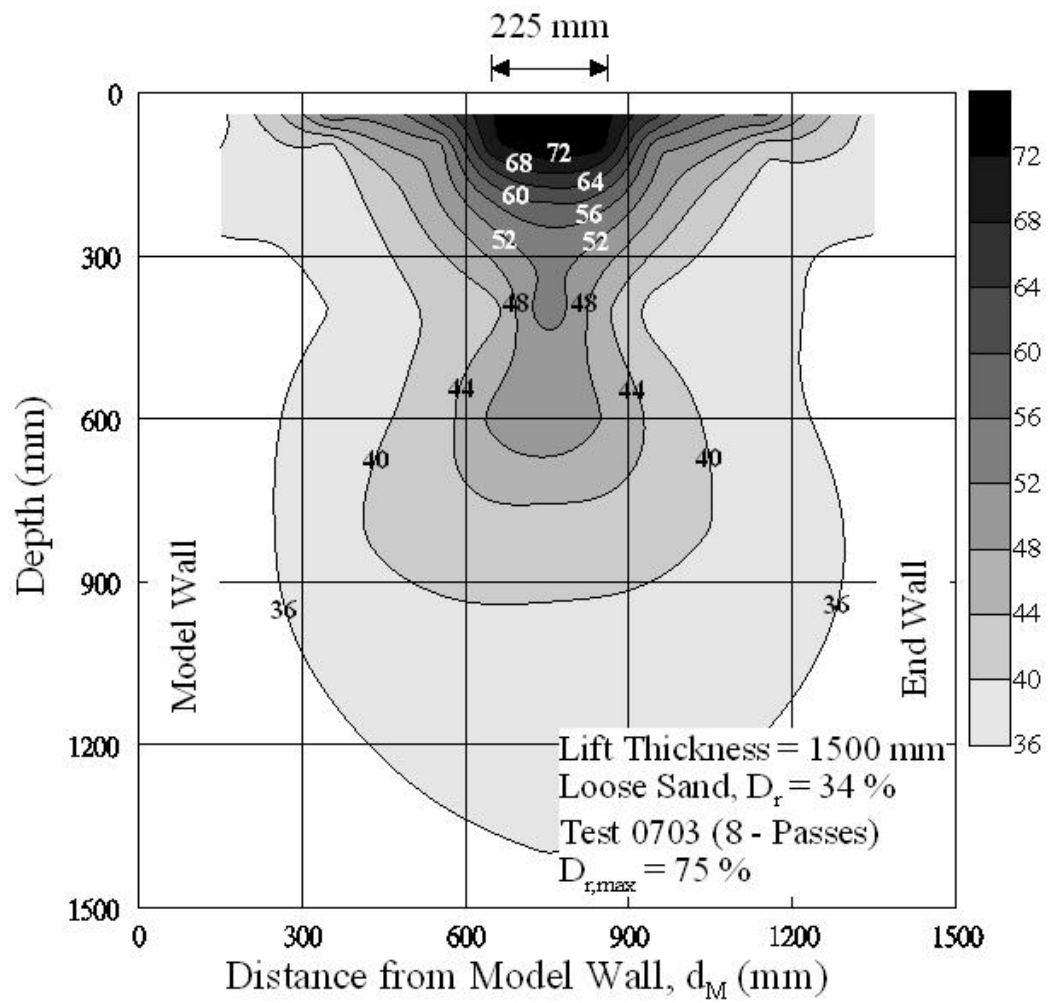


Fig. 6.20. Contours of Relative Density after 8 – Passes of Compactor

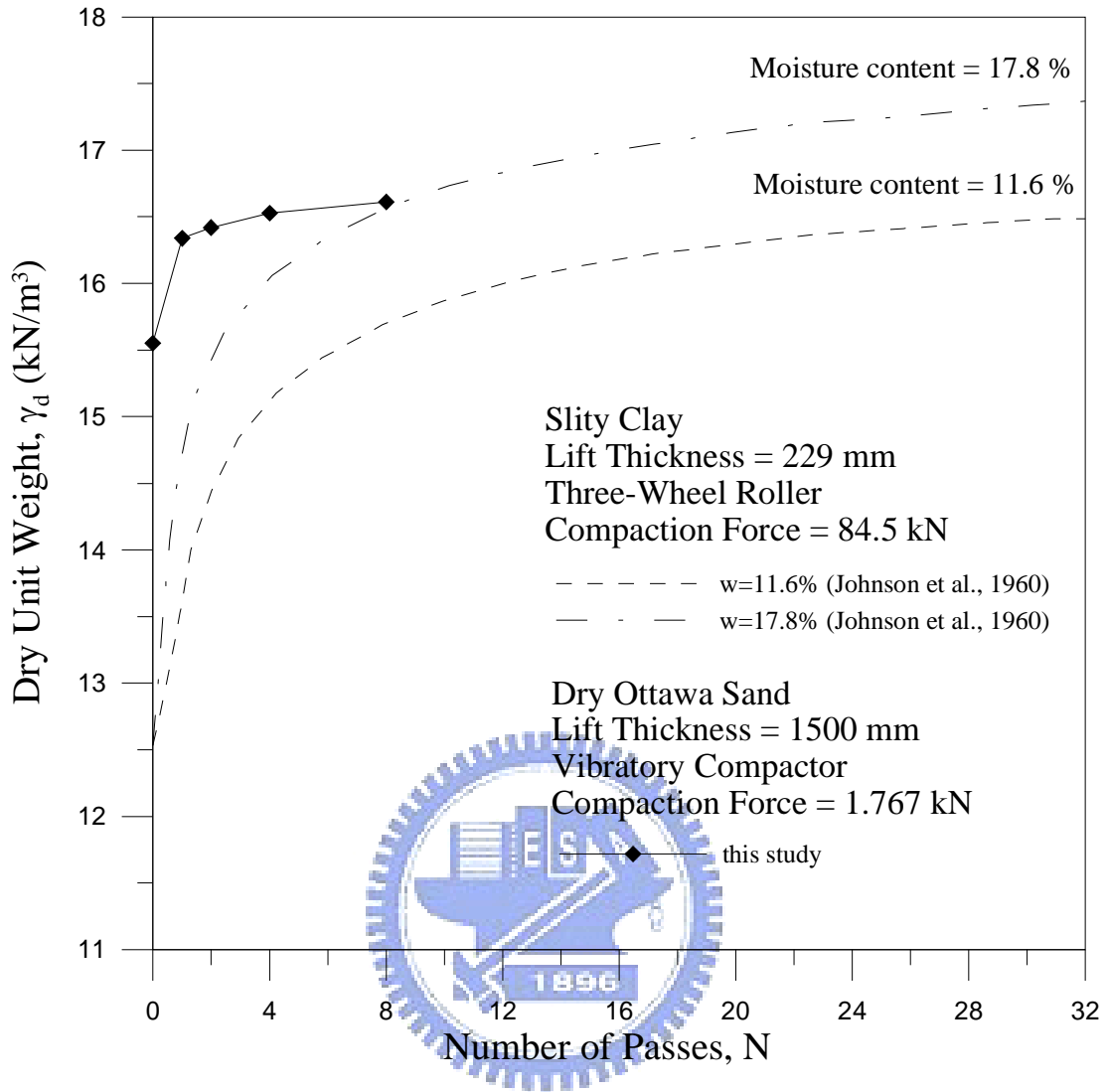


Fig. 6.21. Comparison between Test Results from Laboratory and Test Results from Field (Johnson et al., 1960)

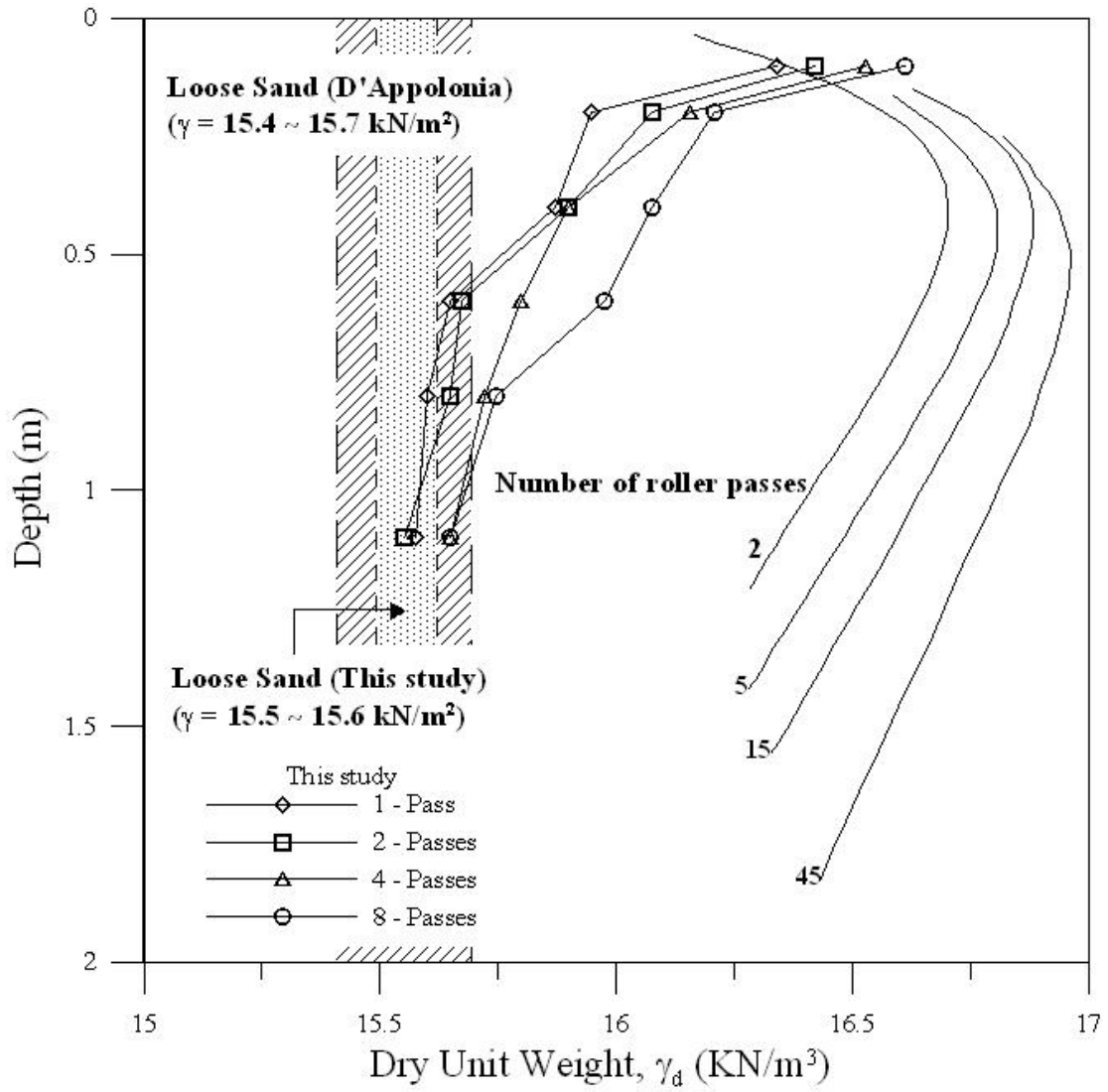


Fig. 6.22. Comparison between Test Results from Laboratory and Test Results from Field (D'Appolonia et al., 1969)

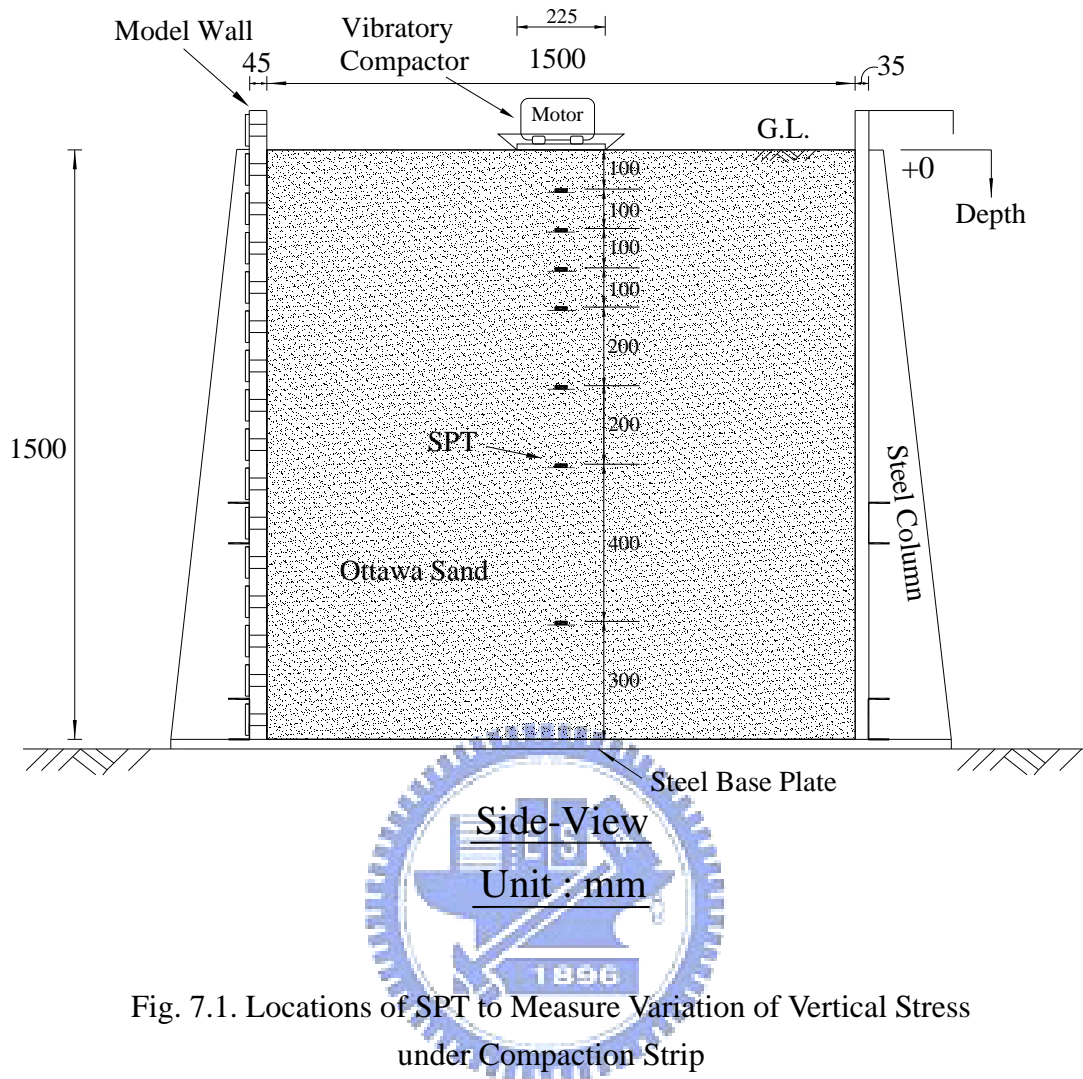


Fig. 7.1. Locations of SPT to Measure Variation of Vertical Stress under Compaction Strip

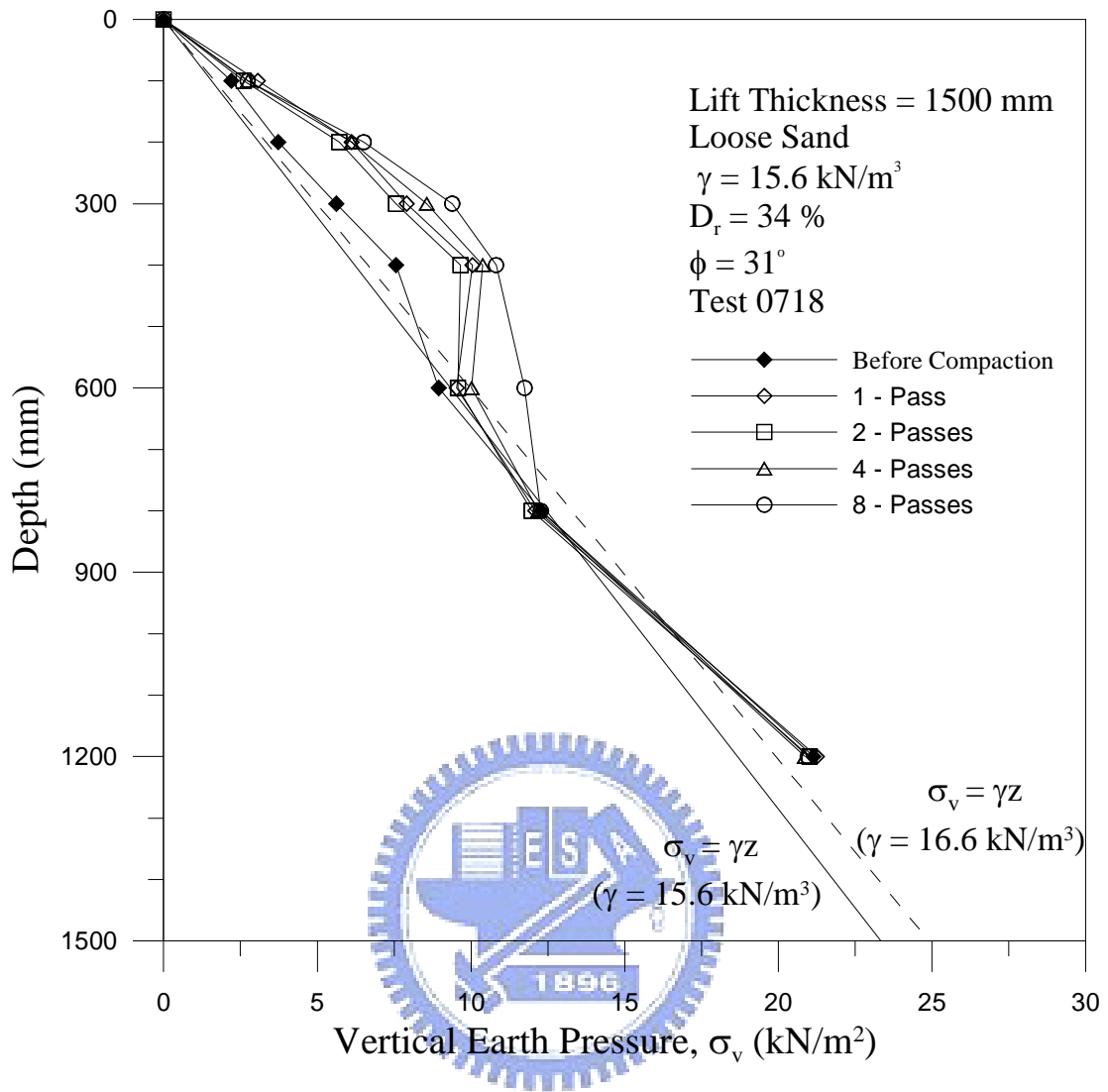


Fig. 7.2. Distribution of Vertical Stress under Compaction Lane

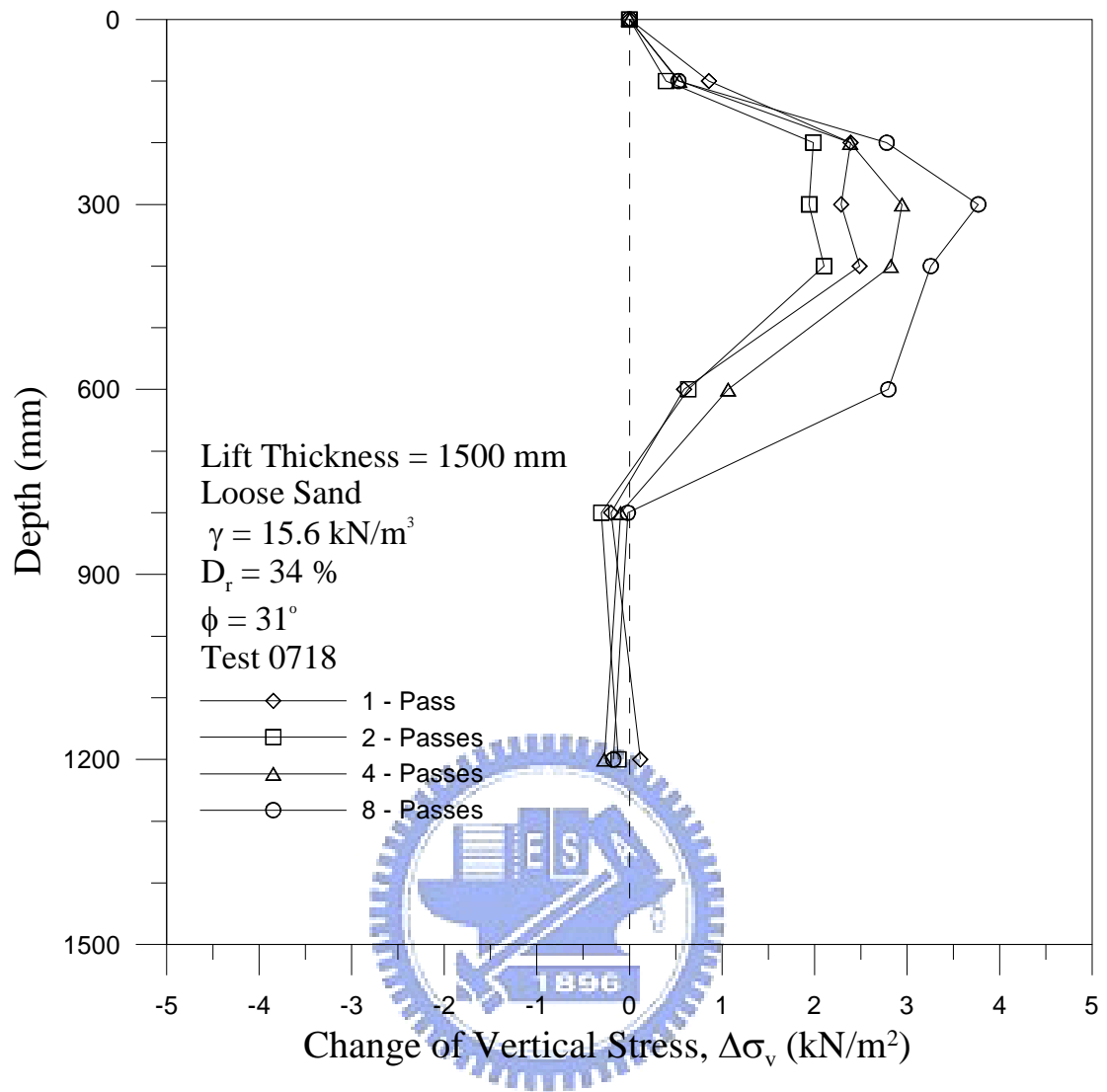


Fig. 7.3. Change of Vertical Stresses under Compaction Strip

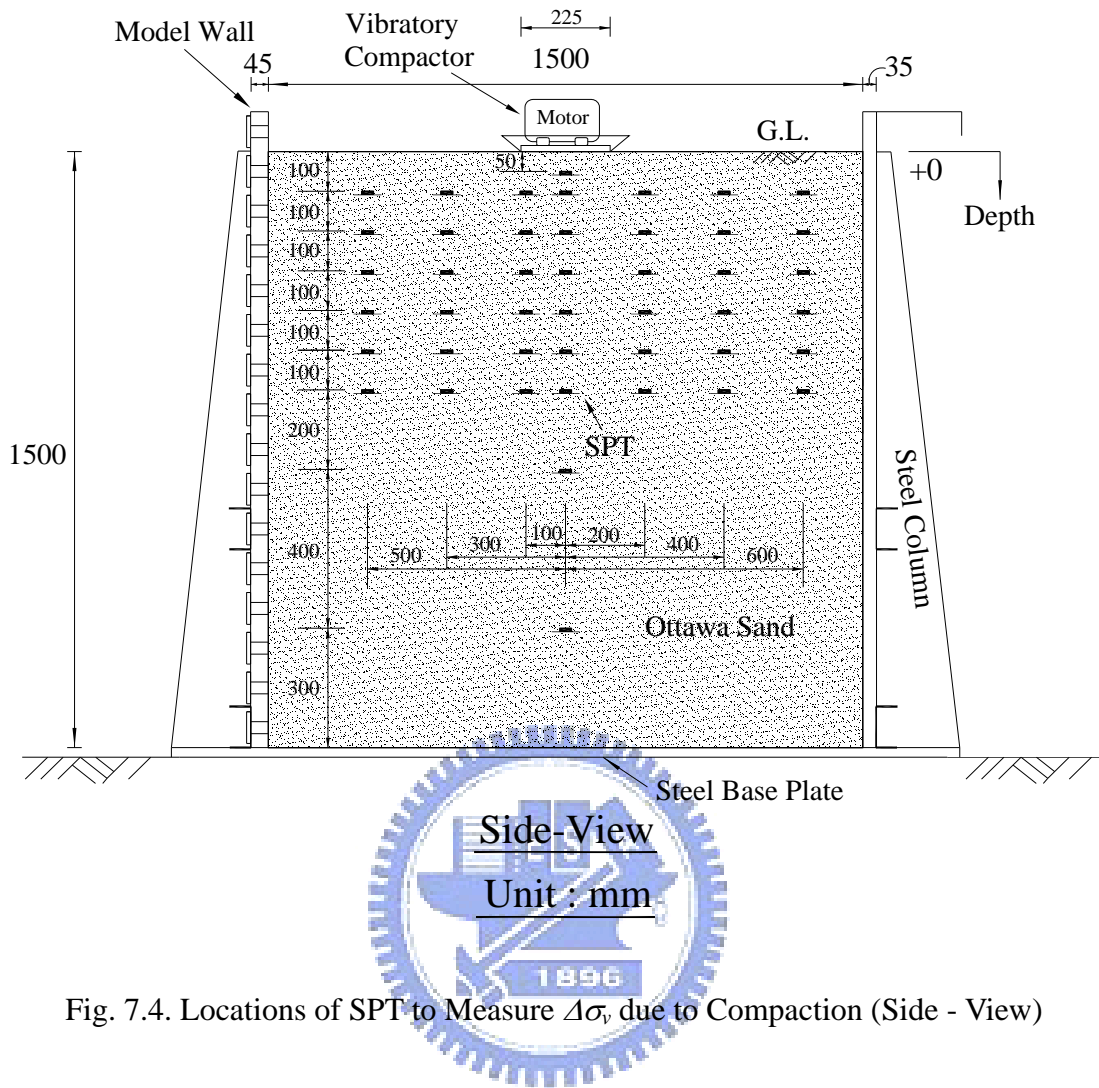


Fig. 7.4. Locations of SPT to Measure $\Delta\sigma_v$ due to Compaction (Side - View)

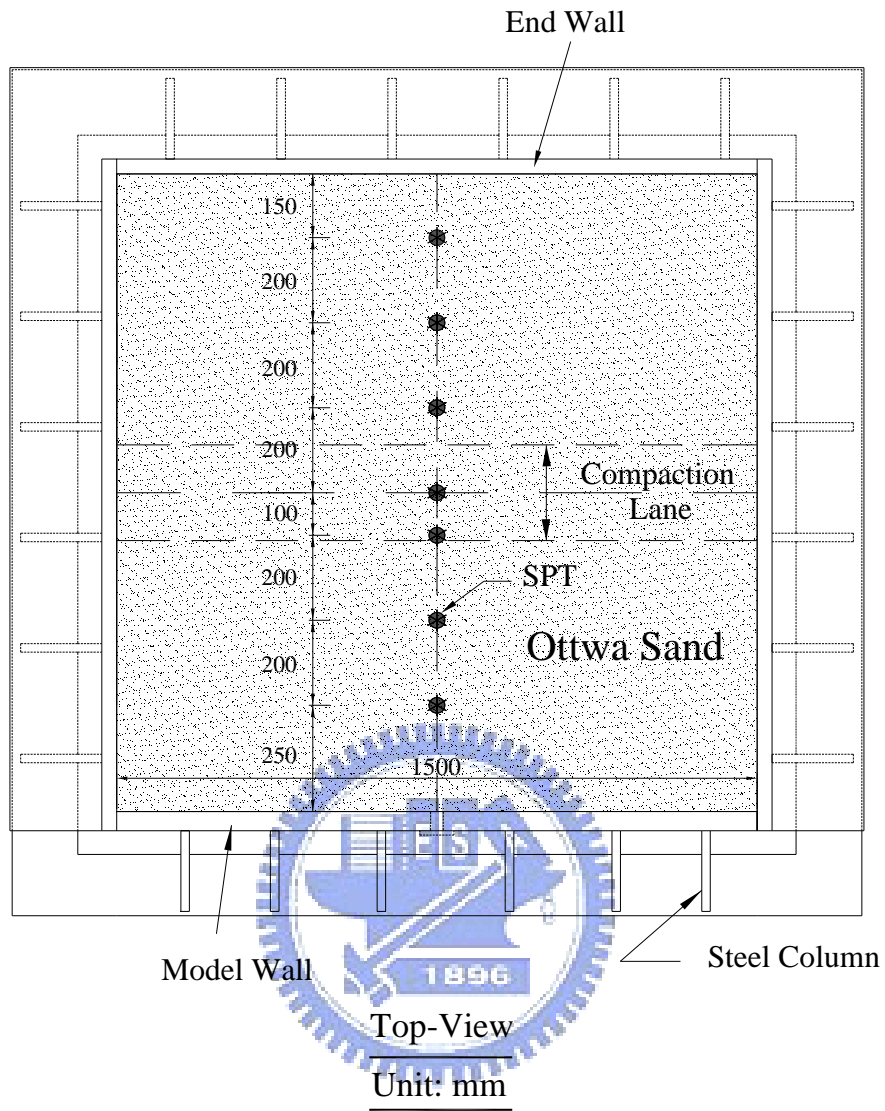


Fig. 7.5. Locations of SPT to Measure $\Delta\sigma_v$ due to Compaction (Top - View)

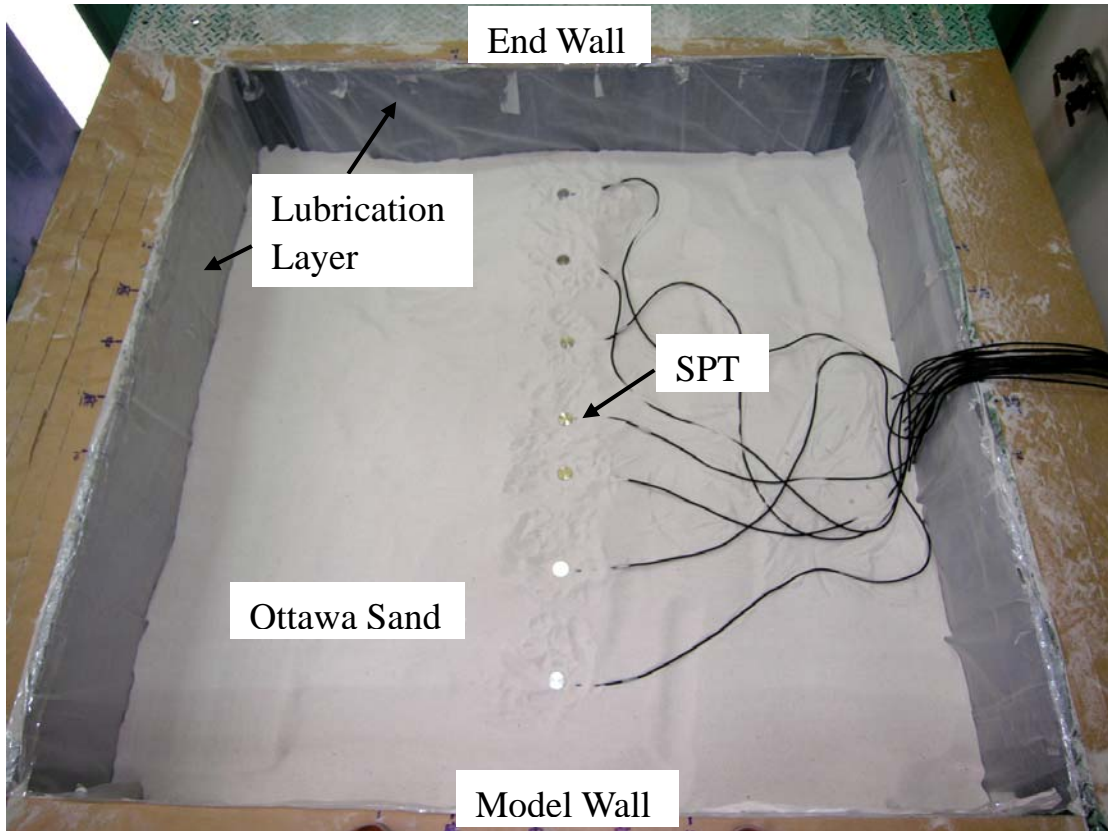


Fig. 7.6. Locations of SPT at Same Elevation

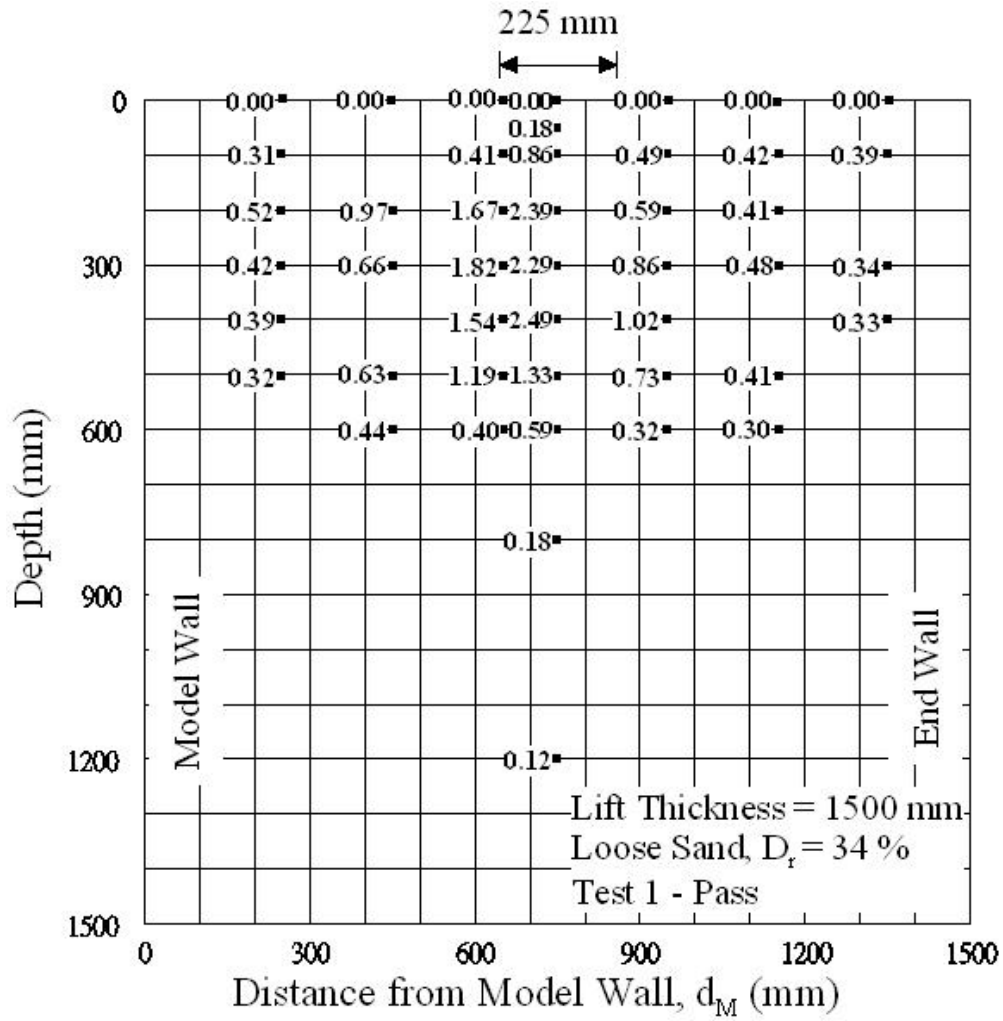


Fig. 7.7. $\Delta\sigma_v$ at Grid Points after 1 – Pass of Compactor

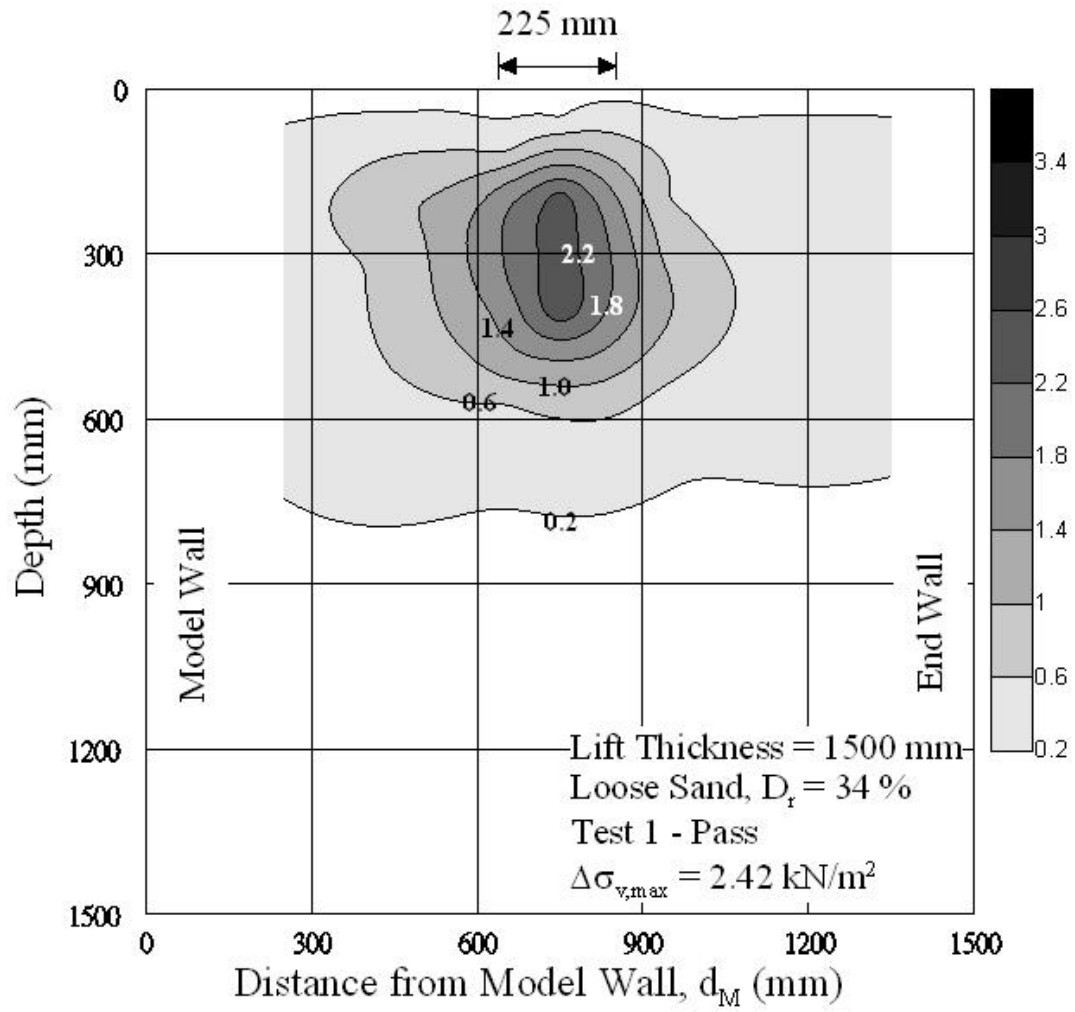


Fig. 7.8. Contours of $\Delta\sigma_v$ after 1 – Pass of Compactor

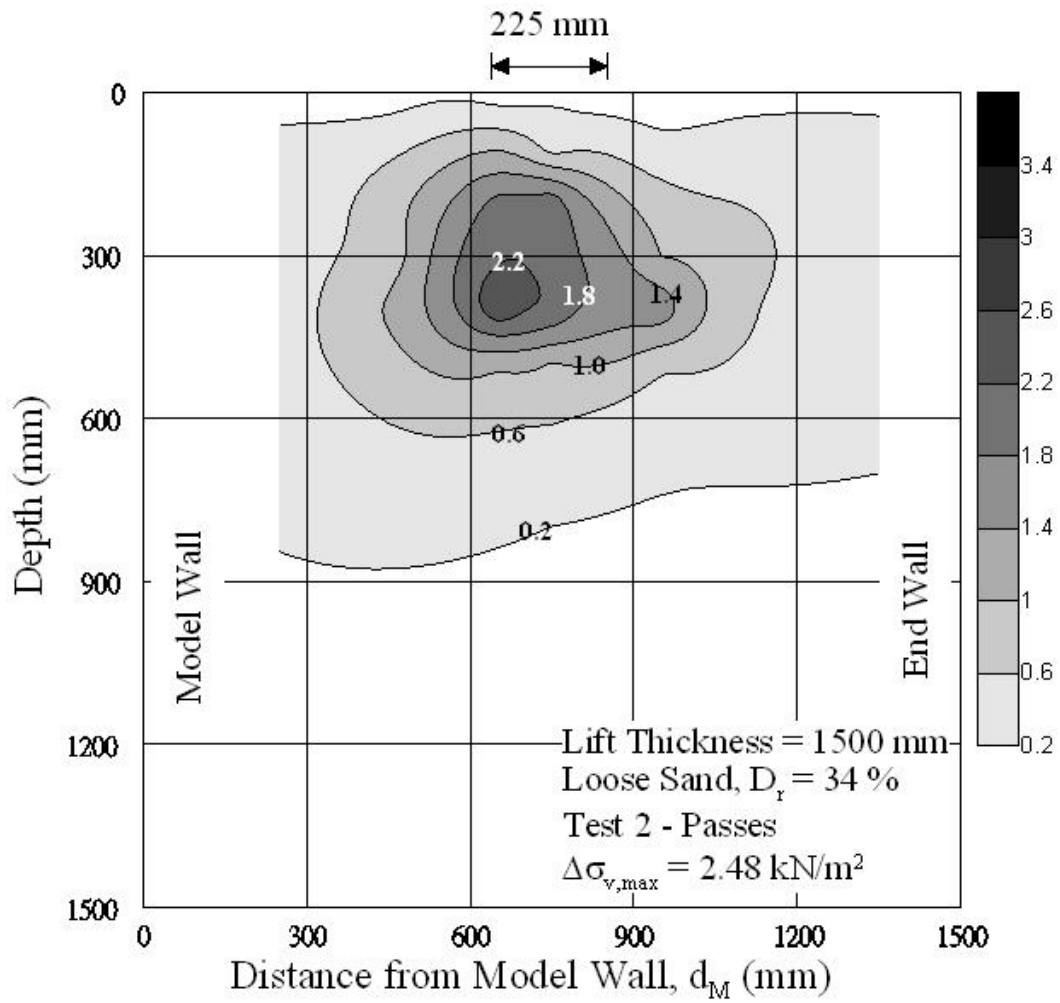


Fig. 7.9. Contours of $\Delta\sigma_v$ after 2 – Passes of Compactor

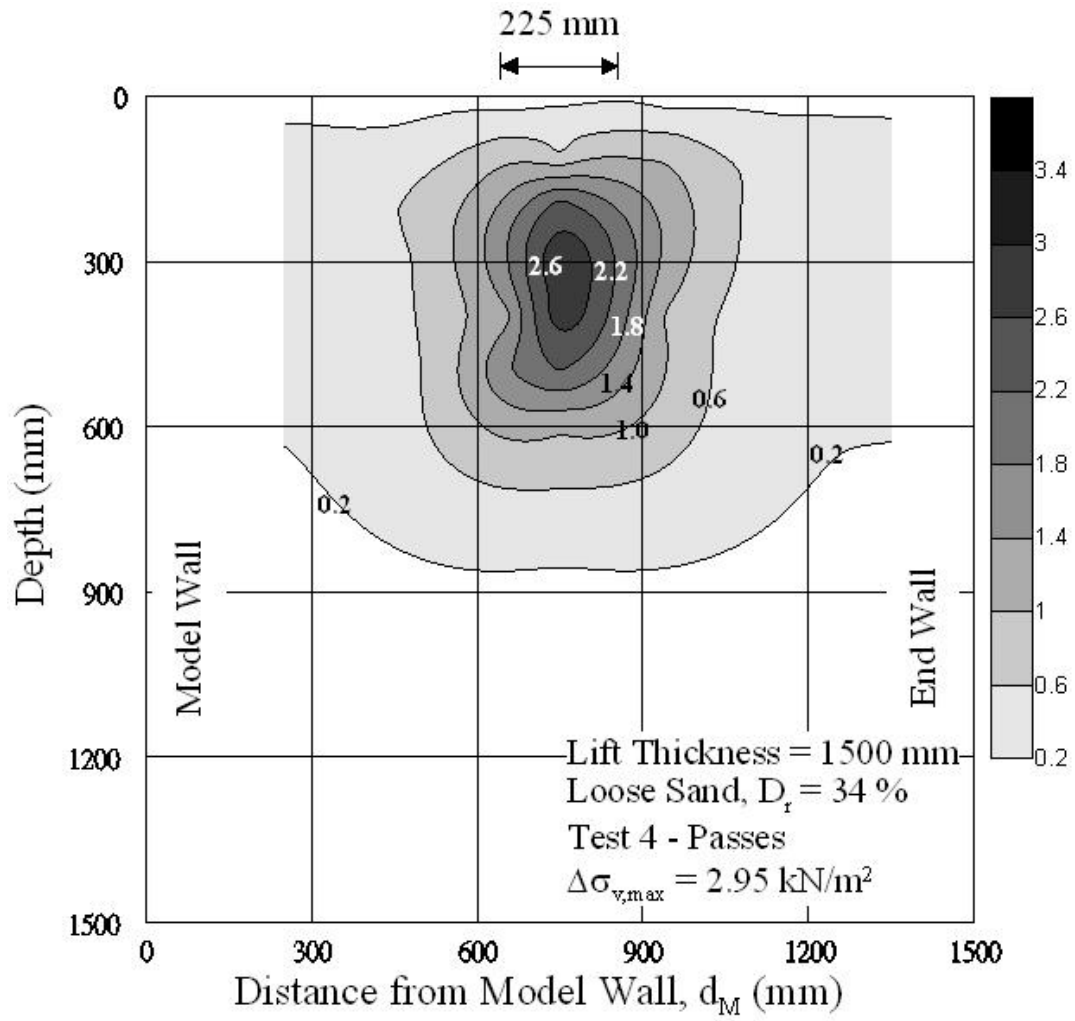


Fig. 7.10. Contours of $\Delta\sigma_v$, after 4 – Passes of Compactor

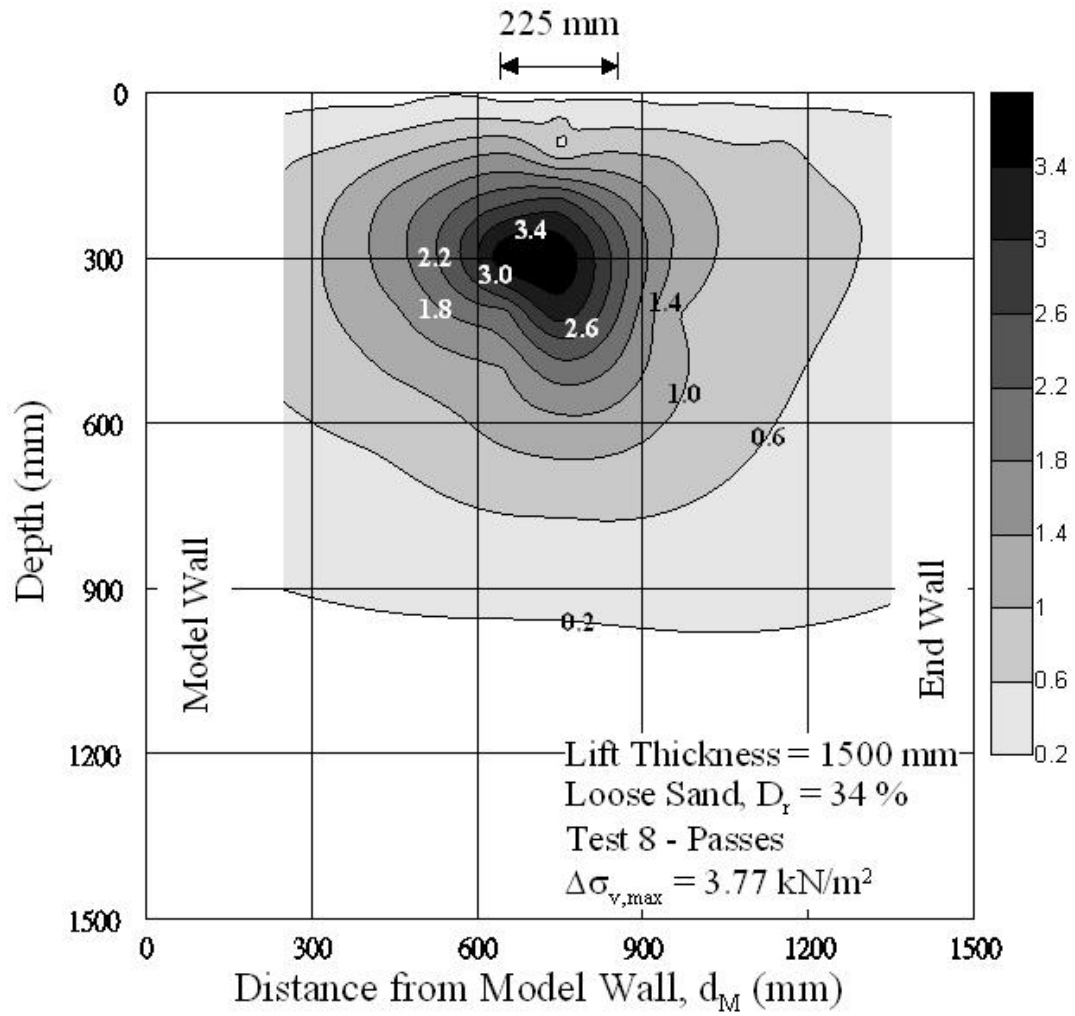


Fig. 7.11. Contours of $\Delta\sigma_v$, after 8 – Passes of Compactor

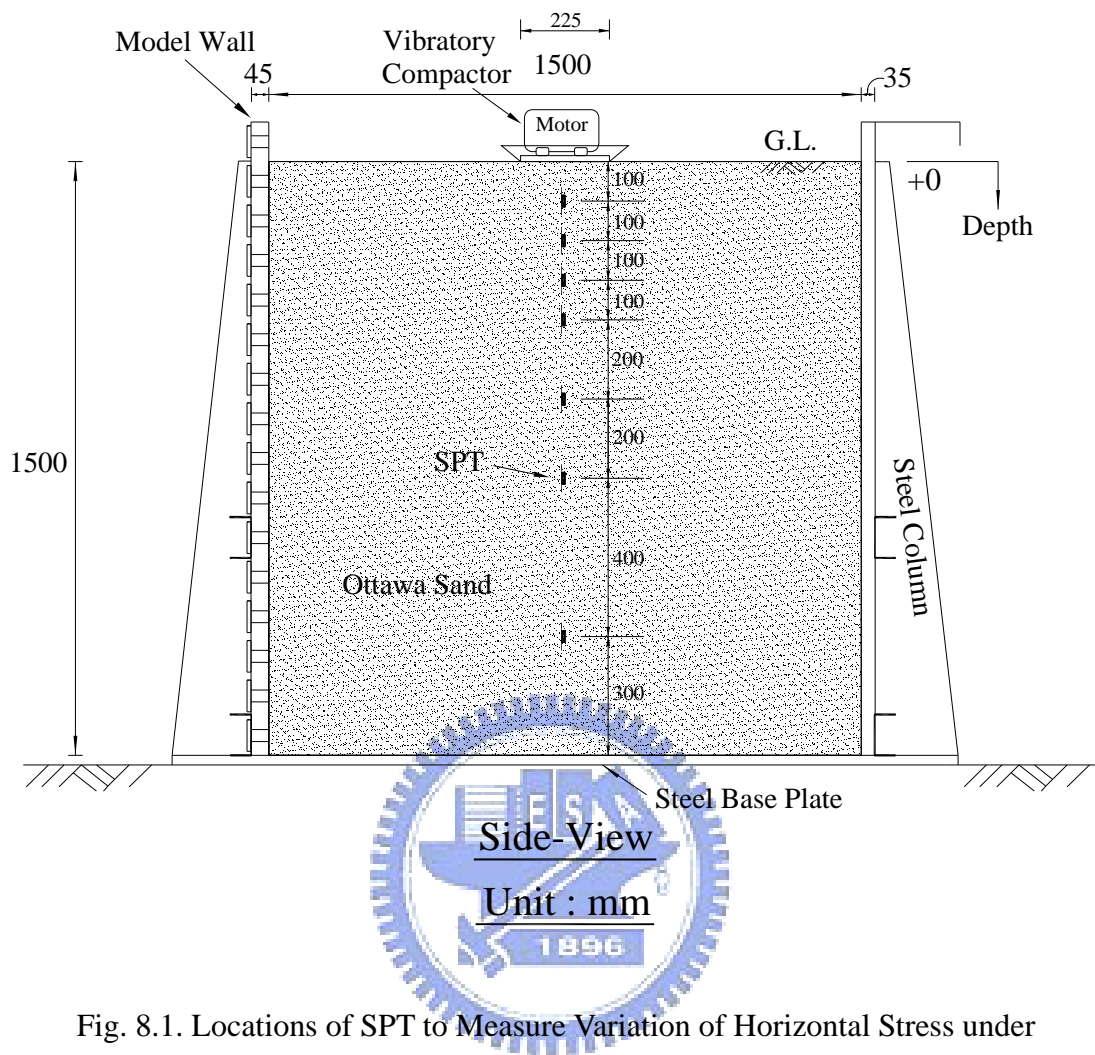


Fig. 8.1. Locations of SPT to Measure Variation of Horizontal Stress under Compaction Lane

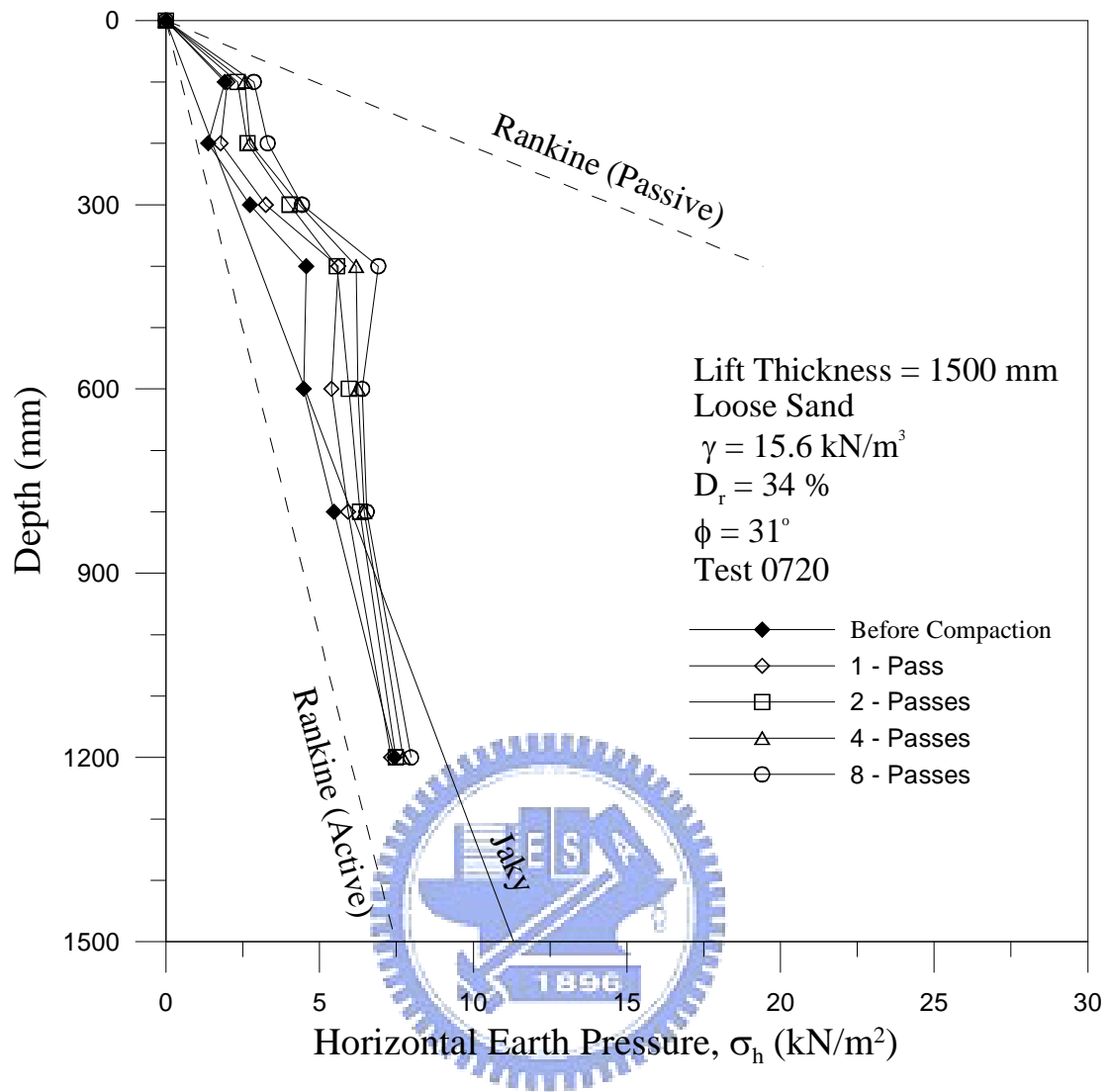


Fig. 8.2. Distribution of Vertical Stress under Compaction Lane

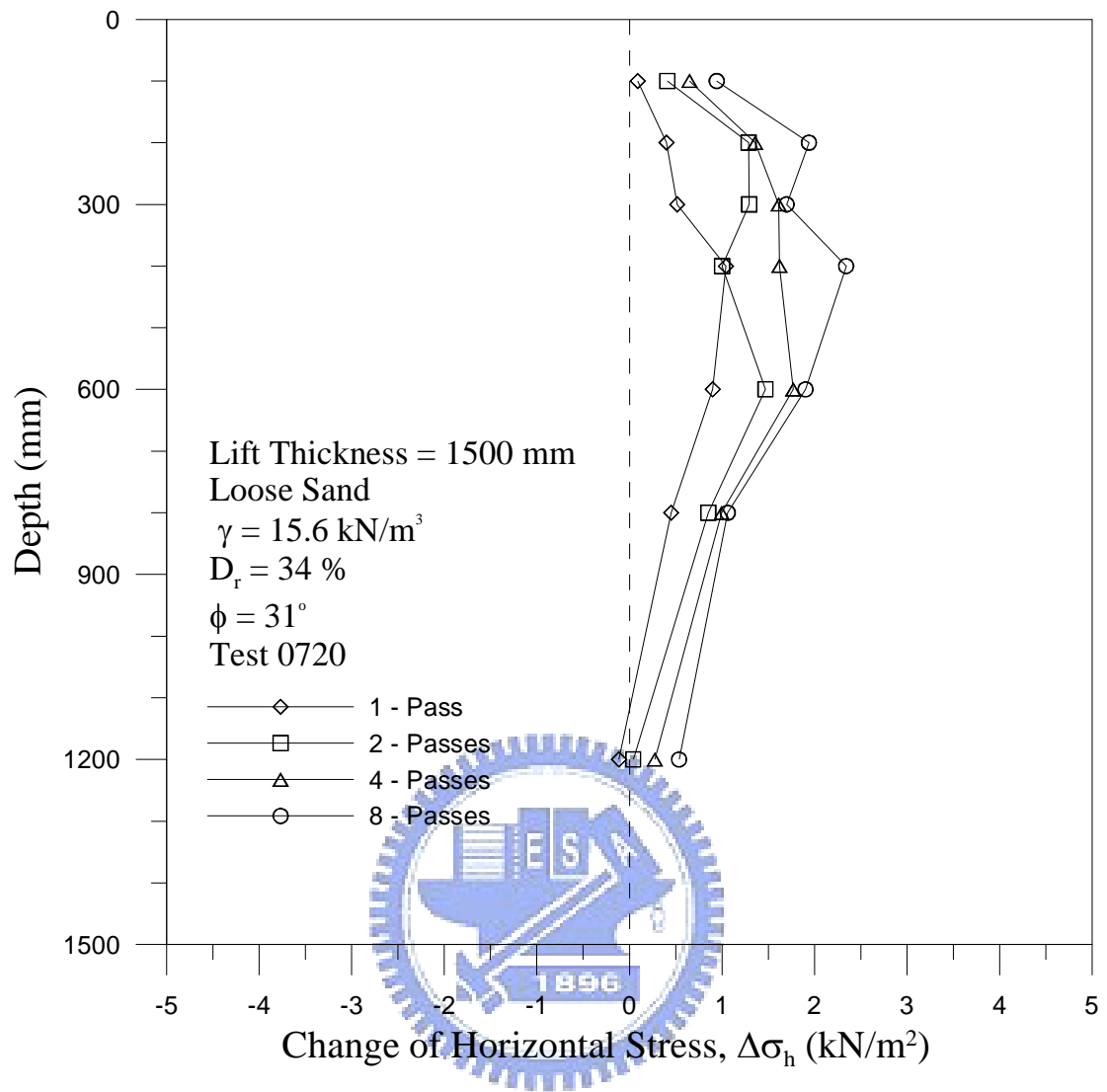


Fig. 8.3. Change of Horizontal Stresses under Compaction Lane

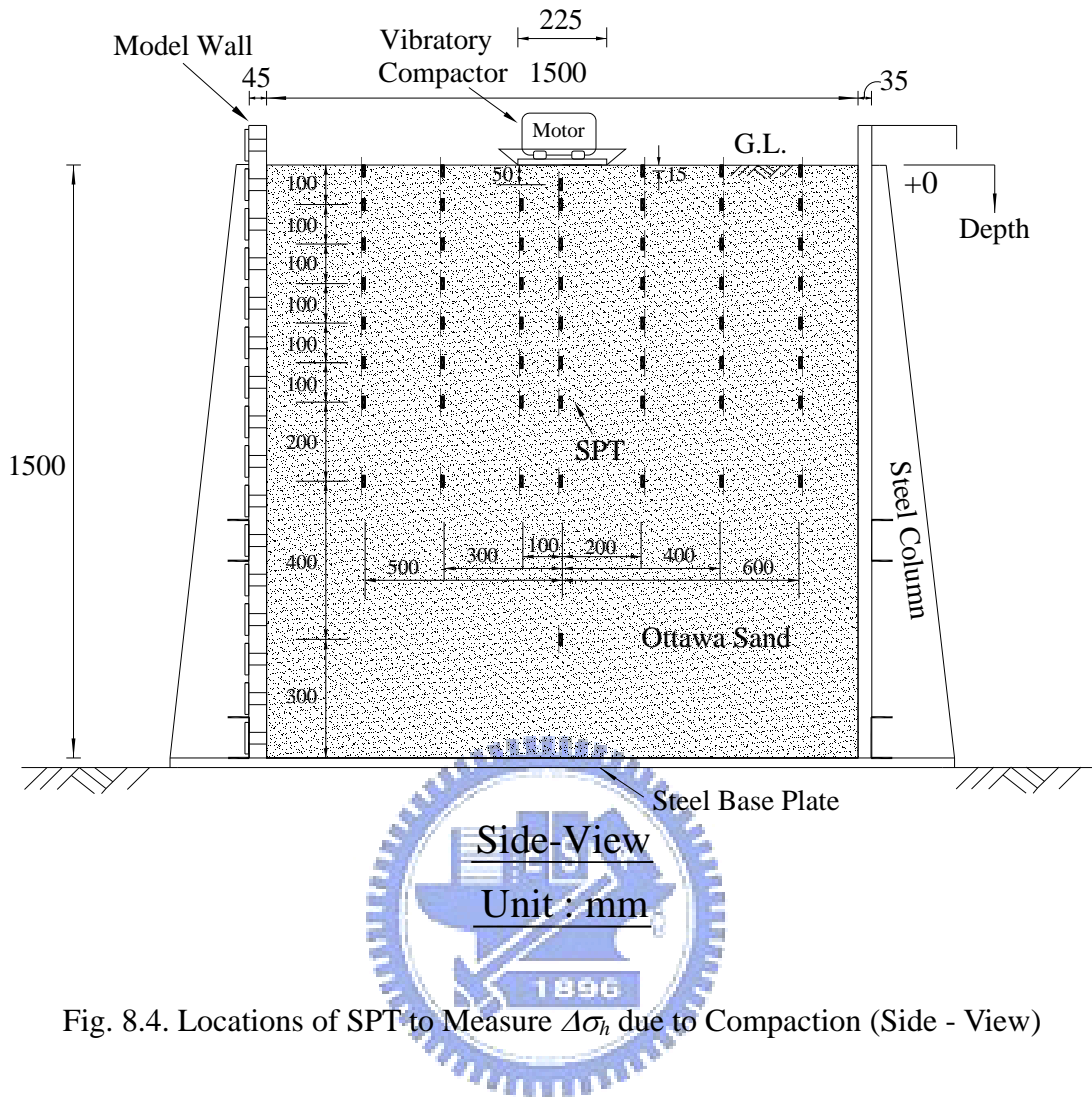


Fig. 8.4. Locations of SPT to Measure $\Delta\sigma_h$ due to Compaction (Side - View)

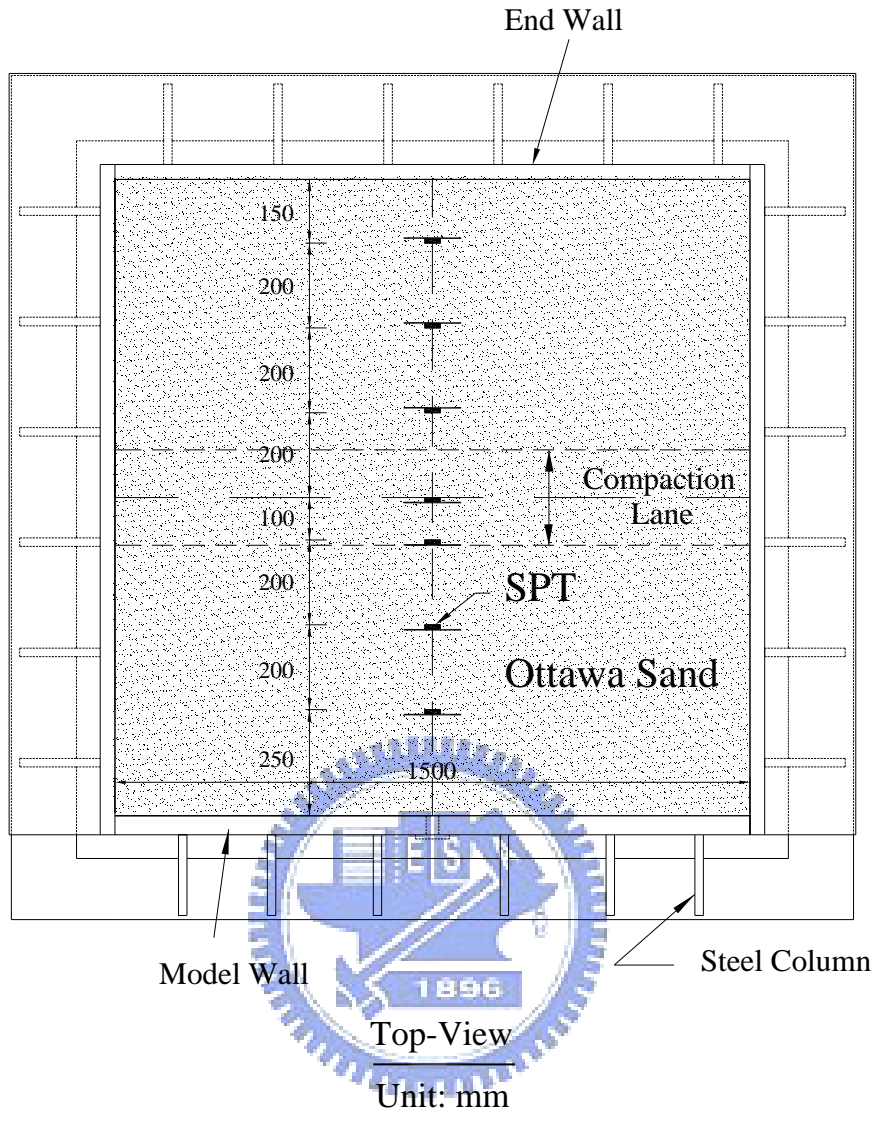


Fig. 8.5. Locations of SPT to Measure $\Delta\sigma_h$ due to Compaction (Top - View)

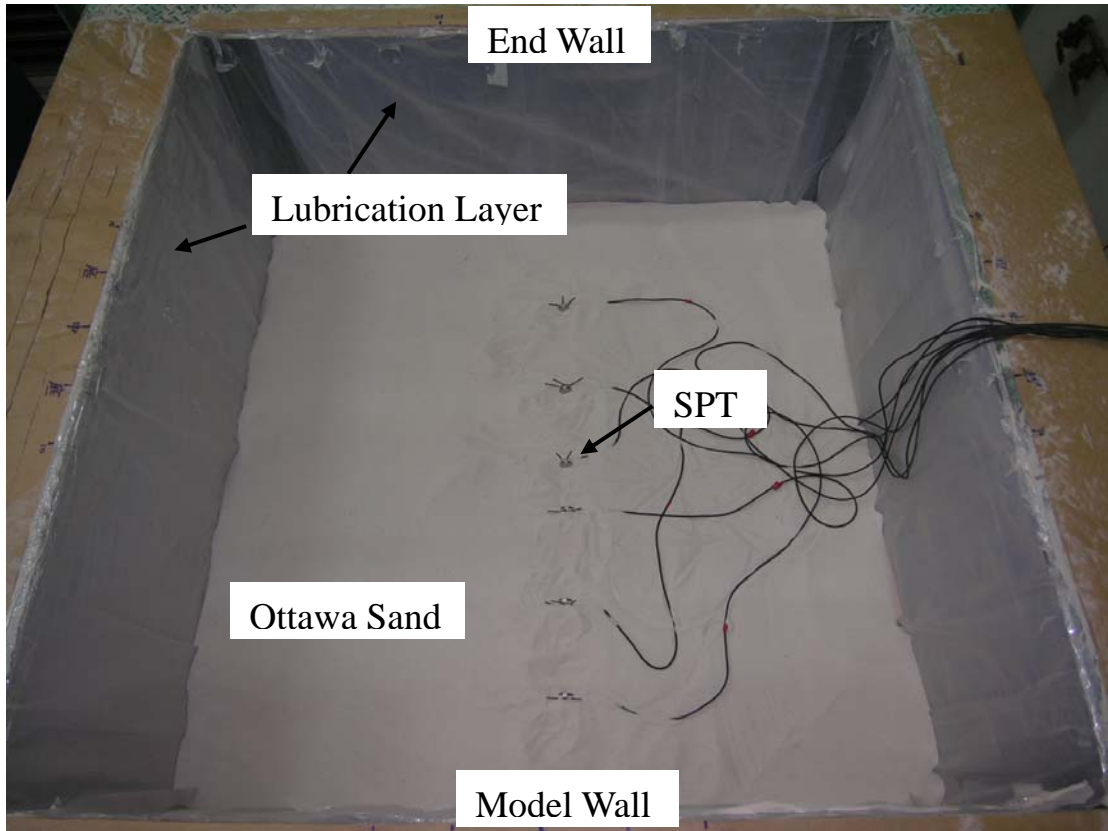


Fig. 8.6. Locations of SPT at Same Elevation



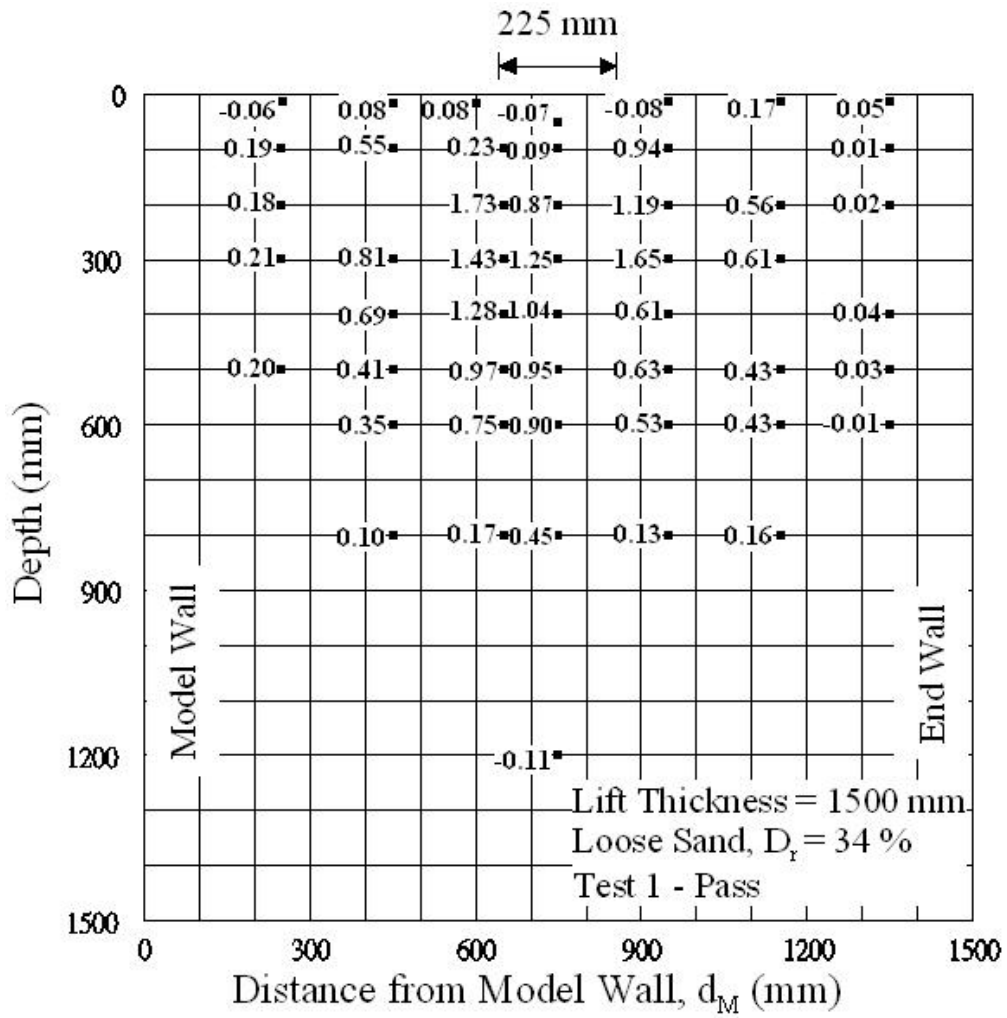


Fig. 8.7. $\Delta\sigma_h$ at Grid Points after 1 – Pass of Compactor

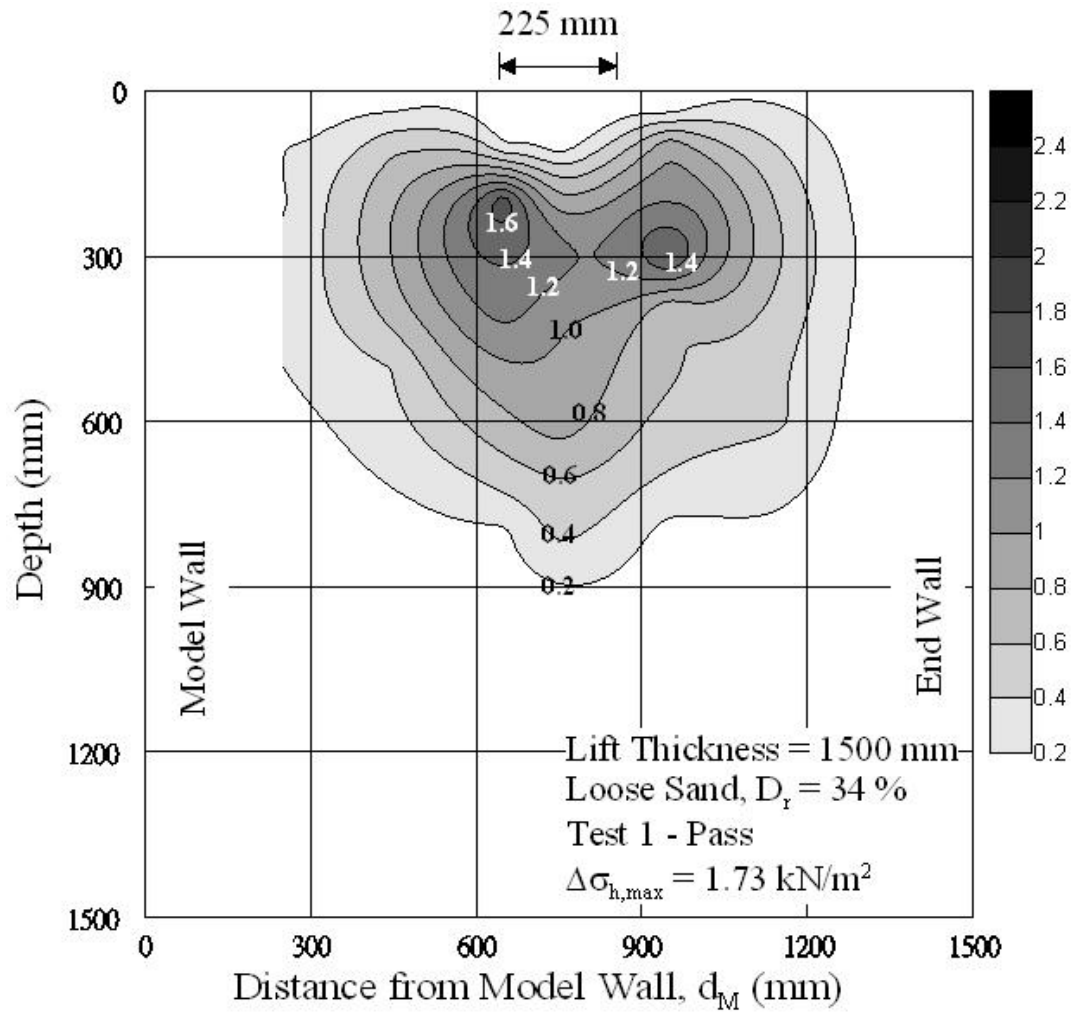


Fig. 8.8. Contours of $\Delta\sigma_h$ after 1 - Pass of Compactor

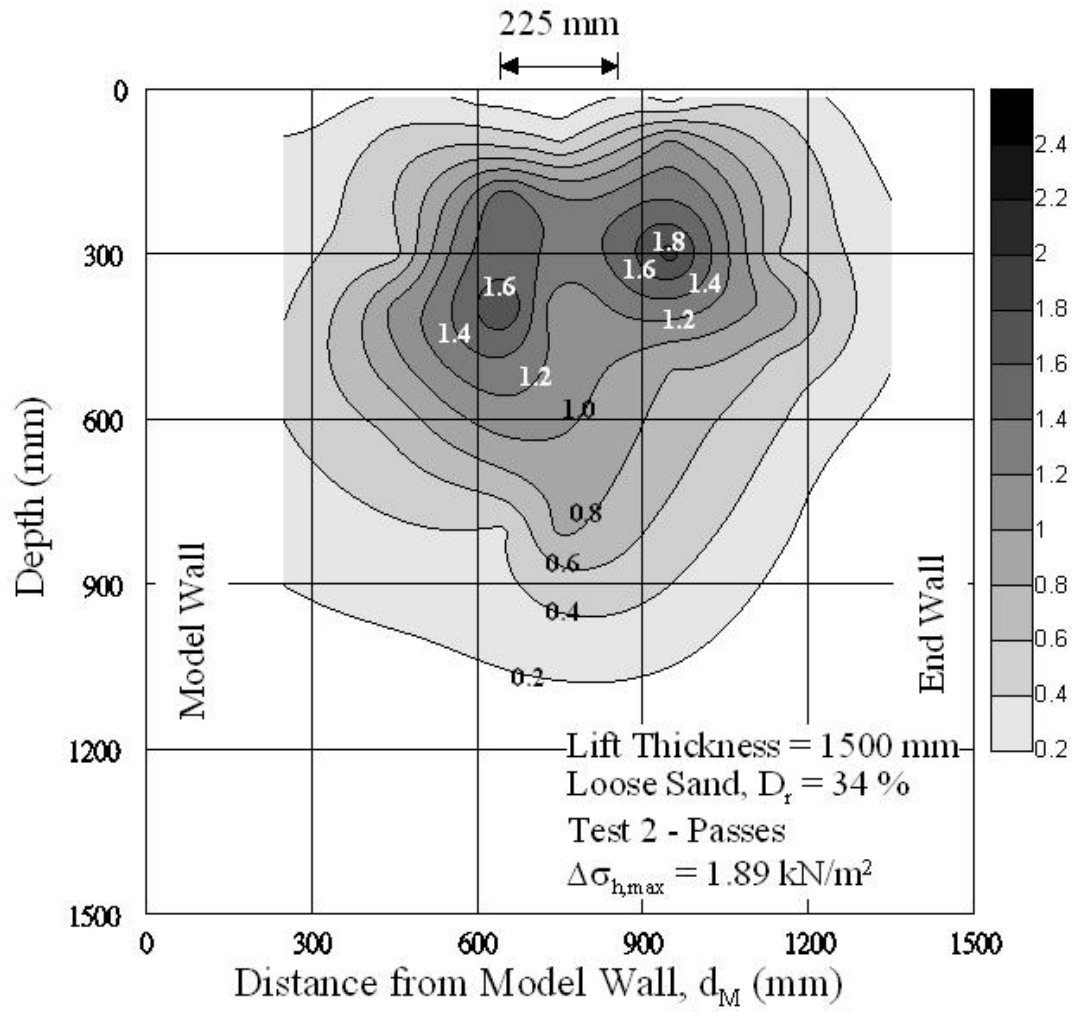


Fig. 8.9. Contours of $\Delta\sigma_h$ after 2 - Passes of Compactor

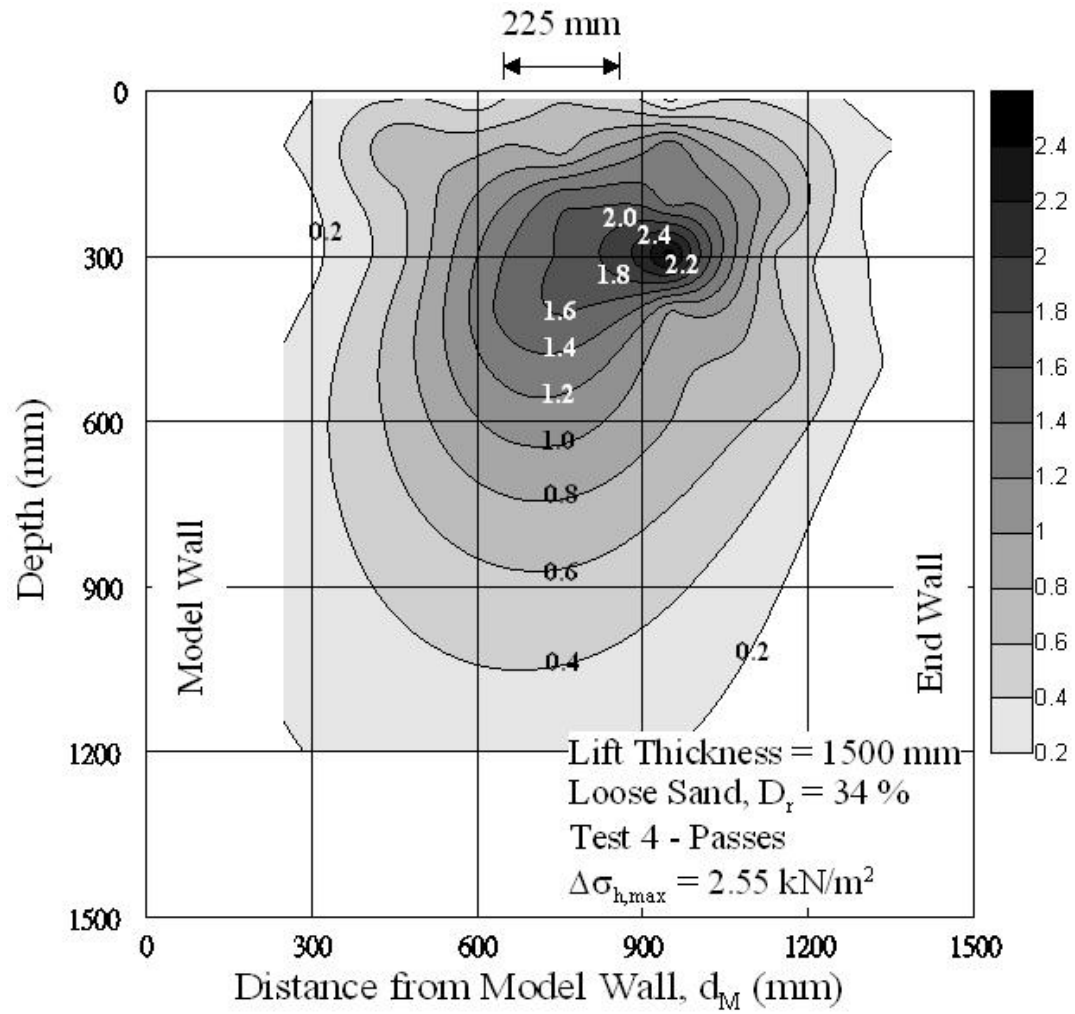


Fig. 8.10. Contours of $\Delta\sigma_h$ after 4 – Passes of Compactor

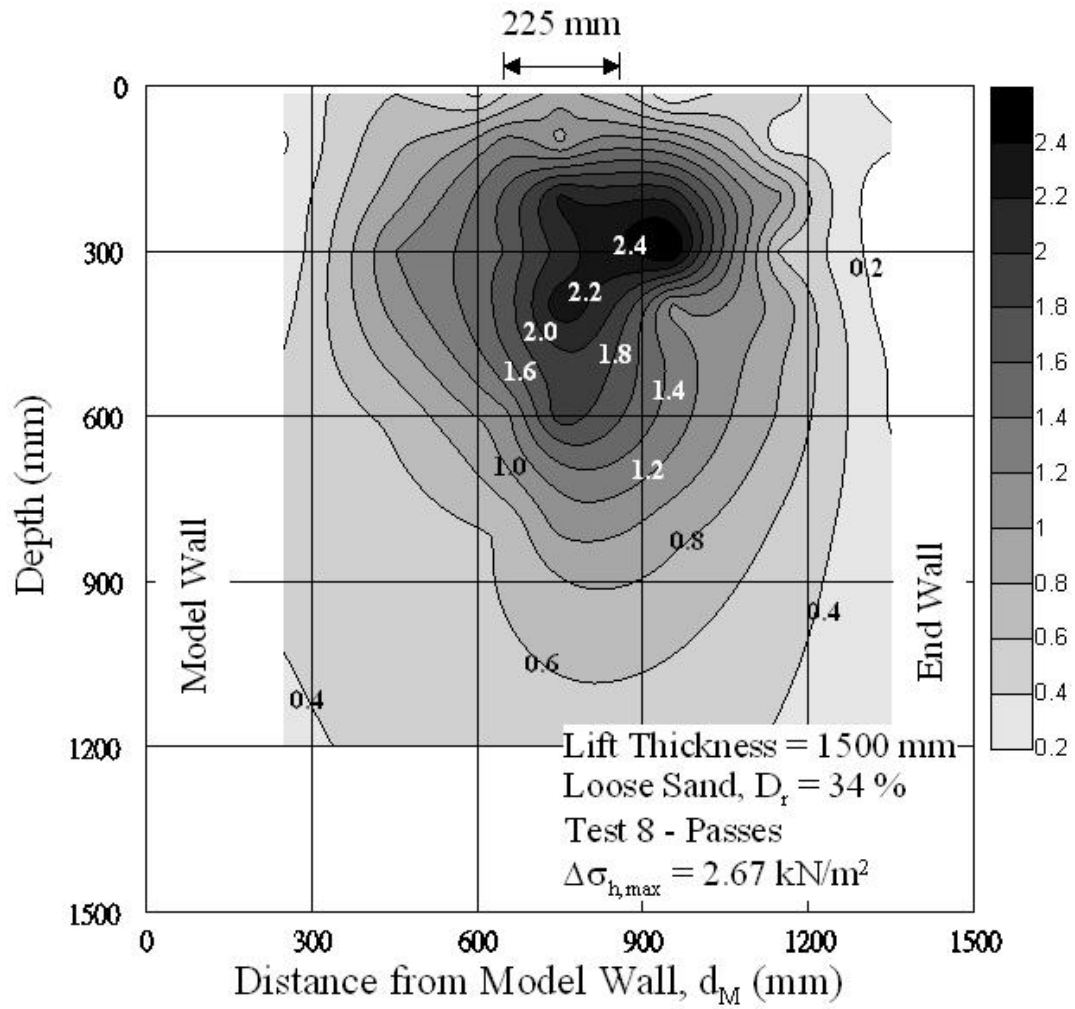


Fig. 8.11. Contours of $\Delta\sigma_h$ after 8 – Passes of Compactor

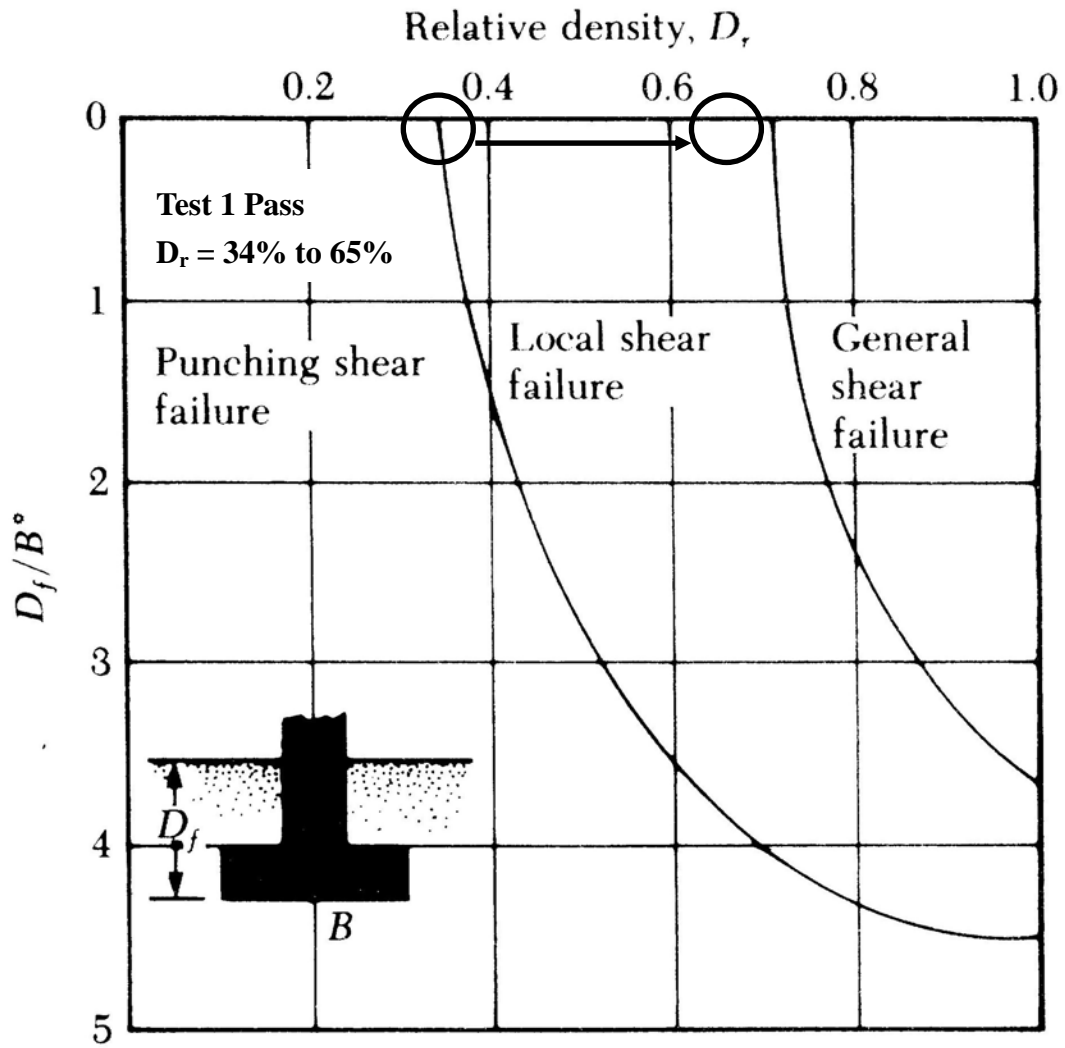


Fig. 8.12. Comparison between Change of Relative Density after 1 Pass of Compactor in This Study and Vesic's Theory (1973).

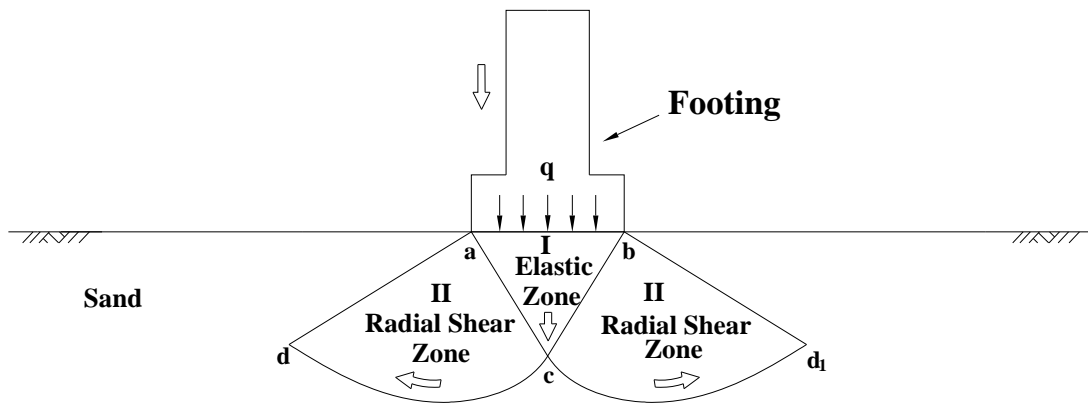


Fig. 8.13. Bearing Capacity Failure in Soil (after Vesic, 1973)



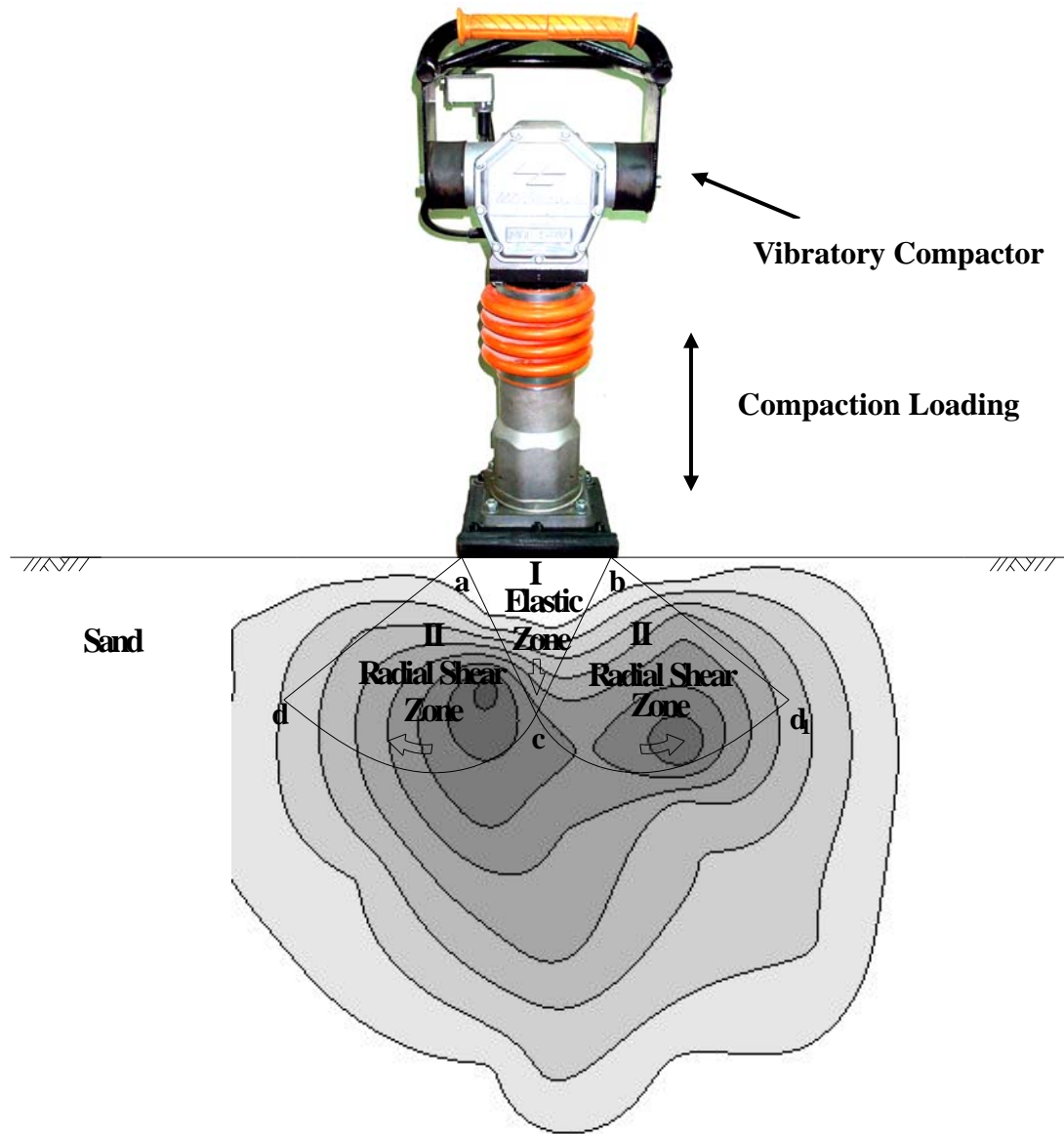


Fig. 8.14. Comparison between Test Results and Local Shear Failure (Vesic, 1973)

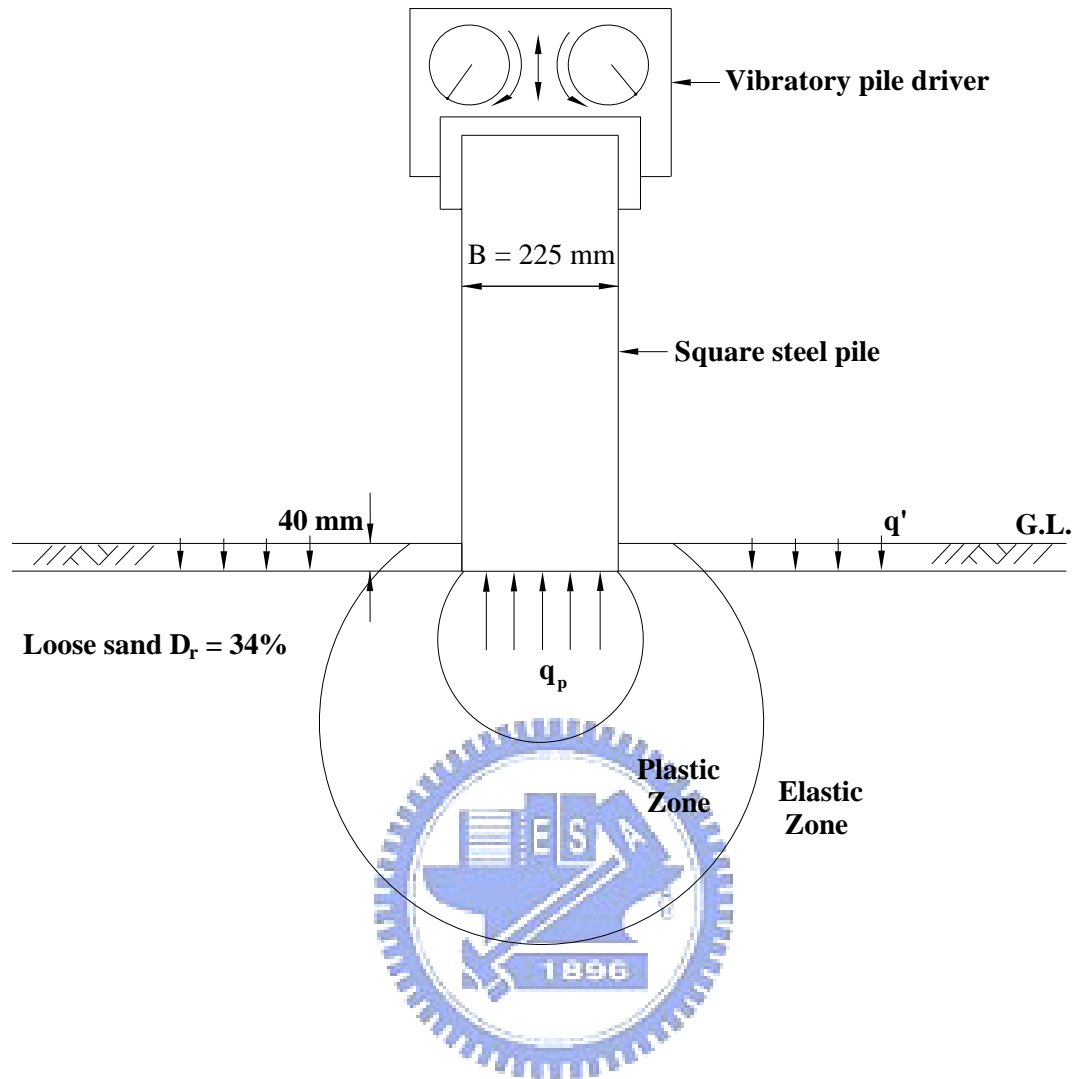


Fig. 8.15. Influence Zone Assumed for Piles in Sand (after Yang, 2006)

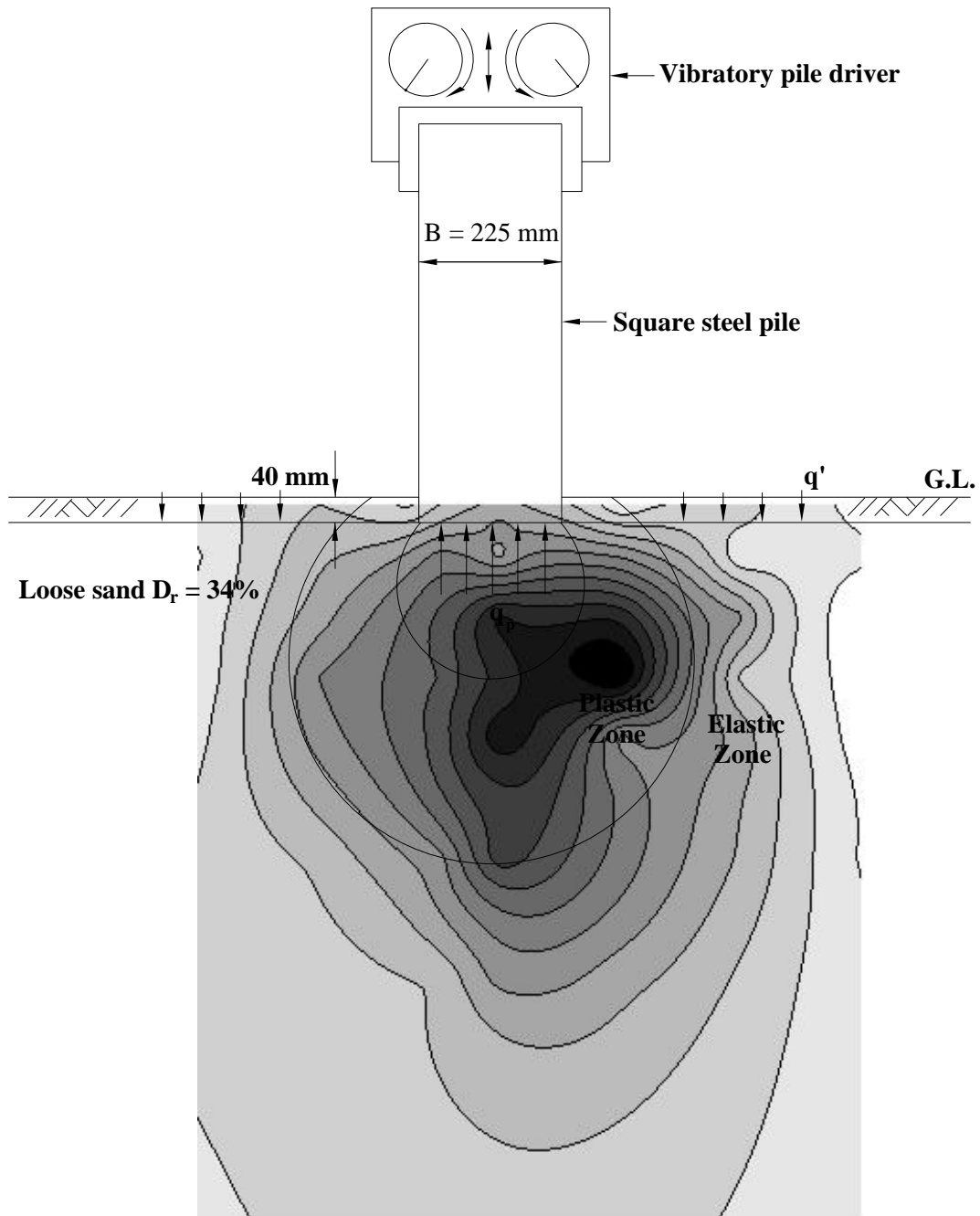


Fig. 8.16. Comparison between Test Results and Influence zone for Piles in Sand (Yang, 2006)

Appendix A

Calibration of Soil Pressure Transducers

To investigate the vertical and horizontal earth pressure in the backfill, strain-gage type soil pressure transducers (SPT) were used. The transducers BE-2KCM17 manufactured by KYOWA has an effective diameter of 22 mm and was embedded in the backfill to monitor the earth pressure variation in the soil mass. Since the pressure acts between soil particles and the transducer is quite different from the pressure that acts between liquid and transducer, it is necessary to calibrate the transducer in an environment similar to that for the actual testing condition. A special system was designed for the calibration of the strain-gage type soil pressure transducers. The system consists of the calibration device, air-pressure control system, signal conditioner, and data acquisition system, as indicated in Fig. A.1. The typical photograph of the system is shown in Fig. A.2.

The calibration device is a shallow cylindrical chamber with an inner diameter of 400 mm and a height of 30mm and it is made of a solid steel plate, which is the same material as the model retaining wall. To calibrate the in-soil transducer, as indicated in Fig. A.1, a thin layer of sand was placed into the chamber to form a sand bed then the soil pressure transducer was placed on the sand bed. On top of the transducer, a 10 mm-thick sand layer was placed in the calibration device. Then the 0.2 mm-thick rubber membrane was placed over the sandy layer. As indicated in Fig. A.1, a uniformly distributed air-pressure was applied on the membrane, over the soil particles, and transmitted to the transducer. The output voltage of the transducer was found to

increase linearly with the increasing applied pressure.

In Fig. A1, a rubber O-rings was arranged to prevent air leakage between the chamber and the cap. It should be noted that the air pressure applied for the calibration of transducer should be consistent with the operating pressure range for experiments. For this study, the transducers which measured the horizontal earth pressure were calibrated for the pressure range of 0 ~ 9.81 kN/m². The pressure range of 0 ~ 98.1 kN/m² was suitable for the transducers which measured the vertical earth pressure. To reduce the effect of sidewall friction, the thickness of sand layer in the chamber should be limited, so that the side-friction between the sand the sidewall of the chamber could be minimized. Fig. A.3 to Fig. A.10 shows the test results of the soil pressure transducers calibrated without the compressible layer. Table A.1, A.2 summarizes of the calibration factors of soil pressure transducers used in this study.

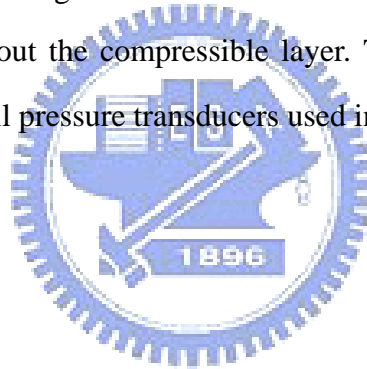


Table A.1. Soil Pressure Transducer Calibration Factors

Type	Transducer No.	Dynamic Strain Amplifier		Capacity (kN/m ²)	Calibration Function P=[Factor]*V (kN/m ²)
		No.	Calibration Setter($\mu \xi$)		
BE-2KCM17	090170001	1	283	98.1	P=38.222V
BE-2KCM17	090170002	2	275	98.1	P=38.012V
BE-2KCM17	090170003	3	302	98.1	P=37.284V
BE-2KCM17	090170004	4	288	98.1	P=37.816V
BE-2KCM17	090170005	5	282	98.1	P=38.097V
BE-2KCM17	090170006	6	289	98.1	P=37.472V
BE-2KCM17	090170007	7	300	98.1	P=38.343V
BE-2KCM17	090170008	8	269	98.1	P=37.534V

Calibration pressure range : 0~98.1 kN/m²

Table A.2. Soil Pressure Transducer Calibration Factors

Type	Transducer No.	Dynamic Strain Amplifier		Capacity (kN/m ²)	Calibration Function P=[Factor]*V (kN/m ²)
		No.	Calibration Setter($\mu \xi$)		
BE-2KCM17	9Z0080001	9	305	98.1	P=18.303V
BE-2KCM17	9Z0080002	10	340	98.1	P=17.684V
BE-2KCM17	9Z0080003	11	345	98.1	P=19.821V
BE-2KCM17	9Z0080004	12	350	98.1	P=18.510V
BE-2KCM17	9Z0080005	13	333	98.1	P=20.209V
BE-2KCM17	9Z0080006	14	316	98.1	P=19.923V
BE-2KCM17	9Z0080007	15	378	98.1	P=20.825V
BE-2KCM17	9Z0080008	16	325	98.1	P=19.552V

Calibration pressure range : 0~9.81 kN/m²

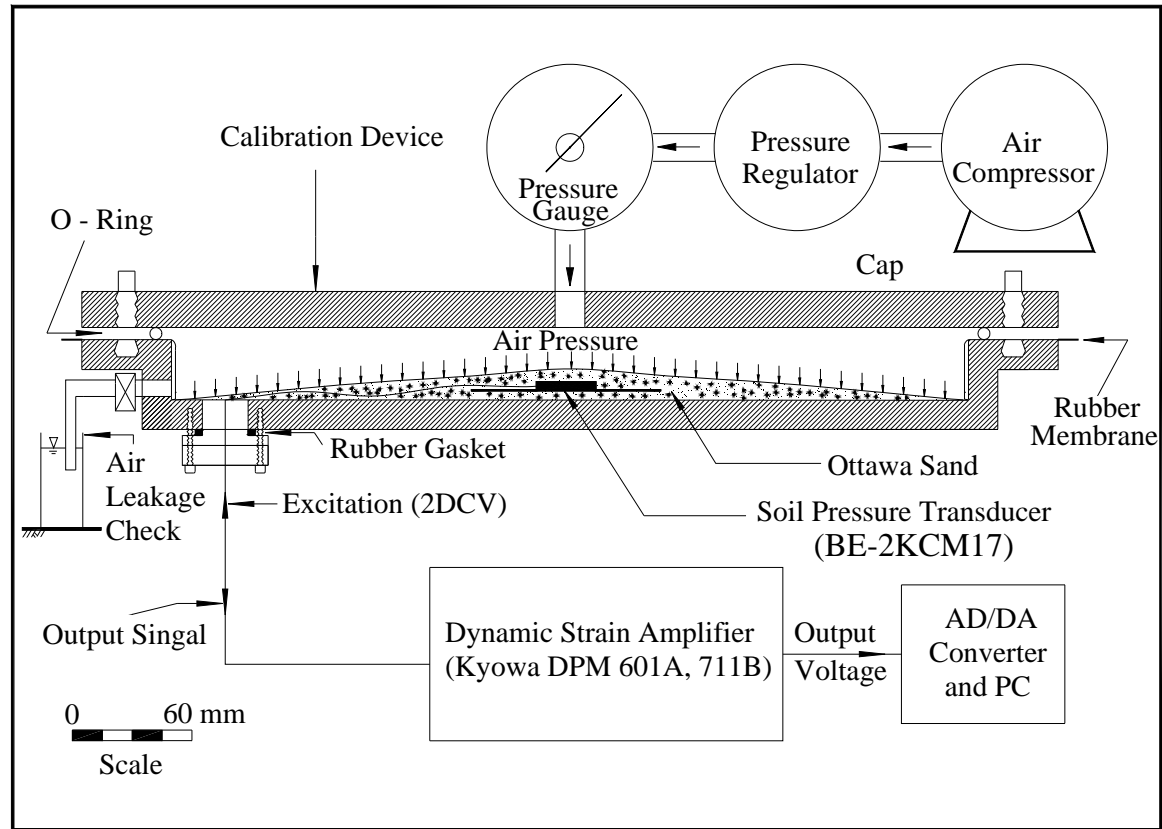


Fig. A1. Schematic Diagram of in-soil Soil Pressure Transducer Calibration System

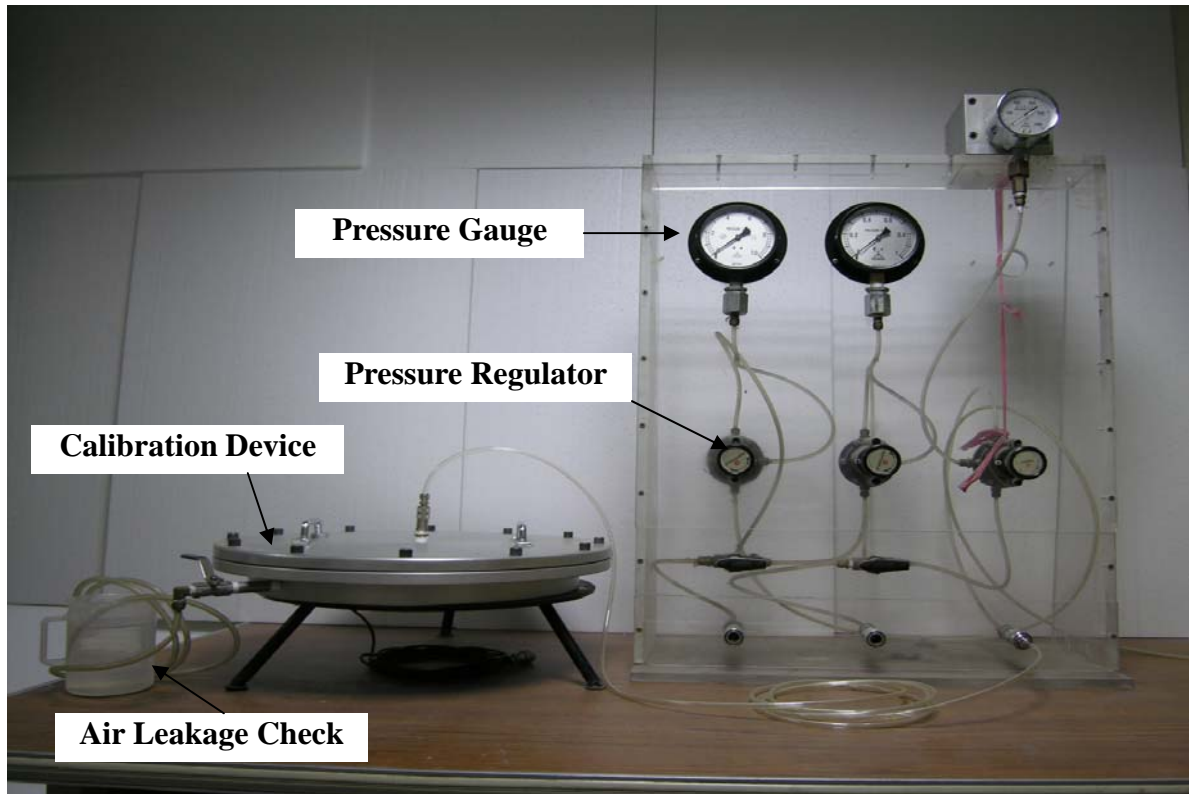


Fig. A.2. Photograph of Soil Pressure Transducer Calibration System



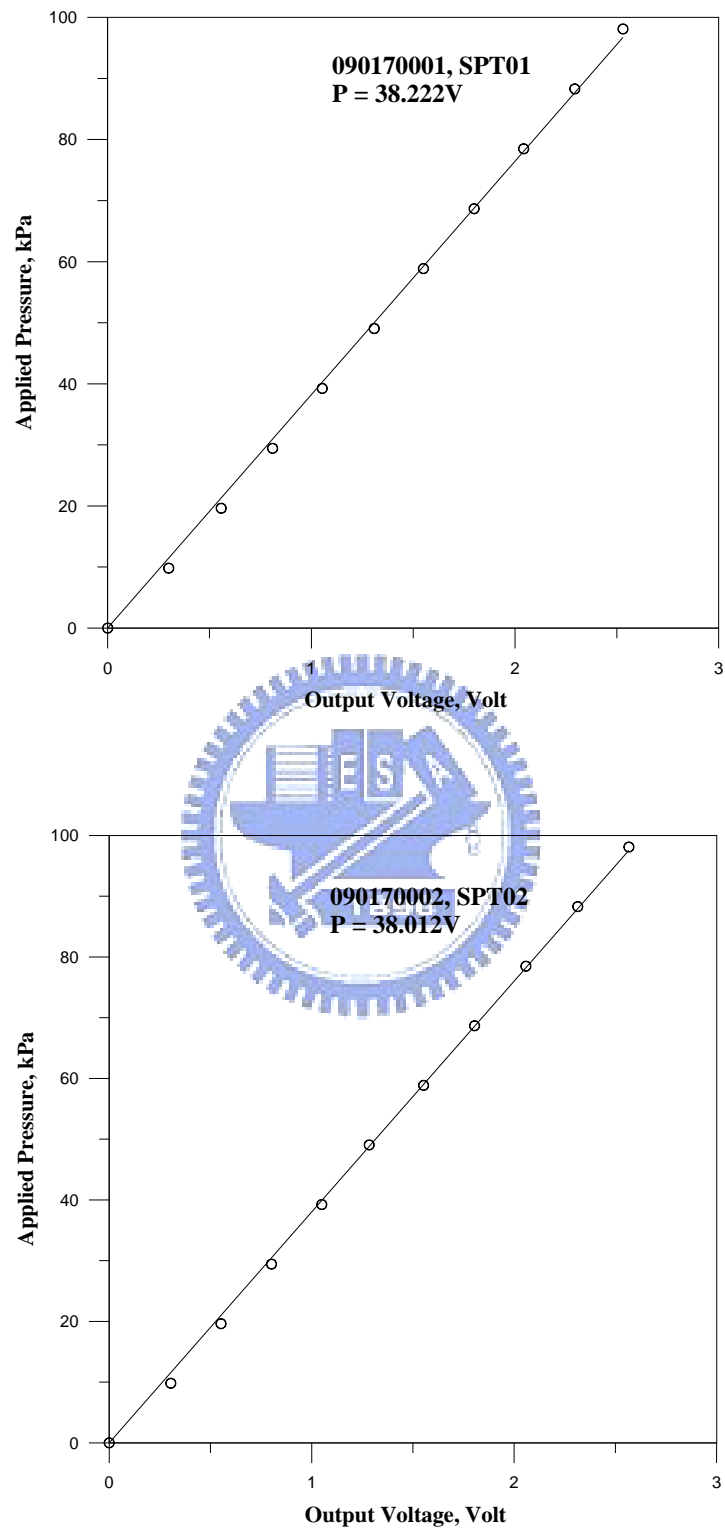


Fig. A.3. Applied pressure versus voltage output for soil pressure transducer SPT01 and SPT02

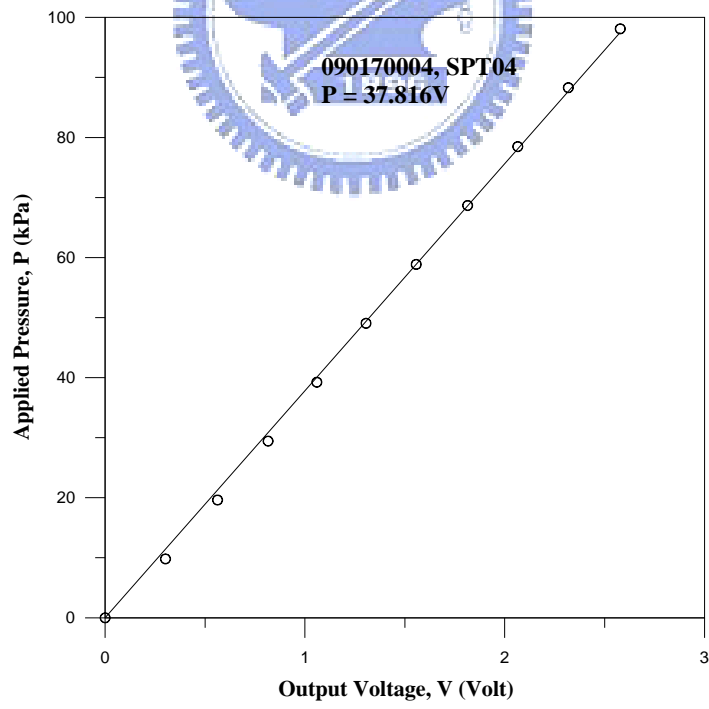
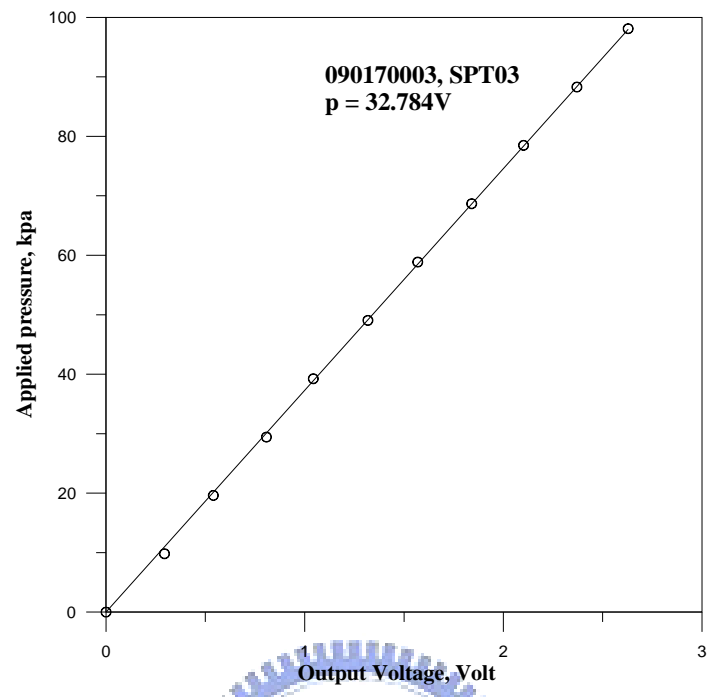


Fig. A.4. Applied pressure versus voltage output for soil pressure transducer SPT03 and SPT04

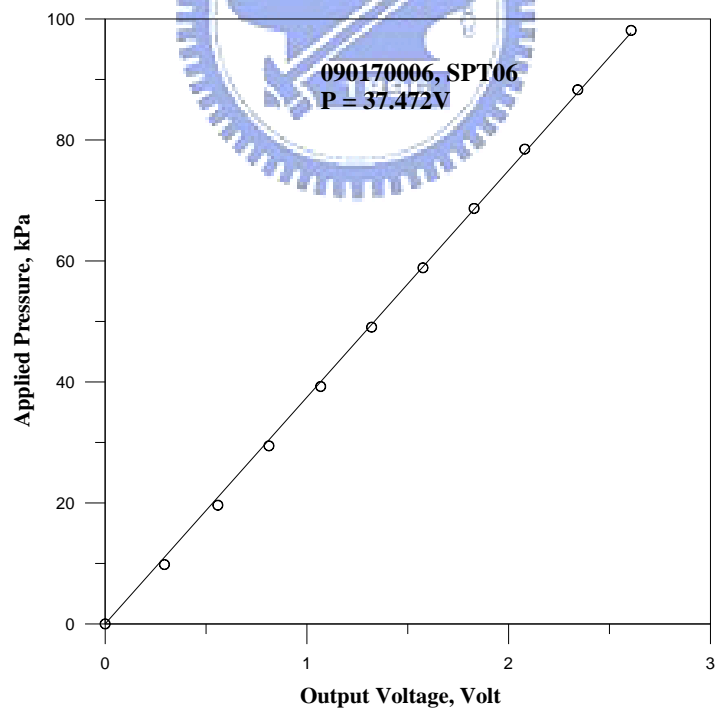
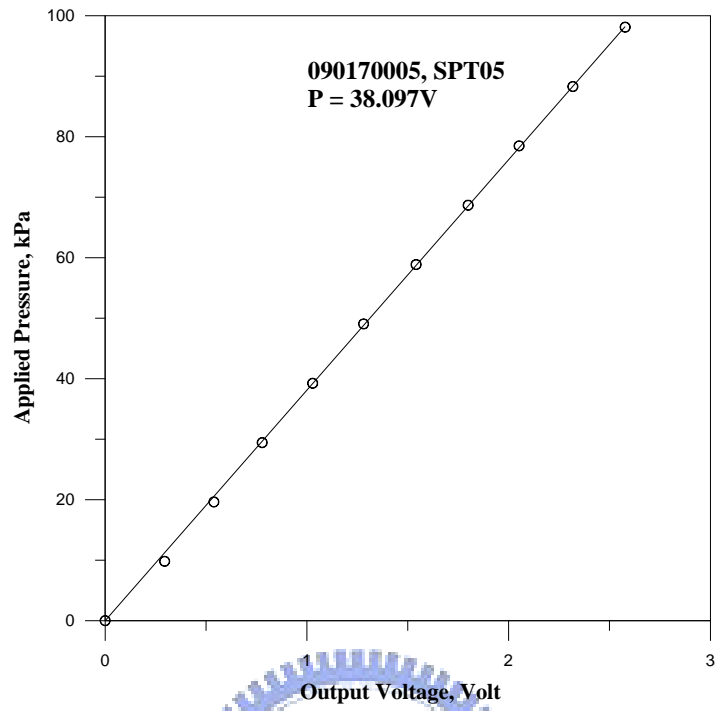


Fig. A.5. Applied pressure versus voltage output for soil pressure transducer SPT05 and SPT06

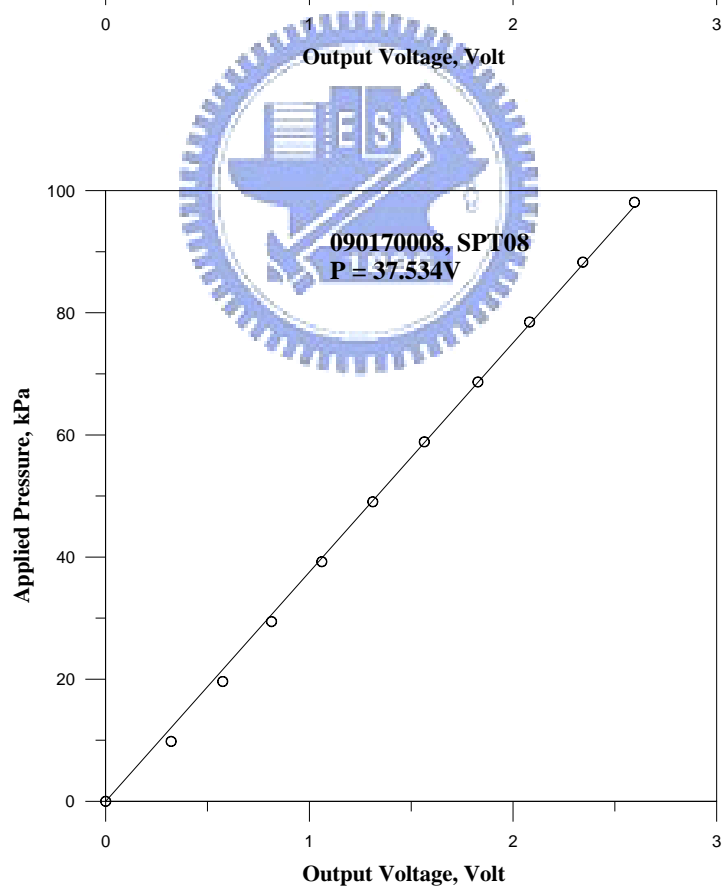
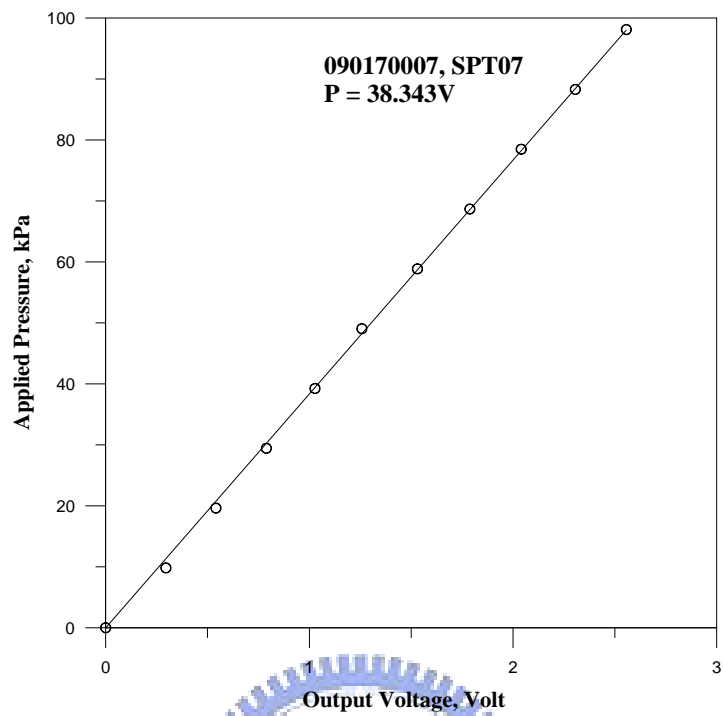


Fig. A.6. Applied pressure versus voltage output for soil pressure transducer SPT07 and SPT08

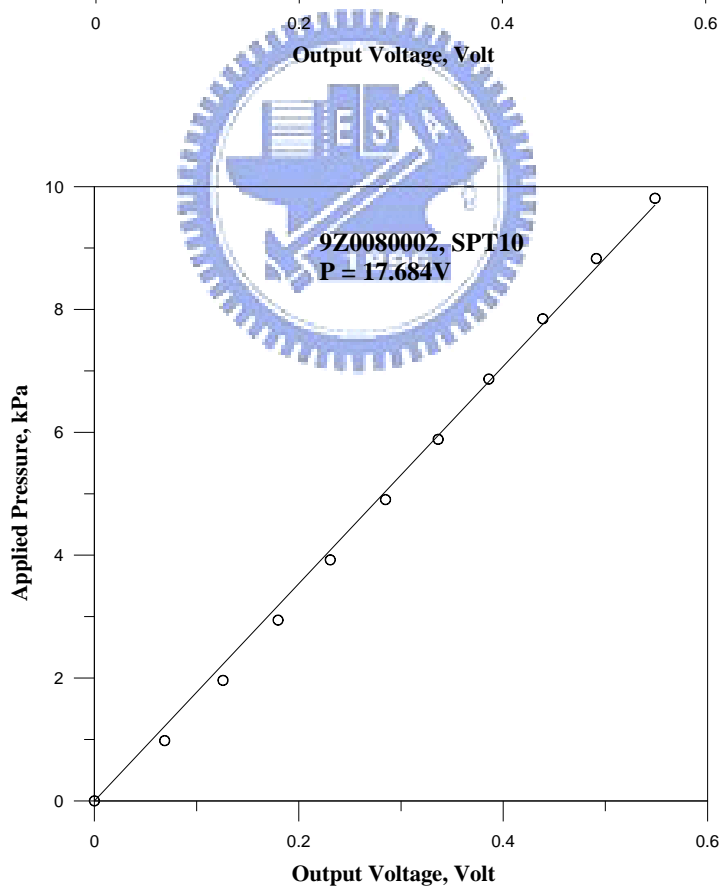
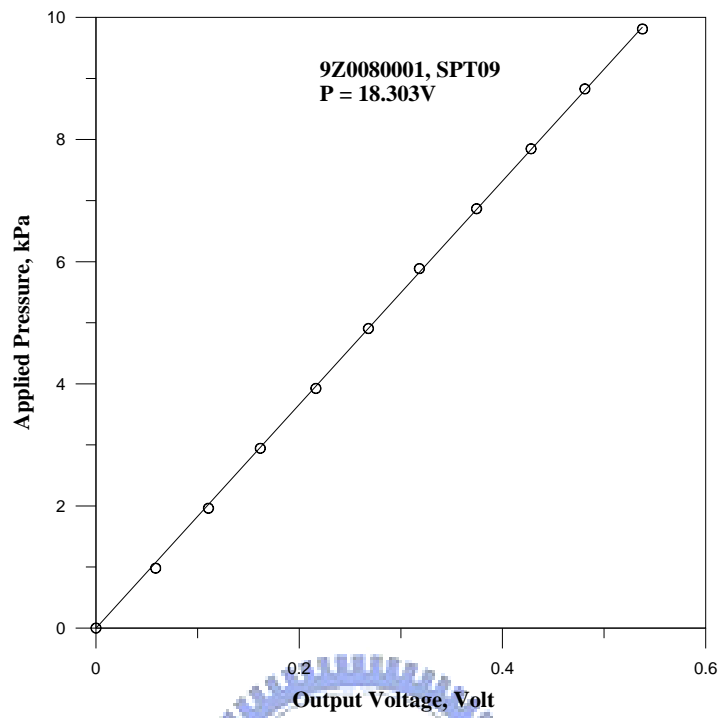


Fig. A.7. Applied pressure versus voltage output for soil pressure transducer SPT09 and SPT10

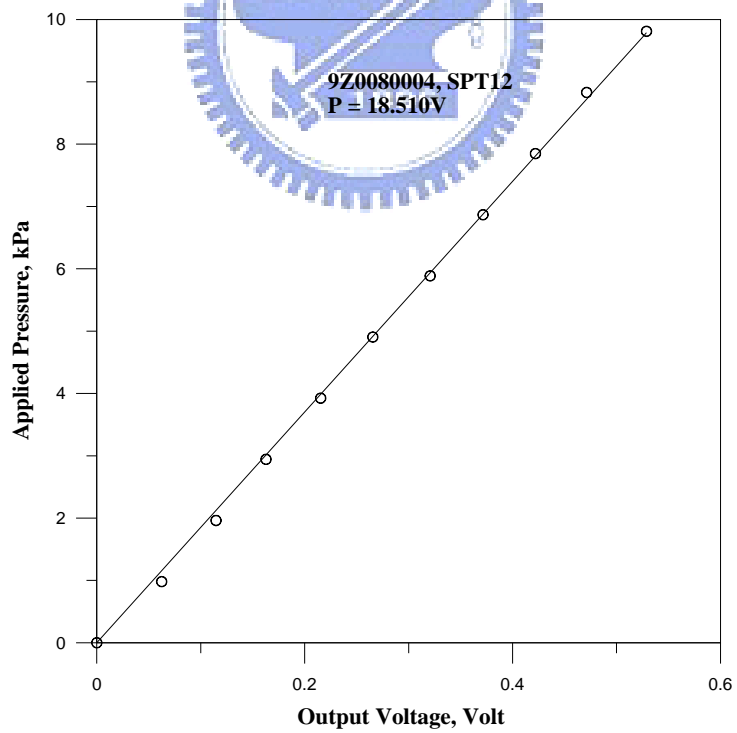
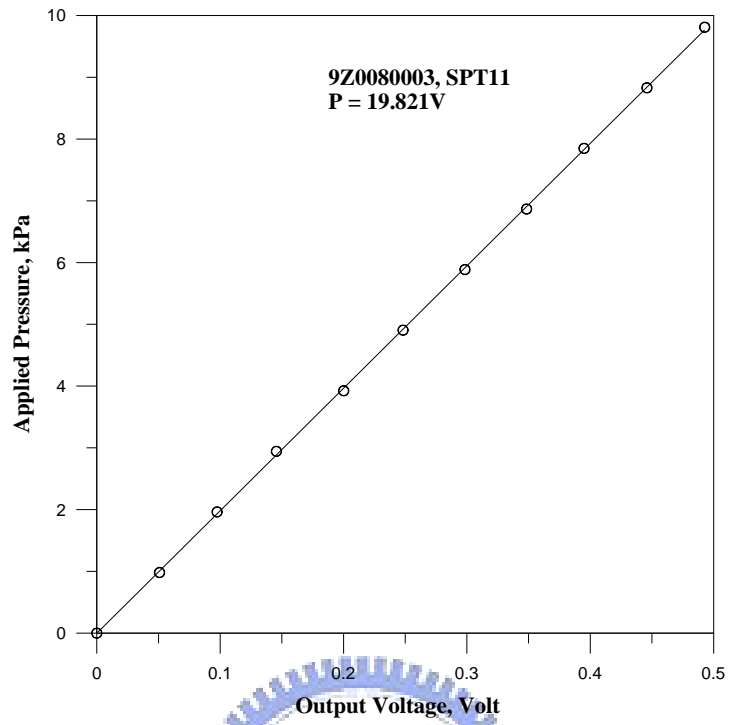


Fig. A.8. Applied pressure versus voltage output for soil pressure transducer SPT11 and SPT12

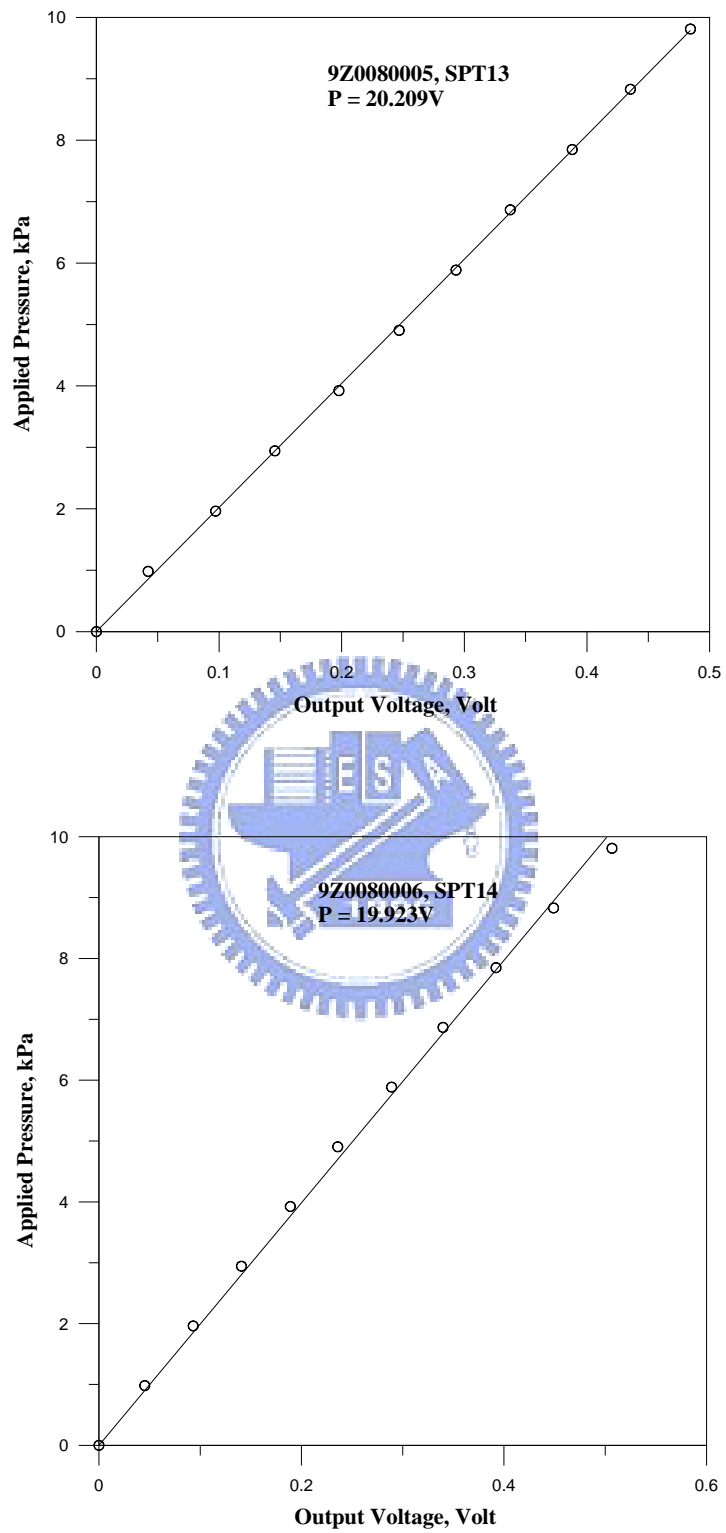


Fig. A.9. Applied pressure versus voltage output for soil pressure transducer SPT13 and SPT14

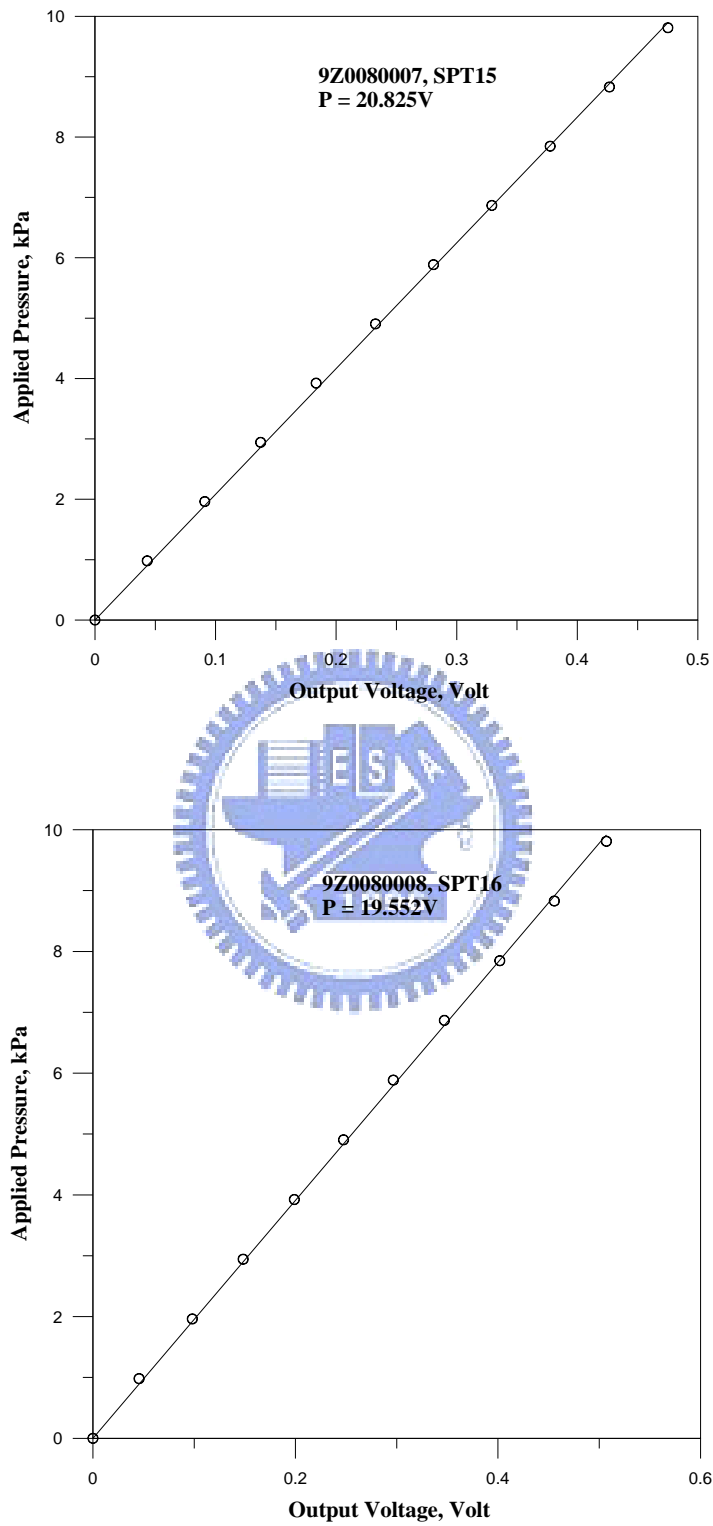
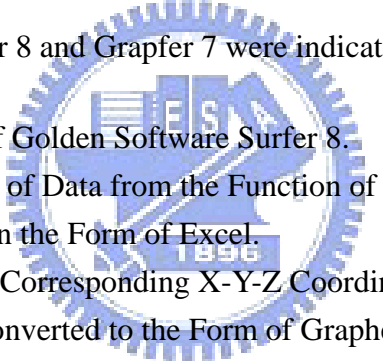


Fig. A.10. Applied pressure versus voltage output for soil pressure transducer SPT15 and SPT16

Appendix B

Operation of Softwares Surfer 8 and Grapher 7

This Appendix introduces the operating procedure of softwares Surfer 8 and Grapher 7. Surfer 8 interpolates with the values at grid points to form the data files of the contour line. Grapher 7 draws the contours by open the data files (Grapher Grid). The details of operation of Surfer 8 and Grapher 7 were indicated in the following:

- 
- Step 1. Open the Program of Golden Software Surfer 8.
 - Step 2. Choose the Function of Data from the Function of Grid.
 - Step 3. Open the Test Data in the Form of Excel.
 - Step 4. Choose Test Data to Corresponding X-Y-Z Coordinate.
 - Step 5. The Test Data are Converted to the Form of Grapher Grid.
 - Step 6. Open the Program of Golden Software Grapher 7.
 - Step 7. Choose the Function of XY Grid in Contour Maps from the Function of Graph.
 - Step 8. Open the Foregoing Saved file of Grapher Grid.
 - Step 9. The Contours was Drawn by Surfer 7 with Adjust the Show Type.

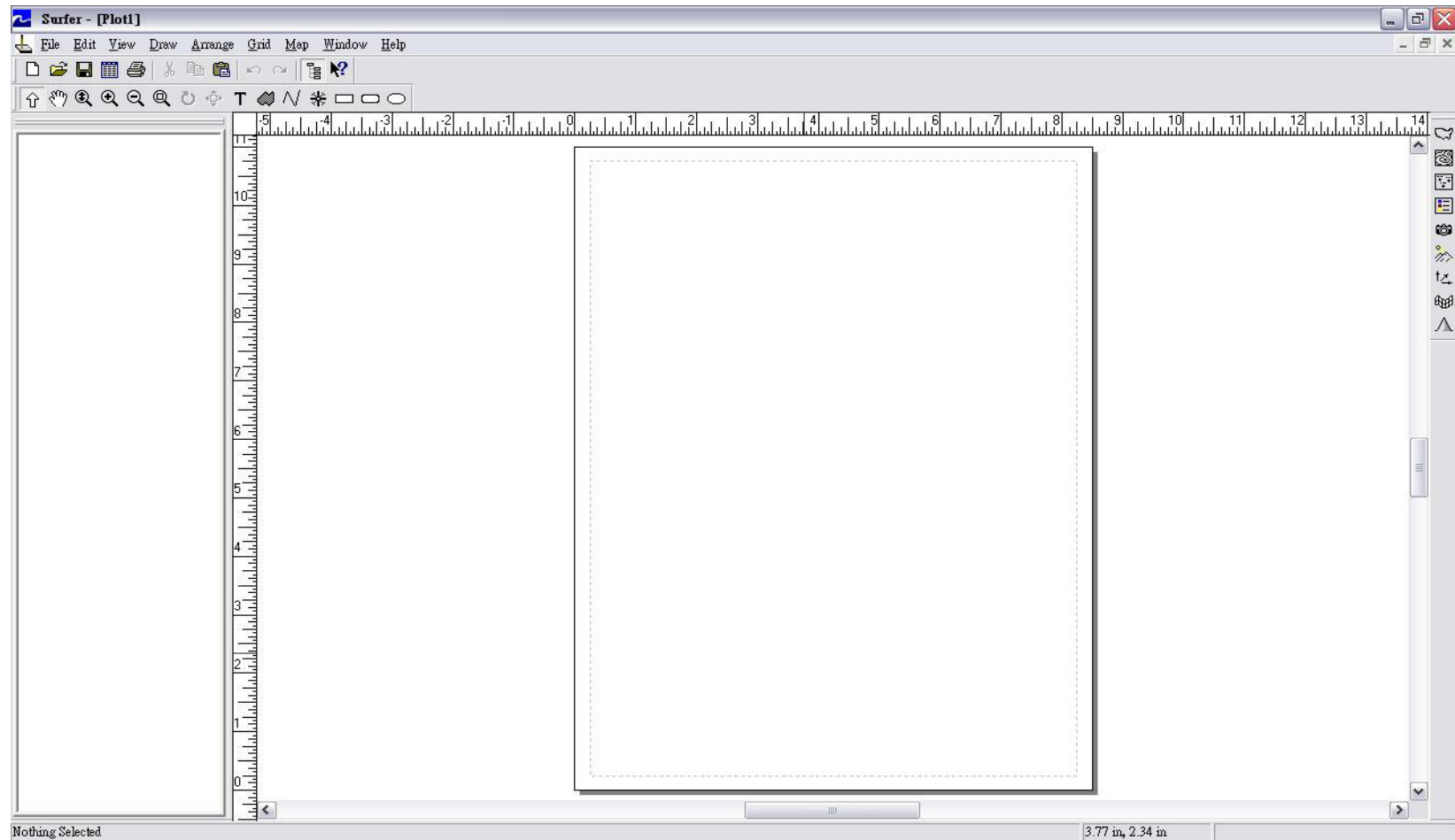


Fig. B.1. Open the Program of Golden Software Surfer 8

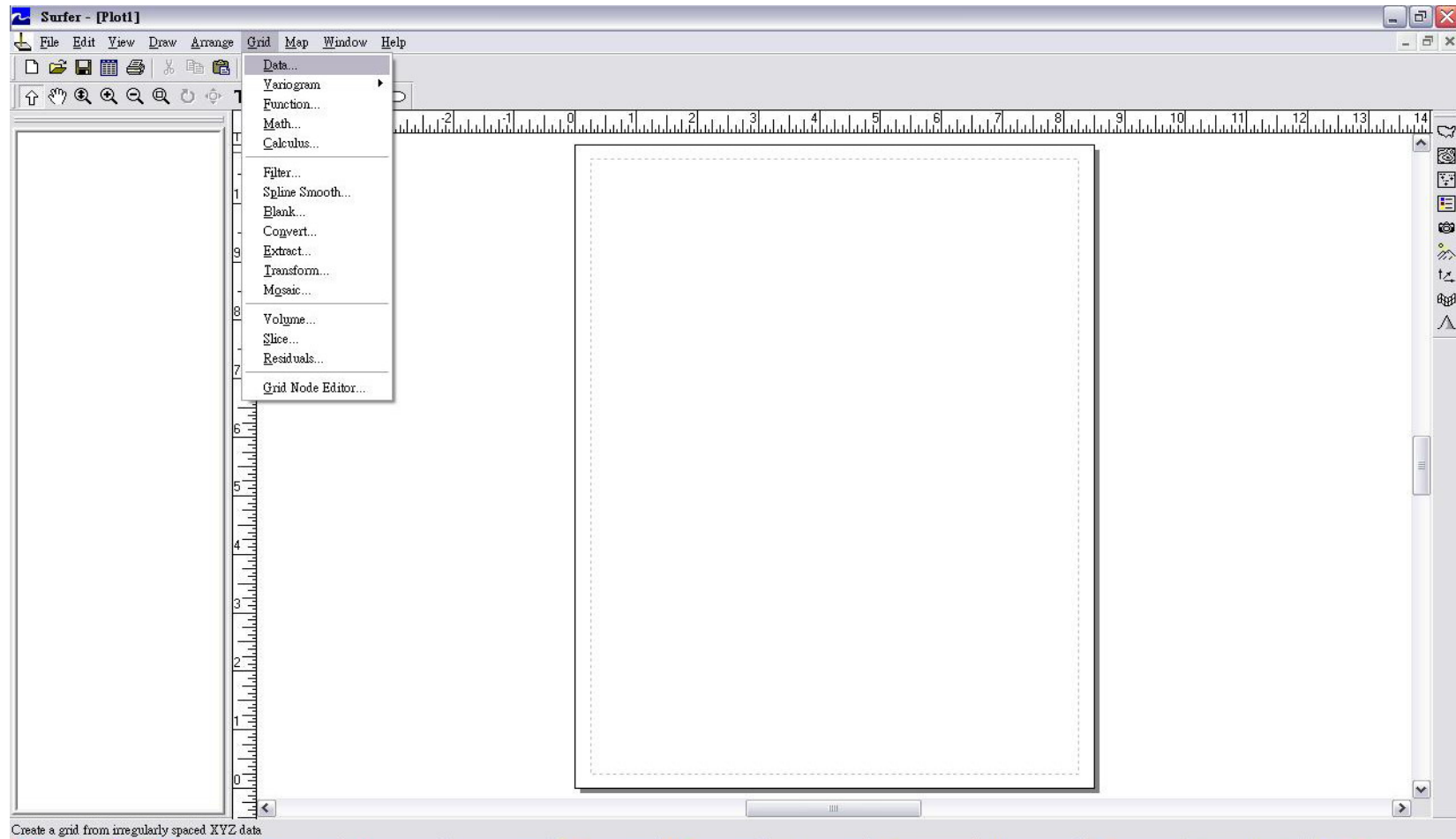


Fig. B.2. Choose the Function of Data from the Function of Grid

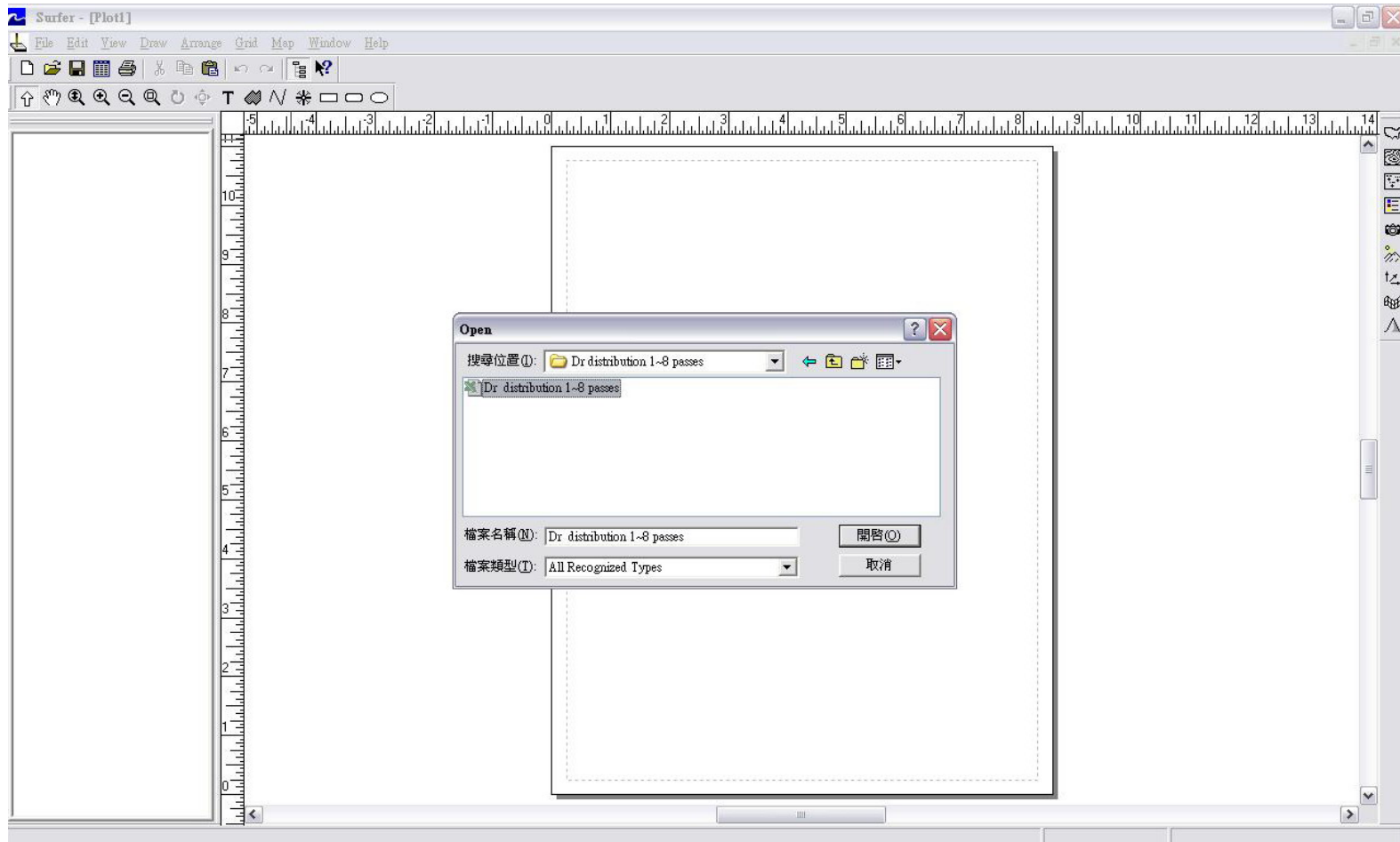


Fig. B.3. Open the Test Data in the Form of Excel

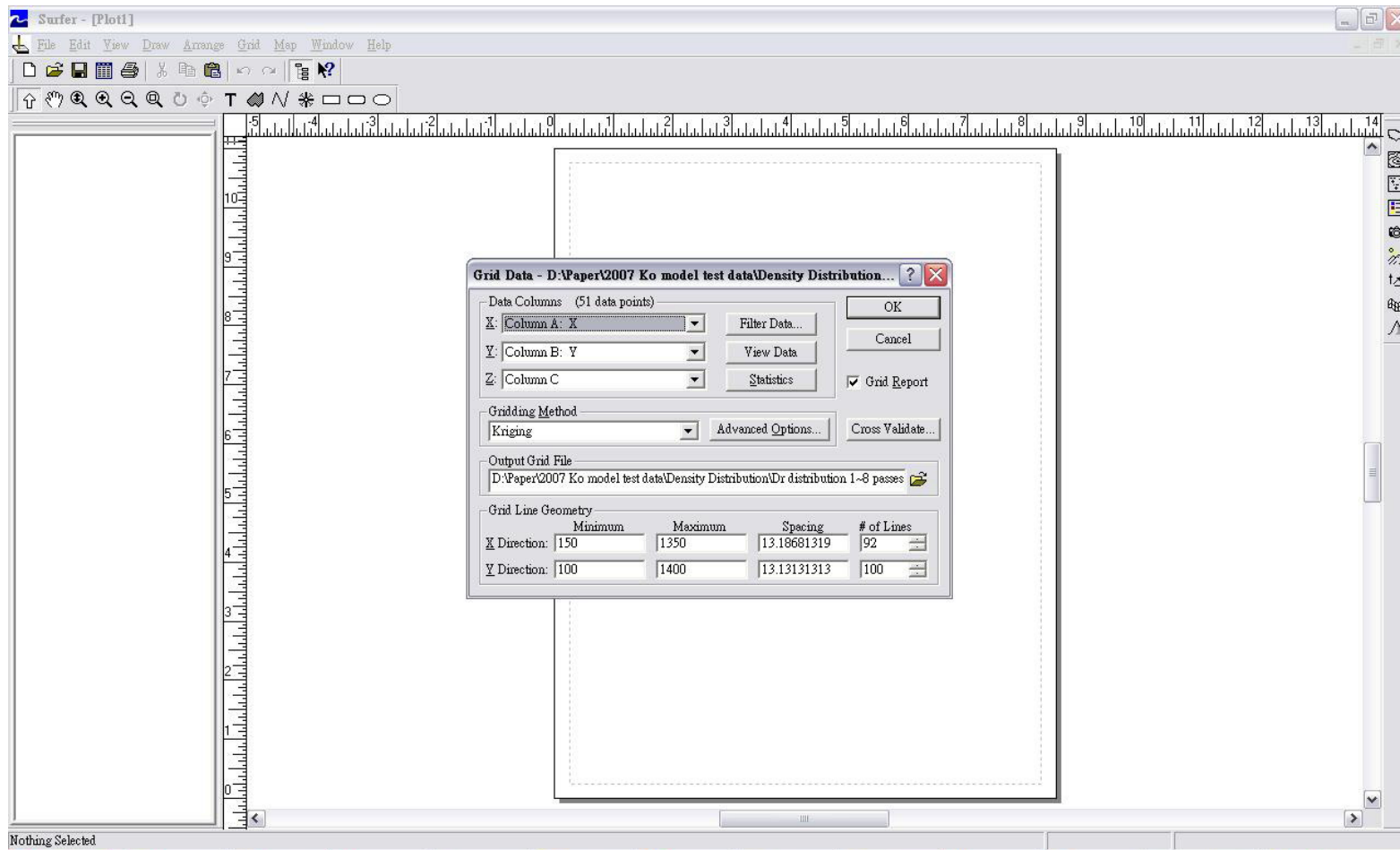


Fig. B.4. Choose Test Data to Corresponding X-Y-Z Coordinate

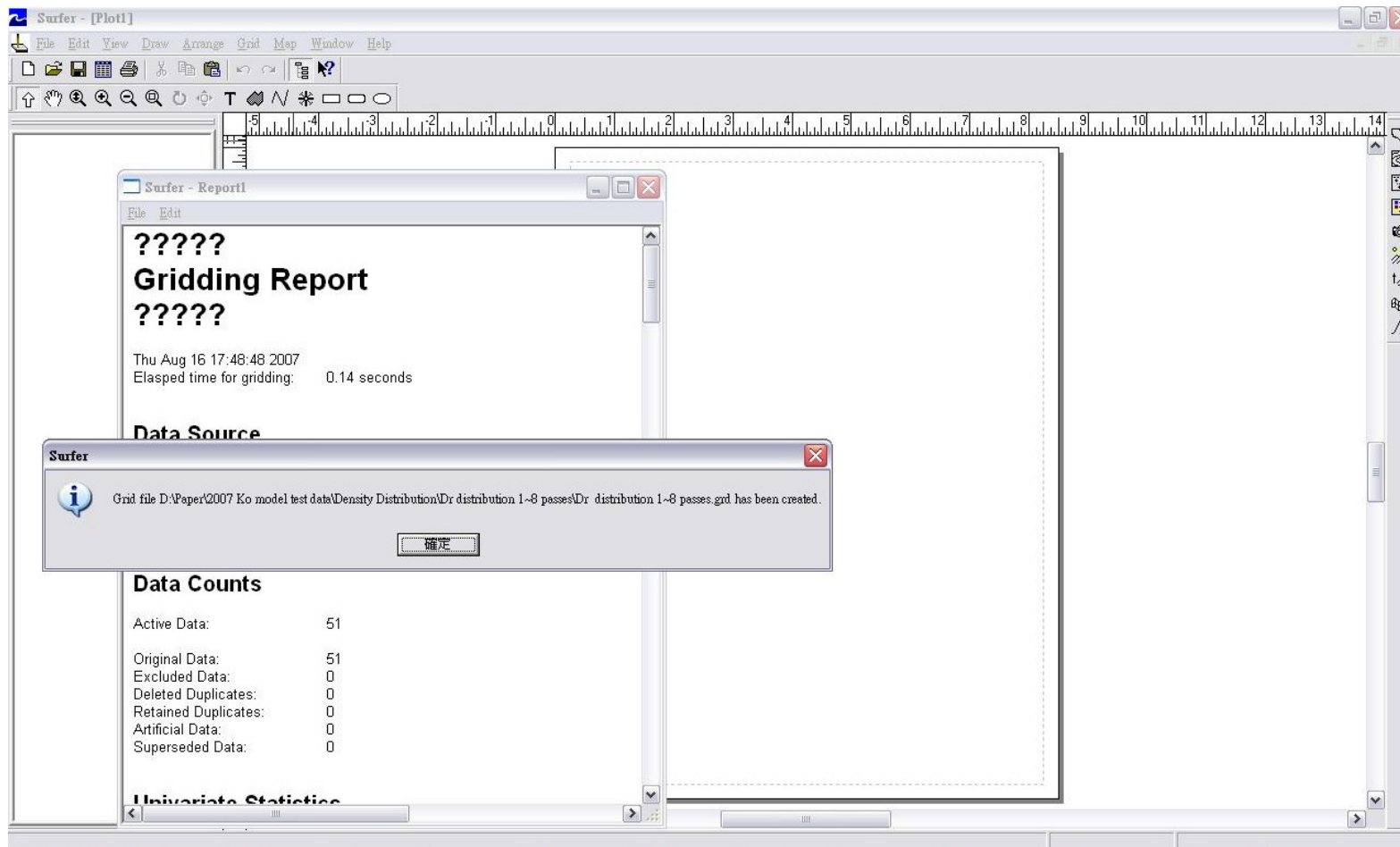


Fig. B.5. The Test Data are Converted to the Form of Grapher Grid

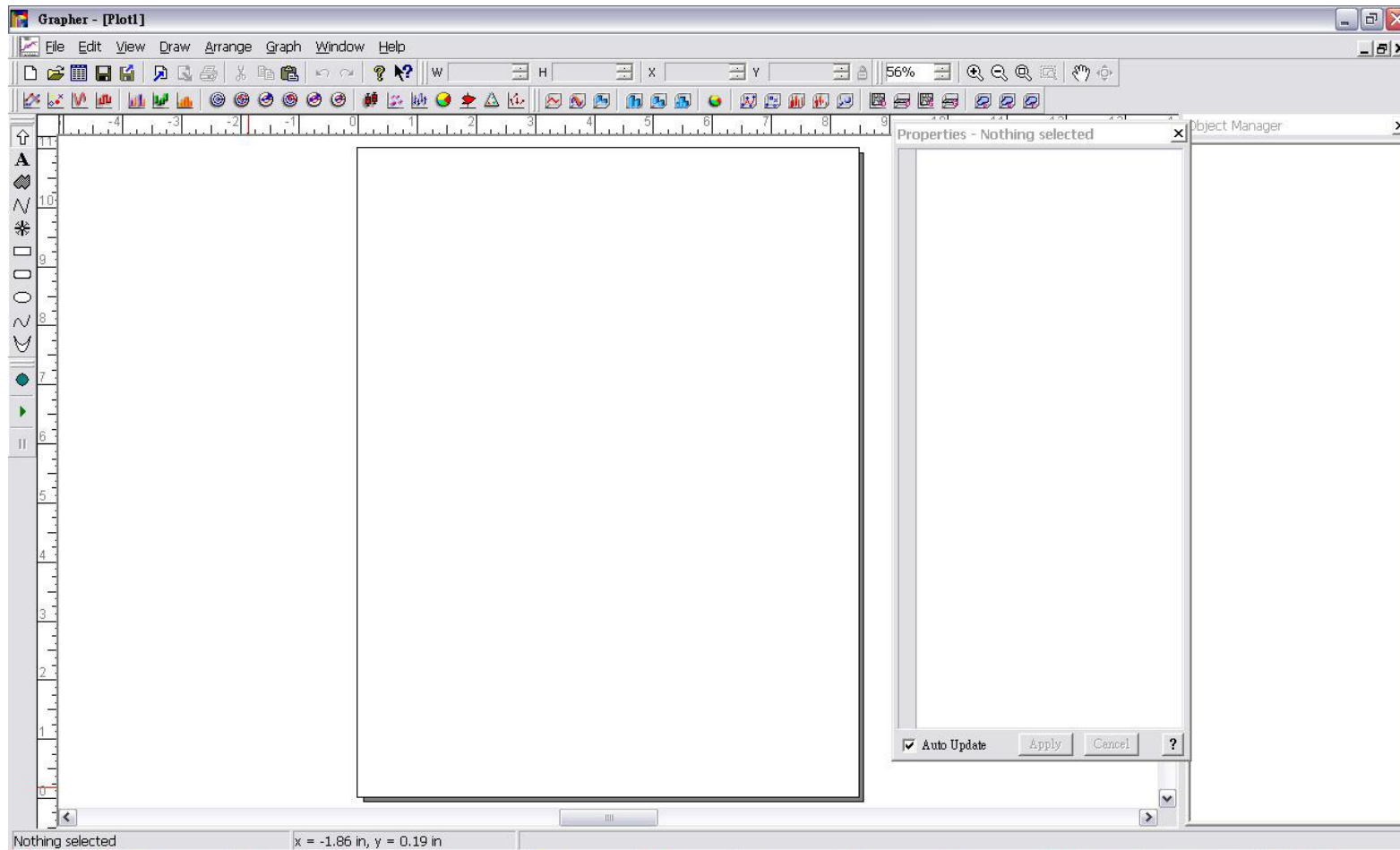


Fig. B.6. Open the Program of Golden Software Grapher 7

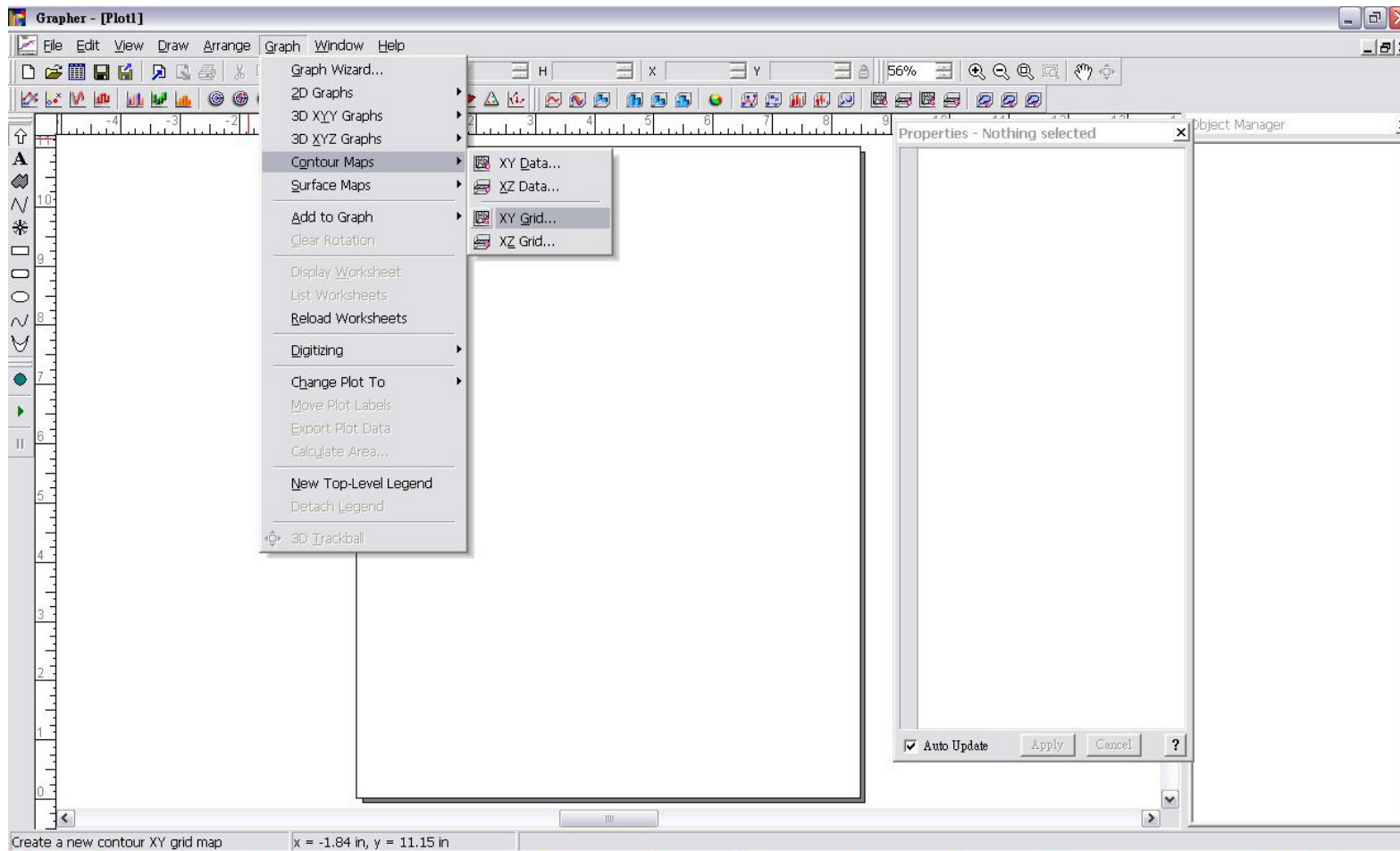


Fig. B.7. Choose the Function of XY Grid in Contour Maps from the Function of Graph

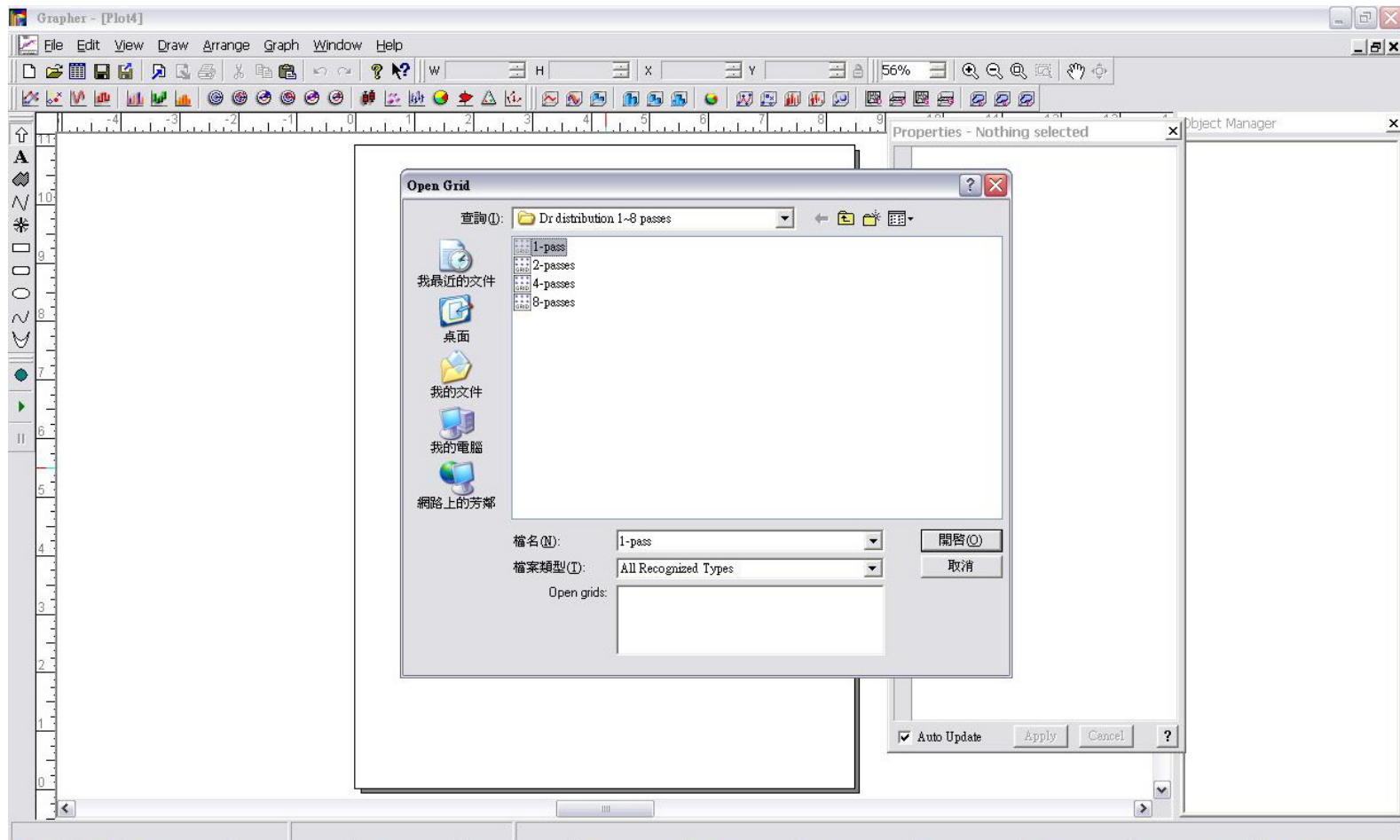


Fig. B.8. Open the Foregoing Saved file of Grapher Grid

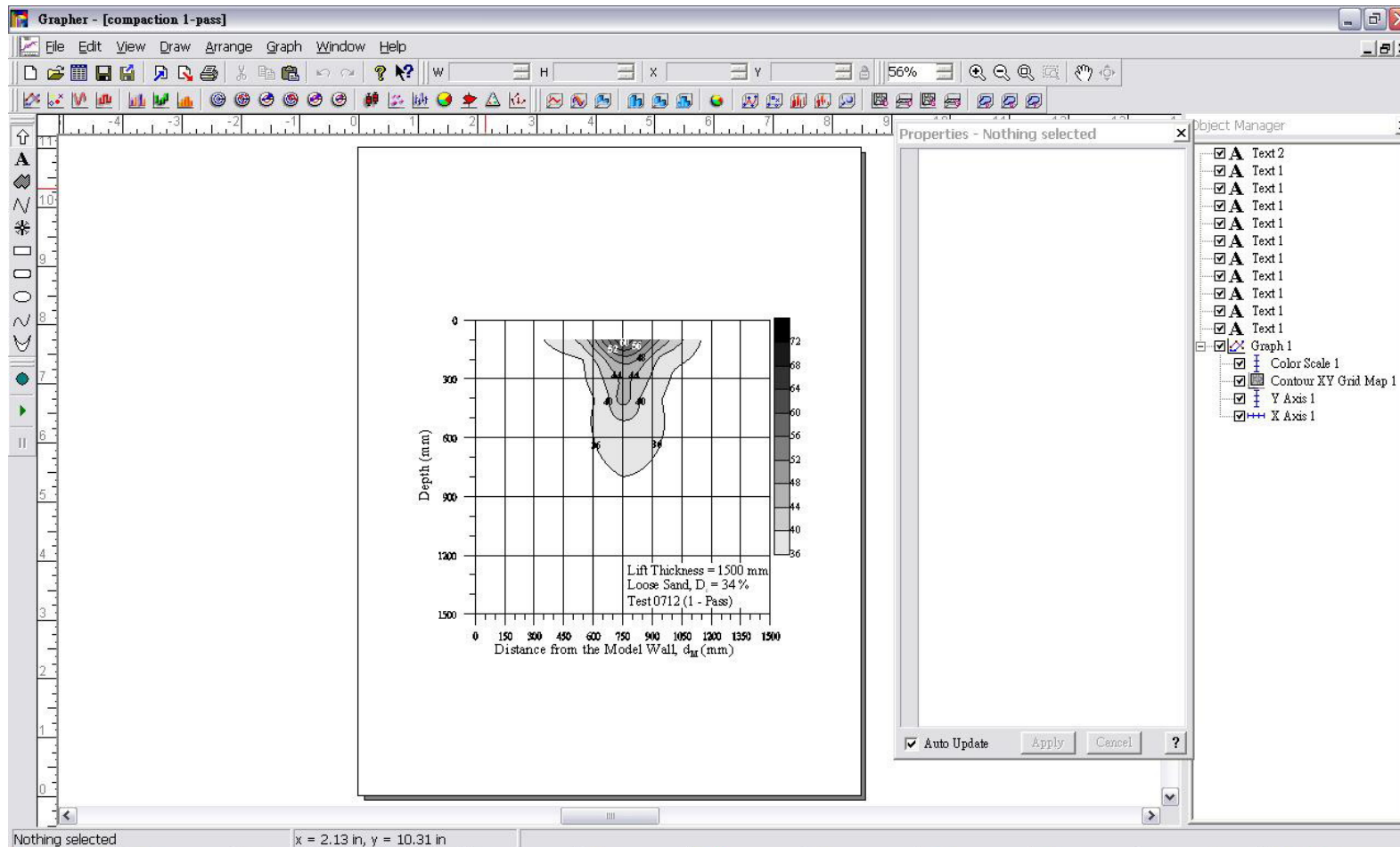


Fig. B.9. The Contours was Drawn by Surfer 7 with Adjust the Show Type.

Appendix C

Test Results at Grid Points

Appendix C shows the values of test results at grid points including three parts : (1) relative density of sand; (2) change of vertical stress; and (3) change of horizontal stress in the soil mass. The values at grid points were interpolated to establish the contour maps.



C1. Relative Density of Sand at Grid Points

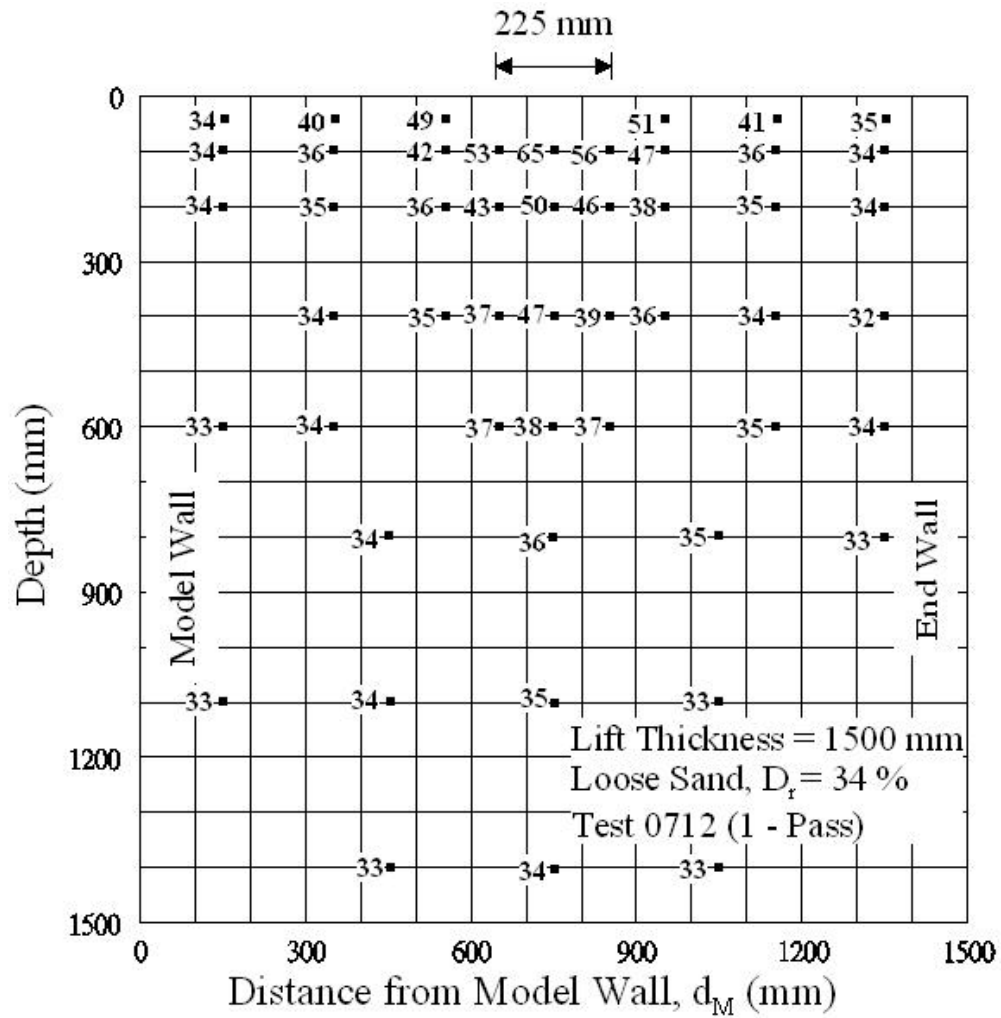


Fig. C1.1. Relative Density of Sand at Grid Points after 1 – Pass of Compactor

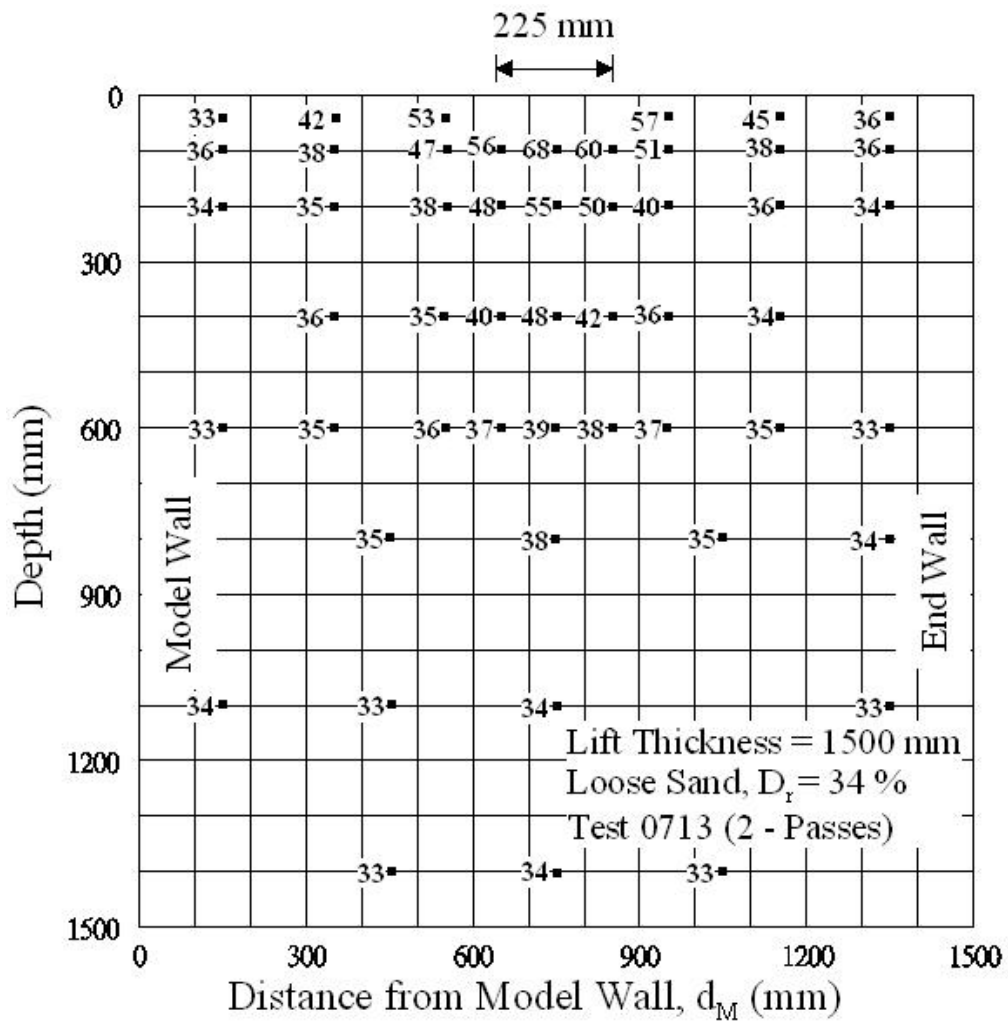


Fig. C1.2. Relative Density of Sand at Grid Points after 2 – Passes of Compactor

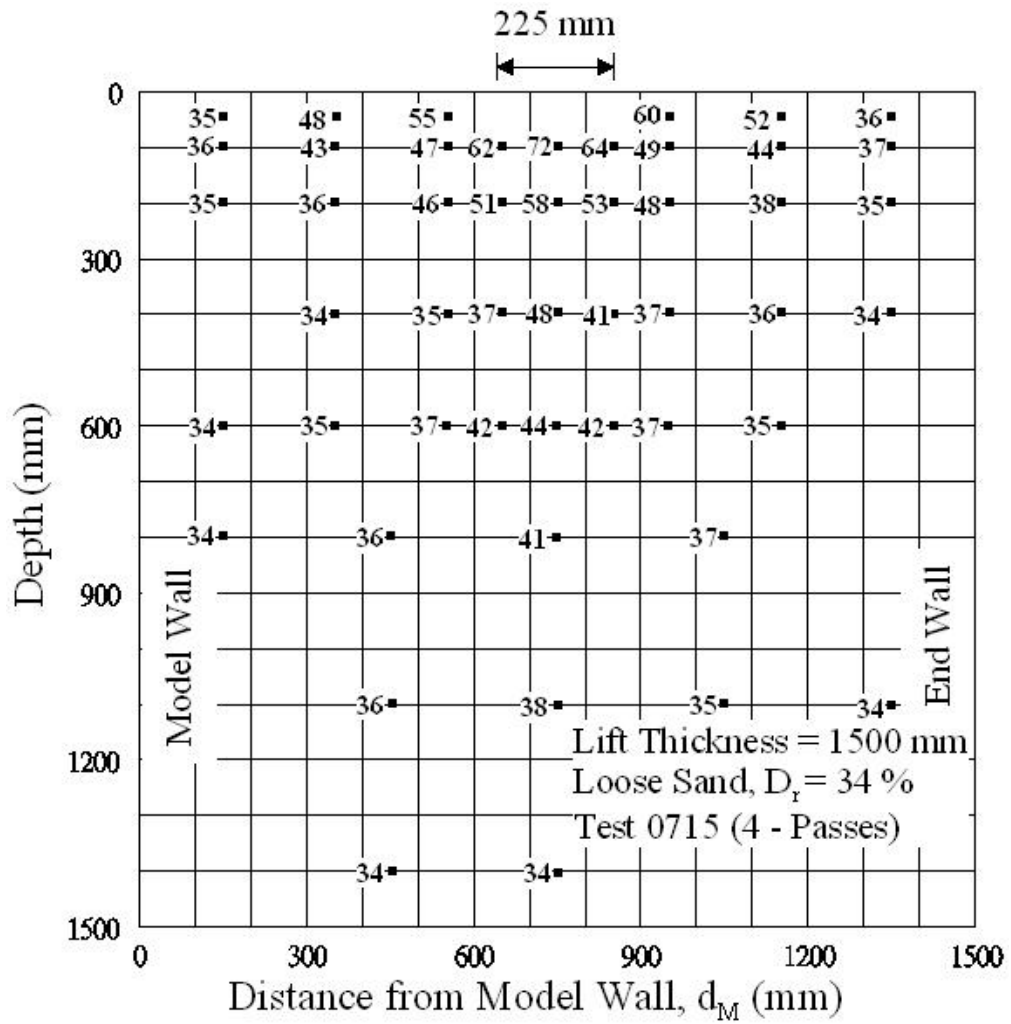


Fig. C1.3. Relative Density of Sand at Grid Points after 4 – Passes of Compactor

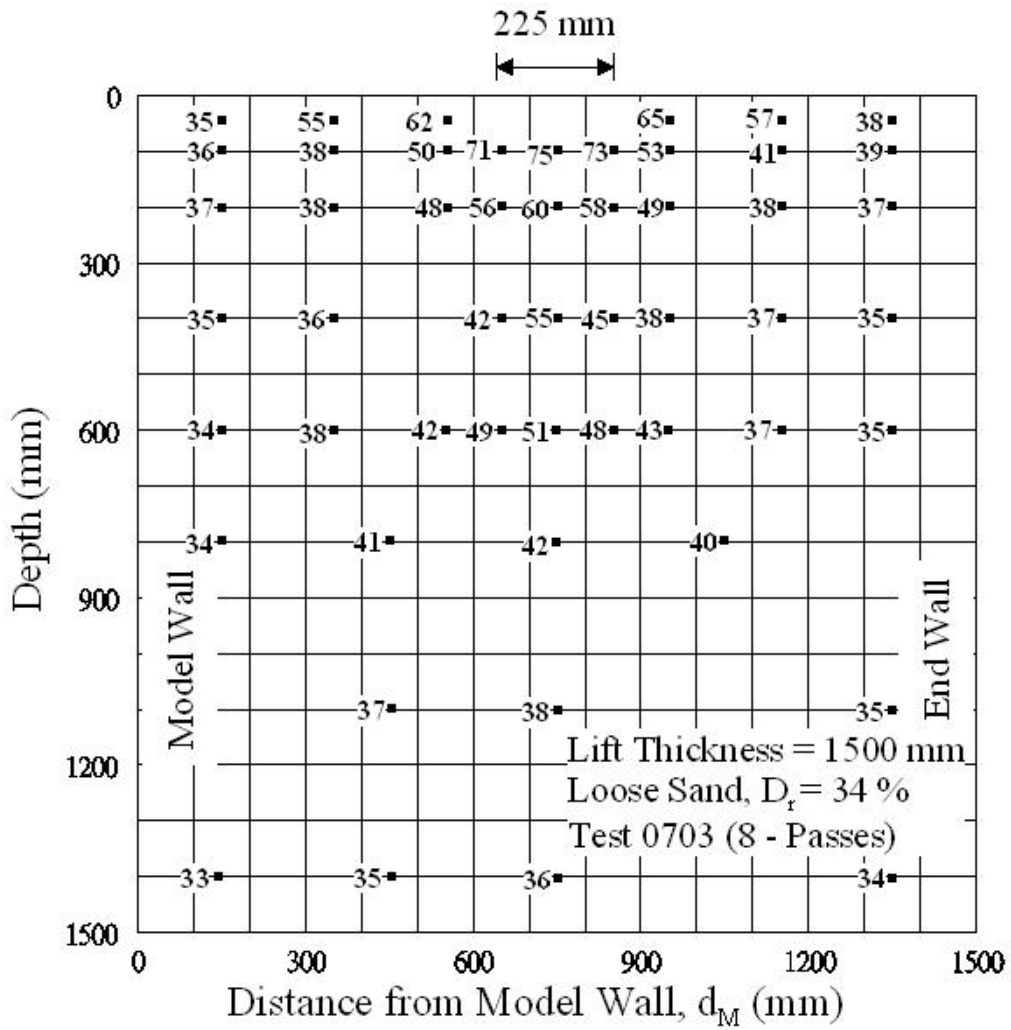


Fig. C1.4. Relative Density of Sand at Grid Points after 8 – Passes of Compactor

C2. $\Delta\sigma_v$ at Grid Points

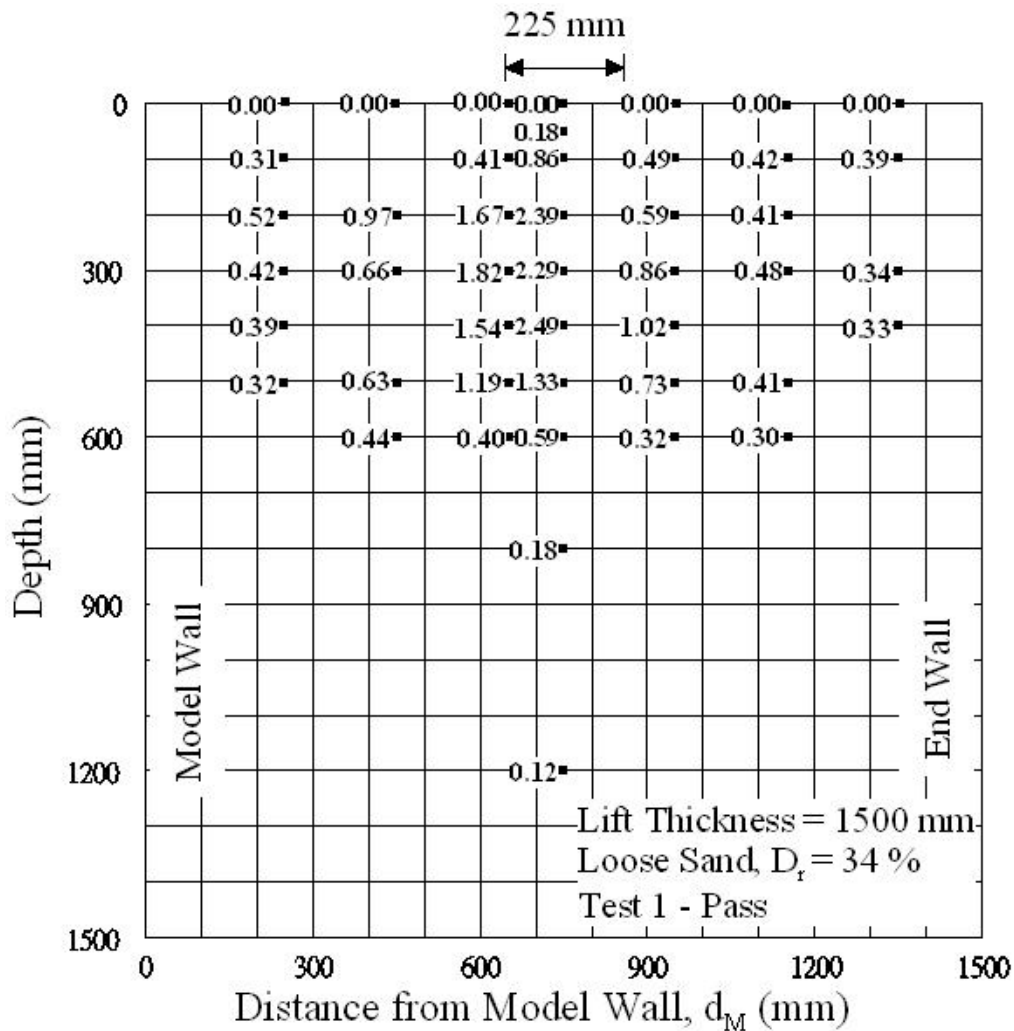


Fig. C2.1. $\Delta\sigma_v$ at Grid Points after 1 – Pass of Compactor

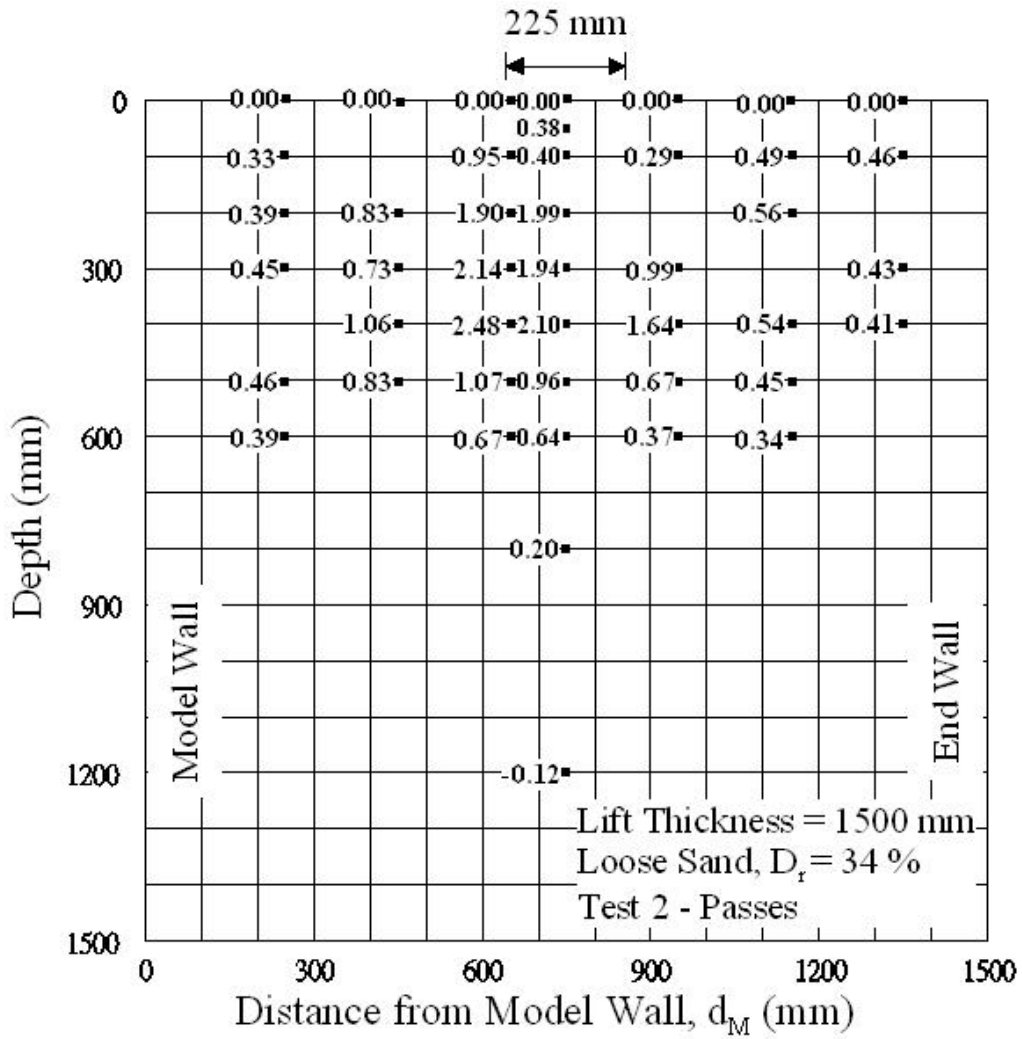


Fig. C2.2. $\Delta\sigma_v$ at Grid Points after 2 – Passes of Compactor

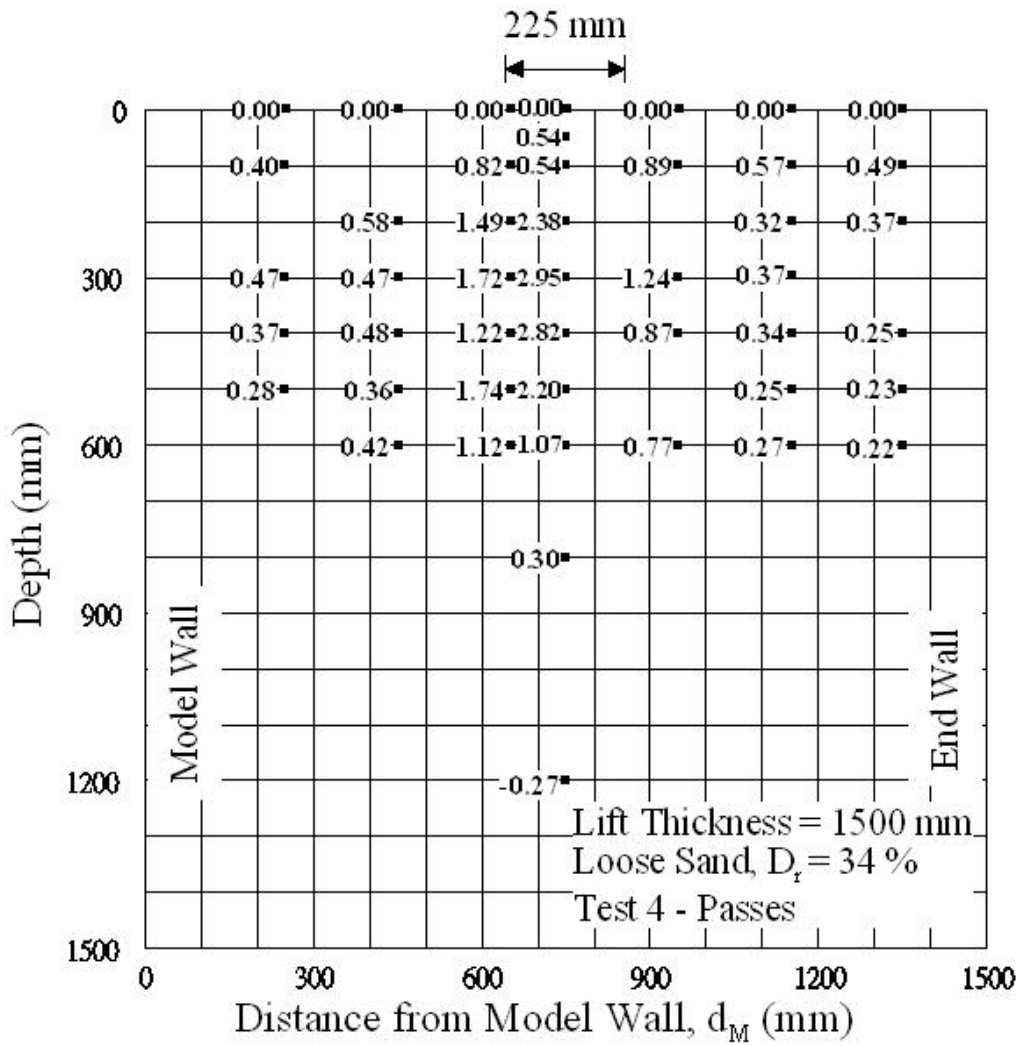


Fig. C2.3. $\Delta\sigma_v$ at Grid Points after 4 – Passes of Compactor

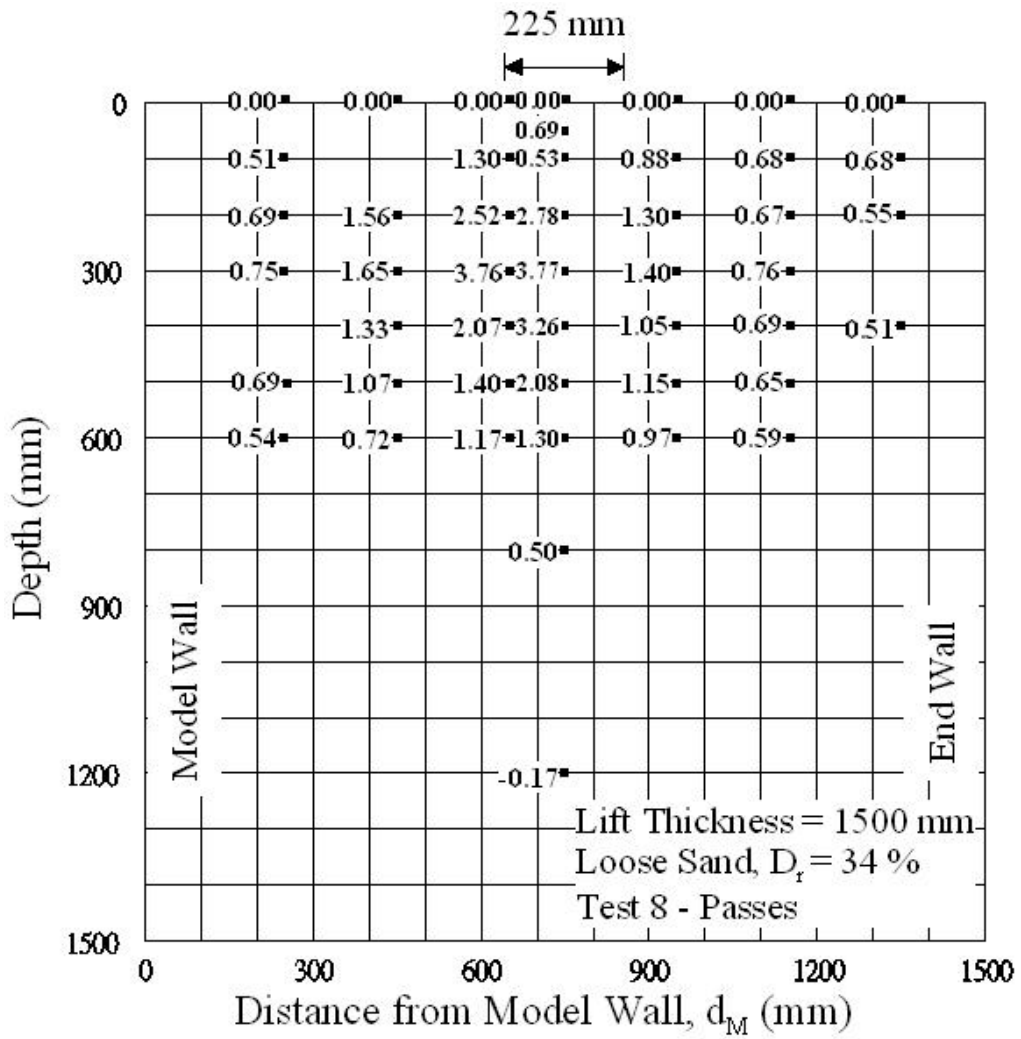


Fig. C2.4. $\Delta\sigma_v$ at Grid Points after 8 – Passes of Compactor

C3. $\Delta\sigma_h$ at Grid Points

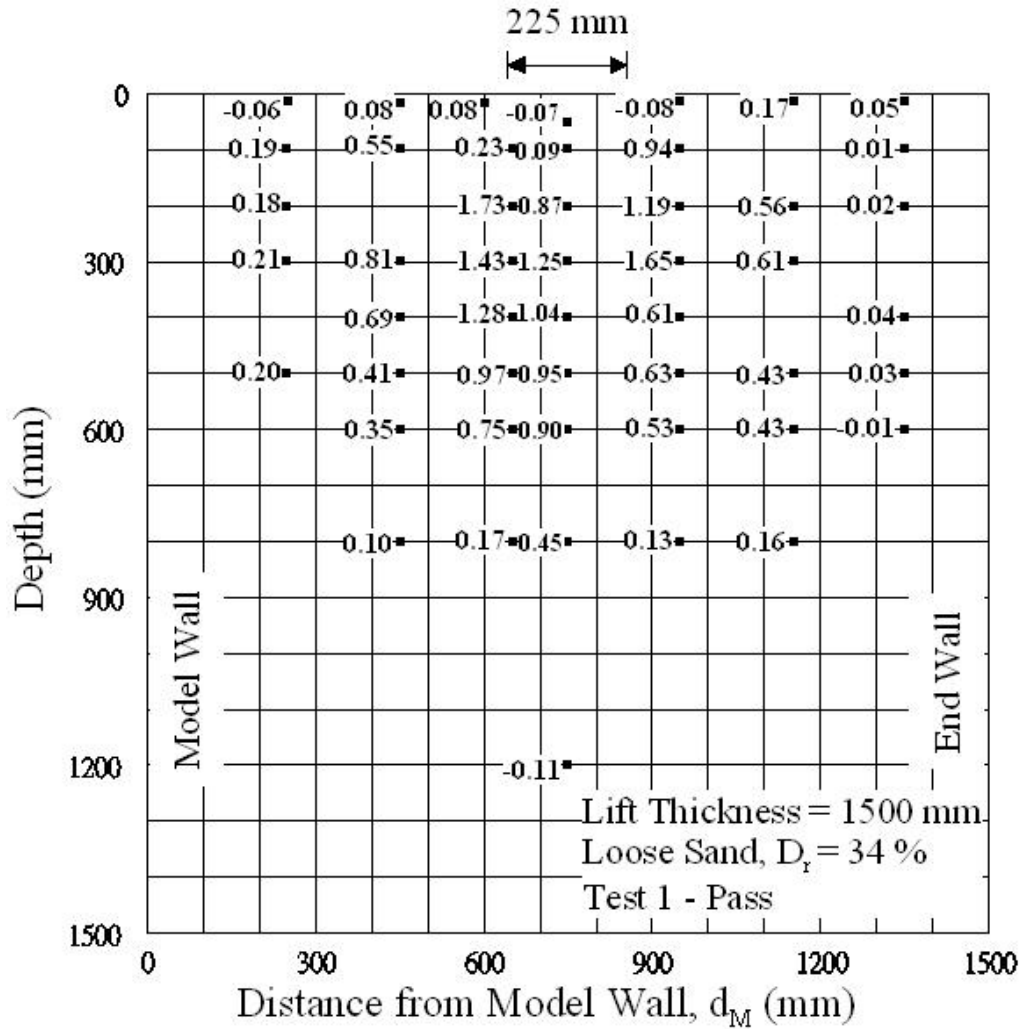


Fig. C3.1. $\Delta\sigma_h$ at Grid Points after 1 – Pass of Compactor

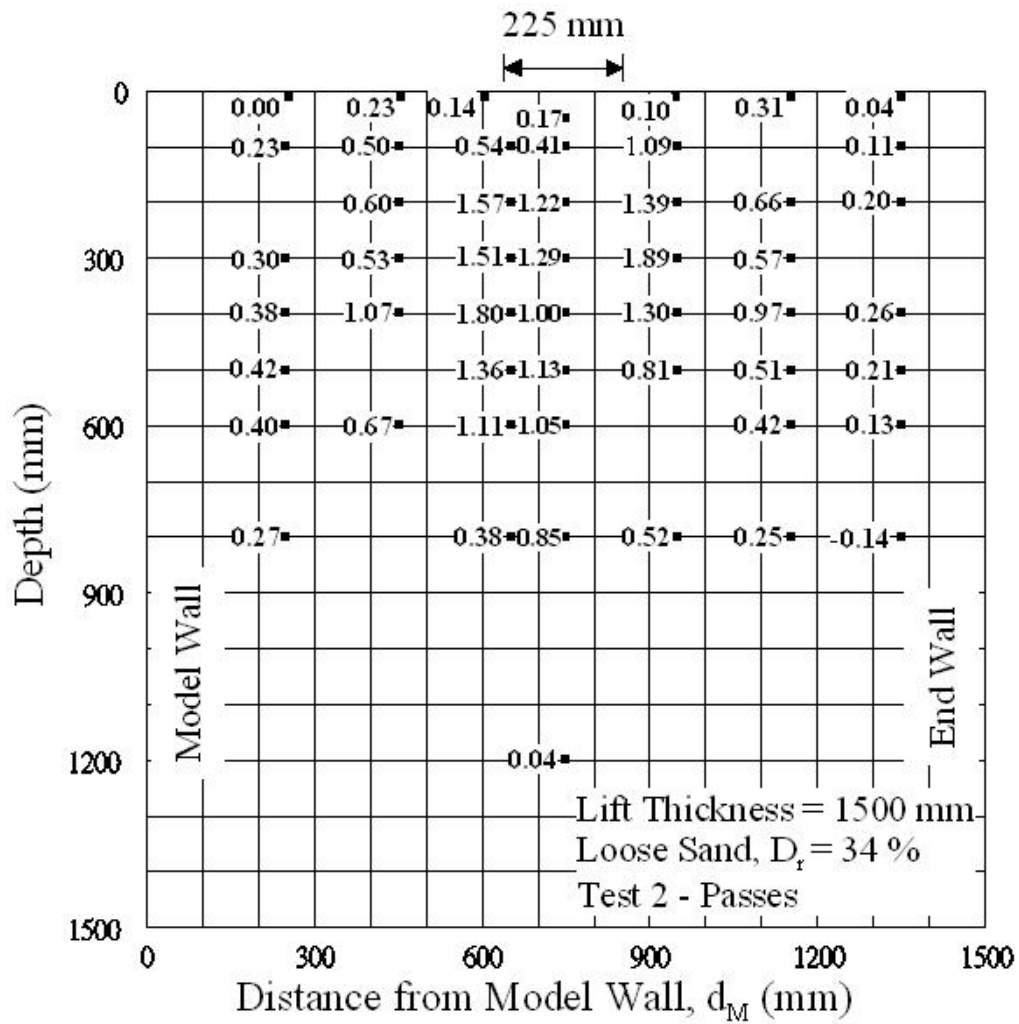


Fig. C3.2. $\Delta\sigma_h$ at Grid Points after 2 – Passes of Compactor

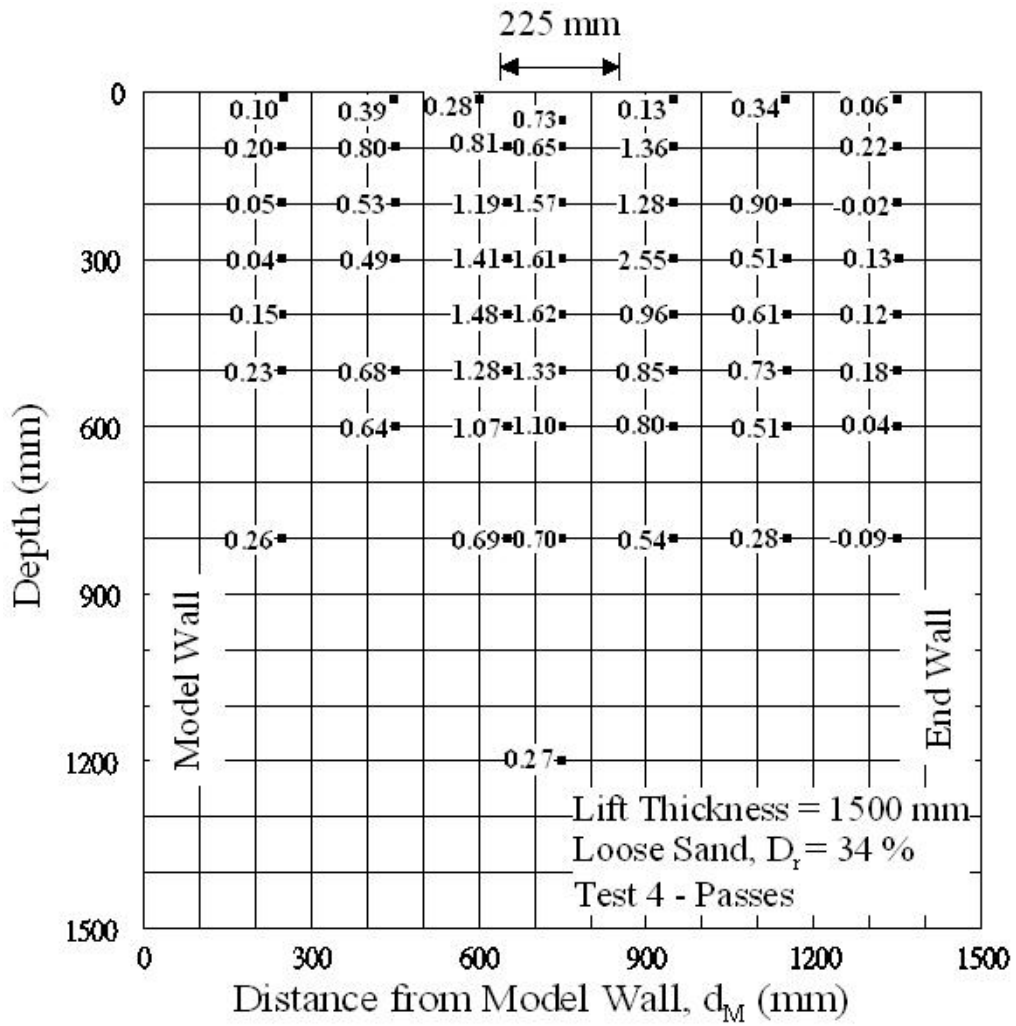


Fig. C3.3. $\Delta\sigma_h$ at Grid Points after 4 – Passes of Compactor

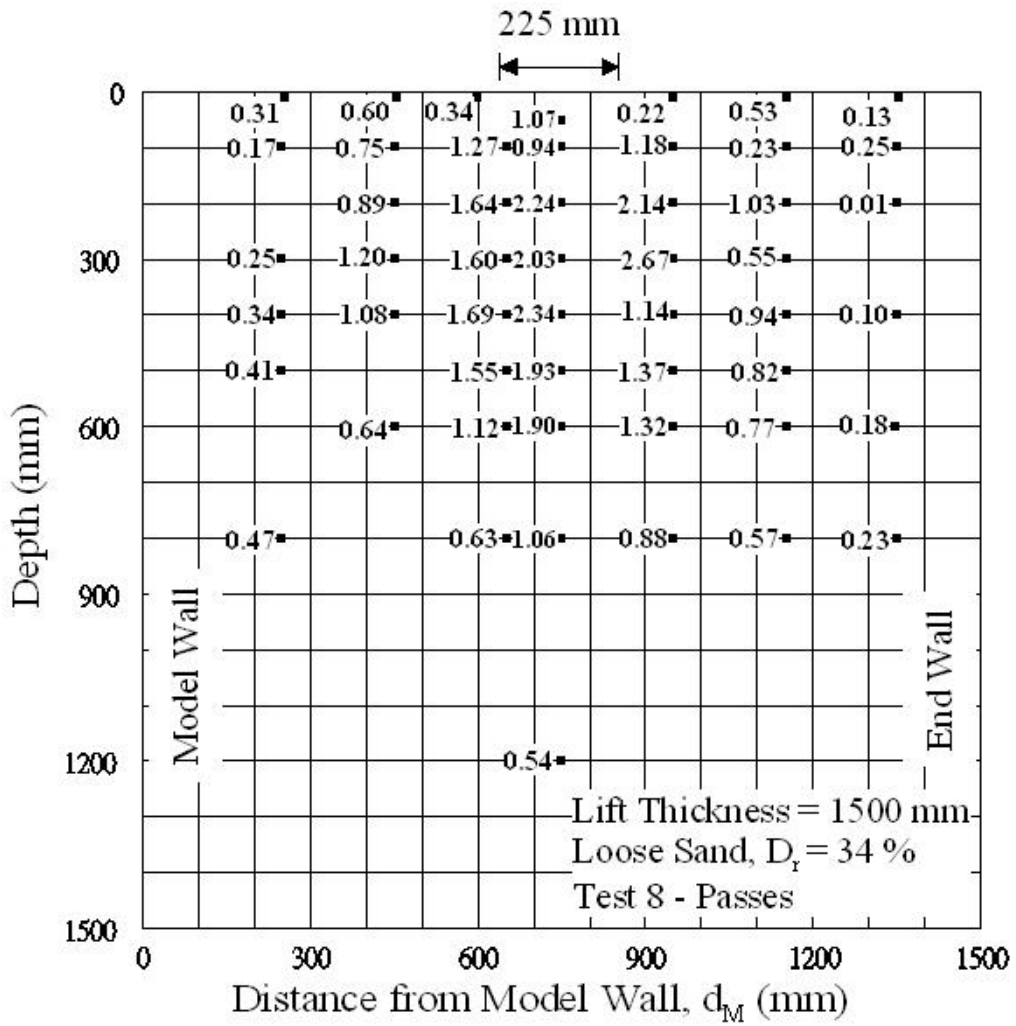


Fig. C3.4. $\Delta\sigma_h$ at Grid Points after 8 – Passes of Compactor